

Electronic Thesis and Dissertation Repository

July 2012

Response of Foundations to Random Cyclic Loads

Alireza Varshoi
The University of Western Ontario

Supervisor
Dr. Tim. A. Newson
The University of Western Ontario

Graduate Program in Civil and Environmental Engineering
A thesis submitted in partial fulfillment of the requirements for the degree in Master of
Engineering Science
© Alireza Varshoi 2012

Follow this and additional works at: <https://ir.lib.uwo.ca/etd>



Part of the [Geotechnical Engineering Commons](#)

Recommended Citation

Varshoi, Alireza, "Response of Foundations to Random Cyclic Loads" (2012). *Electronic Thesis and Dissertation Repository*. 625.
<https://ir.lib.uwo.ca/etd/625>

This Dissertation/Thesis is brought to you for free and open access by Scholarship@Western. It has been accepted for inclusion in Electronic Thesis and Dissertation Repository by an authorized administrator of Scholarship@Western. For more information, please contact wlsadmin@uwo.ca.

Response of Foundations to Random Cyclic Loads

Thesis Format: Monograph

By

Alireza Varshoi

Graduate Program in Civil and Environmental Engineering

A thesis is submitted in partial fulfillment
of the requirements for the degree of
Master of Engineering Science

The School of Graduate and Postdoctoral Studies
The University of Western Ontario
London, Ontario, Canada

© Alireza Varshoi 2012

The University of Western Ontario
School of Graduate and Post Graduate Studies

CERTIFICATE OF EXAMINATION

Supervisor	Examiners
Dr. Timothy A. Newson	Dr. M. Hesham El Naggar
	Dr. Craig Miller
	Dr. John R. Dryden

The thesis by
Alireza Varshoi

entitled:

Response of Pile Foundations to Random Cyclic Loads

is accepted in partial fulfillment of the
requirements for the degree of
Master of Engineering Science

Date _____

Chair of the Thesis Examination Board

ABSTRACT

Variable amplitude cyclic loads due to natural phenomena are common for laterally loaded piles. A series of small scale cyclic model test have been performed in the Boundary Layer Wind Tunnel Laboratory. Random loads from a boundary layer wind field were applied to a model consisting of a pile, pole and plate. The same setup was also tested under static conditions for comparison. Hyperbolic projection was used to represent the load – displacement relations. Initial stiffness and hyperbolic capacity were obtained from this method. The number of load cycles was found to affect the behavior of the laterally loaded piles. Load cycles were counted using the Rainflow method. Hyperbolic capacity and initial stiffness were found to decrease with increasing numbers of loading cycles. Displacement for laterally loaded piles was greater in the wind tunnel tests compared to static tests. Alternative approaches were used to assess the accumulation of ground-line displacement.

Keywords: Laterally Loaded Piles, Random Variable Amplitude Cyclic Loads, Wind Load, Hyperbolic Load-Displacement Curve, p-y Method, Rainflow Cycle Counting Method, Ground-line Displacement.

**To Mir-Hossein Mousavi,
Incarcerated, Yet Green**

ACKNOWLEDGMENTS

Graduate school starts with great aspiration to learn new subjects, to face challenging problems, and finishes with sanguineness to leave a remarkable footprint. I could not have been able to complete this, without the support of technical and the endless help of staff and professors of the Civil & Environmental Engineering department at Western.

I like to extend my sincere gratitude towards my supervisor, Dr. Timothy A. Newson. I am truly grateful for the opportunity I was given to work in his research group. His wealth of experience, insightful suggestion, and great enthusiasm will be with me for years to come.

I thank Saeed Sasanian and his lovely wife, Bahareh, for their firm determination and positive comments, particularly during these final months.

My Western experience was filled with enjoyable moments with great colleagues. I genuinely acknowledge Erol, Padma, Joonkyu, Meckkey, Behrang, Naemeh, Kimberly, Katie, Bahman, Martin, and Michelle.

I also thank my friends, Minoo, Farhang, Sina, Rasoul, and Ehsan for all the pleasant moments during this journey.

The last but not the least, I am indebted to my parents, my brother, and my grandmother, for their never-ending faith and trust in me, for their motivation and guide during my life. I know they have been truly proud of what I have accomplished.

CONTENTS

CERTIFICATE OF EXAMINATION	ii
ABSTRACT	iii
ACKNOWLEDGMENTS	v
TABLE OF CONTENTS	vi
LIST OF TABLES	x
LIST OF FIGURES	xii
LIST OF APPENDICES	xviii
LIST OF SYMBOLS	xix
1. INTRODUCTION	1
1.1 OVERVIEW	1
1.2 CYCLIC LATERAL LOADING OF PILES	2
1.3 AIMS OF THE RESEARCH.....	5
1.4 THESIS CONTENT.....	6
2. RESEARCH BACKGROUND	9
2.1 OVERVIEW	9
2.2 CHARACTERISTICS OF WIND	10
2.2.1 <i>Nature of Wind</i>	10
2.2.2 <i>Wind Speed and its Variations</i>	11
2.2.3 <i>Wind Loads on Structures</i>	14
2.2.4 <i>Wind Field Randomness</i>	18
2.3 LATERAL BEHAVIOR OF PILES	23

2.3.1 Ultimate Capacity under Lateral Loads	24
2.3.2 Serviceability under Lateral Loads	32
2.3.3 Effect of Cyclic Loads on Response	38
2.4 SUMMARY	48
3. METHODOLOGY AND TESTING PROGRAM	49
3.1 OVERVIEW	49
3.2 COMPONENTS OF TESTING PROGRAM.....	50
3.2.1 The Boundary Layer Wind Tunnel Laboratory	50
3.2.2 Silica Sand Properties	51
3.2.3 Wind Tunnel Sand Box	55
3.2.4 Model Piles, Pole and Plate.....	56
3.2.5 Static Test Setup.....	57
3.3 WIND TUNNEL TESTS	58
3.3.1 Instrumentation.....	59
3.3.2 Procedure	63
3.3.3 Data Processing.....	64
3.4 STATIC TESTS	73
3.4.1 Instrumentation.....	74
3.4.2 Procedure	74
3.5 SUMMARY	75
4. EFFECTS OF RANDOM WIND LOADS.....	76
4.1 OVERVIEW	76
4.2 RANDOM WIND LOAD CHARACTERIZATION	77

4.2.1 Drag Coefficient Measurement.....	77
4.2.2 Turbulence Intensity Estimation	82
4.2.3 Gust and Peak Factors	83
4.2.4 Dynamic Response Characteristics	85
4.2.5 Probability Distribution of the Wind Field.....	94
4.2.6 Cycle Counting Method	101
4.3 SUMMARY	110
5. RESPONSE OF PILES TO LATERAL LOADS.....	112
5.1 OVERVIEW	112
5.2 STATIC RESPONSE OF PILES TO LATERAL LOADS	113
5.2.1 Hyperbolic Representation of Load-Displacement	114
5.2.2 Location of the Zero Rotation Point	115
5.2.3 Static Ground-line Tests	117
5.2.4 Static Moment Tests	126
5.3 RANDOM VARIABLE AMPLITUDE CYCLIC LOADING	131
5.3.1 Hyperbolic Interpretation of the Cyclic Results	132
5.3.2 Accumulated Displacement	151
5.4 ALTERNATIVE APPROACHES FOR ASSESSING RANDOM CYCLE EFFECTS	156
5.5 SUMMARY	170
6. CONCLUSIONS.....	172
6.1 SUMMARY OF RESEARCH	172
6.2 KEY STUDY FINDINGS	173
6.3 FUTURE WORKS	175

REFERENCES	177
CURRICULUM VITAE.....	201

LIST OF TABLES

TABLE 2-1. SUGGESTED VALUE FOR CYCLIC LOAD RATIO FACTOR, F_L (LONG & VANNESTE, 1994)	44
TABLE 3-1. DIMENSIONS OF WIND TUNNEL #2	51
TABLE 3-2. DIMENSIONS OF MODEL PILES, POLE AND PLATE.....	57
TABLE 3-3. LIST OF WIND TUNNEL TESTS	59
TABLE 3-4. INSTRUMENTATION USED IN WIND TUNNEL TESTING.....	60
TABLE 3-5. LASER DISPLACEMENT TRANSDUCERS DISTANCE FROM PLATE AND X COMPONENT IN TEST PRT-MM60-4	68
TABLE 3-6. ANGLE OF TWIST OF THE PLATE IN TEST PRT-MM60-4	70
TABLE 3-7. LIST OF STATIC TESTS ON MODEL PILES	73
TABLE 4-1. STATISTICAL PROPERTIES OF INSTANTANEOUS DRAG COEFFICIENT	82
TABLE 4-2. LEVEL CROSSINGS OF TEST PRT-MM60-4.....	99
TABLE 4-3. DETAIL OF RAINFLOW COUNTING FOR MEAN WIND SPEED 3.4 M/S IN TEST PRT-MM60-4	104
TABLE 4-4. STATISTICAL PARAMETERS FOR CYCLE AMPLITUDES IN TEST PRT-MM60-4	108
TABLE 5-1. HYPERBOLIC PARAMETERS OF STATIC TESTS	121
TABLE 5-2. THEORETICAL INITIAL STIFFNESS FOR MODEL PILES IN GROUND-LINE TESTS	124
TABLE 5-3. HYPERBOLIC PARAMETERS FOR STATIC MOMENT TESTS.....	129
TABLE 5-4. RESULTS OF WIND TUNNEL TEST PRT-MM60-4.....	133

TABLE 5-5. HORIZONTAL FORCE AND APPLIED BENDING MOMENT IN TEST PRT-MM60-4	135
TABLE 5-6. SUMMARY OF WIND TUNNEL TEST ON SHORT PILES AND COMPARISON WITH STATIC TESTS	138
TABLE 5-7. COMPARISON OF INITIAL STIFFNESS AND HYPERBOLIC CAPACITY IN WIND TUNNEL TESTING ON MEDIUM PILE.....	142
TABLE 5-8. NUMBER OF CYCLES WITH AMPLITUDE GREATER THAN $H_A/3$ & $H_A/10$	145
TABLE 5-9. DAMAGE ACCUMULATION FOR TEST PRT-MM60-4.....	165

LIST OF FIGURES

FIGURE 2-1. FLUCTUATIONS OF WIND SPEED ABOUT ITS MEAN VALUE	12
FIGURE 2-2. DYNAMIC EXCITATION FREQUENCY RANGES UNDER WIND OR EARTHQUAKE (HOLMES, 2001)	15
FIGURE 2-3. RANDOM VIBRATION APPROACH TO RESONANT DYNAMIC RESPONSE (DAVENPORT, 1963)	18
FIGURE 2-4. ILLUSTRATION OF PEAKS AND ZERO UPWARD CROSSINGS	21
FIGURE 2-5. FACTORS FOR BRINCH-HANSEN EQUATION (HANSEN, 1961).....	26
FIGURE 2-6. SHALLOW AND DEEP MODE OF FAILURES (REESE ET AL., 1974).....	28
FIGURE 2-7. ON PILE FORCE PROFILE (AGAIBY ET AL., 1992)	29
FIGURE 2-8. EFFECT OF ECCENTRICITY ON DEPTH OF ROTATION (AGAIBY ET AL., 1992)..	30
FIGURE 2-9. ULTIMATE CAPACITY (BORDEN & GABR, 1987).....	31
FIGURE 2-10. HYPERBOLIC INTERPRETATION OF LOAD-DISPLACEMENT (MANOLIU ET AL, 1985)	31
FIGURE 2-11. SUBGRADE REACTION MODULUS (REESE & VAN IMPE, 2010)	35
FIGURE 2-12. DEVELOPED P-Y CURVES FROM (A) STATIC TEST, (B) CYCLIC TEST (REESE ET AL., 1965)	37
FIGURE 2-13. TWO DISTINCT PHASES IN THE BEHAVIOR OF LATERALLY LOADED PILE IN SAND (CUELLAR ET AL., 2009)	40
FIGURE 2-14. COMPARISON BETWEEN TEST RESULTS AND PREDICTED CURVES (LONG & VANNESTE 1994)	41
FIGURE 2-15. TWO-WAY VS. ONE-WAY LATERAL LOAD	43
FIGURE 2-16. LOAD CHARACTERIZING FACTORS (LEBLANC ET AL., 2010)	47

FIGURE 3-1. THE BOUNDARY LAYER WIND TUNNEL #2	50
FIGURE 3-2. GRAIN SIZE DISTRIBUTION OF SILICA SAND	52
FIGURE 3-3. RESULT OF DIRECT SHEAR TEST ON SILICA SAND (DELJOU, 2012)	53
FIGURE 3-4. RESULT OF DIRECT SHEAR TEST ON SILICA SAND (DELJOU, 2012)	54
FIGURE 3-5. RESULTS OF OEDOMETER ON SILICA (OTTAWA) SAND	55
FIGURE 3-6. SUPPORTING SYSTEM OF THE WIND TUNNEL SAND BOX	56
FIGURE 3-7. STATIC TEST BOX	58
FIGURE 3-8. INSTRUMENTS IN WIND TUNNEL TESTS	62
FIGURE 3-9. RAW DATA OF LASER DISPLACEMENT TRANSDUCER 1 IN WIND TUNNEL TEST PRT-MM60-4	65
FIGURE 3-10. RAW DATA OF LASER DISPLACEMENT TRANSDUCER 2 IN WIND TUNNEL TEST PRT-MM60-4	65
FIGURE 3-11. RAW DATA OF LASER DISPLACEMENT TRANSDUCER 3 IN WIND TUNNEL TEST PRT-MM60-4	66
FIGURE 3-12. RAW DATA OF PITOT 2 IN WIND TUNNEL TEST PRT-MM60-4.....	66
FIGURE 3-13. RAW DATA OF STRAIN GAUGE BRIDGE IN WIND TUNNEL TEST PRT-MM60- 4.....	67
FIGURE 3-14. DEMONSTRATION OF DISPLACEMENT CALCULATION FROM THE LTs	69
FIGURE 3-15. LASERS FROM REAR VIEW	70
FIGURE 3-16. LOCATING ZRP FROM LASER DISPLACEMENT TRANSDUCERS READINGS.....	72
FIGURE 3-17. STATIC GROUND-LINE TEST.....	75
FIGURE 4-1. WIND AND BODY AXES (HOLMES, 2001).....	77
FIGURE 4-2. PILE, POLE AND PLATE MODEL.....	78

FIGURE 4-3. THE MEASURED BENDING MOMENT VS. MEAN WIND SPEED	79
FIGURE 4-4. DRAG COEFFICIENT VARIATION FOR DIFFERENT MEAN WIND SPEEDS	80
FIGURE 4-5. INSTANTANEOUS DRAG COEFFICIENT	81
FIGURE 4-6. LONGITUDINAL TURBULENCE INTENSITY VS. MEAN WIND SPEED.....	83
FIGURE 4-7. PEAK FACTOR VARIATION VS. MEAN WIND SPEED	84
FIGURE 4-8. GUST FACTOR VARIATION VS. MEAN WIND SPEED	85
FIGURE 4-9. RESPONSE OF POLE AND PLATE IN THE FREE DECAY TEST	87
FIGURE 4-10. NATURAL FREQUENCY FROM THE FREE DECAY TEST	87
FIGURE 4-11. PSD OF WIND SPEED FLUCTUATIONS	90
FIGURE 4-12. PSD OF AERODYNAMIC FORCE	90
FIGURE 4-13. PSD OF RESPONSE – ACCELEROMETER	91
FIGURE 4-14. MECHANICAL ADMITTANCE.....	92
FIGURE 4-15. AERODYNAMIC ADMITTANCE (VICKERY, 1965)	93
FIGURE 4-16. MEAN WIND SPEED OF 4.6 M/S	95
FIGURE 4-17. MEAN WIND SPEED 7.1 M/S	96
FIGURE 4-18. MEAN WIND SPEED OF 8.5 M/S	97
FIGURE 4-19. UPWARD ZERO CROSSINGS AND PEAKS IN AN IDEAL NARROW BAND PROCESS	99
FIGURE 4-20. TIME-HISTORIES WITH DIFFERENT IRREGULARITY FACTOR (DIRLIK, 1985)	100
FIGURE 4-21. THE RAINFLOW METHOD (DIRLIK, 1985)	102
FIGURE 4-22. TIME-HISTORY OF WIND SPEED TEST PRT-MM60-4	103

FIGURE 4-23. PROBABILITY DISTRIBUTION OF CYCLE AMPLITUDE FOR MEAN WIND SPEED OF 3.4 M/S	106
FIGURE 4-24. PROBABILITY DISTRIBUTION OF CYCLE AMPLITUDE FOR MEAN WIND SPEED OF 7.11 M/S	106
FIGURE 4-25. PROBABILITY DISTRIBUTION OF CYCLE AMPLITUDE FOR WIND SPEED OF 9.4 M/S.....	107
FIGURE 4-26. SKEWNESS AND KURTOSIS OF CYCLE AMPLITUDES FOR TEST PRT-MM60-4	109
FIGURE 4-27. CYCLE AMPLITUDE VARIATIONS WITH MEAN WIND SPEED FOR TEST PRT- MM60-4	110
FIGURE 5-1. SIMPLIFIED BROMS YIELD STRESS DISTRIBUTION (AGAIBY ET AL., 1992)...	116
FIGURE 5-2. HYPERBOLIC EVALUATION OF SHORT PILE IN GROUND-LINE TESTING.....	118
FIGURE 5-3. HYPERBOLIC EVALUATION OF MEDIUM PILE IN GROUND-LINE TESTING.....	119
FIGURE 5-4. HYPERBOLIC EVALUATION OF LONG PILE IN GROUND-LINE TESTING	120
FIGURE 5-5. COMPARISON OF HYPERBOLIC CAPACITY WITH OTHER SOLUTIONS FOR LATERALLY LOADED PILES	121
FIGURE 5-6. YIELD STRESS IN SAND VS. DEPTH FROM CLASSIC SOLUTIONS.....	123
FIGURE 5-7. EFFECT OF PILE GEOMETRY ON HYPERBOLIC CAPACITY OF PILES IN GROUND- LINE TESTS.....	125
FIGURE 5-8. EFFECT OF PILE GEOMETRY ON INITIAL STIFFNESS OF PILES IN GROUND-LINE TESTS.....	125
FIGURE 5-9. HYPERBOLIC EVALUATION OF SHORT PILE IN MOMENT TESTING.....	127
FIGURE 5-10. HYPERBOLIC EVALUATION OF MEDIUM PILE IN MOMENT TESTING.....	128

FIGURE 5-11. COMPARISON OF HYPERBOLIC CAPACITY WITH BROMS SIMPLIFIED SOLUTION (1964) FOR THE MOMENT TESTS.....	129
FIGURE 5-12. VARIATION OF INITIAL STIFFNESS WITH E/D.....	130
FIGURE 5-13. WIND SPEED INCREMENTS FOR TESTS ON MEDIUM PILE	132
FIGURE 5-14. HYPERBOLIC EVALUATION OF WIND TUNNEL TEST PRT-SM30-1	136
FIGURE 5-15. HYPERBOLIC EVALUATION OF WIND TUNNEL TEST PRT-SM60-1	137
FIGURE 5-16. HYPERBOLIC EVALUATION OF WIND TUNNEL TEST PRT-MM30-2.....	139
FIGURE 5-17. HYPERBOLIC EVALUATION OF WIND TUNNEL TEST PRT-MM60-4.....	140
FIGURE 5-18. HYPERBOLIC EVALUATION OF WIND TUNNEL TEST PRT-MM90-1.....	141
FIGURE 5-19. VARIATION OF INITIAL STIFFNESS WITH TOTAL NUMBER OF LOAD CYCLES FOR THE SHORT PILE.....	143
FIGURE 5-20. VARIATION OF HYPERBOLIC CAPACITY WITH TOTAL NUMBER OF LOAD CYCLES FOR THE SHORT PILE	143
FIGURE 5-21. VARIATION OF INITIAL STIFFNESS WITH TOTAL NUMBER OF LOAD CYCLES FOR MEDIUM PILE.....	144
FIGURE 5-22. VARIATION OF HYPERBOLIC CAPACITY WITH TOTAL NUMBER OF LOAD CYCLES FOR MEDIUM PILE	144
FIGURE 5-23. VARIATIONS OF HYPERBOLIC CAPACITY WITH RESPECT TO DIFFERENT INTERPRETATION FOR NUMBER OF CYCLES	146
FIGURE 5-24. VARIATIONS OF HYPERBOLIC CAPACITY WITH RESPECT TO DIFFERENT INTERPRETATION FOR NUMBER OF CYCLES	147
FIGURE 5-25. NORMALIZED HYPERBOLIC CAPACITY FOR WIND TUNNEL TESTS	148
FIGURE 5-26. CONSTANT WIND SPEED TEST RESULT	151

FIGURE 5-27. LOAD-DISPLACEMENT CURVE FOR MEDIUM PILE IN SAND.....	153
FIGURE 5-28. LOAD-DISPLACEMENT CURVE FOR SHORT PILE IN SAND.....	154
FIGURE 5-29. DEGRADATION PARAMETER FOR TEST PRT-MM30-2.....	155
FIGURE 5-30. DEGRADATION PARAMETER FOR TEST PRT-MM60-4.....	155
FIGURE 5-31. DEGRADATION PARAMETER FOR TEST PRT-MM90-1.....	156
FIGURE 5-32. LOAD – GROUND-LINE DISPLACEMENT CURVES FOR TEST PRT-MM60-4	158
FIGURE 5-33. LOAD – ACCELERATION CURVES FOR TEST PRT-MM60-4	160
FIGURE 5-34. LOAD – STRAIN CURVES FOR TEST PRT-MM60-4	162
FIGURE 5-35. SKEWNESS AND KURTOSIS OF GROUND-LINE DISPLACEMENT FLUCTUATIONS FOR TEST PRT-MM60-4.....	163
FIGURE 5-36. VARIATIONS OF $H_A1/3$ & $H_A1/10$ FOR GROUND-LINE DISPLACEMENT FLUCTUATIONS IN TEST PRT-MM60-4	164
FIGURE 5-37. VARIATIONS OF $H_A1/10$ OF GROUND-LINE DISPLACEMENT FLUCTUATIONS WITH CYCLE AMPLITUDES IN TEST PRT-MM60-4	165
FIGURE 5-38. ACCUMULATION OF DAMAGE WITH MEAN LOAD LEVEL.....	166
FIGURE 5-39. GROUND-LINE DISPLACEMENT AND WIND SPEED FLUCTUATIONS FOR MEAN WIND SPEED OF 7.1 M/S FOR TEST PRT-MM60-4.....	167
FIGURE 5-40. GROUND-LINE DISPLACEMENT AND WIND SPEED FLUCTUATIONS FOR MEAN WIND SPEED OF 8.5 M/S FOR TEST PRT-MM60-4.....	168
FIGURE 5-41. GROUND-LINE DISPLACEMENT AND WIND SPEED FLUCTUATIONS FOR MEAN WIND SPEED OF 9.4 M/S FOR TEST PRT-MM60-4.....	168
FIGURE 5-42. PIPELINE UPLIFT MECHANISM (DELJOU, 2012).....	169

LIST OF APPENDICES

Appendix A Instrument Calibration	178
Appendix B Pictures	180
Appendix C Wind Tunnel Results	185

LIST OF SYMBOLS

Symbol	Description
a	Degradation Parameter after Little & Briaud (1988)
A	Coefficient in p-y Method Proposed by API (2003) for Cyclic Loads
A_D	Constant in S-N Relation depends on the Material
A_F	Frontal Area (m^2)
A_k	Dimensionless Constant in Leblanc et al. (2010) for Stiffness Variation
b	Plate Breadth (mm)
B	Pile Diameter (mm)
c	Soil Cohesion (kPa)
C_c	Soil Coefficient of Curvature
C_d	Dirlik Irregularity Factor
C_D	Drag Coefficient
C_F	Force Coefficient
C_{if}	Random Process Irregularity Factor
C_u	Soil Coefficient of Uniformity
d	Displacement Measured in Laser Displacement Transducers (cm)
D	Pile Length (mm)
D_{NB}	Damage under a Narrow Band Process

e	Load Eccentricity (cm)
E_p	Pile Material Young's Modulus (GPa)
E_{py}	Reaction Modulus in P-Y Curves Approach (MPa)
E_s	Soil Constrained Elastic Modulus (MPa)
$E(0)$	Zero Crossing per Second
$E(P)$	Number of Peaks per Second
f	Frequency (Hertz)
f_0	Natural Frequency of the Structure (Hertz)
$f_p(s)$	Probability Density Function of Peaks
f_{nd}	Non-Dimensional Frequency
F_C	Soil Density Factor after Long & Vanneste (1994)
F_D	Drag Force (N)
F_I	Pile Installation Factor after Long & Vanneste (1994)
F_L	Cyclic Load Factor after Long & Vanneste (1994)
F_s	Frequency of Data Acquisition (Hertz)
g	Peak Factor
G	Gust Factor
G_s	Soil Specific Gravity
h	Plate Height (mm)
H	Horizontal Load (N)
$H_{A1/3}$	Amplitude of Largest 1/3 of the Cycles (m/s)

$H_{A1/10}$	Amplitude of Largest 1/10 of the Cycles (m/s)
H_c	Capacity Corresponding to a Displacement Criterion (N)
H_h	Hyperbolic Capacity of Pile (N)
H_{hw}	Hyperbolic Capacity of Pile in Wind Tunnel Test (N)
H_{hs}	Hyperbolic Capacity of Pile in Static Test (N)
H_u	Ultimate Horizontal Capacity (N)
$ H(f) ^2$	Mechanical Admittance
i_x	Dirlik Standardized Variable
I_m	Pile Moment of Inertia (m^4)
I_u	Turbulence Intensity
I_{ysH}, I_{ysM}	Dimensionless Compliance for Ground-line Displacement after Davies & Budhu (1984)
$I_{\theta H}, I_{\theta M}$	Dimensionless Compliance for Rotation after Davies & Budhu (1984)
k_{py}	Coefficient of the Soil Reaction Modulus (MPa/m)
k	<i>von</i> Karman's Constant in Logarithmic Law
\tilde{k}	Stiffness from Leblanc et al. (2010) (N/m)
K	Ratio of Pile Material Young's Modulus over Soil Young's Modulus
K_o	At Rest Earth Pressure Coefficient
K_a	Rankine Maximum Active Soil Pressure Coefficient
K_i	Pile Lateral Initial Stiffness (N/mm)
K_{iw}	Pile Lateral Initial Stiffness in Wind Tunnel Test (N/mm)

K_{is}	Pile Lateral Initial Stiffness in Static Test (N/mm)
K_p	Rankine Maximum Passive Soil Pressure Coefficient
K_{PS}	Pile-Soil Stiffness Ratio (GPa/m)
K_q, K_c	Yield Stress factors from Hansen (1961) Ultimate Capacity Calculation
K_s	Structure Stiffness (N/m)
L	Pole Length (mm)
L_a	Pile Active Length (m)
L_e	Pile Effective Length (m)
m	Increase in Soil Young's Modulus Factor
m_D	Exponent in S-N Relation
M	Applied Moment (N.m)
M_L	Lumped Mass (M)
M_R	Moment in Static test after Leblanc et al. (2010) (N.m)
N	Number of Loading Cycles
N_F	Number of Loading Cycles until Failure
N_q	Bearing Capacity Factor
$p(x)$	Probability Distribution Function
$P(x)$	Cumulative Distribution Function
P_u	Yield Stress of Soil (kPa)
r	Pile or Pole Cross Section Radius (mm)
R_h	Cyclic Load Ratio

R_n	Ratio of the Coefficients of Soil Reaction Moduli
$R_x(\tau)$	Autocorrelation Function
R_s	Cyclic Strain Ratio
s	Cycle Amplitude (m/s)
$S(f)$	Power Spectral Density Function
T	Period of Cycle Counting (sec)
U	Wind Speed (m/s)
u^*	Frictional Velocity (m/s)
\hat{U}	Peak Wind Speed (m/s)
\bar{U}	Mean Wind speed (m/s)
$w(i_x)$	Peak Probability Density for a Wide Band Process after Dirlik (1985)
y	Deflection in Pile (mm)
y_s	Pile Ground-line Displacement (mm)
z	Depth below the Ground Surface (cm)
z_0	Roughness Length (m)
z_h	Height above Ground Surface (m)
Z_r	Depth of Zero Rotation Point (cm)
α	Angle of Attack (Radian)
β	Factor in Power Law
β_s	Skewness
β_k	Kurtosis

α_t	Twist Angle (Radian)
Γ	Gamma Function
γ	Soil Unit Weight (kN/m^3)
δ	Logarithmic Decrement
δ_p	Deflection in Pole (mm)
ε	Lateral Strain (%)
η	Percentage of Critical Damping
θ	Pile Rotation (Degree)
ϑ	Angle ranges from $\phi/2$ to $\phi/3$ after Reese et al. (1974)
Λ	Rigidity Assessment Factor after Poulos & Hull (1989)
μ_k	k^{th} Moment of Power Spectral Density
$\nu_0(f)$	Rate of Mean Crossing in a Narrow Band Process
ξ_b, ξ_c	Load Factors after Leblanc et al. (2010)
ρ_a	Air Density (kg/m^3)
σ_{BM}	Normal Stress due to Bending Moment (MPa)
σ'_{v0}	Vertical Effective Stress (kPa)
σ_U	Standard Deviation of the Longitudinal Wind Speed
τ_0	Surface Shear Stress (kPa)
ϕ'_p	Soil Peak Internal Friction Angle (Degree)
$\phi'_{\text{critical state}}$	Soil Critical State Angle of Internal Friction (Degree)
φ	Soil Dilatation Angle (Degree)

$\chi(f)$	Aerodynamic Admittance
Ω	Angle equal to $(45 + \phi/2)$ after Reese et al. (1974)
ω	Angular Frequency (Radian/s)

INTRODUCTION

1.1 Overview

Global demands for energy have been increasing over the last few decades and a major challenge of the modern era will be supplying this need, as oil and gas reserves begin to decline. Consequently, the demand for clean and cost effective alternative energy sources has been increasing. In particular, wind power is gradually becoming a significant renewable energy resource from both an economical and environmental stand-point.

In recent years, many countries have set targets for using renewable energy resources. According to the “Global Status Report on 2011” these targets now exist in 98 countries (REN, 2011). Canada is now the 9th largest producer of wind energy in the world with a current installed capacity of more than 5GW, which is equal to 2.3% of Canada’s total energy demand. In addition, more than 6GW of wind energy projects are already contracted to be built in Canada over the next five years. Ontario is expected to install more than 5600 MW of new wind energy by 2018, creating 80,000 “person-years” of employment.

In common with offshore platforms and wind turbines, towers, radio antenna, sign posts and other tall structures, can all be subjected to significant lateral loads from environmental agents, such as, ice flows, wind or sea waves. In most of these cases, the horizontal load is applied above ground level and thus an additional moment acts on the

foundation. The foundation of these infrastructures should be able to withstand the effects of these combined vertical, horizontal and moment loads for the life of the project.

Piles are often effective and economical foundations for structures subjected to lateral and moment loads, and the offshore industry often uses this type of foundation. They are preferred over other alternatives for a number of additional reasons, including straightforward installation procedures compared to other offshore foundation alternatives. Piles have been used extensively for first generation offshore wind farms, where a number of wind turbines can be constructed on a relatively soft and consistent subsoil profile. In addition, piles are a conventional foundation alternative for sign posts and radio antenna.

The cyclic lateral loads acting on these types of foundation are usually stochastic in nature and the design process should account for the effects of this type of loading on the short and long term performance of the structure.

1.2 Cyclic Lateral Loading of Piles

The design of lateral loading of piles can be treated like a classical foundation problem, where the ultimate capacity and serviceability limit states are satisfied. However, Agaiby et al. (1992) suggested that it is difficult to identify the distinction between global stability and tolerable deformations, since instability is often defined for a deformation limit for a laterally loaded pile, rather than a load limit and unlimited deformation as is common for shallow foundations. Consequently, a number of researchers have suggested that the problem should be treated in a different way (Reese & Matlock, 1956).

Ultimate capacity of a laterally loaded pile can be predicted through limit equilibrium solutions (e.g. Hansen, 1961; Broms, 1964). The rigidity of a pile is a key issue in the calculation of the ultimate capacity. The ultimate capacity for a rigid pile is defined as complete yielding of the soil along the foundation, while for more flexible foundations it may also be equal to the structural capacity of the pile material. These solutions have limited applicability for a number of reasons, including not providing any pre-failure information.

These deficiencies have been overcome by using the subgrade reaction modulus approach (e.g. Winkler springs), in which soil resistance (p) is predicted as a function of the lateral deflection of the pile (y). This method is widely known as the p - y curves technique. Available design methodologies for piles under lateral loads are generally based on subgrade reaction modulus. The method has also been adopted for the main onshore and offshore design codes, such as, API (2003) and DNV (2007), and was initially developed from the results of static lateral pile field tests.

The subgrade reaction modulus has gained its reputation owing to low numbers of failures. However, it is recognized that simplifying the soil behavior by modeling it using linear or nonlinear springs can introduce conservatism and error into the analyses through disregarding soil continuity. In addition, the approach is also highly empirical and is often used beyond its originally developed database; cyclic loading effects in particular have introduced further approximation and empiricism.

Recently, greater emphasis has been put on accommodating lateral loads on structures. Environmental phenomena such as wind, sea waves or earthquakes can impose random

cyclic loads on structures. While numerous infrastructures are designed in accordance to the p-y method to sustain these environmental lateral loads, it seems that this method is incapable of accounting for some of the more important aspects of the problem (e.g. Little & Briaud, 1988; Long & Vanneste, 1994). Reese et al. (1974) modified their initial p-y method to consider the effects of the cyclic loads. However, in their recommendations, they did not account for characteristics of the cyclic loads (e.g. one-way vs. two-way cyclic load or constant vs. variable amplitude cycles). The proposed p-y method by Reese et al. (1974) faced further criticisms after failing to predict results of two cyclic tests performed in 1982 in Tampa Bay (Long & Vanneste, 1994). Also, an inability to take into account the contributions of the number of load cycles has been another criticism of the p-y method. Moreover, the use of the p-y method often fails to account for the permanent deformation that accumulates with increasing cycles (Achmus et al., 2009). This is of particular importance for new forms of structures, such as, wind turbines, since the loading state is generally different from that experienced by offshore platforms, where much experience for design has been taken. Lastly, the method is based on the results obtained from slender and flexible pile tests, and it is being utilized for many offshore wind farms where the piles behave in a rigid fashion (Leblanc et al., 2010).

Despite many attempts to address the effects of cyclic lateral loads, some aspects of the cyclic behavior of laterally loaded piles are yet to be fully understood and predictive methods are relatively crude and under developed. An inability to predict the accumulated displacement and possible stiffness degradation in the soil under the action of cyclic loads may endanger the functionality of infrastructure. A few researchers have

attempted to incorporate various degradation parameters in the p-y method (e.g. Long & Vanneste, 1994; Lin & Liao, 1999), but the effects of random variable amplitude cyclic loads have been hardly assessed. The difficulties arise from two main factors: (1) random variable amplitude loading is hard to generate at full scale or even in conventional soil mechanics laboratories; (2) control of the test conditions, and characterization of the random variable amplitude cyclic loads and the response of the foundation system are difficult to assess. Thus, more research is needed to address different aspects of natural random cyclic loads (e.g. wind or sea waves) and provide understanding for better predictive design tools.

1.3 Aims of the Research

The current research project addresses a problem at the interface of both geotechnical and structural engineering. The novelty of the current research arises from studying the behavior of laterally loaded piles under truly stochastic wind fields, to observe the effects of randomness in the cyclic loads. A system consisting of a pile, pole and a plate were tested under stochastic wind loads using a boundary layer wind tunnel. Whilst these tests can be viewed as a scaled physical model system, there has been no attempt to couple the wind and geotechnical scales during the work. Thus, the results can be seen as a proof-of-principle study of random variable amplitude cyclic loading of piles. The aims of the current research project are:

- To study the characteristics of the wind field from a boundary layer wind tunnel as a source of random variable amplitude cyclic loads.

- To study the structural behavior of a model plate, pole and pile system under random variable amplitude cyclic lateral loads and the effect of cyclic loads on the initial stiffness and hyperbolic capacity of the piles.
- To study the effects of lateral load eccentricity and pile geometry on the initial stiffness and hyperbolic capacity of a pile using static model tests.
- To assess different approaches for estimating the number of load cycles and their corresponding amplitudes in a random wind loading process.
- To study the effects of random variable amplitude cyclic loads on the accumulation of the ground-line displacement and other damage indices for piles.

The findings of this study will provide the basis for further studies that will lead to more rational design procedures and raise awareness of the effects of random variable amplitude cyclic loads on the behavior of laterally loaded piles.

1.4 Thesis Content

Chapter 1 introduces the themes of this thesis. The problem of lateral loading of piles is discussed. Available methods for analysis of laterally loaded piles and their deficiencies are described. Research aims are described along with the novelty of the approach. Lastly, the methodology to achieve these aims is introduced.

Chapter 2 describes the background of the current state of the art research in the area. Firstly, wind engineering terminologies are introduced and then knowledge on the estimation of the wind induced loads on structures is presented. To aid the understanding of wind loading concepts, background on random vibration theory is also presented. Available methods for prediction of the ultimate capacity of a laterally loaded pile are

described. The serviceability of a laterally loaded pile is reviewed. The methods used to count the number of loading cycles are also introduced. Finally, emphasis is placed on research which accounts for the effects of random cyclic loads on the behavior of laterally loaded piles.

Chapter 3 describes the test methodology used in this study. Properties of the small scale models are described. Ottawa sand has been used in the current study and its geotechnical properties obtained from conventional geotechnical laboratory tests are presented. The instrumentation of the wind tunnel and static tests is discussed and calibration methods are described. Testing procedures and the data acquisition approaches are also discussed. The Boundary Layer Wind Tunnel Laboratory at Western University was used in this research and it is introduced as part of this chapter. The data analysis process of this research is also described.

Chapter 4 explains the characteristics of wind as a source of cyclic random variable amplitude loads on infrastructure. The load coefficients, gust and peak factors and turbulence intensity are calculated based on the results obtained from the wind tunnel testing. The estimation of the lateral loads generated from the wind flow is presented with various methods of cycle counting for the random wind load time-history. Probability density functions of wind speed and cycle amplitudes are also presented.

Chapter 5 shows the results obtained from the wind tunnel and the static tests. The ultimate capacities of the model piles along with their initial stiffnesses are reported and comparisons are made. A series of aspects that affect the behavior of the laterally loaded piles is presented and their effects are illustrated with the results obtained in this study. A

degradation parameter that illustrates the effect of the number of loading cycles on pile ground-line displacement is obtained and presented. Finally, alternative approaches are presented to assess the accumulation of ground-line displacement.

Chapter 6 provides the main conclusions from the study and makes suggestions for directions of future works.

RESEARCH BACKGROUND

2.1 Overview

Chapter 2 introduces literature covering the current research project. Wind characteristics are covered to give a general overview of wind induced loads and their impacts on structures. Different methods for counting the number of loading cycles in variable amplitude cyclic processes are reviewed. This chapter also covers the behavior of laterally loaded piles, available methods of analysis, and their shortcomings and advantages.

Laterally loaded piles have been an on-going research topic for at least 65 years (Terzaghi, 1955). The two limit states of ultimate capacity and serviceability should be satisfied within tolerable ranges for laterally loaded piles through economical design. Many factors affect the response of laterally loaded piles, amongst these are: pile head fixity condition, pile flexural rigidity, pile geometry, soil initial condition, ground-water condition, lateral load characteristics and load eccentricity. This chapter includes an overview of the available methods for analysis of laterally loaded piles under static and cyclic loads.

Finally, research studies that have investigated the behavior of piles installed in granular soils under cyclic loads will be described. A number of these studies are more recent

compared to much of the literature survey and demonstrate the current demand for design of structures exposed to random variable amplitude cyclic natural loads.

2.2 Characteristics of Wind

In this section, the nature of wind and its characteristics are introduced. Then the available methods for estimation of wind imposed load on structures are discussed.

2.2.1 Nature of Wind

Unequal heating of the earth's surface from the sun produces pressure gradients; atmospheric motion caused from this pressure gradient, is called "wind". Earth rotation, topography and roughness of the ground surface affect this atmospheric flow. The "boundary layer" describes the region in which atmospheric flow is affected by friction at the earth's surface; wind exists in this layer that may extend up to 1 km above the ground surface (Holmes, 2001).

Wind can impose a pressure on structures. Since this pressure is a function of wind speed, it is often onerous to measure or predict. A portion of this complexity is due to variations of the wind speed in space and time. Wind speed fluctuations are affected by earth topography, while mean wind speed increases with height from the ground surface. Due to a high level of complexity in wind time-histories, statistical parameters are often used for their description (Davenport, 1961).

Another issue of complexity in prediction of wind induced loads arises from the fact that response is a function of structural shapes and their dynamic characteristics.

2.2.2 Wind Speed and its Variations

Historically, the design wind speed for any project was chosen to be the highest instantaneous speed recorded as close as possible to the site of the project. This approach was assumed to be conservative, although it was not cost effective or precise for design. This traditional approach seemed to be easy and straightforward, however, very soon it faced a number of criticisms. Baker (1884), Stanton (1925) and Bailey & Vincent (1939) studied the approach in more detail, but they did not suggest reduction of the design wind speed, although they mentioned the chance of some alleviation. Davenport (1961) commented on their work as inconclusive due to a lack of a statistical framework. The traditional approach relied significantly on measuring devices and it was understood that the response characteristics of the measuring device had certain influences on the recorded wind speed. Moreover, issues like difference in topography and surface roughness cannot be neglected and should be taken into account.

As an alternative, Sherlock (1947) suggested the replacement of instantaneous peak by mean values of the wind speed. His initial recommendation was the mean value over a 5-minute period, although today the mean value over a 10-minute period is recommended. Furthermore, he suggested using the mean wind speed value for design purposes and applying “gust factors” to take into account the fluctuations of the wind speed. Gust factors were meant to compensate for the reduction from the peak value to the mean value of the wind speed. Figure 2-1 illustrates the fluctuations of the instantaneous wind speed about its mean value for one of the wind tunnel tests in this study. Solari (1993) argued that different procedures developed for gust factors resulted in conflicting solutions and noticeable inconsistencies.

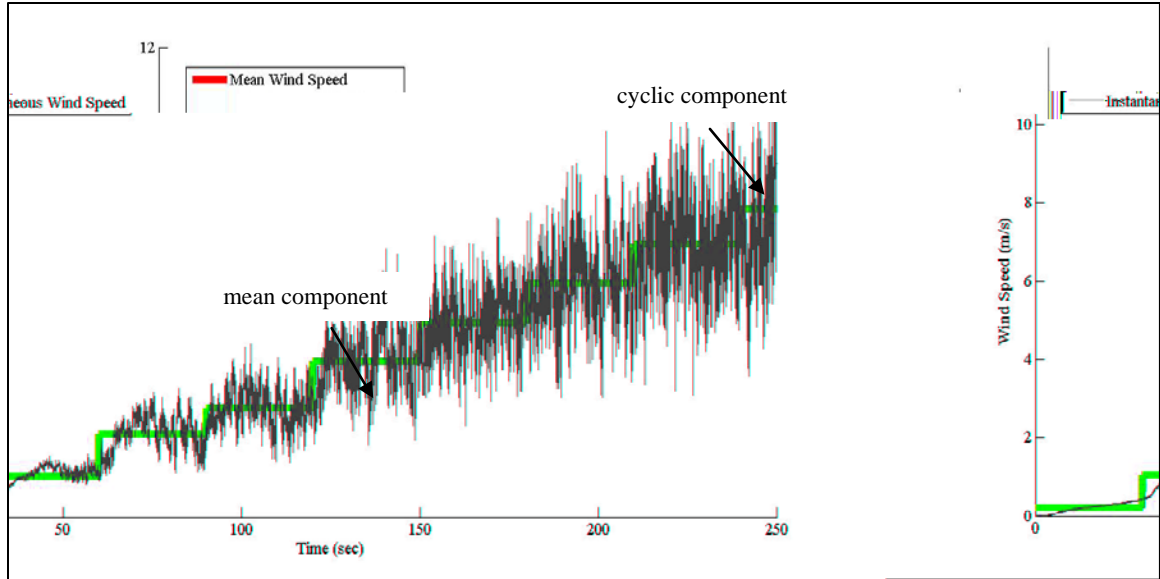


Figure 2-1. Fluctuations of Wind Speed about its Mean Value

Mean wind speed also varies with height. The variations of the wind speed with height from the ground surface are significant especially for high-rise buildings and sky scrapers. Power and logarithmic laws are used conventionally to obtain the mean wind speed at any height above the ground surface. Logarithmic approximations, as in equation 2.2, assumes that the rate of change in the mean wind speed, $\bar{U}(z)$, with height is function of surface shear stress, τ_0 , air density, ρ_a , and these parameters are implemented in a logarithmic law through frictional velocity, U_* as in equation 2.1.

$$\tau_0 = \rho_a \cdot U_*^2 \quad (2.1)$$

$$\bar{U}(z) = \frac{U_*}{k} \log_e(z_h/z_0) \quad (2.2)$$

Where, z_0 is the roughness length, k is von Karman's constant (dimensionless), which has been experimentally found to be equal to 0.4. (Holmes, 2001), and z_h is the height above the ground.

On the other hand, a power law expression is often used (equation 2.3) but has no theoretical background (Holmes, 2001).

$$\bar{U}(z_h) = \bar{U}_{10} \left(\frac{z_h}{10} \right)^\beta \quad (2.3)$$

Where, \bar{U}_{10} is the mean wind speed at 10 m height, β is function of the terrain roughness and it is calculated from equation 2.4.

$$\beta = \left(\frac{1}{\log_e \left(\frac{z_{ref}}{z_0} \right)} \right) \quad (2.4)$$

Holmes (2001) suggested that by setting the reference height, z_{ref} , equal to 50 m the power law gives values very close to the logarithmic law.

Wind speed also changes with variations of surface roughness. The roughness length, z_0 , has been implemented in the logarithmic and power laws to account for this. Z_0 describes the roughness in different terrains. Throughout this research an equivalent “open country” terrain was used in the wind tunnel, which has a roughness length of 0.01 to 0.05 m according to Australian Standard for Wind Loads, (AS1170.2, 1989).

Turbulence or gustiness of the wind speed was measured as part of the wind tunnel testing program. Turbulence can be obtained for any wind speed interval as the ratio of the standard deviation of the wind speed in that interval over its mean value. In wind engineering, it is common to relate the turbulence intensity with the surface roughness. Holmes (2001) suggests that standard deviation of the longitudinal wind speed, σ_U , is equal to $2.5U^*$ and by using the logarithmic law to represent the mean wind speed, equation 2.5 was suggested for estimation of the turbulence intensity, I_u .

$$I_u = \frac{1}{\log_e\left(\frac{z}{z_0}\right)} \quad (2.5)$$

Hence, the wind speed record can be broken into two parts: the mean value which can be considered to be steady state (with a constant component) and the fluctuating part, which can be highly random and may have a high level of variations.

2.2.3 Wind Loads on Structures

Section 2.2.2 shows that the wind is a highly random phenomenon. It is also important to assess the susceptibility of any structure to resonance under dynamic wind loading. There is a potential for resonant responses under dynamic loads for structures with natural frequencies (f_0) less than about 1 Hz (Holmes, 2001). In addition, ASCE standard (ASCE 7-05) classifies a structure as dynamically sensitive, or flexible if $f_0 < 1$ Hz. It is often acceptable for many structures with natural frequency greater than 1 Hz to use the quasi-static assumption for calculation of the wind load. In the case of quasi-static, the structure responds directly to the applied force. In this section, the dynamic properties of a structure, assessment of its potential for resonance, the quasi-static wind load and dynamic wind load are introduced.

Natural frequency of the structure, f_0 , is an important parameter to assess sensitivity to resonance. Natural frequency can be obtained from theoretical approaches with knowledge of the stiffness and mass of the structure, or more accurately from free decay dynamic release tests as can be seen in Chapter 4. Figure 2-2 shows the frequency ranges where structures might be sensitive to resonance under earthquake or wind loads.

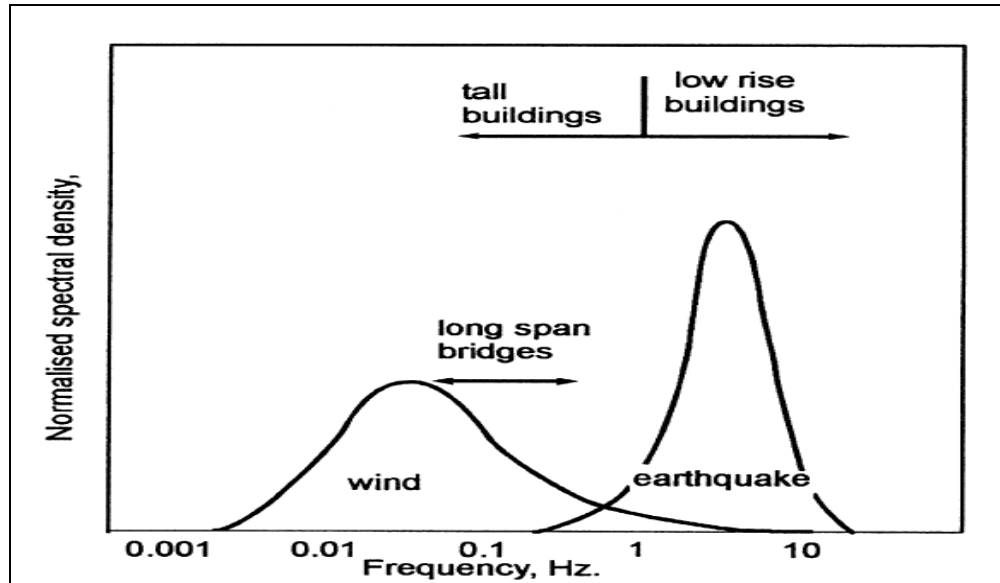


Figure 2-2. Dynamic Excitation Frequency Ranges under Wind or Earthquake (Holmes, 2001)

For non-sensitive resonant structures (i.e. structure with $f_0 > 1$ Hz), the drag force, F_D , acting on the structure in the along-wind direction can be found using equation 2.6.

$$F_D = 0.5 \rho_a C_D A_F U^2(t) \quad (2.6)$$

Where, ρ_a is air density, A_F is frontal area, and $U(t)$ is instantaneous wind speed. We will discuss the important component of the equation 2.6 which is known as the drag coefficient, C_D .

Bearman (1971) obtained the drag coefficient of different plate sizes in smooth and turbulent flow with a series of experiments. He suggested values of 1.107 in smooth and 1.195 in turbulent flow for 6X6 inch plates, which is comparable with the plate used in the model tests of this project. Free-stream turbulence is believed to increase the drag force on the normal plate slightly. This increase results from the reduction of the leeward or base pressure, rather than an increase in frontal face pressure (Bearman, 1971). He also added that more turbulence will increase the rate of entrainment of the air into separated

shear layers. From this process, the radius of curvature of wind flow tends to reduce and causes a reduction of base pressure.

Letchford (2001) studied drag coefficients on a range of rectangular signboards with varying aspect ratios for a range of wind directions. He suggested the value of 1.15 for a rectangular shape mounted at the same height above the ground surface equal to its breadth. An increase in drag coefficient was proposed with increasing height from the ground surface. The drag force coefficient was seen to remain approximately constant up to a wind direction of 45° to the normal and then to decrease almost linearly beyond this angle.

Quinn et al. (2001) also studied the wind imposed load on signs with and without a frame. They suggested that the sign shape has a negligible effect on the magnitude of the wind load, while the existence of a mounting frame increases the wind induced forces. They obtained drag coefficients for both perpendicular and inclined signs to the wind flow. For a 75 cm sign mounted on a 1 meter height pole, the drag coefficient increased from 1.05 to 1.10 with a 22.5° inclination of the sign.

Ginger et al. (2012) studied cantilevered highway road-signs and obtained a drag coefficient of 1.2 for winds approaching from any direction within $\pm 50^\circ$ from a line normal to the plate on either side.

On the other hand, dynamic response of structures under wind load is important for structures with a natural frequency of 1 Hz or less. Dynamic analysis of structures under wind load is usually performed with spectral density approach in the frequency domain. Figure 2-3 shows the relation between spectral densities of wind speed, wind force and

response of the structure. In the bottom row, two admittance functions are introduced: Mechanical and Aerodynamic. Aerodynamic admittance, $\chi(f)$, is a frequency dependent transfer function, which links the fluctuating force to the along-wind fluctuating component of the wind. Aerodynamic admittance is presented in equation 2.7 (Vickery, 1965) in terms of non-dimensional frequency, f_{nd} , which is given in equation 2.7.

$$f_{nd} = \frac{fb}{\bar{U}} \quad (2.7)$$

Where, b is equal to the width of the plate, f is frequency and \bar{U} is the mean wind speed.

$$\chi(f) = \frac{1}{1+(f_{nd})^{4/3}} \quad (2.8)$$

On the other hand, mechanical admittance, $|H(f)|^2$, (equation 2.9) links the wind force spectra and the response spectral density.

$$|H(f)|^2 = \frac{1}{\left[1-\left(\frac{f}{f_0}\right)\right]^2 + 4\eta^2\left(\frac{f}{f_0}\right)^2} \quad (2.9)$$

Where, η is percentage of critical damping of the system.

By using these two admittance functions, the spectral density of the response, $S_x(f)$, can be related to the spectral density of the wind speed fluctuations, $S_U(f)$ knowing the stiffness, K_s of the system as shown in equation 2.10.

$$S_x(f) = \frac{1}{K_s} |H(f)|^2 \frac{4\overline{F_D^2}}{\bar{U}^2} S_U(f) \quad (2.10)$$

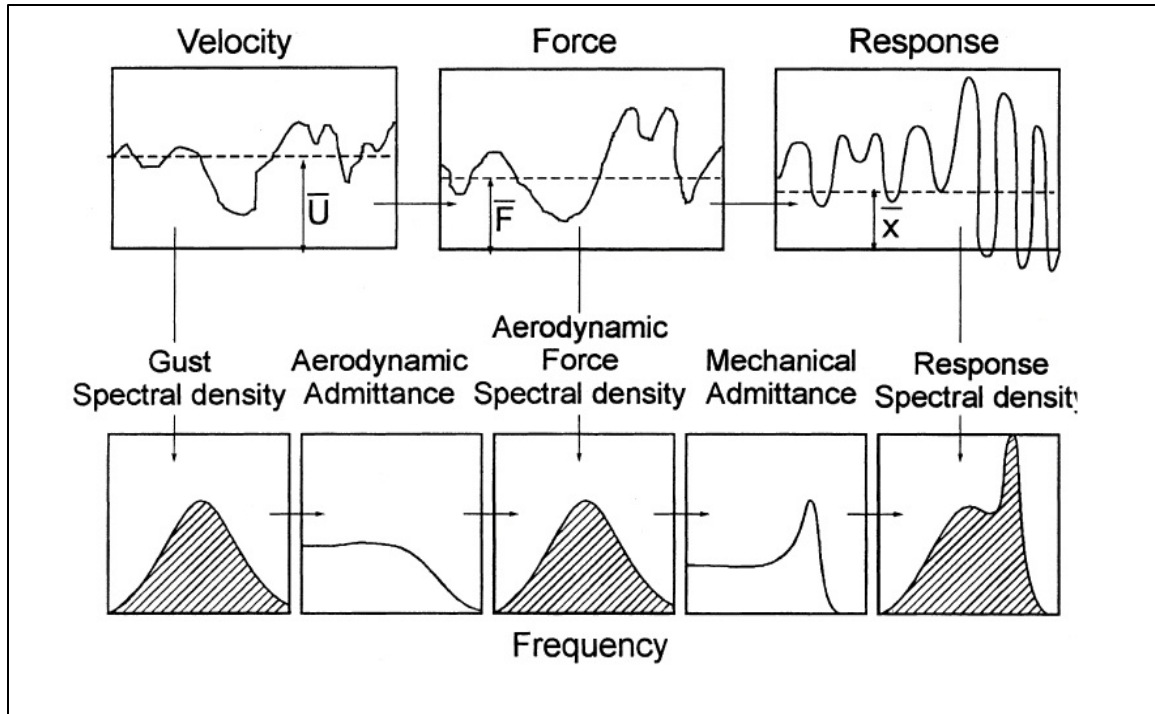


Figure 2-3. Random Vibration Approach to Resonant Dynamic Response (Davenport, 1963)

2.2.4 Wind Field Randomness

This section gives an overview of random processes, describes their characteristics and introduces common terminologies. The number of cycles in a random variable amplitude process and its statistical properties are discussed.

A process is described as random (or stochastic) if it can only be determined statistically. In the other words, random process cannot be predicted, although we are able to record it as soon as it occurs. Each record from a random process is called a sample and the total collection of the samples is called an ensemble. It is of interest to predict the value of a random process over any fraction of time. The probability distribution function, $p(x)$, gives the density of the distribution of a specific value in a random process. Moreover, the cumulative distribution function, $P(x)$, is the area under $p(x)$ and has a value between

zero and one. The cumulative distribution function gives the probability that a sample value of the random process is less than a specific value.

A random process is said to be stationary if the probability distributions obtained for the ensemble do not depend on absolute time. Wind and sea waves are usually treated as random stationary processes for practical purposes. In a stationary random process, mean, mean square, variance and standard deviation are all independent of time.

It is advantageous to study a periodic function in the frequency domain. This is usually performed with a Fourier series for a periodic function. A stationary random process cannot be represented by Fourier series directly, although it is possible to apply Fourier analysis to the autocorrelation function of a random process. Power spectral density, $S(f)$, gives the power of the signal at any frequency band. The area under the graph of power spectral density against frequency gives the mean square value of a stationary random process. Equation 2.11 gives the moments of the power spectral density where, μ_k is the k^{th} moment:

$$\mu_k = \int_0^{\infty} f^k S(f) df \quad (2.11)$$

A process whose spectral density occupies a narrow range of frequencies is known as a narrow band process. The along-wind response of structures with low natural frequencies is usually considered to be narrow band. Moreover, wind induced narrow band vibrations can be taken to have a normal or Gaussian probability distributions; if this is the case, the peaks (amplitudes) will have a Rayleigh distribution (Holmes, 2001). The number of cycles or fluctuations can be obtained from level crossings in a narrow band process. The number of level crossings is obtained by measuring the rate of the exceedance during a

time-history of a certain limit level. Rice (1954) developed two important relationships for the number of zero (mean) crossings per second, $E(0)$, and the number of peaks per second, $E(P)$, from moments of power spectral density as can be seen in equations 2.12 and 2.13.

$$E(0) = \sqrt{\frac{\mu_2}{\mu_0}} \quad (2.12)$$

$$E(P) = \sqrt{\frac{\mu_4}{\mu_2}} \quad (2.13)$$

The number of peaks per second, $E(P)$, and upward zero crossings per second, $E(0)$, are obtained from the moments of the power spectral density. Moreover, it is possible to calculate irregularity factor, C_{if} as in equation 2.14.

$$C_{if} = \sqrt{\frac{\mu_2^2}{\mu_0\mu_4}} \quad (2.14)$$

Figure 2-4 illustrates the counting of the peaks and zero crossings.

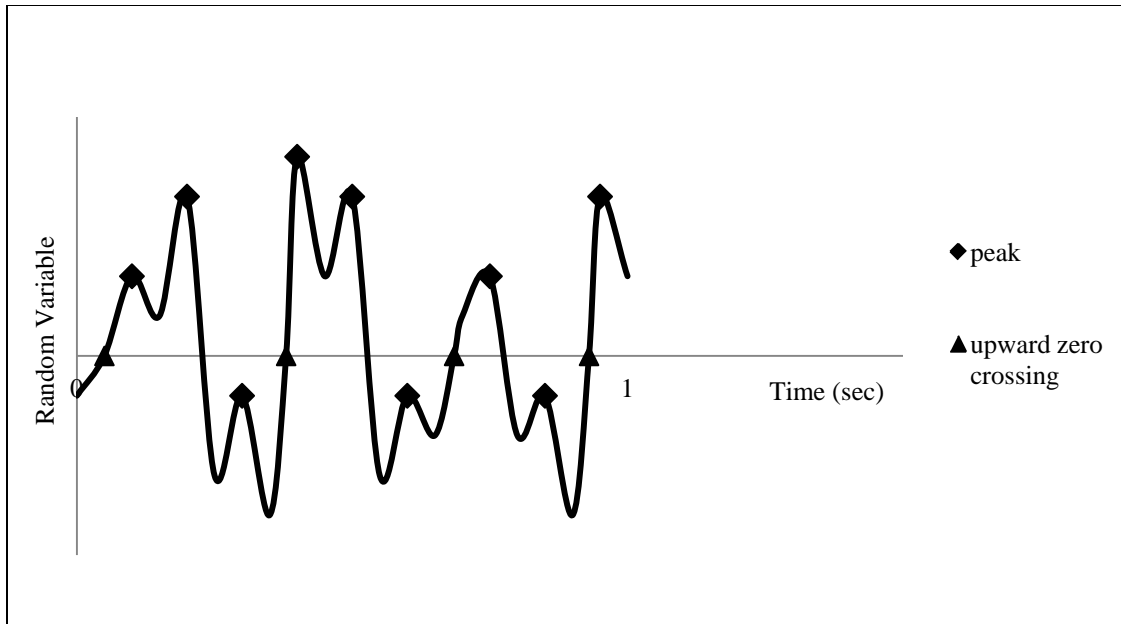


Figure 2-4. Illustration of Peaks and Zero Upward Crossings

The random time-history in Figure 2-4 has four zero upward crossings and nine peaks.

Thus, the irregularity factor is equal to 0.44.

The total number of cycles, $N(s)$, with amplitudes in the range s to δs can be obtained by using equation 2.15:

$$N(s) = v_0^+ T f_p(s) \cdot \delta s \quad (2.15)$$

Where, v_0^+ is the rate of crossing of the mean stress and can be assumed to be equal to natural frequency of vibration for narrow band resonant, $f_p(s)$ is the probability distribution of the peaks and T is the time of cycle counting. Also, damage under a narrow band process, D_{NB} , can be obtained in a “closed-form” as in equation 2.16.

$$D_{NB} = \frac{v_0^+ T}{A_D} (\sqrt{2}\sigma)^{m_D} \Gamma\left(\frac{m_D}{2} + 1\right) \quad (2.16)$$

Where, A_D is a constant depending on the material, Γ is gamma function, σ is the standard deviation of the time-history, and m_D is the exponent in the S-N relation (equation 2.17)

$$N_F s^{m_D} = A_D \quad (2.17)$$

Where, s is cycle amplitude, and N_F is the number of cycles until failure.

Allotey and El Naggar (2008) described two possible forms of nonlinear damage accumulation: (1) stress-dependent nonlinear damage accumulation and (2) stress-independent nonlinear damage accumulation. For the former, damage accumulation is both nonlinear and load-level dependent, and the Palmgren-Miner rule is not applicable. For the latter, although the damage evolution is nonlinear, the damage rate changes in the same manner at each stress level and the Palmgren-Miner rule is applicable (in terms of the summation of incremental damage over different load ratios).

Holmes (2001) suggested that equation 2.16 is a good model of the behavior for vortex-shedding induced vibrations in low turbulence conditions, but is not a representative of the background (subresonant) along-wind loading conditions, which results in a random wide band response of the structure.

Wide band random vibration consists of contributions over a broad range of frequencies.

Dirlik (1985) introduced a standardized variable i_x , seen in equation 2.18.

$$i_x = \frac{x}{\sigma_x} \quad (2.18)$$

He suggested equation 2.19 for peak probability density, $w(i_x)$, for a case of a wide band process:

$$w(i_x) = \frac{c_d}{\sqrt{2\pi}} e^{-i_x^2/2c_d^2} + C_{if} i_x e^{-i_x^2/2} [1/2 + \operatorname{erf}(C_{if} i_x/c_d)] \quad (2.19)$$

Where, C_{if} is irregularity factor, and C_d is defined as:

$$C_d = \sqrt{1 - C_{if}^2} \quad (2.20)$$

The shape of $w(i_x)$ depends on the irregularity factor, C_{if} as defined in equation 2.14. As C_{if} approaches zero, then $w(i_x)$ approaches a standard Gaussian probability density function.

The rainflow method proposed initially by Matsuishi & Endo (1968) is an acceptable method to count the number of cycles for a wide band random process, and has been introduced as one of the methods for counting the number of cycles in ASTM E1049 in the time domain.

Hancock & Bommer (2005) studied different approaches for counting the number of cycles in an earthquake record. They suggested that different definitions of loading cycles would be better suited to different applications, however amongst the generic definitions of the number of cycles, the rainflow counting definition has the merit of including all peaks in the time series without putting undue emphasis on non-zero crossing peaks.

2.3 Lateral Behavior of Piles

In common with other foundations, piles should satisfy two limit states: ultimate capacity and serviceability. Foundations that were subject to significant lateral and moment loads were first encountered in the offshore oil and gas industry. Offshore oil and gas platforms

are usually installed on piles, and most of the progress in the field of laterally loaded piles is owed to this industry. Increasing demand for new energy resources has led to an increase in the number of wind turbines and since the monopile is a widely used foundation for offshore wind turbines, much research has been recently conducted on this type of foundation.

In this section, methods and interpretations based on the ultimate capacity will be presented and then serviceability limit states will be discussed. It should be noted that, it is very hard to distinguish between these two criteria for laterally loaded piles. Agaiby et al. (1992) stated that “For laterally loaded piles, the distinction between stability and tolerable deformations may not be justified completely, because very often the criterion chosen for defining stability is a deformation value, rather than the unlimited deformation that typically is associated with instability.” Bearing this in mind, it is notable that recent publications are mostly concerned with displacement or rotation criteria for wind turbine applications.

2.3.1 Ultimate Capacity under Lateral Loads

Failure that corresponds to the ultimate capacity of a laterally loaded pile can be considered to be complete yielding of the soil along the pile depth or a structural failure in the pile material. Model piles of the current study are rigid and the latter mode of failure is not applicable, so the main focus herein will be on soil yielding along the pile length. In addition, this study is limited to cohesionless soil (i.e. sand), although equivalent analyses exist for clays, but these will not be discussed.

Terzaghi suggested that for a laterally loaded pile, the capacity will not exceed half of the soil vertical bearing capacity. The yield stress of soil, p_u , is the maximum average horizontal soil resistance at the pile-soil interface.

Hansen (1961) provided one of the earliest solutions for the ultimate capacity of a laterally loaded pile. His solution is based on different failure scenarios for ground surface, moderate and deep depths for a rigid square cross-section pile. For the ground surface, the yield stress is the difference between the passive and active stress coefficients. For moderate depths, the equilibrium of Rankine passive wedges is considered, which is assumed to be as wide as the foundation itself. Finally for deeper depths, the yield stress is calculated from the assumption of failure in the horizontal plane. Hansen mentioned that at deeper depth, rupture lines would not reach the ground surface. Eventually, equation 2.21 was suggested for yield stress, as below:

$$P_u(\text{Hansen}) = \sigma'_{v0}K_q + cK_c \quad (2.21)$$

Where, σ'_{v0} = vertical effective stress, c = soil cohesion, and K_q and K_c are factors from Figure 2-5. Christensen (1961) validated Hansen's (1961) method with 26 model tests and commented that it is conservative to take the value of ϕ' corresponding to the plane strain condition.

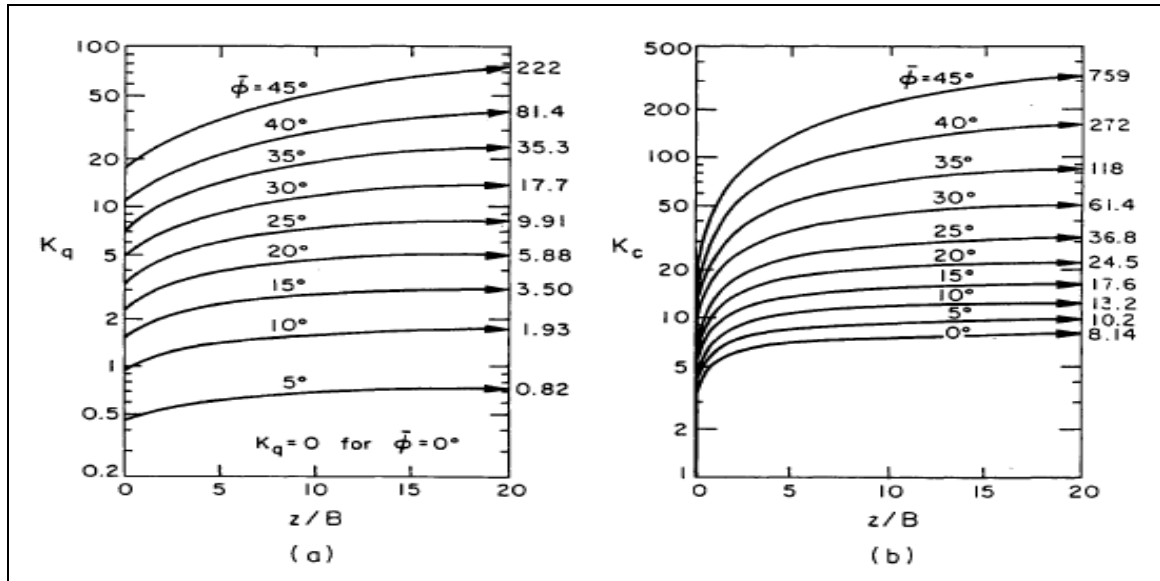


Figure 2-5. Factors for Brinch-Hansen Equation (Hansen, 1961)

The most famous interpretation of yield stress around a laterally loaded pile was presented by Broms (1964). Broms method is empirical and relies on back-calculated values from full-scale pile tests. Broms suggested equation 2.22 for yield stress in cohesionless soil, which is equal to three times the maximum full passive Rankine pressure, K_p . He also stated that passive pressure would mobilize after rotations of approximately 0.006 radians in loose sands.

$$P_u(\text{Broms}) = 3\gamma z \tan^2\left(45^\circ + \frac{\phi'}{2}\right) \quad (2.22)$$

Where, γ is the soil unit weight, z is depth and ϕ' is the soil internal friction angle.

Although Broms did not subdivide failure modes into shallow or deep depths, he suggested that at the ground surface, the sand would move upward. With increasing depth this upward movement would be replaced by lateral movement of soil to the back of the pile.

Kishida & Nakai (1977) performed theoretical studies for a laterally loaded pile with extensive deformations and confirmed the multiplier three in equation 2.22 for the friction angles ranging from 30° to 40°.

Meyerhof & Ranjan (1972) also studied the ultimate capacity of rigid free standing piles under horizontal load. They defined the ultimate horizontal load, H_u , as the load at which ground-line displacement of the pile increases continuously with no further increase of the load, or the ground-line displacement begins to increase at a rate out of proportion to the rate of increase of the load. Meyerhof & Ranjan assumed a passive Coulomb state mobilized in front of the pile, with an active state on the other side of the pile. The active force is usually neglected, since it is small compared to the passive force. Meyerhof & Ranjan considered two different cases for shallow and deep modes of failure and the earth pressure coefficient varied with the depth/diameter ratio of the pile and the internal friction angle of the sand. They implemented the bearing capacity factor N_q , for a strip footing and suggested equation 2.23 for yield stress in sand:

$$p_u(\text{Meyerhof}) = \gamma z K_o N_q \quad (2.23)$$

Where, K_o , is coefficient of earth pressure at rest.

Reese et al. (1974) also considered two different scenarios for shallow and deep failure. In shallow failures, the 3-D wedge shown in Figure 2-6a was assumed to form in front of the shaft. On the other hand, a deep failure mechanism gives a plane strain mode of failure. The deep failure mode is sketched in Figure 2-6b. Equations 2.24 and 2.25 are for the shallow and deep mode of failure, respectively.

$$P_u(Reese) = \gamma z \left[\frac{K_o z \tan \phi \sin \Omega}{\tan(\Omega - \phi) \cos \vartheta} + \frac{\tan \Omega}{\tan(\Omega - \phi)} (b + z \tan \Omega \tan \vartheta) + K_o z \tan \Omega (\tan \phi \sin \Omega - \tan \vartheta) - K_a B \right] / B \quad (2.24)$$

$$P_u(Reese) = K_a \gamma z (\tan^8 \Omega - 1) + K_o \gamma z \tan^4 \Omega \quad (2.25)$$

Where, Ω is angle that was suggested to be equal to $(45^\circ + \phi/2)$, ϑ is angle that ranges from $\phi/2$ to $\phi/3$, and K_a is Rankine active coefficient.

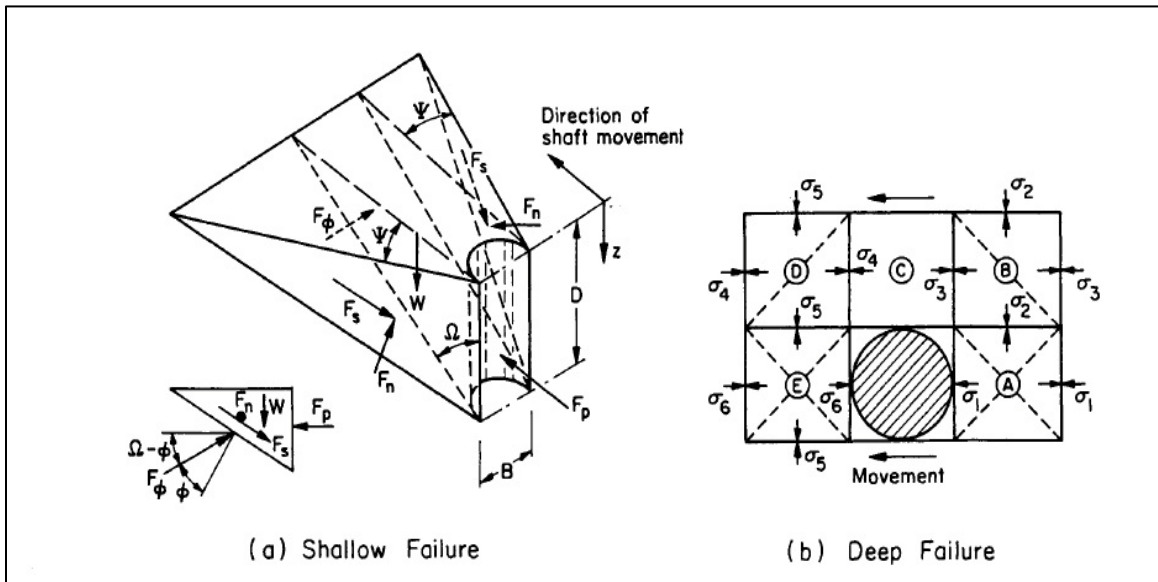


Figure 2-6. Shallow and Deep Mode of Failures (Reese et al., 1974)

The transition depth from shallow to deep for Reese et al. (1974) is 21.6 times the pile diameter. Hence, the shallow mode is thought to govern the behavior of small scale model piles.

General agreement exists between the above mentioned interpretations and models. Subdivision of the problem into deep and shallow failures is explicitly implemented in many of the described solutions, however, for Broms (1964) the transition in failure mode is recognized, but is not implemented.

Based on the yield stress distributions around the pile and considering static equilibrium; ultimate lateral load capacity, H_u of the pile can be calculated for moment tests, i.e. load applied at some height above the ground surface and ground-line tests, i.e. only horizontal load.

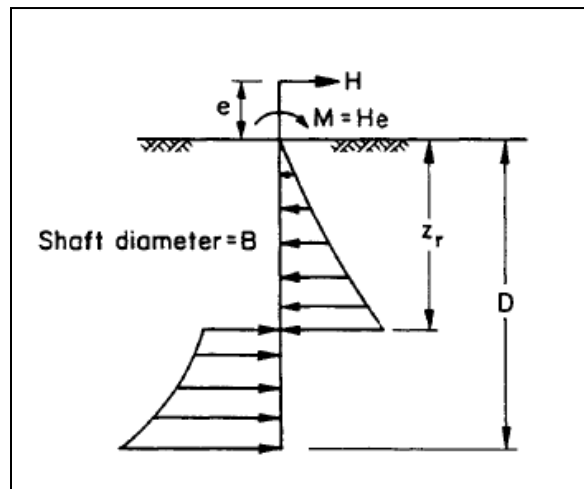


Figure 2-7. On Pile Force Profile (Agaiby et al., 1992)

As it can be seen in Figure 2-7, depth of rotation, (Z_r), is important for calculating H_u . This depth can be obtained by trial and error and consideration of force and moment equilibrium. Agaiby et al. (1992) studied the depth of rotation, Z_r , and believed that Z_r/D ranges from 0.794 to 0.708 for load eccentricity from 0 to 20 (Figure 2-8). In Figure 2-7, H is horizontal load, e is load eccentricity, and D is pile length.

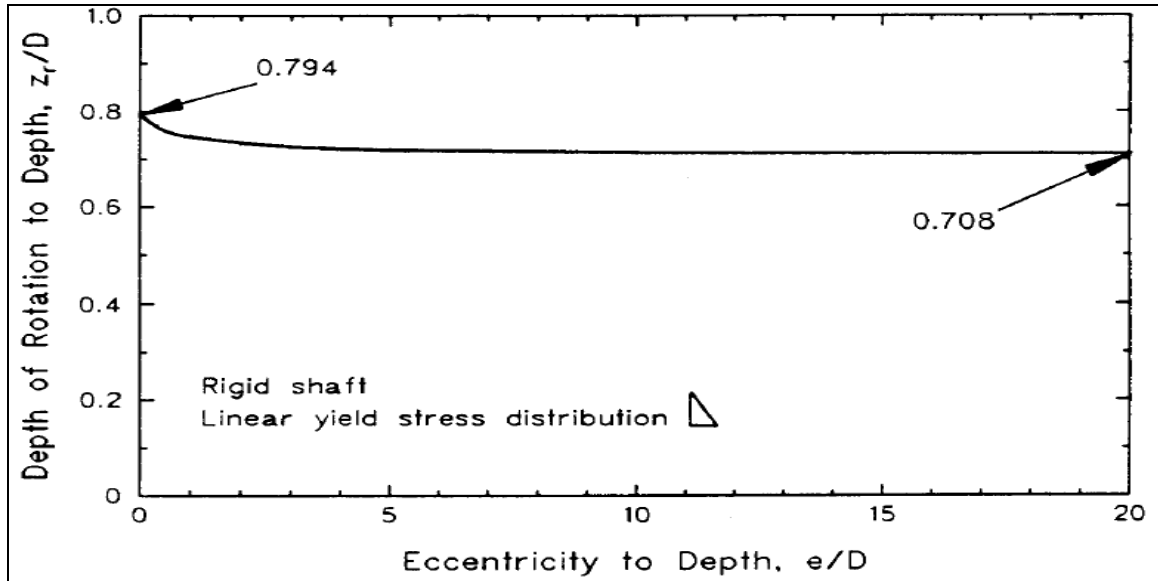


Figure 2-8. Effect of Eccentricity on Depth of Rotation (Agaiby et al., 1992)

Equation 2.26 gives the value of H_u , after determining Z_r .

$$H_u = \int_0^{Z_r} p_u B dz - \int_{Z_r}^D p_u B dz \quad (2.26)$$

Where, B is equal to the pile diameter.

Currently there is no globally accepted definition for capacity of laterally loaded piles for different problems. Some recommendations relate capacity to certain limits of the displacement or rotation of the pile. For instance, Reese & Wang (2008) limit the maximum rotation at the foundation level to be equal to 0.001 radians and Achmus et al. (2009) suggested the maximum mudline rotation for offshore wind turbines constructed on monopiles should be less than 0.5° .

Borden & Gabr (1987) provided an alternative interpretation which relates the ultimate capacity to displacement. They suggested that the ultimate capacity is a load

corresponding to the horizontal tangent on the load-displacement curve as can be seen in Figure 2-9.

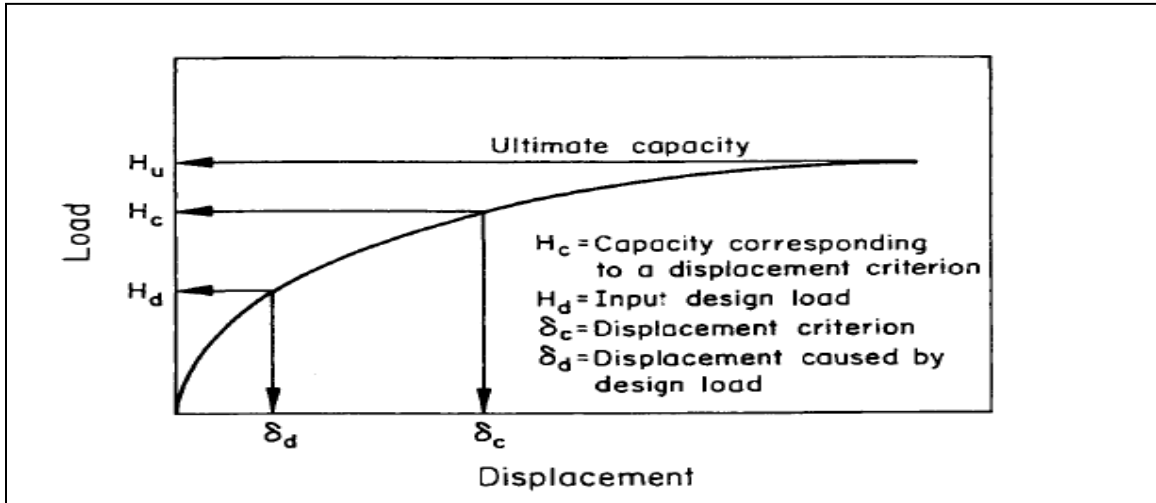


Figure 2-9. Ultimate Capacity (Borden & Gabr, 1987)

Manoliu et al. (1985) suggested the use of a hyperbola to be fitted to the load-displacement curve. Their interpretation introduced two terms known as the hyperbolic capacity, H_h (N), and initial stiffness, K_i (N/m) as can be seen in Figure 2-10.

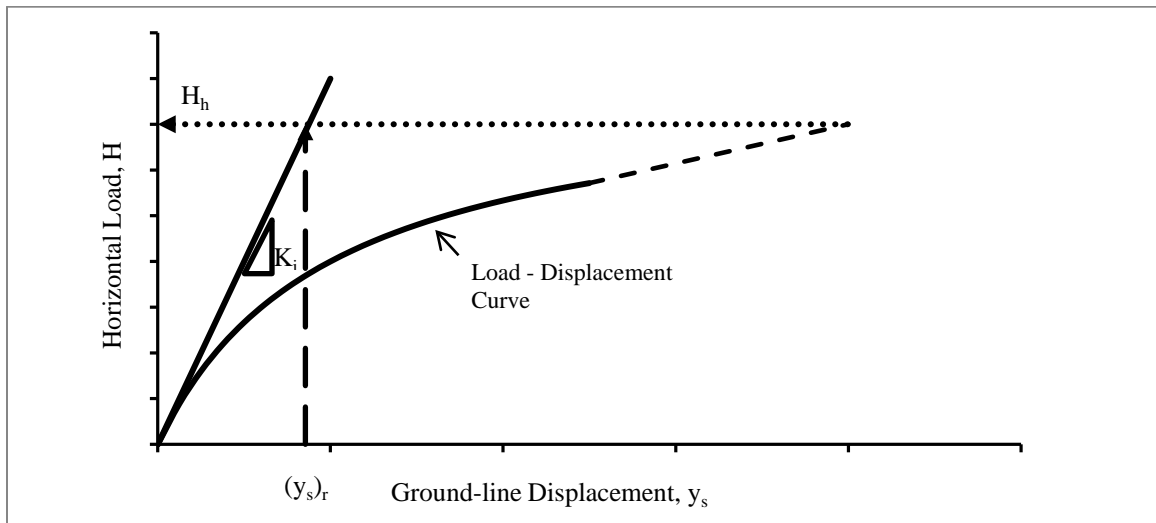


Figure 2-10. Hyperbolic Interpretation of Load-Displacement (Manoliu et al, 1985)

The Manoliu et al. (1985) method is preferred to Borden & Gabr (1987) method for data analysis in the current research; it gives two quantities to compare different scenarios and these parameters can be obtained and implemented into a load - displacement relation as shown in equation 2.27. The Manoliu et al. (1985) method gives a robust tool to compare the results obtained from the experiments or numerical analysis, as can be seen in Agaiby et al. (1992) and Achmus et al. (2009).

$$H = \frac{K_t y_s}{1 + y_s / (y_s)_r} \quad (2.27)$$

Where, $(y_s)_r$ is equal to H_h/K_i .

The ultimate capacity determined from the Borden & Gabr (1987) or Manoliu et al. (1985) methods may not necessarily be in agreement with the classic solutions; the Manoliu et al. (1985) and Borden & Gabr (1987) methods are based on the displacement whilst the classic solutions are based on instability criteria.

2.3.2 Serviceability under Lateral Loads

Serviceability of piles is often a more stringent limit state for infrastructure. As has been described in Section 2.3.1 some of the definitions for ultimate capacity are based on ground-line displacement or rotation. It is of interest to predict the displacement of piles under lateral loads, because in many practical cases functionality may be threatened after certain levels of displacement (this is particularly true for wind turbines).

There are two main categories for prediction of the displacement of laterally loaded piles. One is generally known as the “Continuum Approach” and the other one is the “Subgrade

Reaction Modulus”. These two general methods will be discussed in Sections 2.3.2.1 and 2.3.2.2, respectively.

2.3.2.1 Continuum Models

Soil is often assumed to be a continuum, although in many areas, simplifying assumptions are used to reduce the level of complexity involved in modeling 3D continuum soil media.

Poulos published two papers in 1971 and 1973 based on the elastic continuum approach for predicting the lateral deflections in a laterally loaded pile. Banerjee & Davies (1978) and Randolph (1981) also adopted this approach by considering soil as an elastic continuum and using the boundary element or finite element methods. These papers were limited to elastic conditions and consequently low strain levels, which might not be justified in many practical cases.

Two papers in 1987 were published by Davies and Budhu to describe the lateral behavior of piles using the elastic continuum approach to take into account soil yielding. In these papers the soil was modeled as an elastic – perfectly plastic material. For utilizing this method, pile length should be greater than the effective length, which has been defined as a length beyond which the pile length has no effect on the load - deformation response of pile under lateral loading. Effective length, L_e , can be calculated from equation 2.28:

$$\frac{L_e}{B} = 1.3K_{PS}^{2/9} \quad (2.28)$$

Where, B is pile diameter and pile-soil stiffness ratio, K_{PS} , is defined in equation 2.29:

$$K_{PS} = E_p/mB \quad (2.29)$$

Where, E_p is Young's modulus of the pile material and m is a constant that presents the increase in soil Young's modulus. Equations 2.30 and 2.31 give ground-line displacement, y_s , and rotation, θ , in piles:

$$y_s = I_{y_s H} \frac{H}{mB^2} + I_{y_s M} \frac{M}{mB^3} \quad (2.30)$$

$$\theta = I_{\theta H} \frac{H}{mB^3} + I_{\theta M} \frac{M}{mB^4} \quad (2.31)$$

Where, $I_{y_s H}$, $I_{y_s M}$, $I_{\theta H}$, and $I_{\theta M}$ are dimensionless compliances.

In this method, although soil is not accurately represented, since we consider an elastic model of soil or in the Budhu and Davies (1986) as elastic – perfectly plastic material, it is believed that this form of solution is more representative of reality compared to subgrade reaction modulus methods. Also, the parameters used here can be predicted or correlated from conventional soil investigation methods.

Sa'adon et al. (2009) presented an alternative analytical solution for laterally loaded piles based on the elastic continuum approach. They presented simple equations and flexibility coefficients to obtain ground-line displacement and rotation. The presented equations were verified with some reported in-situ full scale pile load tests. This method is applicable for long piles (i.e. having a length beyond the active length, L_a). The active length, L_a , is defined in equation 2.32:

$$L_a = 0.5BK^{0.36} \quad (2.32)$$

Where, K is ratio of pile material Young's modulus to soil Young's modulus, and B is pile diameter.

Recently, Basu et al. (2009) used the continuum approach to obtain the response of piles by assuming an elastic multi-layer medium and the principle of minimum energy. They used a rigorous analytical model in the research and suggested that further work can be done to account for soil non-linearity.

2.3.2.2 Subgrade Reaction Modulus

In this approach, the reaction modulus, E_{py} , is the key parameter. E_{py} is defined as the resistance from the soil at any point along the pile, p , divided by the deflection of the pile at that point, y , as can be seen in Figure 2-11. E_{py} is a function of depth, z , ground water level and deflection in the pile, y . The reaction modulus was defined by Terzaghi (1955) as a function of coefficient of subgrade reaction, k_{py} . Terzaghi suggested increasing the k_{py} with depth, z . The values at the ground surface are available from Terzaghi for different relative densities of sand and ground water conditions. Also, it is important to keep in mind that E_{py} is different from soil Young's modulus, E_s , which was used in the elastic continuum approach.

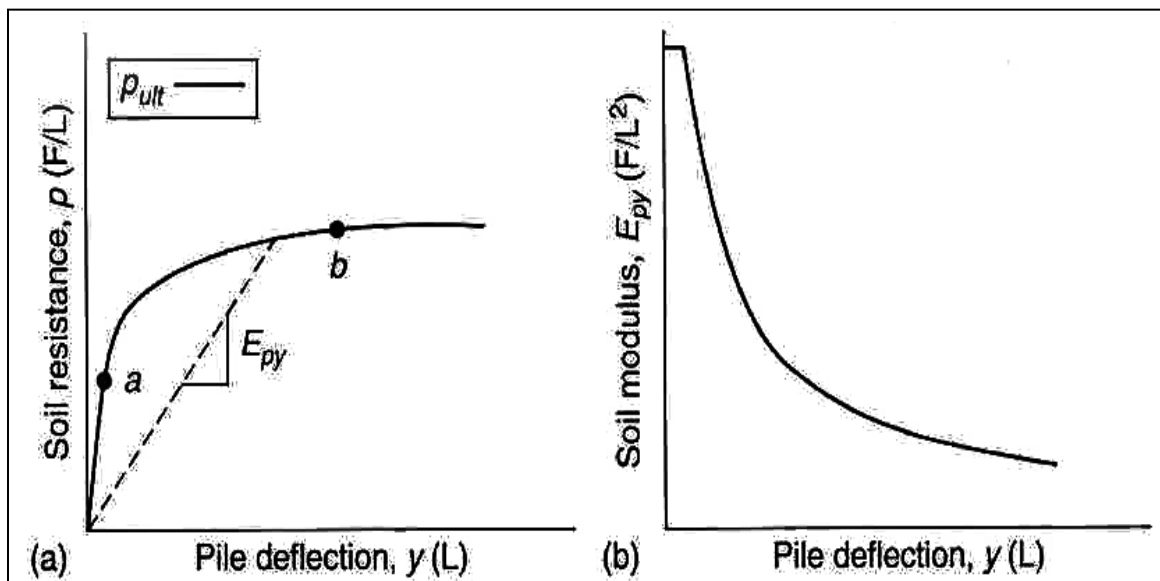


Figure 2-11. Subgrade Reaction Modulus (Reese & Van Impe, 2010)

In this approach, the Winkler spring method is adopted and the soil is modeled by a series of springs. These springs act independently so they can model different soil layers and conditions. The main differential equation used in this solution is the beam on a foundation equation, which was presented by Hetenyi (1946) and is given in equation 2.33.

$$\frac{d^2M}{dx^2} = E_P I_m \frac{d^4y}{dx^4} \quad (2.33)$$

Where, M is the applied moment, I_m is moment of inertia of the pile, and E_P is pile material Young's modulus.

Using a series of assumptions, equation 2.33 can be solved and certain boundary conditions for different head fixity can be implemented. Solutions for pile head deflection, rotation, bending moment, shear force and pile lateral load can be obtained. The effect of vertical load on lateral behavior of piles is neglected in this method.

The concept of the p-y method was suggested over 50 years ago; McClelland & Focht (1958) initially developed this approach. Over the last 40 years, other authors, such as, Matlock & Reese (1962) have contributed to this method and the p-y method is now widely used in the offshore industry through standards like API (2003) and DNV (2007). The p-y method is also accessible through computer software like LPILE[®]. Different in-situ pile tests have resulted in different p-y curves for various soil types, i.e. different E_{py} with pile head fixity conditions. In these curves, p is the net horizontal soil force per unit length and y is shaft displacement at any depth (Figure 2-12).

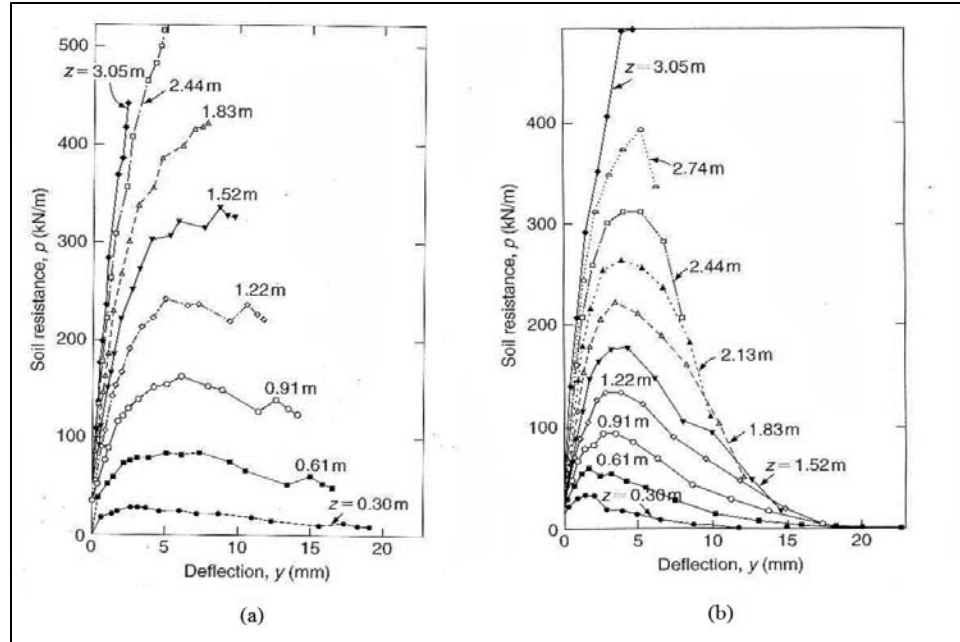


Figure 2-12. Developed p-y Curves from (a) Static Test, (b) Cyclic Test (Reese et al., 1965)

DNV (2007) and API (2003) recommend equation 2.34 for p-y curves in sand.

$$p = Ap_u \tanh\left(\frac{k_{py}z}{Ap_u} y\right) \tag{2.34}$$

Where, k_{py} is the initial modulus of subgrade reaction, and A is equal to 0.9 for cyclic loads, while for static loads A is obtained from equation 2.35 below, which is a function of pile diameter, B , and depth below the ground surface, z . It is worth mentioning that the ultimate resistance per unit length, p_u , remains unchanged for the cyclic loads, which is given in terms of three coefficients depend on soil friction angle (DNV, 2007).

$$A = \left(3 - 0.8 \frac{z}{B}\right) \geq 0.9 \tag{2.35}$$

Duncan et al. (1994) used the so-called characteristic load method. This method approximates p-y curves closely with simple equations. The method is based on some non-dimensional variables which are called characteristic loads and moments. Although

the method was initially designed for ground-line load conditions it can predict the effect of above ground loads (i.e. moment tests) by nonlinear superposition. This method can be used for piles which are long enough so their behavior will not be affected by their length.

The subgrade reaction modulus approach is often criticized because of the discretization of the soil, which is in reality a continuum. Reese & Van Impe (2010) commented on this criticism by saying that the full-scale tests that led to the p-y curves have already satisfied the effect of continuity in the soil. Also, E_{py} cannot be determined through conventional laboratory tests, although some attempts were done to correlate between tests to get E_{py} , there is no general agreement on these correlations.

2.3.3 Effect of Cyclic Loads on Response

The distinct difference between vertical and horizontal loads on piles is that although we can predict the former with high level of certainty, it is very unlikely that we can do so for latter. Horizontal loads may apply to infrastructure from the actions of environmental phenomenon, such as, earthquakes, wind or sea waves; hence their cyclic randomness should be included in analysis. Currently wind turbines and offshore platforms are two ubiquitous instances of laterally loaded piles under random cyclic loads.

Prakash (1962) observed that deflection in laterally loaded piles almost doubled after 40 cycles of loads. As was explained earlier, the soil subgrade reaction modulus is an important parameter in the lateral behavior of piles. Broms (1964) suggested reduction in the coefficient of lateral subgrade reaction to account for effects of repetitive loads.

Moreover, Reese & Van Impe (2010) suggested that near the ground surface, void ratio of sand would tend towards the critical value under cyclic lateral loads. Thus dense sand loosens and vice versa. However, this work needs more experimental works to be developed.

Cuellar et al. (2009) proposed that soil subsidence around pile under constant amplitude cyclic lateral loads in sand is not only associated with soil densification, but also a convective cell flow of sand grains around the pile head. The convective flow is believed to be the result of ratcheting phenomena that was triggered by cyclic low-frequency lateral displacement of the pile. They described the pile-soil interaction under cyclic loads to occur in two distinct phases, a densification phase and a convection dominated phase. In the first phase, the rearrangement of grains starts immediately after the first cycle and is characterized by a “progressive subsidence” of the soil surface surrounding the pile. In the second phase, no further densification occurs and subsequent cycles trigger ratcheting behavior of the piles. Figure 2-13 shows the lateral displacement of a pile in these two distinct phases.

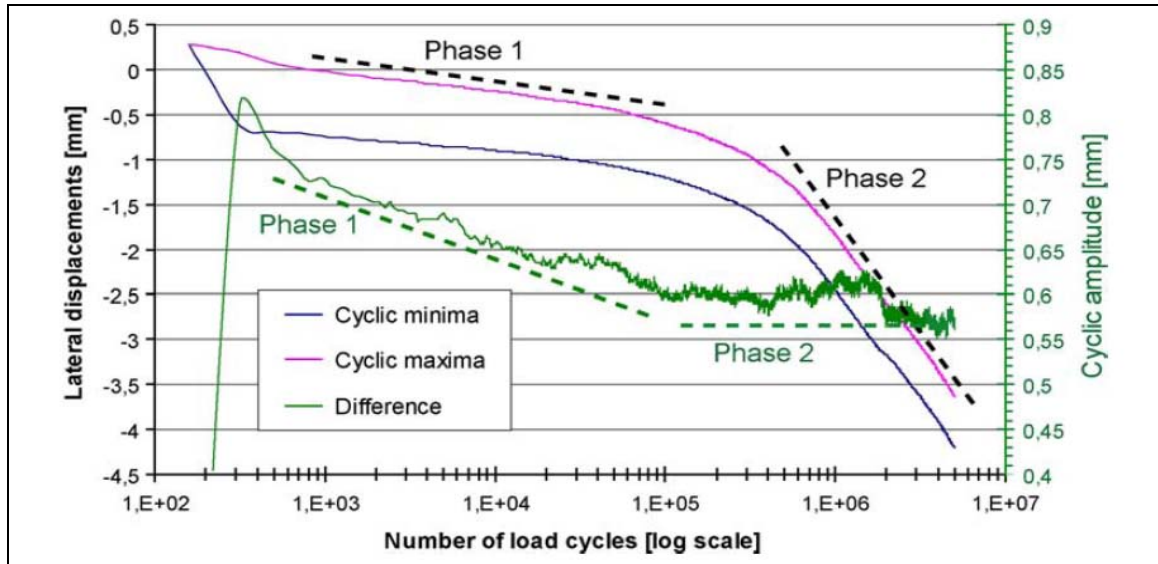


Figure 2-13. Two Distinct Phases in the Behavior of Laterally Loaded Pile in Sand (Cuellar et al., 2009)

Methods used for the prediction of laterally loaded piles were presented in previous sections and the p-y method is still the most favored method of analysis. Subsequent researches based on some modifications to the p-y curves method have attempted to take into account the effects of cyclic loads.

Reese et al. (1974) commented that behavior of sand around a laterally loaded pile may not submit to rational analysis, therefore a considerable amount of empiricism is involved. Two instrumented piles were tested in Mustang Island, Texas with groundwater above the ground surface to replicate offshore conditions. In their method, they used adjustment factors to compare predicted and obtained results. The adjustment factors were obtained for the static and cyclic tests independently. Their analysis was limited to driven piles in sand and they suggested practitioners use the method with extra caution. It is worth mentioning that very limited attention was given to the characteristics of the cyclic load. Also scouring around the laterally loaded piles was not addressed.

The proposed method by Reese et al. (1974) showed good agreement with other sets of tests in 1979 reported by Meyer & Reese, but failed to predict the results of two other tests performed in 1982. Long & Vanneste (1994) commented that because testing conditions were different, it was not reasonable for Reese et al. (1974) to give acceptable results. Figure 2-14 shows the results of test in 1982 (black points) and predicted curves from Reese et al. (1974).

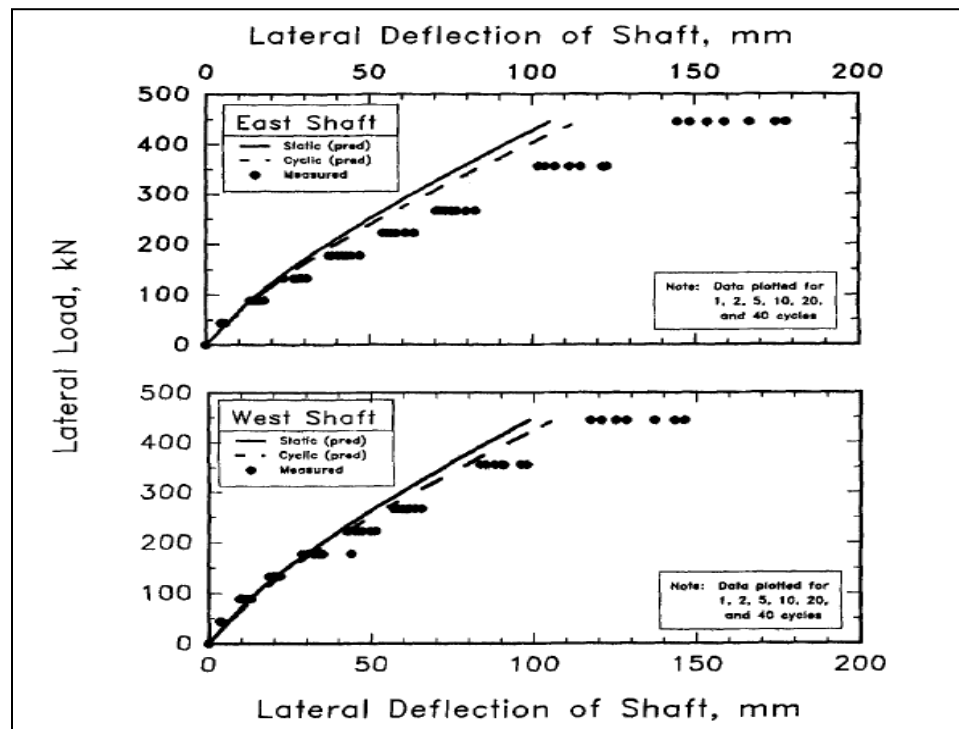


Figure 2-14. Comparison between Test Results and Predicted Curves (Long & Vanneste 1994)

Little & Briaud (1988) studied lateral behavior of six piles under constant amplitude cyclic load with incremental increase and compared them with results obtained from the pressuremeter test. They paid attention to the characteristics of lateral load and the loading – unloading scheme is described in detail in their paper. Twenty load cycles were applied to the piles. The cyclic response of the piles is presented in two ways: first,

through the increase in displacement after cyclic loads and second in terms of cyclic degradation of secant and shear stiffnesses. They used both concrete and steel piles. For steel piles, there was very little degradation in the pile material and the displacement increase was related to the degradation of the soil stiffness. One of the remarkable conclusions from their work is the more damaging effect of initial cycles compared to other cycles. They suggested a modification of the p-y method with application of a degradation factor and the number of cycles built into it as equation 2.36 and 2.37:

$$p_N = p_1 \quad (2.36)$$

$$y_N = y_1 \times N^a \quad (2.37)$$

Where, N is the number of cycles and 'a' is the degradation parameter obtained from the pressuremeter test. They finally commented that further studies would be needed for comparison of confinement around the pressuremeter probe and pile.

Agaiby et al. (1992) studied the behavior of laterally loaded rigid shafts under static and cyclic constant amplitude tests. Model piles were tested in loose, medium dense and dense sands. They confirmed that cyclic loading would eventually cause displacement accumulations, although the accumulation increases at a decreasing rate.

Long & Vanneste (1994) studied the effects of cyclic constant amplitude lateral loads on accumulated ground-line displacement of piles through the results of 34 reported in-situ pile load tests. Their study is more systematic compared to Little & Briaud (1988), since they tried to incorporate the effects of various parameters like soil initial condition, cyclic load characteristics and installation methods. They believed that the characteristics of the cyclic lateral load strongly affect the pile lateral response. The cyclic lateral load was

characterized as either one-way or two-way in this paper (Figure 2-15); with the effects of one-way loading being more pronounced on the accumulated ground-line displacement. Two-way cyclic load was described qualitatively as four quarter cycles and was used as a theoretical basis in this paper.

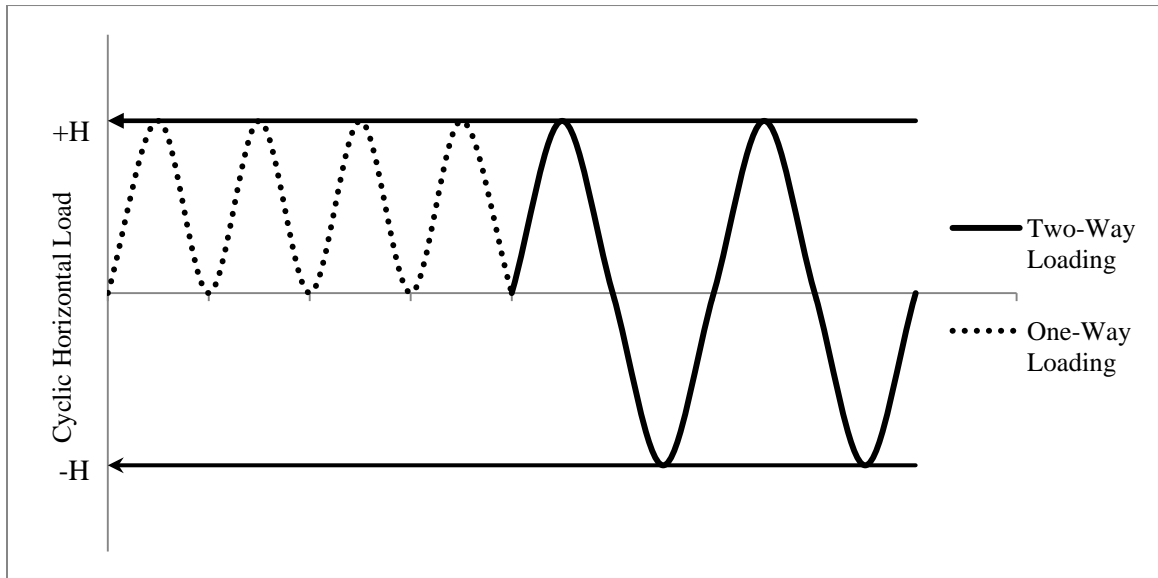


Figure 2-15. Two-Way vs. One-Way Lateral Load

Long & Vanneste (1994) suggested that cyclic loading would reduce the coefficient of the soil reaction modulus, k_{py} , as can be seen in equation 2.38.

$$R_n = \frac{(k_{py})_N}{(k_{py})_1} = N^{-t} \quad (2.38)$$

Where, N is the number of loading cycles, R_n is the ratio of the coefficient of the soil reaction modulus after N^{th} cycle to the coefficient after the first cycle, and t is the degradation parameter shown in equation 2.39, which incorporates the effects of soil conditions, installation methods and cyclic load ratio.

$$t = 0.17 \times F_C \times F_I \times F_L \quad (2.39)$$

Where, F_C , F_I and F_L are factors for soil density, installation method, and cyclic load ratio. Cyclic load ratio, R_H , was introduced as the ratio of the minimum over the maximum lateral loads (H_{\max}/H_{\min}). Table 2-1 gives suggested values of F_L for different cyclic load conditions.

Table 2-1. Suggested Value for Cyclic Load Ratio Factor, F_L (Long & Vanneste, 1994)

Load Ratio, R_H	F_L
-1.0 (two-way loading)	0.2
-0.25	0.4
0.0 (one-way loading)	1.0
0.5	1.0
1.0 (monotonic)	0.0

The degradation parameter, which has typical values of 0.1 to 0.4, can be incorporated in both the p-y method and simple beam on elastic foundation method of Hetenyi (1964) through the coefficient of soil reaction modulus (Long & Vanneste, 1994). In both, the degradation parameter is meant to decrease the soil reaction modulus. This reduction can also be satisfied with modifying the ground-line displacement as can be seen in equation 2.40:

$$y_N = y_1 \cdot N^t \quad (2.40)$$

Where, y_1 is deflection after the first cycle, and y_N , is deflection after the N^{th} cycle.

Lin & Liao (1999) studied the accumulation of permanent strains in sand due to variable amplitude cyclic lateral loads in piles. In this study, a degradation parameter was

obtained from the results of 20 full-scale tests. In their work, they assumed contact at all times at the pile soil interface. Kagawa & Kraft (1980) observed that more than 70% of the pile displacement is concentrated in the soil mass within a two-pile radius distance; hence the lateral strain, ε , can be approximated by equation 2.41.

$$\varepsilon = \frac{y_s}{2.5B} \quad (2.41)$$

Where, y_s is equal to the ground-line displacement of the pile and B is pile diameter. In this study, cyclic strain ratio, R_s , is defined as the ratio of the strain after the N^{th} cycle over the strain after the first cycle as can be seen in equation 2.42.

$$R_s = \frac{\varepsilon_N}{\varepsilon_1} = 1 + t \ln(N) \quad (2.42)$$

The degradation parameter, t , has the same form as in the one obtained by Long & Vanneste (1994), but also includes a depth coefficient. They also used a superposition method to include effects of variable-amplitude cycles, although they used the same concept as Long & Vanneste (1994).

Allotey & El Naggar (2008) studied the effects of soil and pile yielding, gapping and soil cave-in on the response of the pile foundations under lateral cyclic loading. They suggested that adjusting the original p-y curves to account for cyclic degradation resulted in only an increase in the pile maximum displacement.

Achmus et al. (2009) studied the behavior of a monopile under cyclic loading under large numbers of load cycles. Results of drained cyclic triaxial tests were used for developing a numerical model for the prediction of the long-term behavior of the piles under cyclic lateral loads. Accumulation of plastic strain in drained triaxial conditions corresponds to

the decrease in the soil secant modulus. The stiffness degradation obtained from these tests was incorporated into finite element models to represent the pile-soil interaction under action of cyclic lateral loads. They proposed non-dimensional load and displacement factors to predict the accumulated displacements for medium-dense and dense sands under large numbers of loading cycles. They used the hyperbolic presentation of load - displacement introduced by Manoliu et al. (1985). Also the effects of embedment length, loading amplitude and load eccentricity were investigated. The reduction in embedment length increases the accumulated ground-line displacement. They suggested that pile performance under the action of cyclic lateral load is very much dependent on the embedment length. It was understood that the effects of pile diameter is not that significant. The pile performance under the action of the cyclic lateral load can be improved by increasing the pile length, rather than pile diameter. Also, increase in the load eccentricity will cause reductions of the ultimate capacity.

Leblanc et al. (2010) studied the response of stiff piles to large numbers of cyclic lateral loads in sand. They believe that piles for wind turbines should be treated independently from piles used in offshore oil or gas platforms, since the number of loading cycles and their amplitude are very different. They performed their model tests considering various relative densities for sand and lateral loads applied to the model for large number of cycles. Static tests were also performed, so the results of cyclic tests for accumulated rotation could be presented as non-dimensional ratios of the form of equation 2.43.

$$\frac{\Delta\theta(N)}{\theta_s} = \frac{\theta_n - \theta_0}{\theta_s} = T_b(\zeta_b, R_d)T_c(\zeta_c) \cdot N^{0.31} \quad (2.43)$$

Where, θ_s is equal to the rotation in a static test, T_b and T_c are non-dimensional values, depending on the load characteristics and sand relative density given in the form of two plots. ζ_b and ζ_c in Figure 2-16 are factors characterizing cyclic loads as a ratio of maximum and minimum values in a load cycle to the static moment capacity, M_R , as can be seen in equations 2.44 and 2.45.

$$\xi_b = \frac{M_{max}}{M_R} \quad (2.44)$$

$$\xi_c = \frac{M_{min}}{M_{max}} \quad (2.45)$$

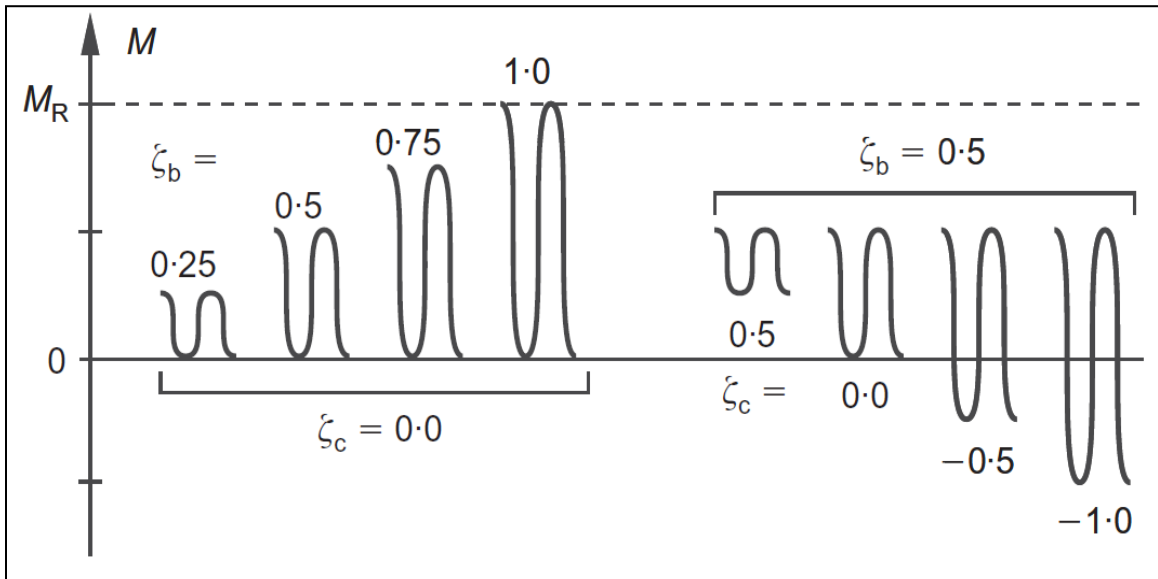


Figure 2-16. Load characterizing Factors (Leblanc et al., 2010)

They suggested increase of stiffness with more numbers of cycles, rather than decrease which is suggested in other papers. They also suggested that the increase of the stiffness is independent from the soil relative density. However, the proposed method has not been verified at full-scale and wind loads are simplified to be constant amplitude cyclic loads, rather than random variable amplitude cyclic loads.

Leblanc et al. (2010) also published a technical paper to include the response of stiff piles to variable amplitude two-way lateral loading in the model described previously. The paper used the method described above (equation 2.43) to calculate the accumulated rotation under random loads. The applicability of Miner's damage rule for accumulation of rotation in laterally loaded pile in sand was verified through a set of tests with varying amplitude loads, and they concluded that "accumulated pile rotation is independent of loading sequence". The rainflow method was then used to decompose the time-series of a random load. The decomposed amplitudes from the rainflow method were used to obtain load characterizing factors (Figure 2-16).

2.4 Summary

In this chapter, wind processes were introduced and necessary parameters for wind property descriptions were presented. Then the subject of laterally loaded piles was discussed in terms of both ultimate capacity and serviceability.

It is understood from the literature that studies incorporating the explicit effects of cyclic loads are limited and may need more validation. Fortunately, some researchers are moving towards the development more representative models of the problem, particularly with an appreciation of the effects of random variable amplitude cyclic loads. Many recent studies have used scaled model tests and numerical analysis to study the problem in more detail and incorporate different factors to ensure more effective designs. However, with respect to random variable amplitude cyclic loads, much more work still needs to be conducted.

METHODOLOGY AND TESTING PROGRAM

3.1 Overview

A significant portion of deep foundation design methods and guidelines are based on empirical relations, which are based on *in situ* tests or laboratory model tests. Pile tests are ubiquitous and small scale model tests have some advantages over field tests. At laboratory scale, there is a good opportunity to study single parameters independently and exert better control over material, and loading states. However, some of the more complex features of prototype behavior cannot be reproduced accurately. The current research is an experimental testing program utilizing small model piles to study the response of laterally loaded rigid piles under static and random variable amplitude load conditions. The methodology herein has been designed to achieve the objectives stated in the first chapter.

The testing program has been performed in two phases. The first phase was performed in the Boundary Layer Wind Tunnel Laboratory, (BLWTL). A small scale model consisting of an aluminum plate, pole and pile was pushed into Ottawa sand, which was pluviated into a sunken box and a simulated wind field was applied to the model. In the second phase, the same setup was placed in a static test box and lateral loads applied to the pole through a cable and system of pulleys. Different aspects of the testing program and materials are described below.

3.2 Components of Testing Program

3.2.1 The Boundary Layer Wind Tunnel Laboratory

The wind tunnel is a powerful experimental tool to model wind flow and structural response at laboratory scale. The wind tunnel is able to generate similar wind characteristics over a terrain approaching an actual site at small scale. The BLWTL at Western University is capable of modeling a wide range of structures and bridges, and has been utilized in the design process of number of infrastructures all over the world. It has two separate tunnels with different applications for a variety of industrial and research purposes.

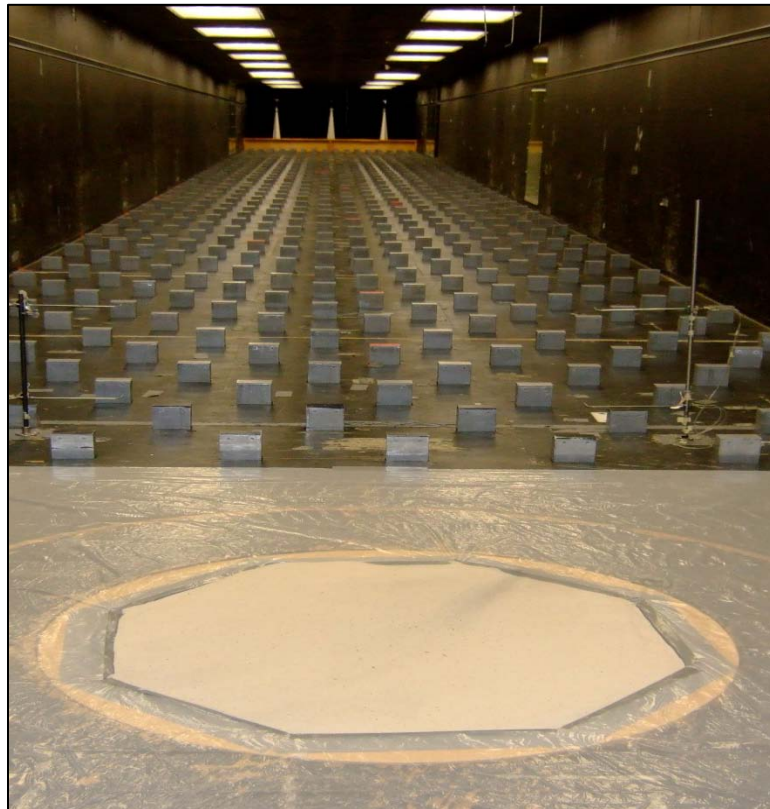


Figure 3-1. The Boundary Layer Wind Tunnel #2

In this testing program, tunnel #2 has been used, which has a maximum wind speed of 100 km/hr (28 m/s). A large fan pulls the air from one end and this generates a circulating flow of wind from the other end. The tunnel accommodates various surface roughnesses with adjustable “roughness” cubes embedded in the wind tunnel surface as can be seen in Figure 3-1. An open country terrain (Roughness length, z_0 , of 0.01-0.05 m) was used in this research; i.e. the cubes were not used. The dimensions of the wind tunnel #2 are given in Table 3-1 (www.blwtl.uwo.ca/Public/BLWTL2.aspx).

Table 3-1. Dimensions of Wind Tunnel #2

Length (m)	Width (m)	Height(m)	Max Speed (km/hr)
39	3.4	2.5	100

3.2.2 Silica Sand Properties

Barco #32 Silica (Ottawa) sand with a sub-angular grain shape was used in this study. The sand mineral content is Quartz. The hardness of the silica sand is equal to 7 Mohs.

Conventional soil classification tests have been performed on samples taken from the silica sand. Grain size distribution analysis has been done in accordance with ASTM D6913 and the particle distribution chart is given in Figure 3-2.

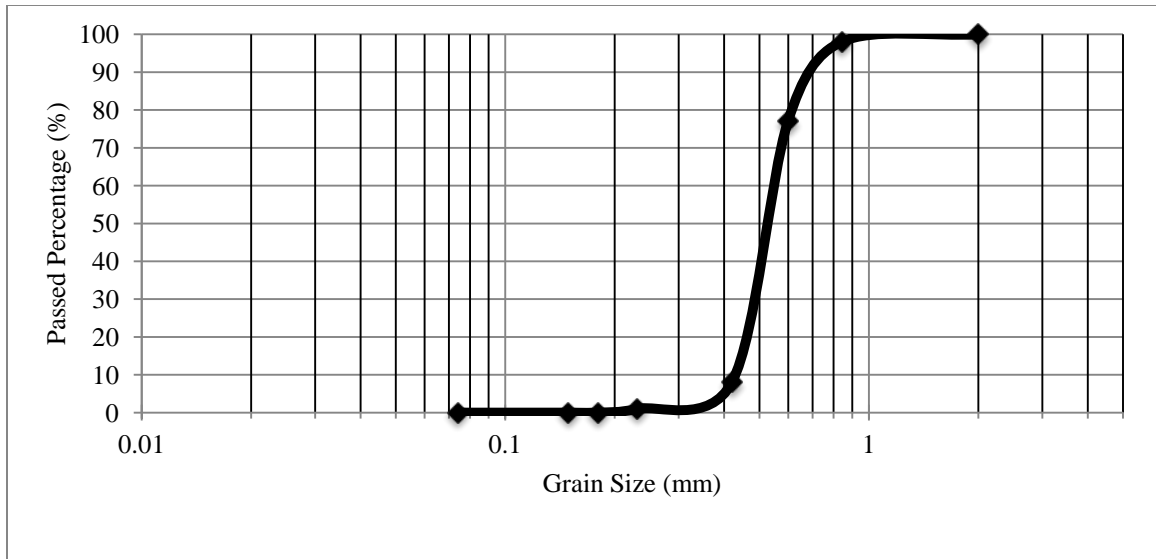


Figure 3-2. Grain Size Distribution of Silica Sand

Values of D_{10} , D_{30} and D_{60} for the silica sand were found to be 0.42, 0.49 and 0.57, respectively. The coefficient of uniformity, C_u , and coefficient of curvature, C_c , have been calculated using equations 3.1 and 3.2 and are equal to 1.4 and 1.0, respectively.

$$C_u = \frac{D_{60}}{D_{10}} \quad (3.1)$$

$$C_c = \frac{D_{30}^2}{D_{10}D_{60}} \quad (3.2)$$

The silica sand is a uniform and well sorted soil due to its low coefficient of uniformity. The value of Specific Gravity, G_s , is reported to be 2.65 for this sand (Deljoui, 2012). Maximum and minimum void ratio for the sand was measured in accordance with ASTM 4254 and was 0.63 and 0.47, respectively. Based on these values, the sand has a maximum and minimum dry density of 17.7 kN/m^3 and 15.9 kN/m^3 , respectively.

Deljoui (2012) performed a series of direct shear box tests on samples of this silica sand to measure the peak friction angle, ϕ'_p , in accordance with ASTM D3080. The measured

peak friction angles varied at very low normal pressures as shown in Figure 3-3. Deljoui (2012) used a peak nonlinear failure envelope to obtain the variation of the shear strength (τ) with vertical effective stress (σ) in its loose condition as presented in equation 3.3 (Deljoui, 2012).

$$\tau = 1.897\sigma^{0.6946} \quad (3.3)$$

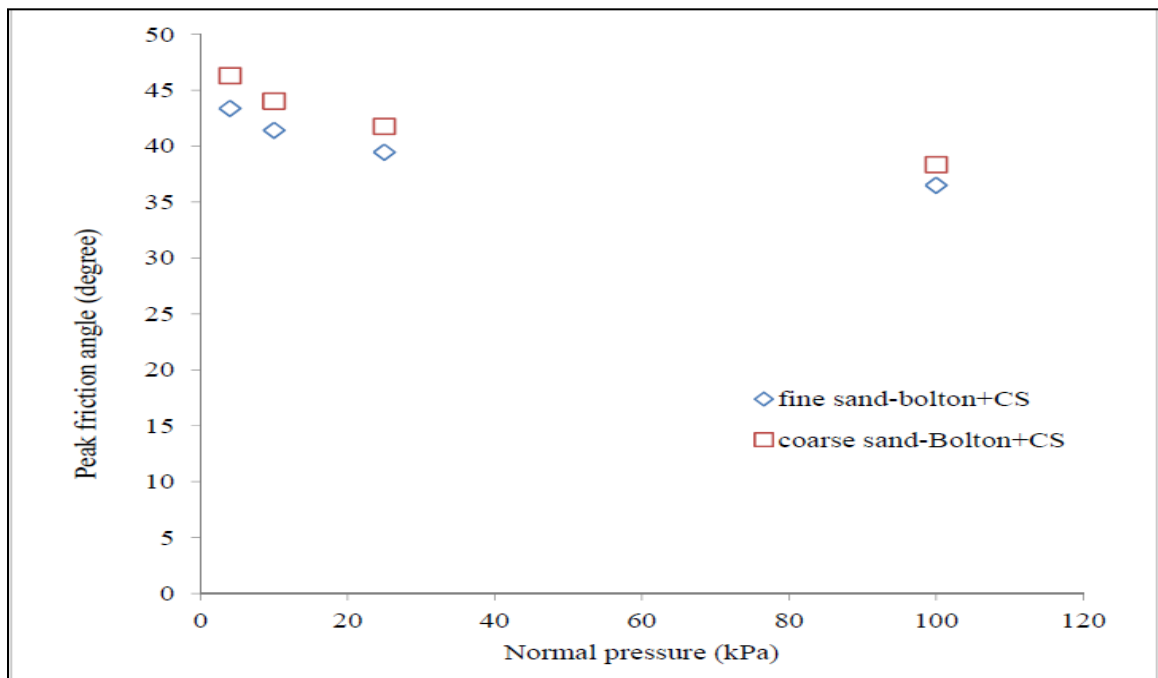


Figure 3-3. Result of Direct Shear Test on Silica Sand (Deljoui, 2012)

Also, the dilation angle, ϕ , was estimated from Bolton's relationship (1986) as shown in Figure 3-4.

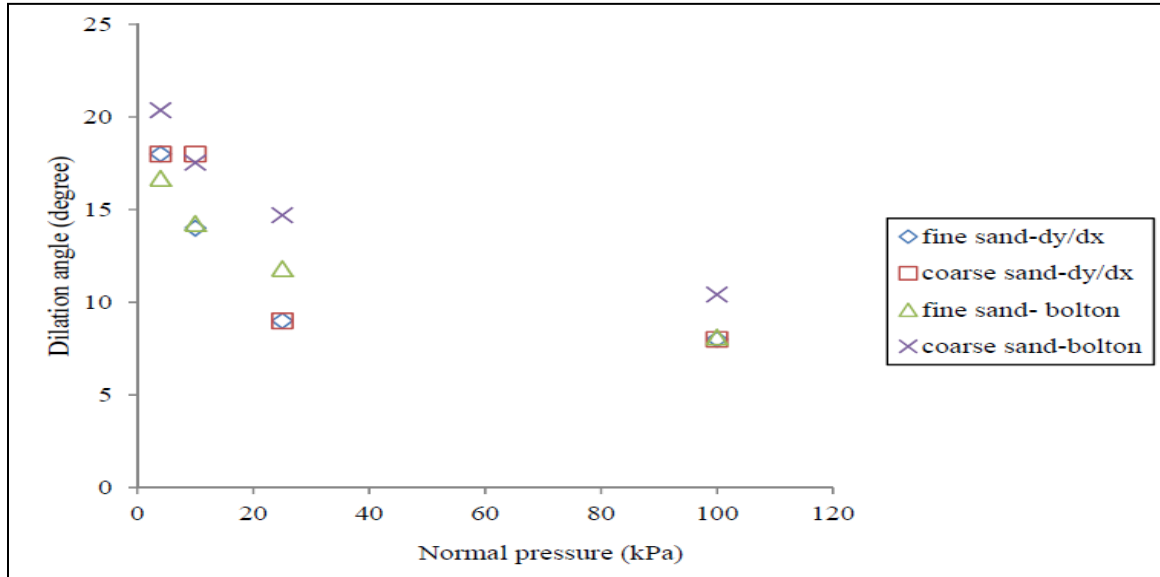


Figure 3-4. Result of Direct Shear Test on Silica Sand (Deljoui, 2012)

Bolton (1986) suggested equation 3.4 which relates peak and critical state friction angle to peak dilation angle for sands in plane strain condition.

$$\phi'_{peak} = \phi'_{critical\ state} + 0.8\phi \quad (3.4)$$

The constrained elastic modulus, E_s , of the silica sand was measured with an oedometer device under low vertical pressures. E_s is a function of effective normal stress as in equation 3.5.

$$E_s = 1111.1\sigma_v^{0.1923} \quad (3.5)$$

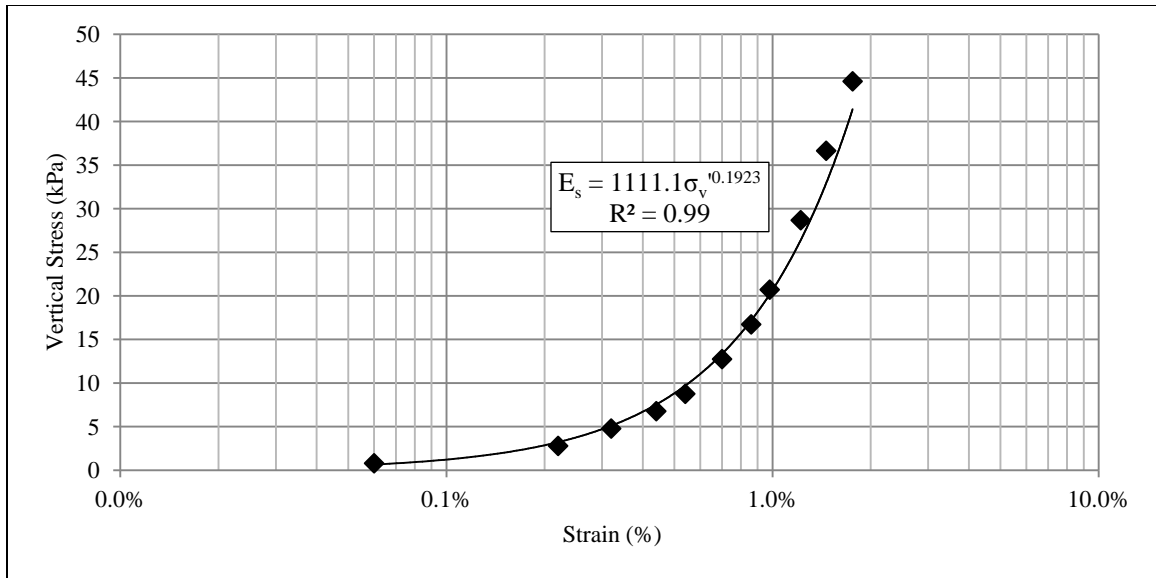


Figure 3-5. Results of Oedometer on Silica (Ottawa) Sand

3.2.3 Wind Tunnel Sand Box

The sand was contained in a sunken hexagonal wooden box which was level with the wind tunnel surface. The box has a side length of 0.51 cm and depth of 1.2 m. It is supported by a column on the lower floor of the tunnel to ensure safety and functionality.

Figure 3-6 shows the supporting structure below the wind tunnel.



Figure 3-6. Supporting System of the Wind Tunnel Sand Box

The sand used in this research program is a standard benchmark soil for laboratory testing. The sand was used in its dry condition and unit weight refers to dry unit weight, γ , of sand. Unit weight of the silica sand was measured in the sand box to be equal to 16.4 kN/m^3 . The same unit weight was applied for the static tests. The estimation is based on the sand density in top 20 cm of the sand box.

3.2.4 Model Piles, Pole and Plate

This research utilizes small scale models for studying cyclic lateral behavior of piles. Due to the difficulty of reconciling the wind flow and soil scaling, no attempt has been made to do this herein. To provide lateral and moment loads on the pile a flat plate and pole were attached and placed in the simulated wind field. The models for the piles, plate and pole were made from aluminum with an elastic modulus 68 GPa. The piles were made in three lengths 5 cm, 10 cm and 20 cm, with a diameter of 2.2 cm and will be referred to from hereon as short, medium and long piles based on their length. Pictures of these

small scale models are available in Appendix B. The moment of inertia, I_m , for a circular shape can be obtained from equation 3.6 in which, r is the radius of pile or pole cross-section.

$$I_m = \frac{\pi r^4}{4} \quad (3.6)$$

Due to their stiffness, all three model piles are assumed to act as rigid bodies, whilst the pole was expected to deflect and act in a flexible fashion. Geometrical properties and dimensions of the model shapes are given in Table 3-2. The model piles were threaded to allow the pole to be screwed into it. The plate had a ring on the centroid of the rear and the pole passed through the ring and was fixed with a cleat on the bottom.

Table 3-2. Dimensions of Model Piles, Pole and Plate

Shape	Length (mm)	Diameter/Thickness (mm)	Mass (g)	Density (kg/m ³)	Frontal Area (m ²)	Moment of Inertia, I_m (m ⁴)
Plate	175	3.17	260	2850	0.0306	7.81E-5
Pole	259	6.43	24	2850	0.0017	8.39E-11
Short Pile	53	22.13	53	2600	0.0017	1.89E-7
Medium Pile	104	22.13	104	2600	0.0035	1.89E-7
Long Pile	199	22.13	208	2600	0.007	1.89E-7

3.2.5 Static Test Setup

Figure 3-7 shows a diagram of the static test box. In this diagram, the pulleys and load cell can be seen. The box is divided into two separate sections by a plexiglass sheet to keep the pulleys clear of the silica sand. The plexiglass sheet has 4 holes at different depths to enable tests with different pile sizes and different eccentricities to be performed. A cable passed through the hole and was connected to a small carabiner, which was used

to pull the model and connect to the load cell. All dimensions in Figure 3-7 are in millimeters. More pictures of the setup are available in Appendix B.

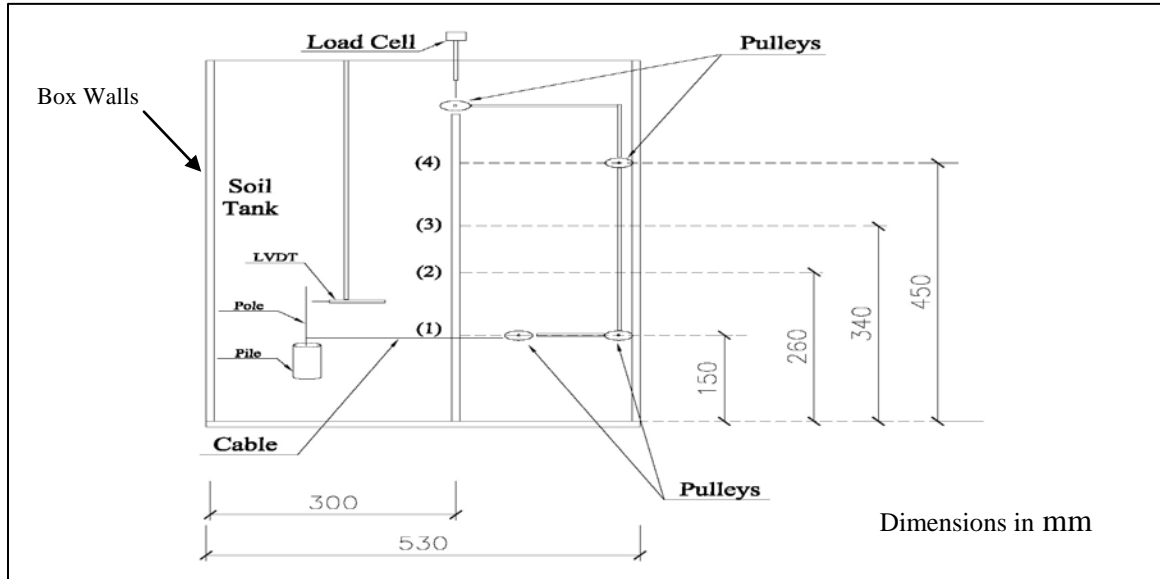


Figure 3-7. Static Test Box

3.3 Wind Tunnel Tests

A series of model scale tests were performed in the BLWT #2. This section will describe the instrumentation, test procedure and data processing of these tests. Table 3-3 presents a list of the performed tests in BLWT #2 and the control conditions.

A total of 19 tests were conducted on different pile, plate and pole sizes and with different incremental (stepped) wind speed increases; of these tests 6 were unique and others were replicates. As can be seen in Table 3-3, the tests are given a code for brevity.

Table 3-3. List of Wind Tunnel Tests

Test Code	Model Pile, (P)	Model Pole, (R)	Fs (Hz)	Interval, (T) (sec)	Data Acquisition Duration (sec)
PRT-MM60-1	Medium	Medium	300	60	720
PRT-MM60-2	Medium	Medium	300	60	540
PRT-MM60-3	Medium	Medium	300	60	540
PRT-MM60-4	Medium	Medium	500	60	665
PRT-MM90-1	Medium	Medium	300	90	900
PRT-MM30-1	Medium	Medium	200	30	360
PRT-MM30-2	Medium	Medium	500	30	335
PRT-MM30-3	Medium	Medium	200	30	480
PRT-MM30-4	Medium	Medium	200	30	430
PRT-MM30-5	Medium	Medium	200	30	400
PRT-SM60-1	Short	Medium	300	60	365
PRT-SM60-2	Short	Medium	300	60	305
PRT-SM60-3	Short	Medium	300	60	305
PRT-SM30-1	Short	Medium	200	30	480
PRT-SM30-2	Short	Medium	200	30	190
PRT-SM30-3	Short	Medium	200	30	190
PRT-LL30-1	Long	Long	200	30	340
PRT-LL30-2	Long	Long	200	30	270
Constant Wind Speed	Medium	Medium	300	90	900

3.3.1 Instrumentation

The sand box was fixed into the wind tunnel surface and instruments such as pitots, hotwire and laser displacement transducers (LT) were installed on rigid mounting rods at

specified locations around the box. The location of the sand box is pre-determined in accordance with the routine procedure of the BLWTL #2.

The instrumentation and logging system of the model tests in the wind tunnel is of extreme importance. The data acquisition system in the wind tunnel records on a pre-determined number of channels. In this testing program, data were logged on 12 channels. Table 3-4 tabulates details of the channels connected to the data logger during each test. Heights are given from above the wind tunnel surface or AWTS (cm).

Table 3-4. Instrumentation Used in Wind Tunnel Testing

Channel No.	Instrument	Height Above Wind Tunnel Surface (cm)
1	Reference Pitot 1	160
2	Reference Pitot 2	160
3	Reference Pitot 3	160
4	Thermometer	NA
5	Laser Displacement Transducer 1	22
6	Laser Displacement Transducer 2	31
7	Laser Displacement Transducer 3	26
8	Pitot 1	40
9	Pitot 2	25
10	Hotwire Anemometer	40
11	Accelerometer	NA
12	Strain Gauge Bridge	NA

The “reference pitots” are three pitots located at top of the wind tunnel, 160cm AWTS.

They have been used for calibration of other pitots and the hotwire anemometer. Two

pitots record wind speeds at two different heights. As is explained in Chapter 2, mean value of wind speed increases with height, thus it is expected that “Pitot 1” records higher wind speed compared to “Pitot 2”. The hotwire anemometer can measure fluctuations in wind speed. The used pitots and hotwire are able to record wind speed up to 4 decimal places. They record wind speed in different units and different conversions are used for them based on their model and manufacturer. The hotwire was adjusted to record 10 ft/sec equal to 1 Volt. The wind speeds were obtained from the hotwire anemometer and pitots in ft/sec converted to m/s, for further analysis. The hotwire was calibrated prior to the testing program by technicians at the BLWTL.

Three LTs were located at three different heights and directed at the back of the plate. The LTs are from the LB1101 series made by Keyence. These LTs are able to measure within a range of 80 mm with resolution of 8 μm . The LTs are able to measure within range of 8 cm precisely; if the obstacle gets as close as 2 cm to the LT head, the data quality goes down and eventually the LT exceeds the working range. The LTs were not zeroed and they were recorded in range of ± 8 Volt as can be seen in Figures 3-9, 3-10 and 3-11. The data logger records 1 cm of displacement as 1 Volt.

An accelerometer was placed just adjacent to the centroid of the plate. The accelerometer was used to obtain the dynamic characteristics of the plate and pole model in the horizontal direction. It was adjusted to measure 1-g as one Volt.

A $\frac{1}{2}$ wheatstone strain gauge bridge was placed just above the pile head on the pole away from neutral axis to measure maximum responses resulting from the wind pressure

applied to the model system. Tests were stopped prior to imposing a high level of strains, to ensure functionality of the bridge for the remaining tests.

Figure 3-8 shows heights of these instruments for the wind tunnel tests measured from the wind tunnel surface. LTs are mounted on a single rod and Figure 3-8 shows them separated from each other for better presentation. Some pictures of these instruments are available in Appendix B.

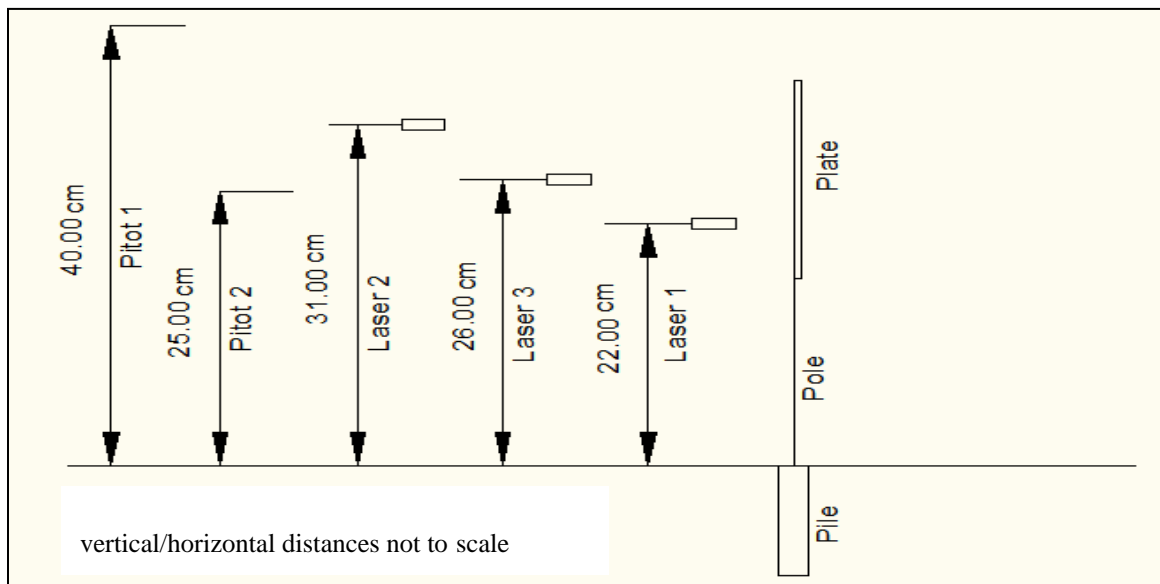


Figure 3-8. Instruments in Wind Tunnel Tests

Calibration for the strain gauge bridge was performed by fixing the pile head and applying bending moments to the model pole by a series of pulleys and weights, while recording the reading of strain gauge. The pole was considered to be a cantilever beam for calibration and strains were calculated and compared with the strain output. The detail of the calibration of the strain gauge bridge is available in Appendix A.

3.3.2 Procedure

Tests in the wind tunnel were performed with the sand box level with the wind tunnel surface. Dry silica sand was poured into the sand box through a #10 sieve from a constant height using air pluviation to achieve a uniform target density. The previously mentioned instruments were fixed to the wind tunnel surface or the outer wooden frame of the sand box. Extra care was given when aligning the LTs and placing them in the horizontal plane. Finally the model consisting of the plate, pole and pile was gently pushed into the silica sand and any local disturbance was gently smoothed and flattened. In some tests the sand box was covered with the plastic sheets to avoid sand transport and accumulating at the end of the tunnel. An assessment of the localized soil movement around the pile due to wind flow was made during the tests and this was found to be negligible (note: U is essentially zero at the air-sand interface). However, after the initial tests that accumulation was found to be minimal and later tests were performed without any plastic sheeting. For each test, channels of the instrumentations were zeroed manually prior to execution of each test. The wind tunnel data acquisition system started recording data with the assigned frequency, F_s , (200-500 Hz). Following the designed test plans, wind reference speeds were increased at pre-determined intervals, manually creating a stepped, incremental wind speed history. These intervals were 30-second, 60-second and 90-second and the wind reference speed increased by 0.5 Volt increment. The wind tunnel fan was stopped once the model plate rotation had exceeded the LT range and failure was assumed.

3.3.3 Data Processing

After completion of the tests for the model piles in the wind tunnel, the raw data was extracted from data acquisition system. A unique file name was generated by the BLWTL data acquisition system and these are available in Appendix C. Files can be checked on the wind tunnel data logger for quick evaluation and they are also accessible through MATLAB on other computers.

For better understanding of the data processing, raw plots of 5 channels for test PRT-MM60-4 will be presented through Figures 3-9 to 3-13. These are raw readings of LT 1 (Channel 5), LT 2 (Channel 6), and LT 3 (Channel 7). Figure 3-12 shows raw wind speed values and greater fluctuations at higher mean wind speeds are exhibited. Based on information from Table 3-3, test PRT-MM60-4 has been recorded for duration of 665 seconds. However, the wind tunnel fan was stopped at a voltage of 4.5V; i.e. at 540 seconds. The test was stopped after excessive movements of the model were observed visually. For each of the loading intervals, statistical values including minimum, maximum, mean and standard deviation were obtained. The mean value represents the corresponding interval for further quasi-static calculations. As can be seen in Figure 3-8, LT 2 (Channel 6) was located at the highest level and the plate got closer to this LT with increasing rotation prior to two others. The statistical values for the last loading interval were chosen from data points acquired between 481 second and 510 second to ensure all “out of range” data are filtered out. The raw data of the strain gauge (Channel 12) is presented in Figure 3-13 and is well below 10 Volts, which ensures the data was “in range”.

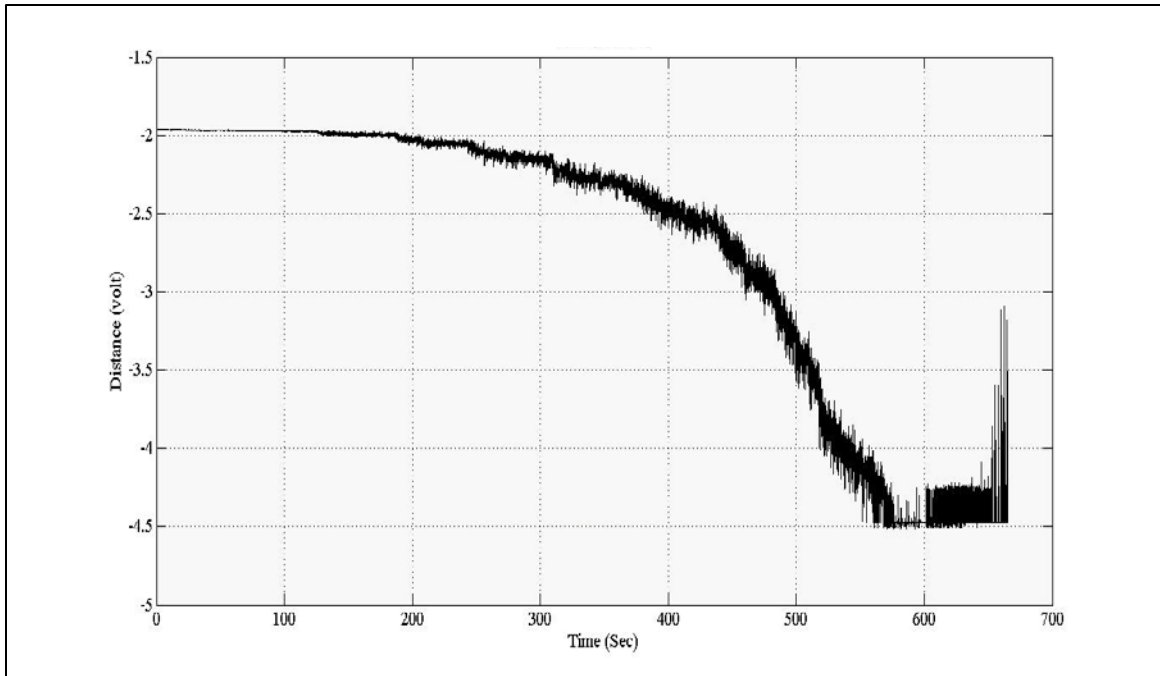


Figure 3-9. Raw Data of Laser Displacement Transducer 1 in Wind Tunnel Test PRT-MM60-4

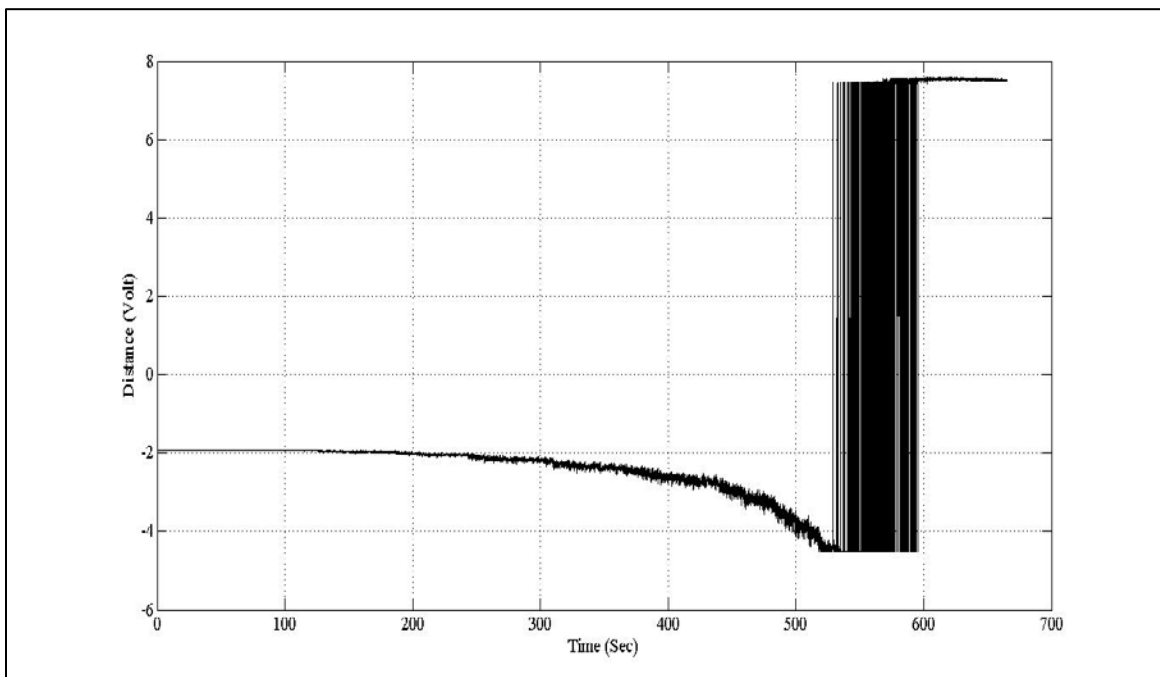


Figure 3-10. Raw Data of Laser Displacement Transducer 2 in Wind Tunnel Test PRT-MM60-4

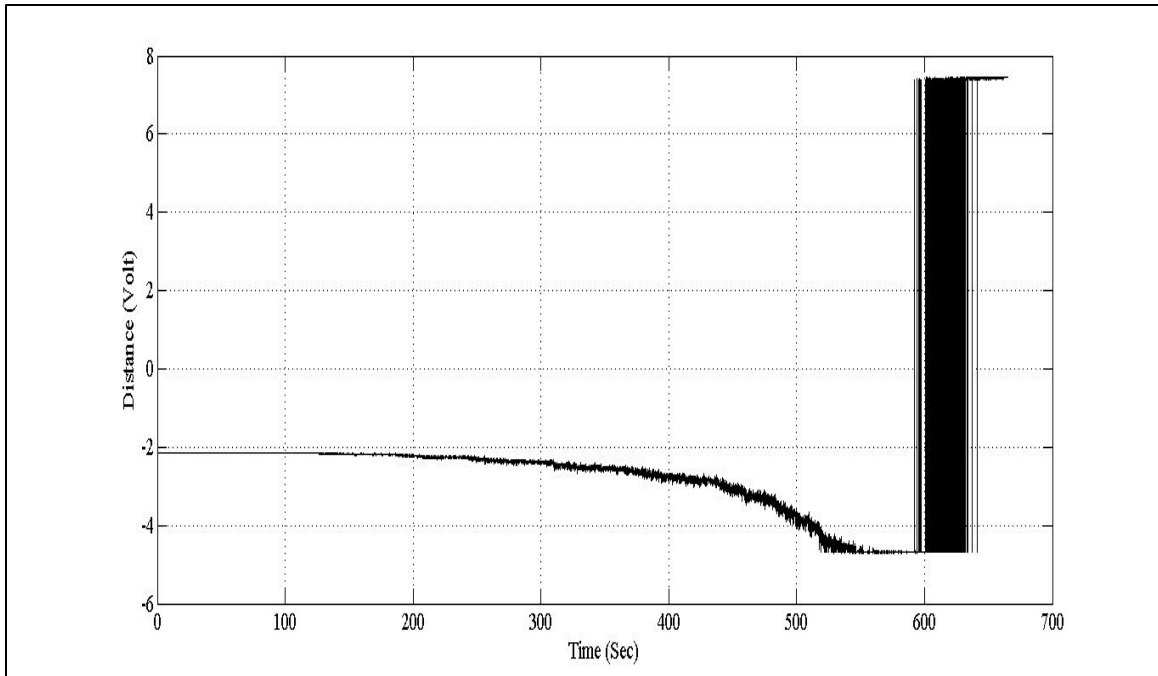


Figure 3-11. Raw Data of Laser Displacement Transducer 3 in Wind Tunnel Test PRT-MM60-4

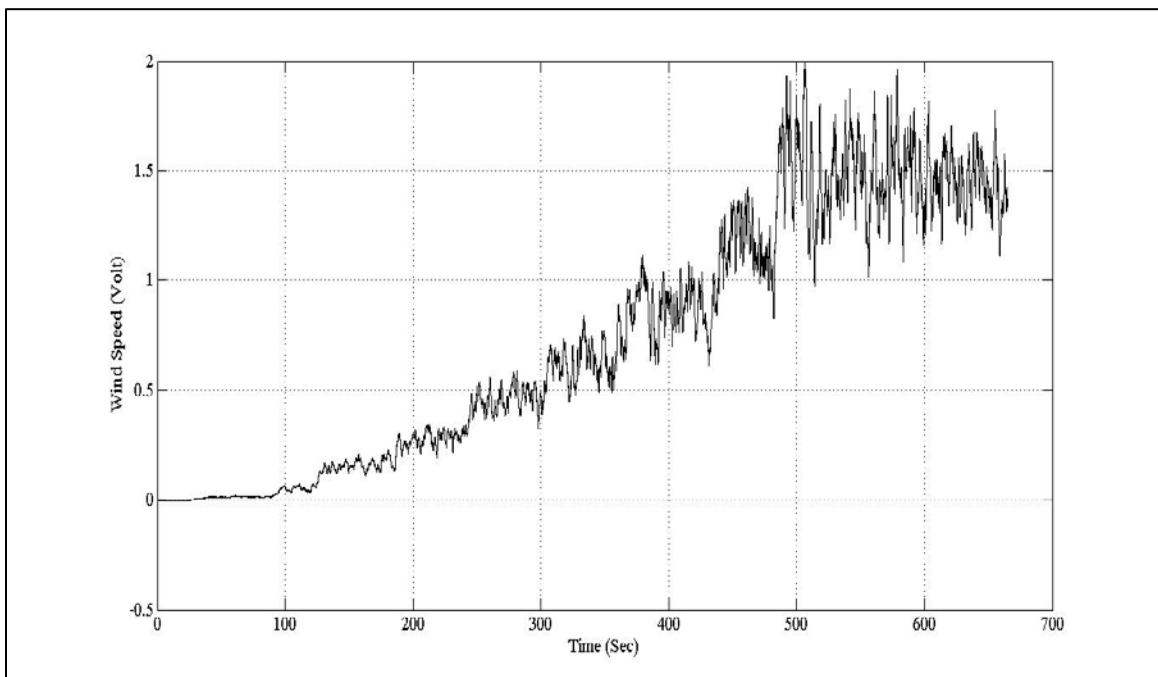


Figure 3-12. Raw Data of Pitot 2 in Wind Tunnel Test PRT-MM60-4

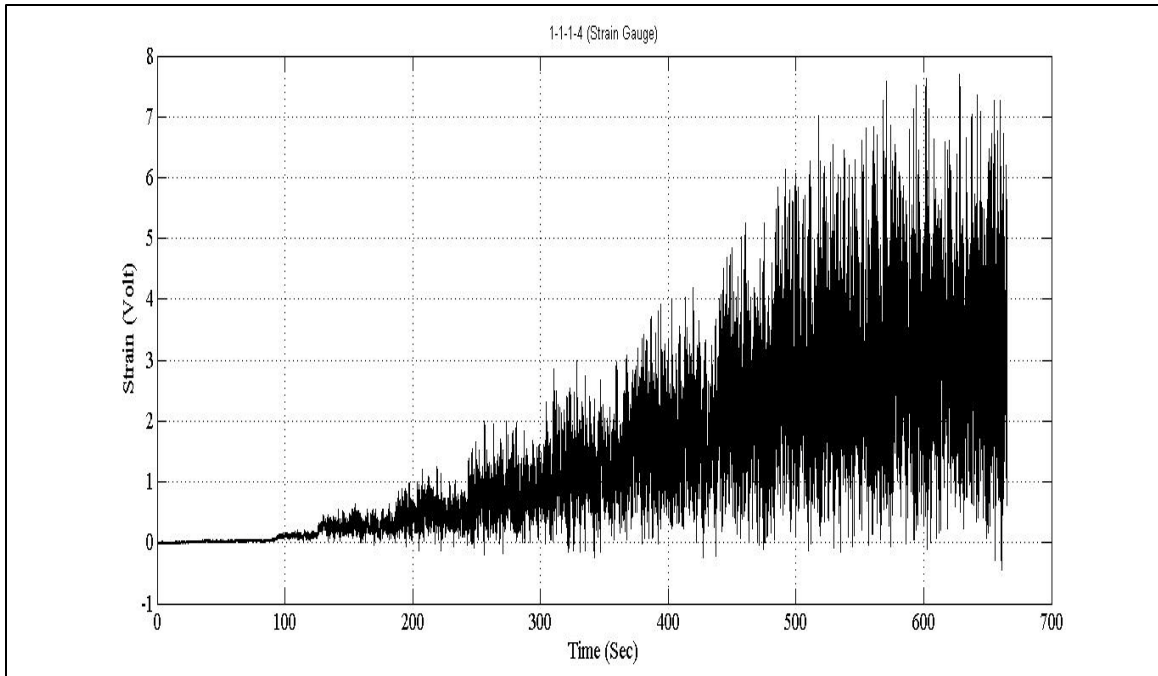


Figure 3-13. Raw Data of Strain Gauge Bridge in Wind Tunnel Test PRT-MM60-4

Table 3-5 tabulates distance from the plate for each of the three laser displacement transducers in test PRT-MM60-4. In the last three columns these distances are referred to the head position of furthest laser displacement transducer (as a datum) so later comparison can be made.

Table 3-5. Laser Displacement Transducers Distance from Plate and X component in Test PRT-MM60-4

Mean Wind Speed (m/s)	LT 1 (cm)	LT 2 (cm)	LT 3 (cm)	X _{laser 1} (cm)	X _{laser 2} (cm)	X _{laser 3} (cm)
0.7	2.550	2.574	2.571	2.574	2.574	2.574
1.3	2.546	2.569	2.567	2.570	2.569	2.570
3.4	2.525	2.541	2.539	2.549	2.541	2.541
4.6	2.480	2.479	2.478	2.504	2.479	2.480
6.1	2.392	2.360	2.368	2.416	2.360	2.370
7.1	2.265	2.188	2.216	2.289	2.188	2.218
8.5	2.088	1.951	2.007	2.112	1.951	2.009
9.4	1.785	1.547	1.645	1.809	1.547	1.647
10.99	1.346	0.950	1.114	1.370	0.950	1.117

LT 1 is located 22 cm ABWS.

LT 2 is located 31 cm ABWS.

LT 3 is located 26 cm ABWS.

As mentioned previously, the pole was not rigid and bent under the wind loads. So the calculation was also corrected for the deflection of the pole using a cantilever model (Figure 3-14). Equation 3.7 is a sample calculation for obtaining the displacement, d , obtained from any of the laser displacement transducers at each load interval (Table 3-6).

$$d_1 = (X_{\text{laser 1}})_{\text{initial}} - (X_{\text{laser 1}}) - \delta_{\text{pole}} \quad (3.7)$$

Where, δ_{pole} can be calculated from equation 3.8.

$$\delta_{\text{pole}} = \frac{F_D L}{3EI_m} \quad (3.8)$$

In which, F_D is applied drag force back-calculated from the strain gauge readings.

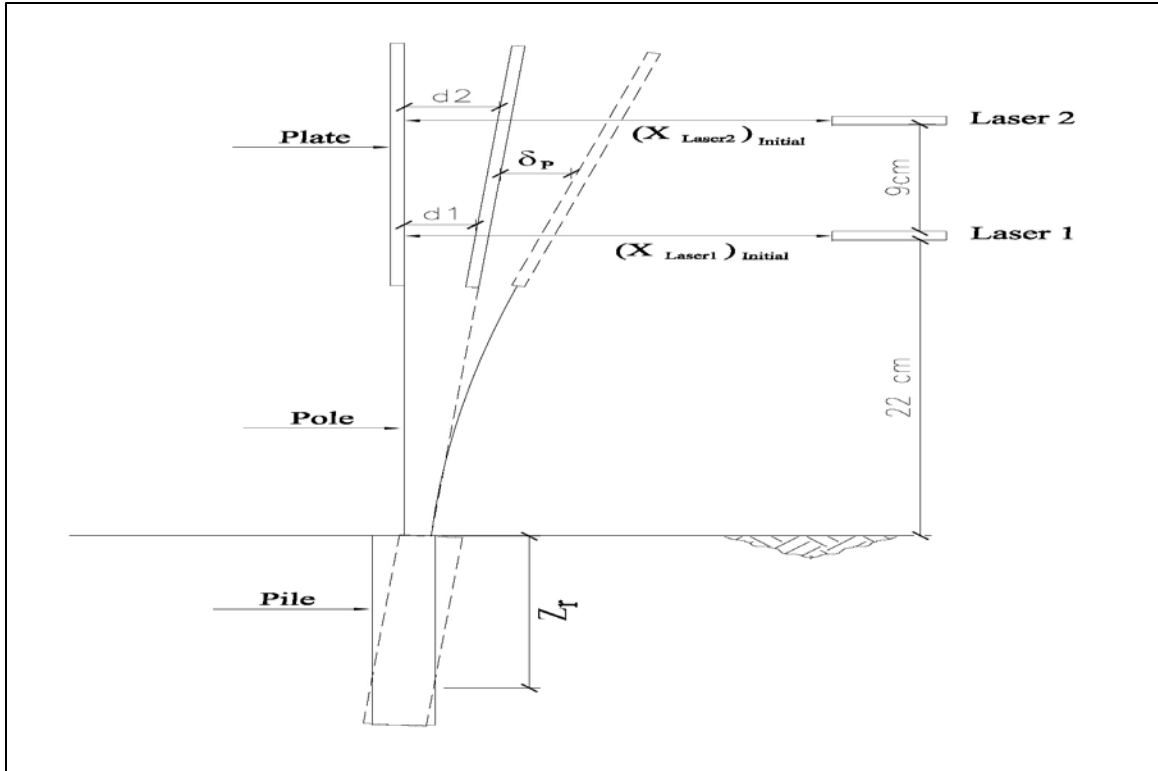


Figure 3-14. Demonstration of Displacement Calculation from the LTs

For obtaining the ground-line displacement and rotation angle, it was necessary to ascertain that the plate was not twisted under wind load. Figure 3-15 shows the locations of three lasers from rear view, it can be seen that laser 3 was located in different vertical planes to measure any possible twist of the plate from vortex shedding.

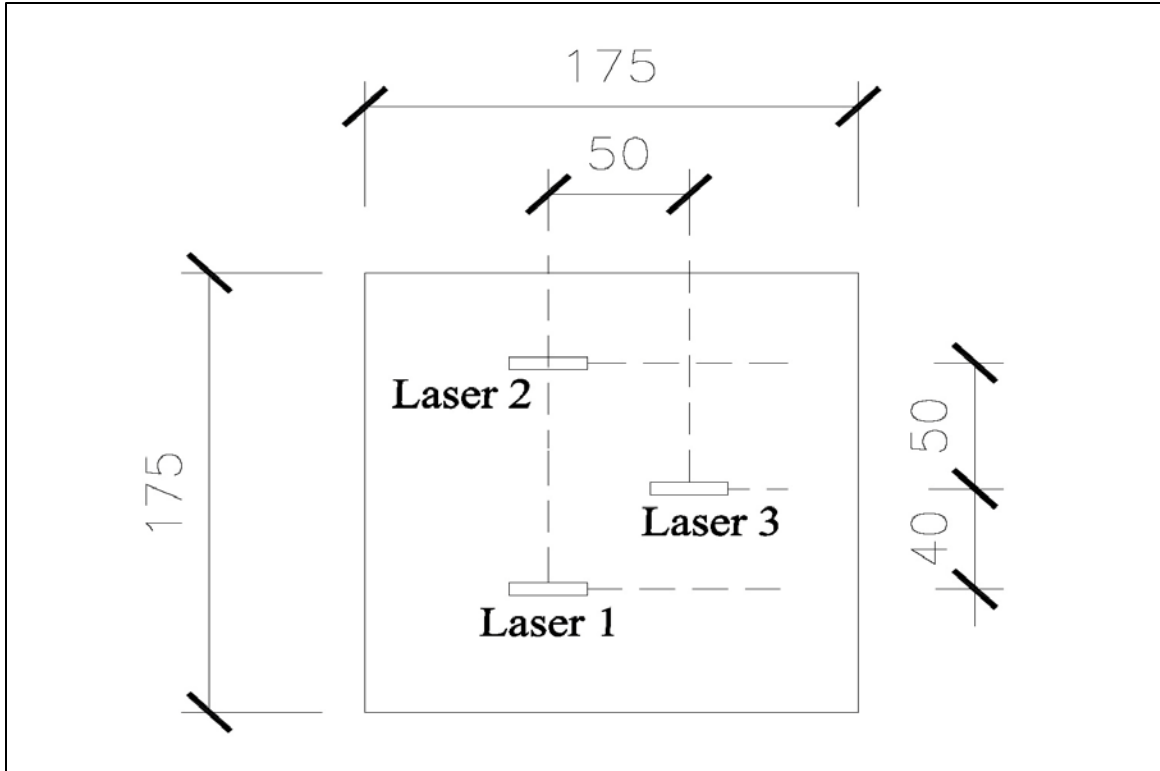


Figure 3-15. Lasers from Rear View

Table 3-6 shows the displacement obtained from any of the lasers and the arbitrary angles formed relative to the ground surface, α_1 , α_2 , and α_3 from lasers 1, 2 and 3, respectively. It can be seen that the twist angle, α_t , is negligible.

Table 3-6. Angle of Twist of the Plate in test PRT-MM60-4

Mean Wind Speed (m/s)	d_1 (cm)	d_2 (cm)	d_3 (cm)	A_1 (degree)	α_2 (degree)	α_3 (degree)	$(\alpha_i)_1$ (degree)	$(\alpha_i)_2$ (degree)
0.74	0.000	0.000	0.000	0.000	0.000	0.000	0.00	0.00
1.27	0.000	0.001	0.000	-0.001	0.001	0.000	0.00	0.00
3.37	0.006	0.014	0.014	0.016	0.026	0.030	0.01	0.00
4.62	0.036	0.061	0.060	0.095	0.113	0.133	0.04	0.02
6.06	0.101	0.157	0.147	0.263	0.290	0.324	0.06	0.03
7.11	0.199	0.300	0.269	0.518	0.554	0.593	0.07	0.04
8.48	0.340	0.501	0.443	0.884	0.926	0.975	0.09	0.05
9.39	0.615	0.877	0.777	1.601	1.620	1.711	0.11	0.09
10.99	0.995	1.416	1.249	2.591	2.615	2.751	0.16	0.14

LTs 1 and 2 were used to obtain ground-line displacement and rotation angle.

The zero rotation depth, Z_r , is the point of rotation of a rigid pile under lateral loading. This depth can be obtained from limit equilibrium as will be discussed in Chapter 5. Also, the Agaiby et al. (1992) recommendations were discussed in Chapter 2. In addition, Z_r was estimated from the displacements obtained from laser displacement transducers (LT) in the wind tunnel tests. As can be seen in Figure 3-16 three LTs are placed above ground level and the ground-line displacement cannot be obtained from them directly. The depth of the point that the model rotates about is needed to obtain the ground-line displacement from the measured rotation angle, θ_1 . The rotation angle can be obtained from readings of any of two LTs, θ_2 ; this angle is compared with an angle formed between the initial model location and any of the LTs assuming the location of Z_r . Through a trial and error process the location of the Z_r can then be estimated. The Z_r location is the height at which these two angles coincide.

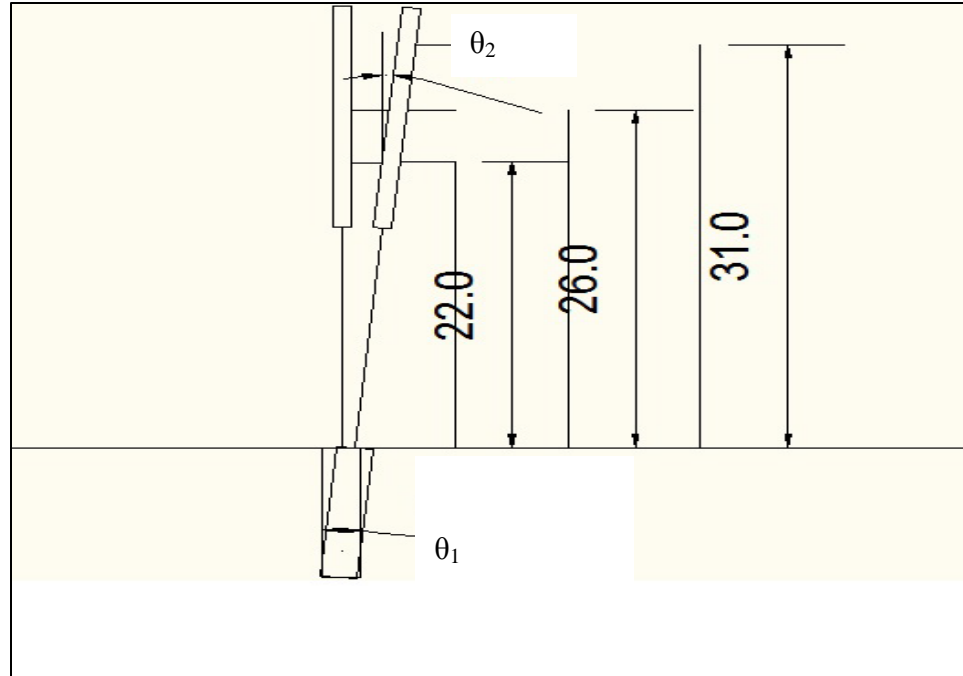


Figure 3-16. Locating ZRP from Laser displacement transducers Readings

Wind fields in the wind tunnel are assumed to be Gaussian stationary random processes. Frequency composition of a natural random phenomenon like wind is robust tool for studying its characteristics and effects.

The power spectral density (PSD), gives the power of the signal at any frequency band. In this research, PSD is calculated for different loading intervals and will be used to give information about statistical characteristics of the signal in Chapter 4. In this research, the wind speed PSD's as well as PSDs of the response of the model were obtained using MATLAB. The time-histories were windowed and then normalized by variance value to give smooth curves. The probability density function is also obtained for the wind speed time-history. These curves are available in Chapter 4.

3.4 Static Tests

A series of static tests were also performed in the Geotechnical Laboratory at Western University. The results of these tests are used in Chapter 5 to give better understanding of the static lateral load behavior of the piles, along with the wind tunnel test results. In common with the wind tunnel tests, silica sand was pluviated into test pit to give unit weight of 16.4 kN/m^3 through a #10 sieve. Loads were applied to the model pole and pile through a system of pulleys and cables.

In total 10 static tests were performed and Table 3-7 tabulates a list of tests, with load eccentricity and linear variable differential transducer, (LVDT) location (ground-line or moment tests). Raw data was extracted from the data logger and it was readily accessible with Microsoft Excel. It should be noted that the moment test for the long pile has not been performed due to geometrical limitations of the box.

Table 3-7. List of Static Tests on Model Piles

Test No.	File Name	Pile	Eccentricity (cm)	LVDT height (cm)
1	S1	Short	25	0
2	S2	Short	25	0
3	S01	Short	0	24
4	S02	Short	0	24
5	M1	Medium	25	0
6	M2	Medium	25	0
7	M01	Medium	0	24
8	M02	Medium	0	24
9	L1	Long	0	24
10	L2	Long	0	24

3.4.1 Instrumentation

The static tests were sparsely instrumented compared to the previously described wind tunnel tests. A linear variable differential transducer (LVDT) was used for measuring the displacement and a load cell for measuring the applied loads. The LVDT was calibrated to give displacement at its location directly through up to 20 mm with an accuracy of 0.001 mm.

The load cell used was a model SB0-200 made by Transducer Techniques. The load cell has the maximum capacity of 200 lbs and recorded up to two decimal places. It was calibrated in tension by applying static weights to a hanger system connected to the load cell. The calibration process is described in Appendix A.

The data acquisition system was a Sciometric Series 7000, which was available in Geotechnical Laboratory at Western University.

3.4.2 Procedure

Static tests were performed in two main modes: ground-line tests and moment tests. The weight of silica sand was determined using the height and same density as in the wind tunnel tests. The silica sand was pluviated into the box up to the pre-determined heights. In common with the wind tunnel tests, the setup consists of pole and pile gently pushed into the silica sand and local disturbance gently flattened. The data acquisition system is manually controlled and started logging prior to each test and halted after visual excess displacement.

In the ground-line tests, the load was applied with nominal load eccentricity of zero and the LVDT was placed on the upper part of the pole to measure displacement. Whilst in

the moment tests, the LVDT reads ground-line displacement and the load carabiner was attached to the pole at the required eccentricity. The eccentricity in the moment tests was chosen to represent the condition in the wind tunnel if the distributed wind load acts at the plate centroid.

Figure 3-17 has been taken from a ground-line test. The load application line and LVDT reading can be observed in this image.



Figure 3-17. Static Ground-line Test

3.5 Summary

This chapter describes the testing methodology for the static and cyclic tests on the plate-pole-pile system. The material properties and sand bed preparation methods are described. The instruments and calibration for both sets of tests are discussed, as well as the testing protocol. Further sections have been included on the data analysis and definitions of the material behavior. The procedures described herein provide information for assessing the results in other parts of this thesis and provide guidance for future researchers.

EFFECTS OF RANDOM WIND LOADS

4.1 Overview

This chapter focuses on the nature of the wind field generated in the wind tunnel and discusses the structural wind loads and their characteristics. Firstly, an investigation of the generated random variable amplitude wind loads is performed. Drag coefficient, turbulence intensity and power spectral density of the wind speed fluctuations are presented, for better characterization of the wind and the associated loads, and to assess their effects on the model tests.

Variation of wind speed around its mean value is studied considering probability distribution functions. The number and amplitude of fluctuations (cycles) in the random wind load history is estimated using the rainflow counting. The results of this chapter will be used in Chapter 5 for studying the behavior of laterally loaded piles under random cyclic loads.

4.2 Random Wind Load Characterization

4.2.1 Drag Coefficient Measurement

In wind engineering, it is a common practice to introduce a non-dimensional force coefficient to calculate wind induced loads (Holmes, 2001), such as, C_F as can be seen in equation 4.1:

$$C_F = \frac{F}{\frac{1}{2}\rho_a U^2 A_F} \quad (4.1)$$

Where, F is aerodynamic force, ρ_a is air density, U is wind speed and A_F is reference area, which is often considered to be equal to the projected frontal area.

Typically, the aerodynamic forces are decomposed into two orthogonal directions. The one parallel to the wind direction is commonly known as the drag force, and the one orthogonal to the drag component is the lift component. The two force components and the angle of attack, α (angle of incidence) are illustrated in Figure 4-1.

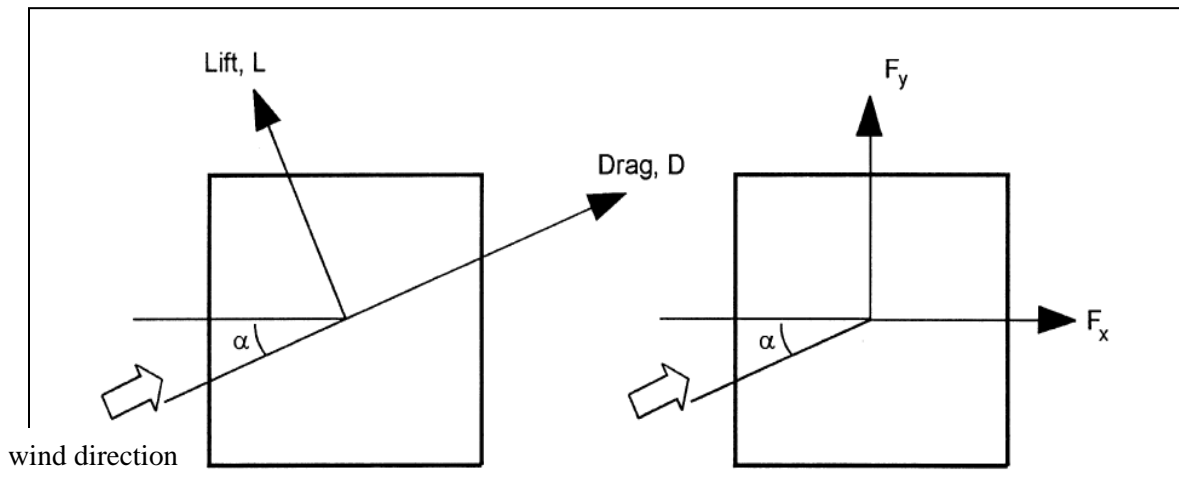


Figure 4-1. Wind and Body Axes (Holmes, 2001)

By considering equilibrium of the forces in Figure 4-1; F_x and F_y can be written as below:

$$F_x = F_D \cos \alpha - F_L \sin \alpha \quad (4.2)$$

$$F_y = F_D \sin \alpha + F_L \cos \alpha \quad (4.3)$$

For a flat plate with its surface normal to wind flow (Figure 4-2), the only aerodynamic force component is the drag force, which is equal to F_x in equation 4.2. Thus, the non-dimensional force coefficient, C_F , in equation 4.1 is equal to drag coefficient, C_D , and was measured for medium size plate (17.5 cm X 17.5 cm) in this testing program. The results of test PRT-LL30-1 are utilized for this purpose. In this test, the long pile acted essentially as a fixed base condition, so a simple cantilever model is applicable (equation 4.4). The drag coefficient was initially calculated based on mean wind speed readings from the pitot located at the same level as the plate centroid. The strain gauge bridge was used to measure the stress from the applied bending moment, σ_{BM} , on the pole. Figure 4-3 shows the measured bending moment at the base of the pole for different mean wind speeds in test PRT-LL30-1.

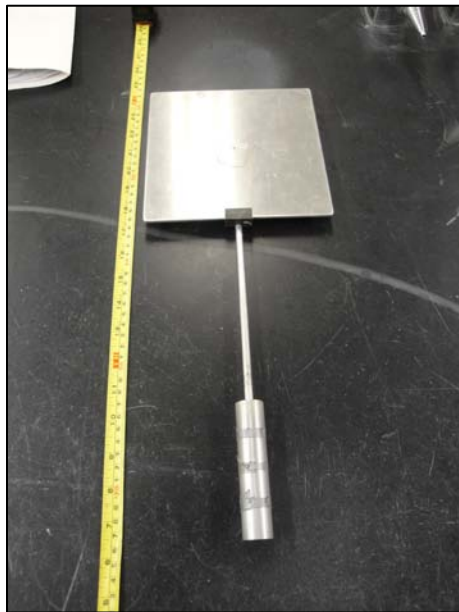


Figure 4-2. Pile, Pole and Plate Model

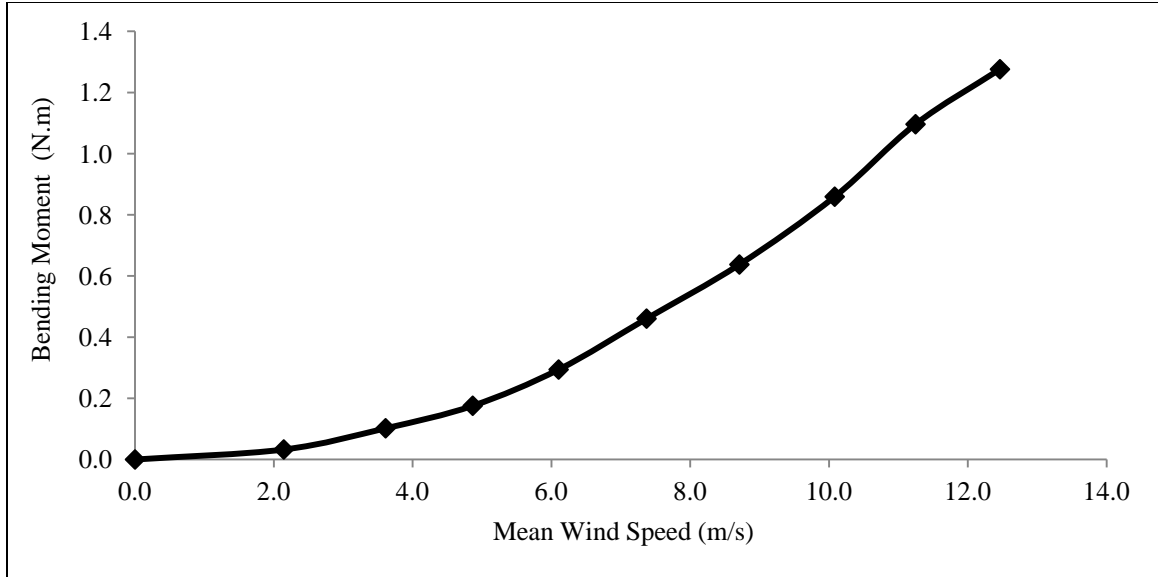


Figure 4-3. The Measured Bending Moment vs. Mean Wind Speed

The back-calculated force from the bending moments measured with the strain gauge bridge is therefore equal to the drag force, F_D , acting on the plate as in equation 4.4.

$$F_D = \frac{M}{e} = \frac{\sigma_{BM} I_m}{re} \quad (4.4)$$

Where, r is radius of the pole, I_m is moment of inertia of the pole cross section, M is bending moment, σ_{BM} is the normal stress due to bending moment, and e is eccentricity equal to 0.4 m for this test (i.e. the lever arm length).

Then, by inputting the drag force, F_D , into equation 4.1 the drag coefficient, C_D was estimated for different mean wind speeds as is shown in Figure 4-4. Measured values for C_D ranged from 0.96 to 1.17. The results are in good agreement with Bearman (1971) who obtained a value of 1.107 in smooth and 1.195 in turbulent flow for a plate size of 6X6 inches. Quinn et al. (2001) also studied the force coefficient for different sign shapes in the UK and obtained a value of 1.06 for square signs of size 750 mm, elevated 1m

above the ground. They also suggested that the “force coefficient is largely insensitive to wind speed.” It is worth mentioning that E.S.D.U. (1970) gives a formula for calculation of the drag coefficient of plates with height/breadth ratio in range of $1/30 < h/b < 30$, in the smooth uniform flow normal to the plate, as shown in equation 4.5:

$$C_D = 1.10 + 0.02[(h/b) + (b/h)] \quad (4.5)$$

The C_D for the plate from equation 4.5 is equal to 1.12.

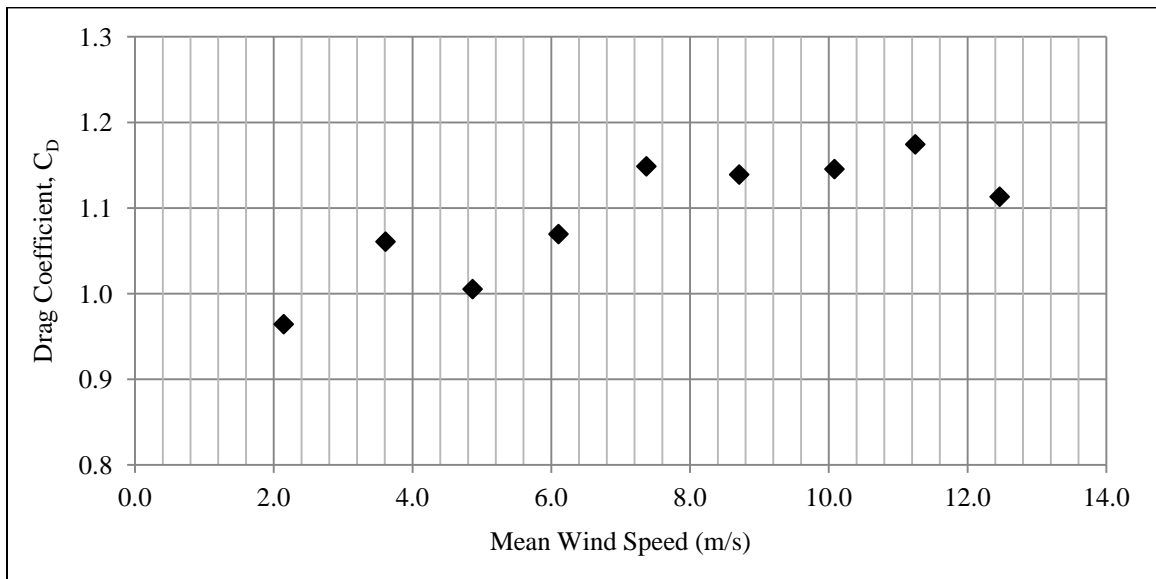


Figure 4-4. Drag Coefficient Variation for Different Mean Wind Speeds

Thus, C_D for the square plate in the boundary layer wind flow is approximately 1-1.2. Sixty percent of the drag can be attributed to positive pressures (above the static pressure) on the front face, and 40% by negative pressures (below the static pressure) on the rear face (E.S.D.U., 1970).

In Figure 4-4, it is shown that C_D is almost insensitive to mean wind speed. Bearman (1971) suggested that higher drag occurred in turbulent flow. In this testing program

turbulence intensity remains almost constant for different mean wind speeds, as can be seen in Figure 4-6 for three different tests including test PRT-LL30-1. Given the literature findings regarding the insensitivity of incidence angle of wind flow on the plate drag coefficient, the compliance of the pole-plate system was assumed to have no effect on the behavior.

It is also of interest to study the variation of the instantaneous drag coefficient in low and high wind speeds. The instantaneous variation of the drag coefficient for low and high wind speeds (mean wind speeds of 3.4 m/s and 9.4 m/s, respectively) was studied for test PRT-MM60-4 and is presented in Figure 4-5.

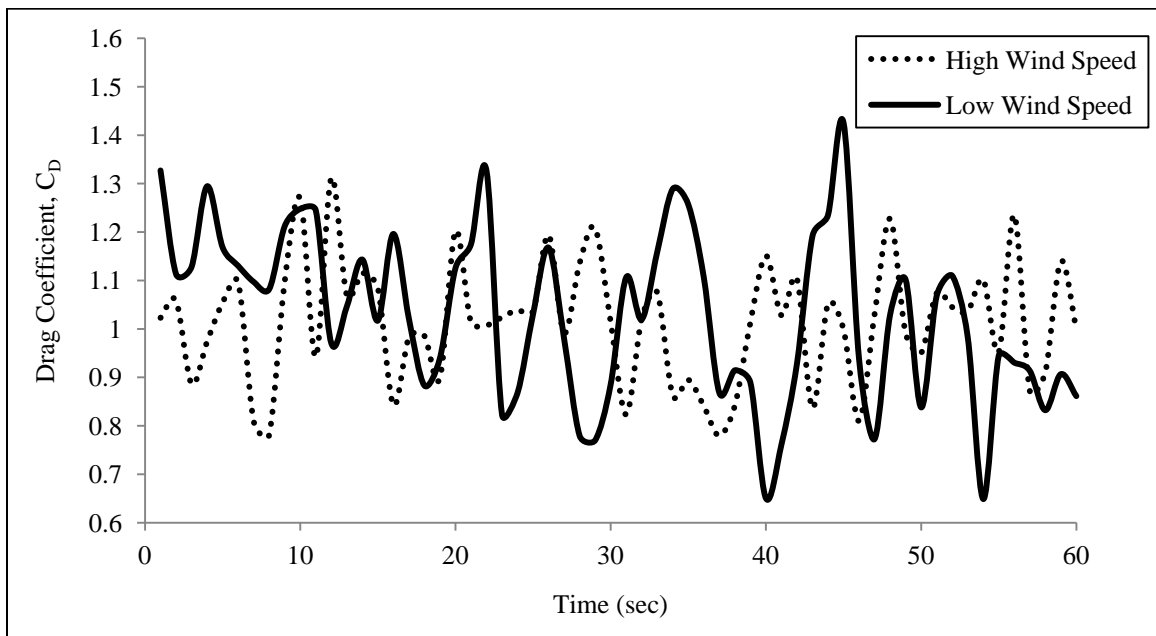


Figure 4-5. Instantaneous Drag Coefficient

The mean drag coefficient is 1.03 for low wind speed and 1.01 for high wind speed. Figure 4-5 shows the relative insensitivity of drag coefficient to wind speed, but also demonstrates that the maximum and minimum can vary from 0.65 to 1.43 (i.e. up to 40%

of the mean value). Table 4-1 tabulates the statistical properties for the low and high wind speeds.

Table 4-1. Statistical Properties of Instantaneous Drag Coefficient

Wind Speed Range	Drag Coefficient			
	Minimum	Maximum	Mean	Standard Deviation
Low	0.65	1.43	1.03	0.18
High	0.78	1.31	1.01	0.13

Throughout this testing program, a C_D of 1.1 will therefore be used.

4.2.2 Turbulence Intensity Estimation

The intensity of Turbulence, I_u , was also measured to show the general level of “gustiness” in the wind record. Turbulence intensity is defined as the ratio of standard deviation of the fluctuating component of wind speed to its mean value (equation 4.6). Turbulence intensity is usually measured in three orthogonal directions in 3-D space; conventionally termed longitudinal, vertical and lateral turbulence intensities. Turbulence intensity varies from one surface roughness to another, and with height from the ground surface. An open country terrain was used throughout this testing program.

$$I_u = \frac{\sigma_u}{\bar{U}} \quad (4.6)$$

Where, \bar{U} is the mean wind speed, and σ_u is the standard deviation of the wind speed.

Figure 4-6 shows the variation of longitudinal turbulence intensity with mean wind speed for three different tests; it is more or less constant beyond a mean wind speed of 2 m/s at a value of around 0.15. High turbulence intensity at low wind speeds might be associated

with low Reynolds number and not forming a full boundary layer in the wind tunnel to reach the pre-determined mean wind speeds.

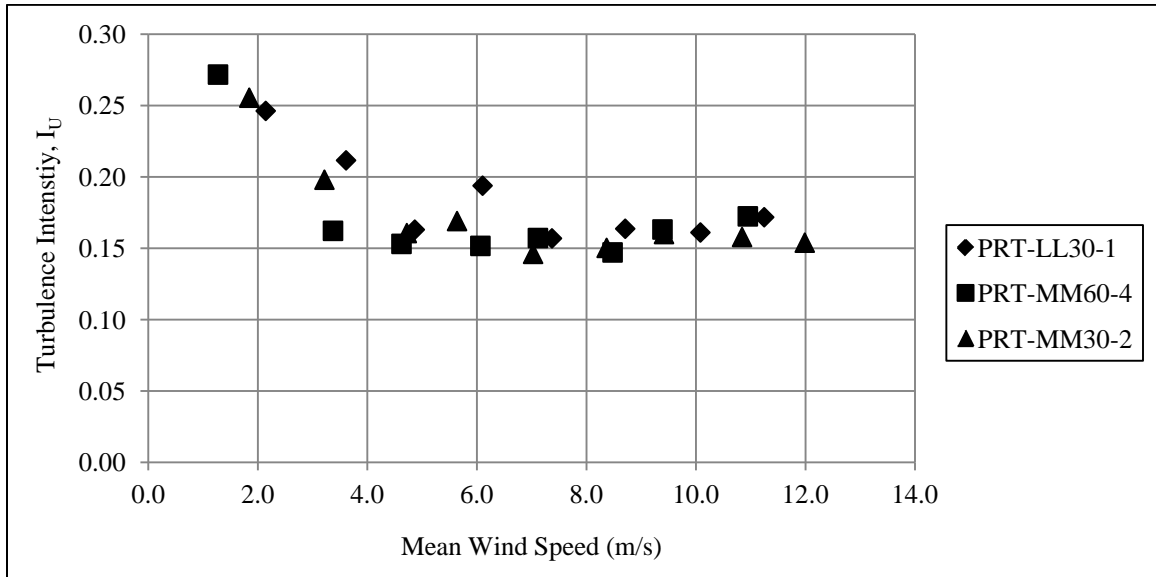


Figure 4-6. Longitudinal Turbulence Intensity vs. Mean Wind Speed

4.2.3 Gust and Peak Factors

Gust and peak factors are commonly used in many wind engineering codes. Random speed variations around the mean of the wind field are taken into account by using a gust or peak factor. These terms have been used interchangeably by some in the literature and caution is needed in using them.

Peak factor, g , as formulated in equation 4.7 is approximately 3.5 (Holmes, 2001), assuming that the longitudinal wind speed has a Gaussian probability distribution.

$$\hat{U} = \bar{U} + g\sigma_U \quad (4.7)$$

Where, \hat{U} is the peak wind speed.

Figure 4-7 illustrates variation of peak factor, g , for different wind speeds. As expected, the obtained value for g is more or less close to 3.5 with some fluctuations. It is worth mentioning that in practical cases, the peak factor is measured over a 10-minute period of a wind speed record. However in the current testing program due to the short wind increment durations, peak factor has been obtained over 1-minute period in tests PRT-MM60-4 and PRT-LL30-1 and over a 30-second period in test PRT-MM30-2.

Comparing Figures 4-6 and 4-7, it can be concluded that there is a reverse relation between peak factor and turbulence intensity and decrease in turbulence intensity leads to an increase in peak factor. However, this is based on very limited data and needs further confirmation.

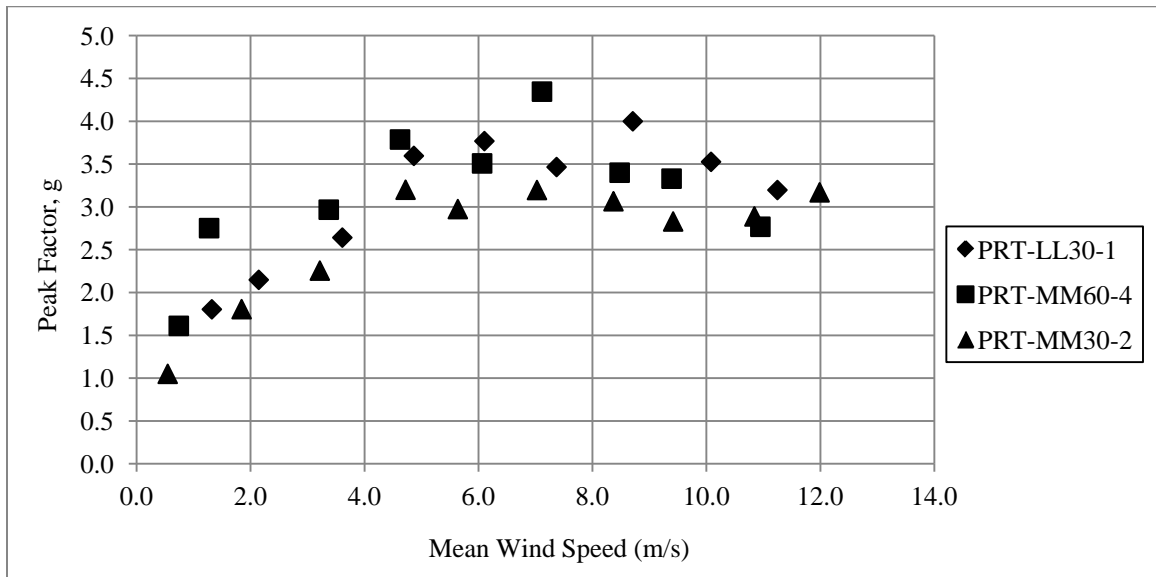


Figure 4-7. Peak Factor Variation vs. Mean Wind Speed

Gust factor, G , is also defined as the ratio of the maximum gust speed to its mean value within a specified time period. This period for tests PRT-LL30-1 and PRT-MM60-4 is 1

minute and 30 seconds for test PRT-MM30-2. Gust factor, G can be obtained from equation 4.8 below:

$$G = \frac{\bar{v}}{v} \quad (4.8)$$

The gust factors obtained for different wind speeds in three wind tunnel tests are presented in Figure 4-8; G is almost constant relative to increase in the wind speed and it remains at about 1.5. These results are comparable with Durst (1960) and Deacon (1955) who reported G of 1.45 for open country terrain over 10-minute periods.

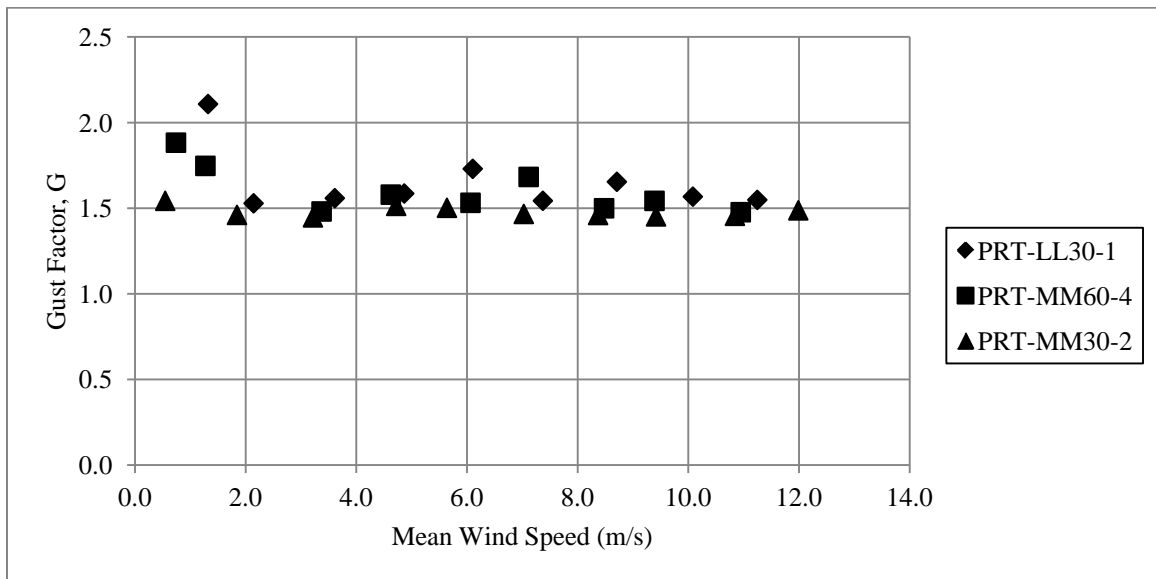


Figure 4-8. Gust Factor Variation vs. Mean Wind Speed

4.2.4 Dynamic Response Characteristics

The dynamic response of the model structure was also investigated. As has been discussed in Chapter 2, due to the turbulent nature of the wind flow, there is a possibility of resonance with applied dynamic loads for structures with a natural frequency of less than 1 Hz.

The damping coefficient and natural frequency of the model test system is determined in this section, as well as the power spectral density of the responses and wind speed. Theoretically, the natural frequency of the plate mounted on a pole may be calculated assuming the stiffness of the pole and mass of the system can be modeled as a lumped mass oscillator. Equation 4.9 gives the angular frequency, ω , and its relation with stiffness and mass of the structure. Angular frequency, ω , can be easily converted and presented in the form of frequency, f (Hz), or period, T (sec).

$$\omega = \sqrt{\frac{K_S}{M_L}} \quad (4.9)$$

Where, K_S is stiffness of a column which is calculated from equation 4.10, and M_L is the lumped mass of the system (Naeim, 2001).

$$K_S = \frac{3EI_m}{L^3} \quad (4.10)$$

Where, E is elastic modulus equal to 68 GPa for aluminum, I_m is moment of inertia, and L is length of the column (values of I_m and L can be found in Table 3-2).

The theoretical natural frequency of the system from equation 4.9 is equal to 9.3 Hz.

A dynamic release, free decay (twang) test has been performed to measure the damping coefficient and natural frequency of the system. Response of the system in the twang test is plotted in Figure 4-9; the logarithmic decrement, δ , from equation 4.11 (Naeim, 2001) can be obtained considering the response of the system in the free decay test.

$$\delta = \ln \frac{v(i)}{v(i+1)} = 2\pi\eta \quad (4.11)$$

Where, η is percentage of critical damping. η is calculated for this system to be equal to 1.7 %. For most structures, the amount of viscous damping in the system varies between 3 % and 10 % of the critical damping (Naeim, 2001).

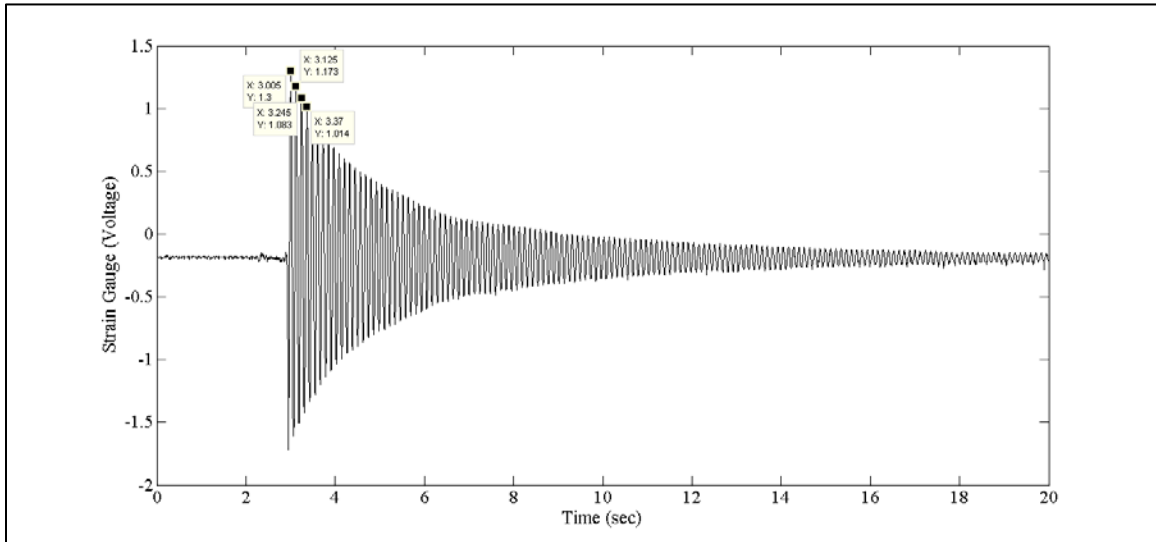


Figure 4-9. Response of Pole and Plate in the Free Decay Test

Figure 4-10 shows the response of the system in frequency domain, where it can be seen that the natural frequency of the system from the twang test is equal to 8.6 Hz.

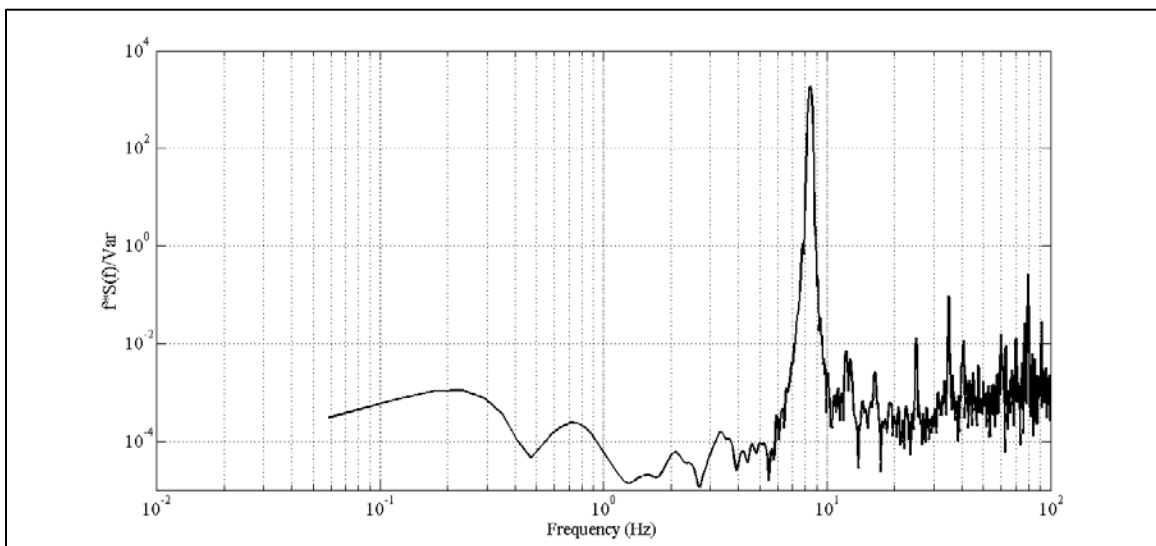


Figure 4-10. Natural Frequency from the Free Decay Test

The theoretical undamped natural frequency from equation 4.9 is 8 % higher than the value obtained in the experiment, which indicates that pole and plate system does not represent an ideal fixed base condition in the sand and may not completely respond as a lumped mass oscillator. It may also be possible that some additional fixity occurred in the lower portion of the pole adjacent to the plate due to the clamping arrangement. It has been found previously that a damped system will display a lower natural frequency (Naeim, 2001), which confirms our findings.

Further information on the system can also be found by investigating the responses during wind loading in the frequency domain. The Fourier transform is not applicable to a random process, since it is not periodic. Moreover for a stationary process, $x(t)$, the condition described by equation 4.12 is not satisfied.

$$\int_{-\infty}^{+\infty} |x(t)| dt < \infty \quad (4.12)$$

However, this problem is overcome by analyzing, not the sample functions of the process itself, but its autocorrelation function, $R(\tau)$. Autocorrelation gives information about the frequencies present in a random process indirectly. If the random process, $x(t)$, is adjusted so that the mean value of the process is zero, then, provided that $x(t)$ has no periodic component,

$$R(\tau \rightarrow \infty) = 0 \quad (4.13)$$

and the condition in equation 4.12 is satisfied. A Fourier transform of $R(\tau)$ is known as a power spectral density, $S(f)$, of the process as can be seen in equation 4.14.

$$S(f) = \frac{1}{2\pi} \int_{-\infty}^{+\infty} R(\tau) e^{-ift} df \quad (4.14)$$

The power spectral density, (PSD), shows the variation of the mean square intensity (power) of the signal for different frequency bands. PSD is the most important quantity considered in studying the dynamic behavior of structures under random loads. Davenport (1961) suggests that if the duration of the record is increased so that intervals between consecutive frequencies become small enough, wind speed can be presented as the relationship in equation 4.15:

$$U_t^2 = \bar{U}^2 + \int_0^\infty \frac{a^2(f)}{2} \cdot df \quad (4.15)$$

Where, $a(f)$ has units of velocity per unit frequency. The integral in equation 4.15 can be denoted as $S(f)$, which is the PSD of the gustiness of the wind record. PSDs of the wind speed fluctuations, drag force and structural response for 3 different mean wind speeds were calculated in MATLAB with a Hamming window. The PSDs were also normalized by the variance of wind speed fluctuations. Figure 4-11 shows the PSDs of the wind speed fluctuations obtained from the hotwire anemometer record, where the peak frequency shows a minor shift slightly to higher frequency with increasing wind speed. The peak frequency of the wind speed in the wind tunnel is just below 1 Hz.

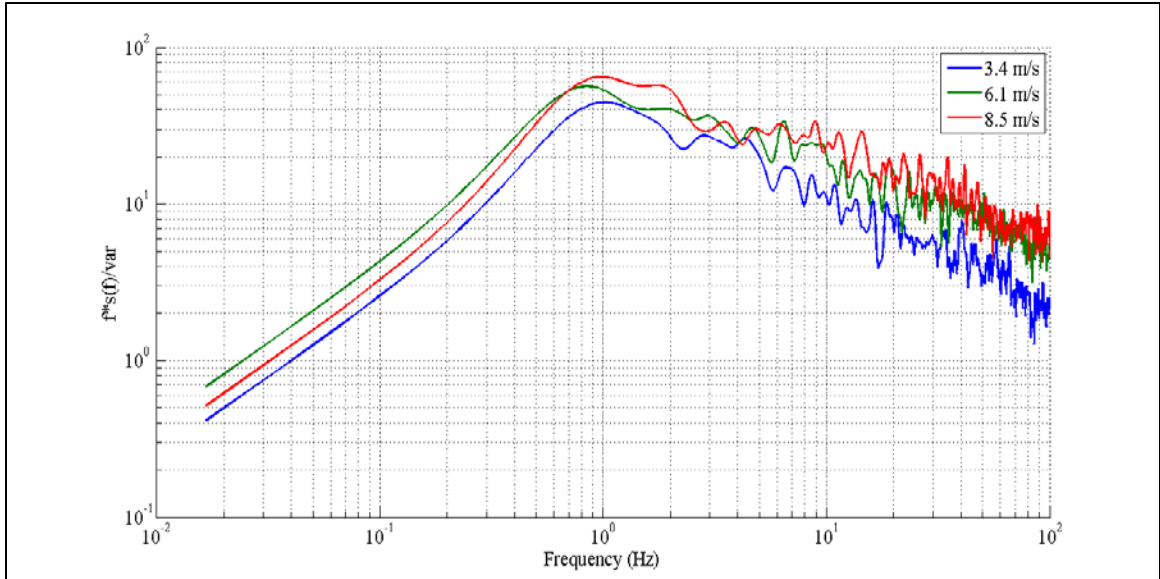


Figure 4-11. PSD of Wind Speed Fluctuations

Figure 4-12 shows the drag force spectra. The drag force spectra are obtained from the drag equation. PSDs of the drag force also show a peak at about 1 Hz.

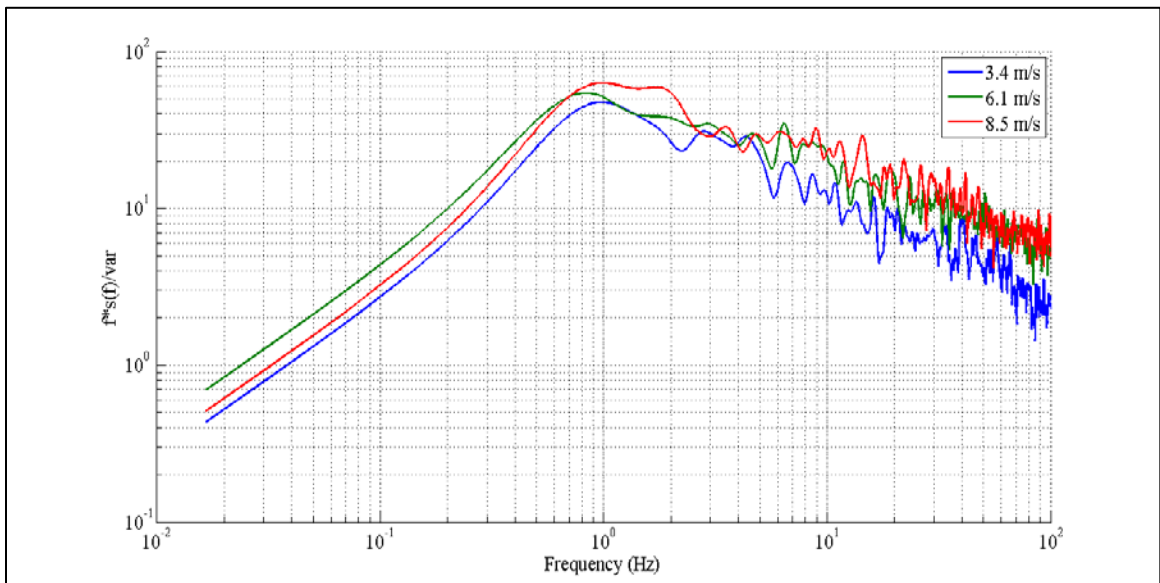


Figure 4-12. PSD of Aerodynamic Force

Figure 4-13 presents the PSDs of the structure responses from the accelerometer on the centroid of the plate for test PRT-MM60-4, which shows the natural frequency of the

system occurs at 8.8 Hz, and is insensitive to wind speed. The spectrum in Figure 4-13 displays the combined effects of aerodynamic and mechanical admittances. The response from the strain gauge also shows the same characteristics and is not presented for the sake of brevity.

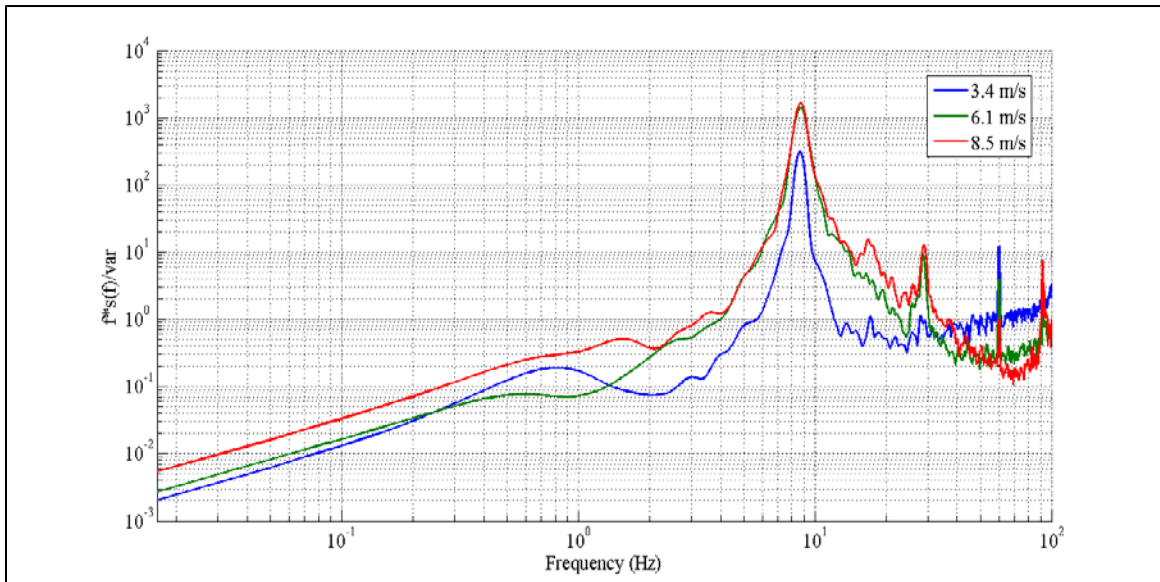
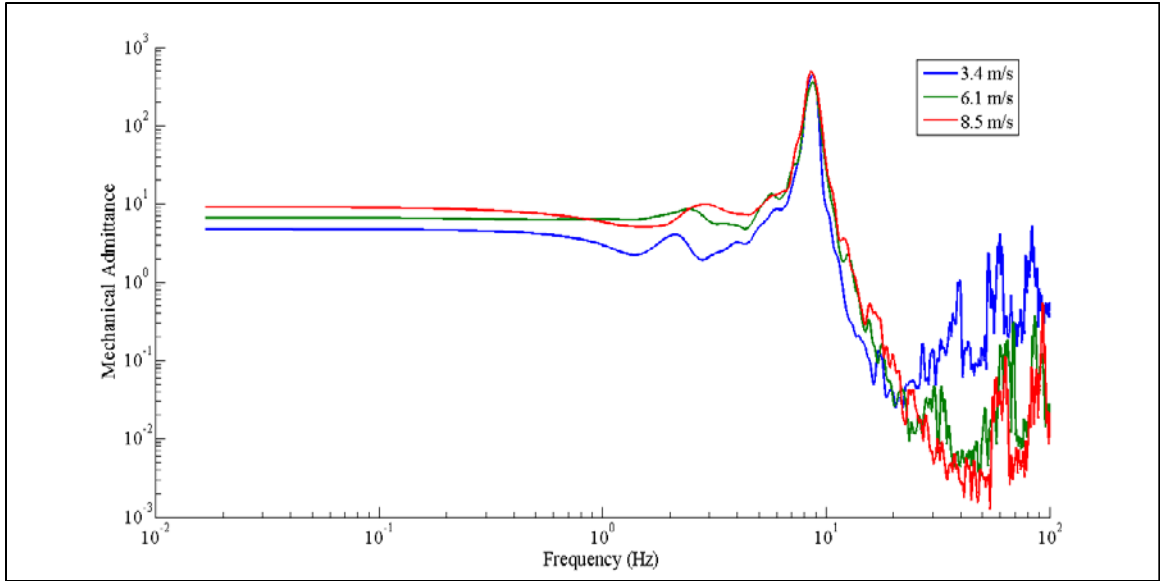


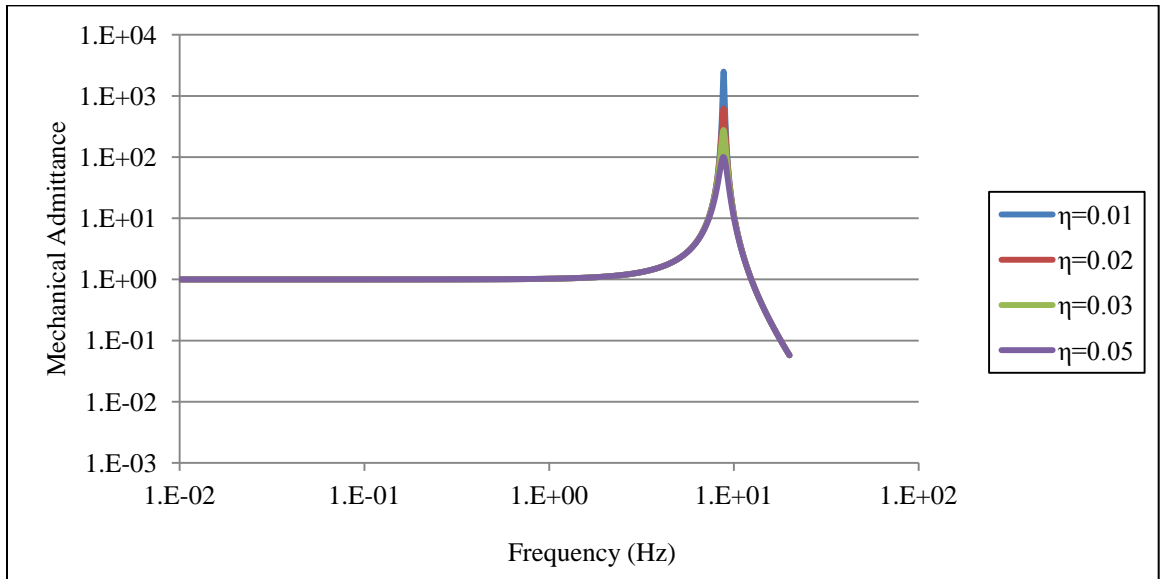
Figure 4-13. PSD of Response – Accelerometer

Thus, it can be concluded that dynamic responses will most likely not be significant and quasi-static assumptions will suffice to calculate the effects of wind on the model piles.

The Davenport spectral approach has two additional aspects: the aerodynamic admittance and mechanical admittance functions. These terms and their significance are covered in Chapter 2 and are presented in Figures 4-14 and 4-15.



(a) Experimental Mechanical Admittance



(b) Theoretical Mechanical Admittance Function

Figure 4-14. Mechanical Admittance

The mechanical admittance of the model has a peak at its natural frequency of 8.8 Hz. The spectrum of the response to wind load from the strain gauge is divided by the drag

force spectrum to obtain the mechanical admittance. From observations of the plate system, the mechanical admittance is a function of natural frequency and damping coefficient, and is insensitive to mean wind speed value. The mechanical admittance confirms the increase of response at the resonant frequency. Figure 4-14(b) shows that the theoretical mechanical admittance from equation 2.8 and suggests that the damping ratio of the plate system is between 3 and 5%.

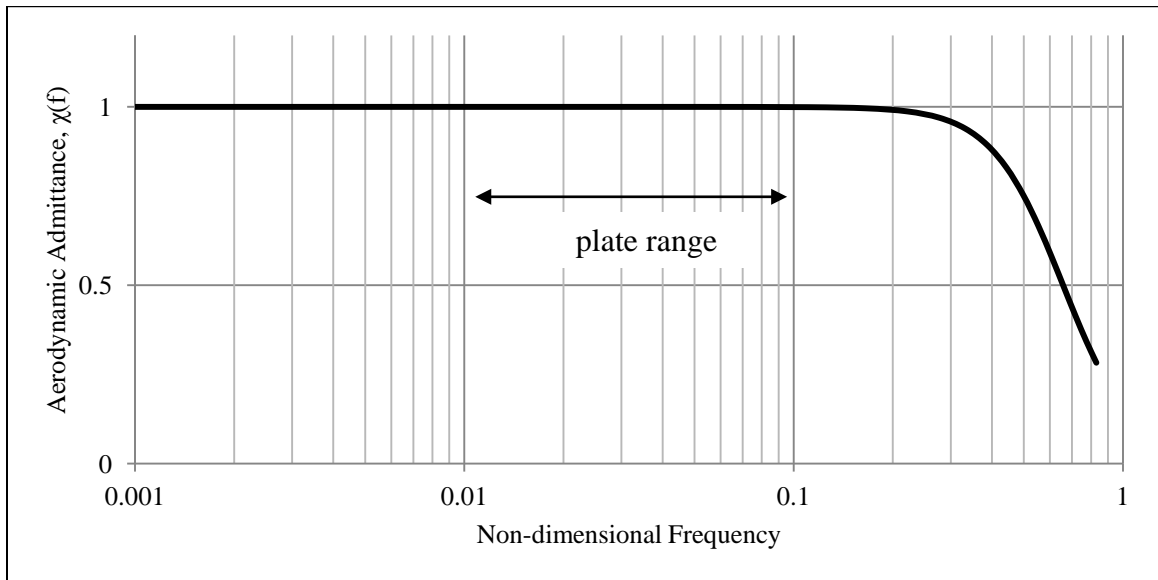
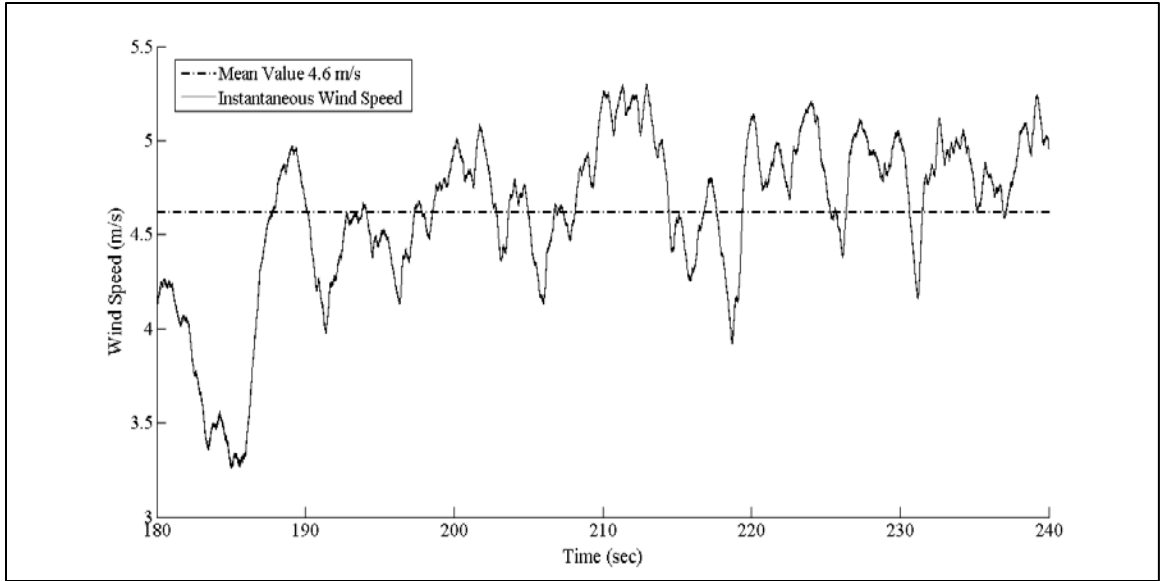


Figure 4-15. Aerodynamic Admittance (Vickery, 1965)

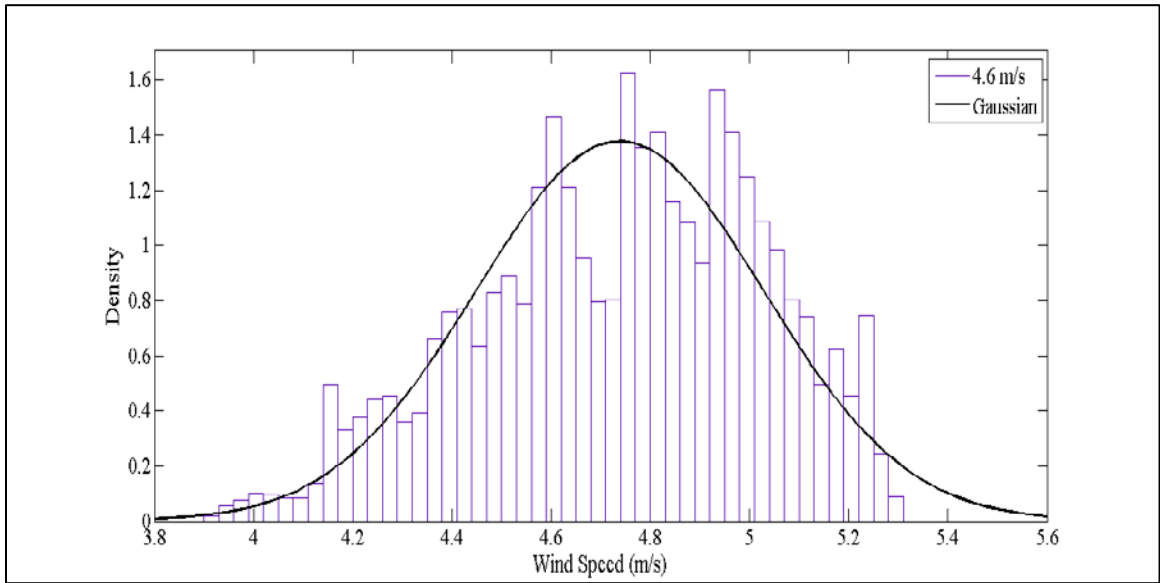
Aerodynamic admittance is used to consider the effects of non-simultaneous wind speed fluctuations over the windward plate face. Aerodynamic admittance, $\chi(f)$, varies between zero and one, and it tends towards 1.0 at low frequencies and for small bodies (Holmes, 2001). The plate used in this testing program has a small frontal area and the wind force spectra correlates fully with the wind speed fluctuations. The non-dimensional frequency for the plate used in this study ranges from 0.01 up to 0.1.

4.2.5 Probability Distribution of the Wind Field

Wind is assumed to be a random process, so we can estimate the occurrence of any particular wind speed through probability distribution functions. Thus, it is important to study the statistical parameters of the wind record. It is assumed that wind like many other naturally occurring processes has a normal or Gaussian probability distribution. Figures 4-16 through 4-18 show wind time-histories for three different wind speeds along with their histograms in test PRT-MM60-4. A normal or Gaussian distribution is also fitted on these histograms. Numbers of bins (bars) have been selected in accordance with Freedman-Diaconis (1981) bin rule.

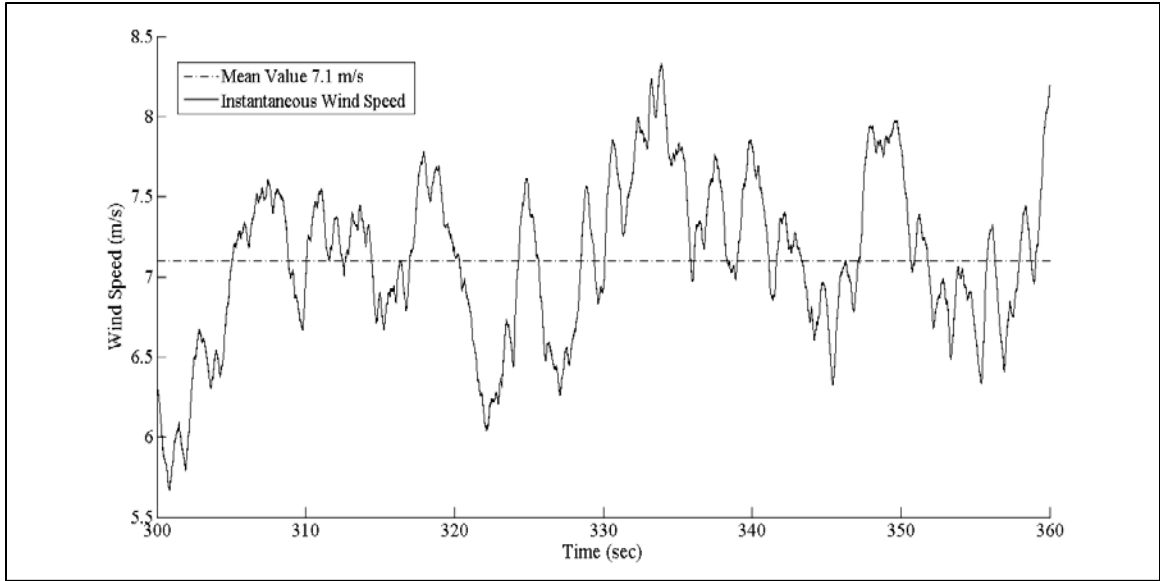


Wind Speed Time-History, $C_{if} = 0.04$

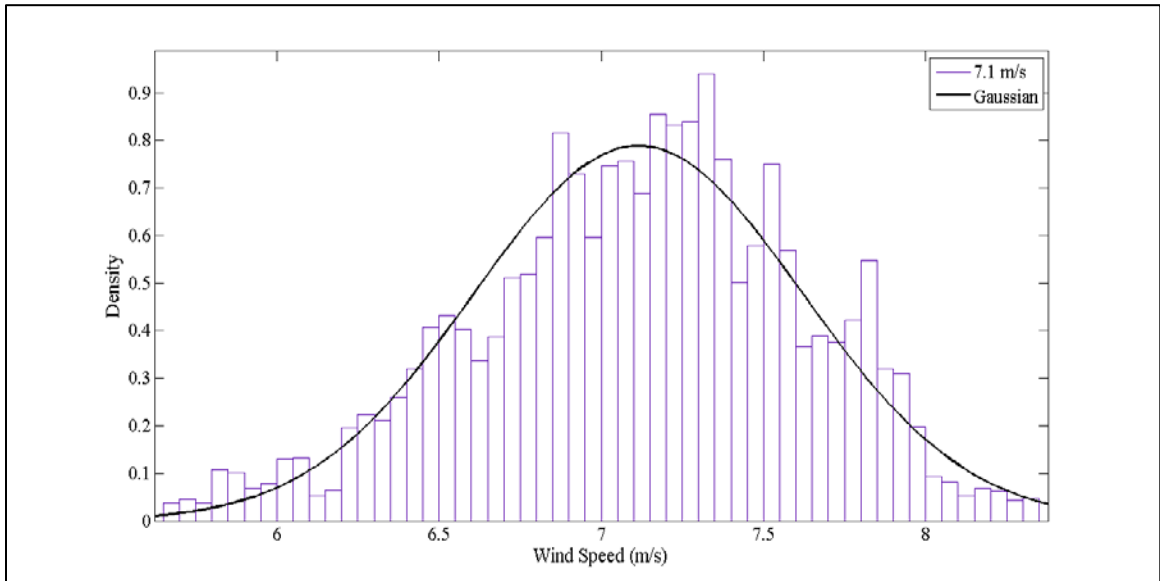


Wind Speed Histogram and Normal Distribution

Figure 4-16. Mean Wind Speed of 4.6 m/s

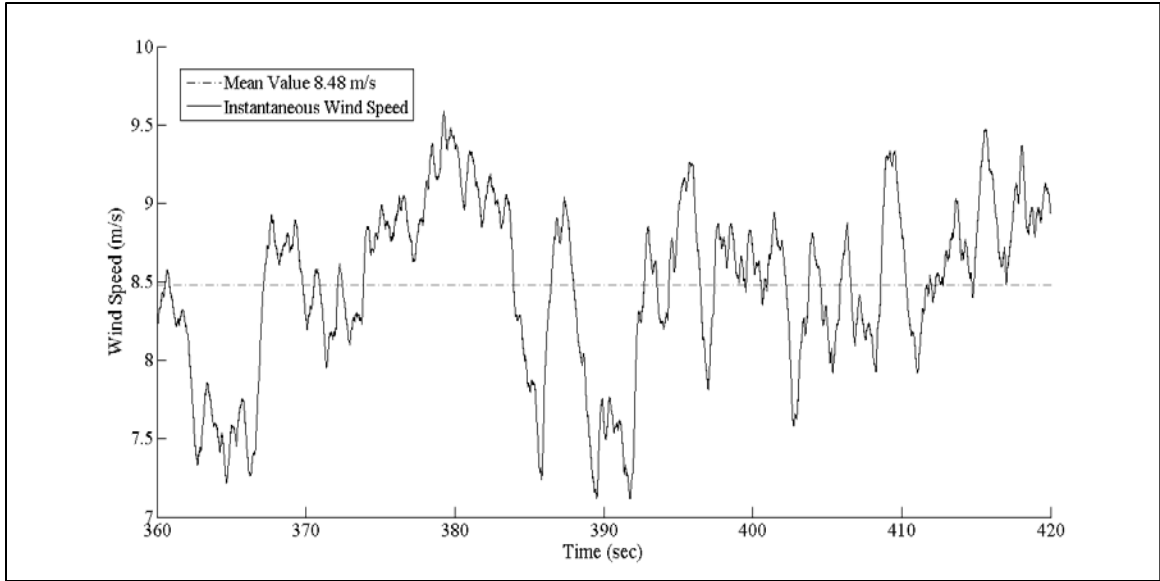


Wind Speed Time-History, $C_{if} = 0.02$

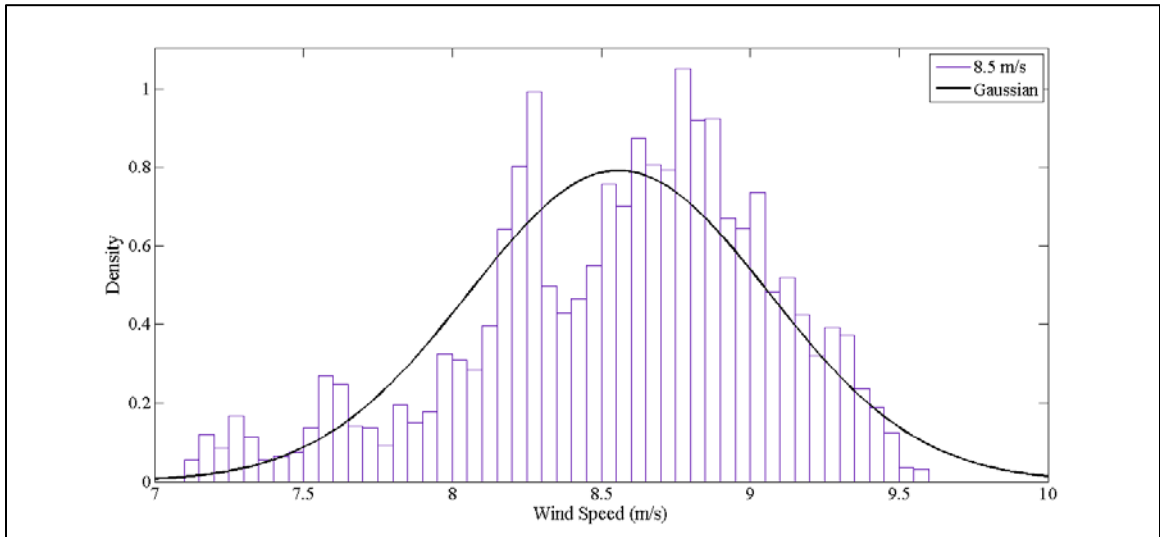


Wind Speed Histogram and Normal Distribution

Figure 4-17. Mean Wind Speed 7.1 m/s



Wind Speed Time-History, $C_{if} = 0.01$



Wind Speed Histogram and Normal Distribution

Figure 4-18. Mean Wind Speed of 8.5 m/s

It can be observed that the wind speed in the wind tunnel is very close to a Gaussian distribution, which means that the wind speed mean value is most probable to occur than values further from it. Figure 4-11 shows the power spectral density of the wind speed at 3 different mean wind speeds. Dirlik (1985) suggests that by considering a narrow-band spectrum of wind speed, the wind speed amplitudes (peaks) will have a Rayleigh distribution (equation 4.16):

$$f_p(s) = \frac{s}{\sigma_U^2} \exp\left(-\frac{s^2}{2\sigma_U^2}\right) \quad (4.16)$$

Where, $f_p(s)$ is the peak probability density function and σ_U is standard deviation of the wind speed.

For a narrow-band process, the irregularity factor (C_{if}) approaches one, which means that the number of upward zero crossings is essentially equal to the number of peaks (Figure 4-19). Level crossings counting is one of the methods that can be used for cycle counting in a narrow band process. Figure 4-19 shows strong correlations between the number of cycles and zero crossings, $E(0)$ or peaks, $E(P)$ in a theoretical narrow band process.

Level crossing counting has the advantage of filtering out small amplitude cycles. However, since we know little about the effects of the wind loading phenomenon on the plate system, filtering the small amplitude cycles might lead to incorrect interpretations of the behavior, particularly if there are numerous small amplitude cycles.

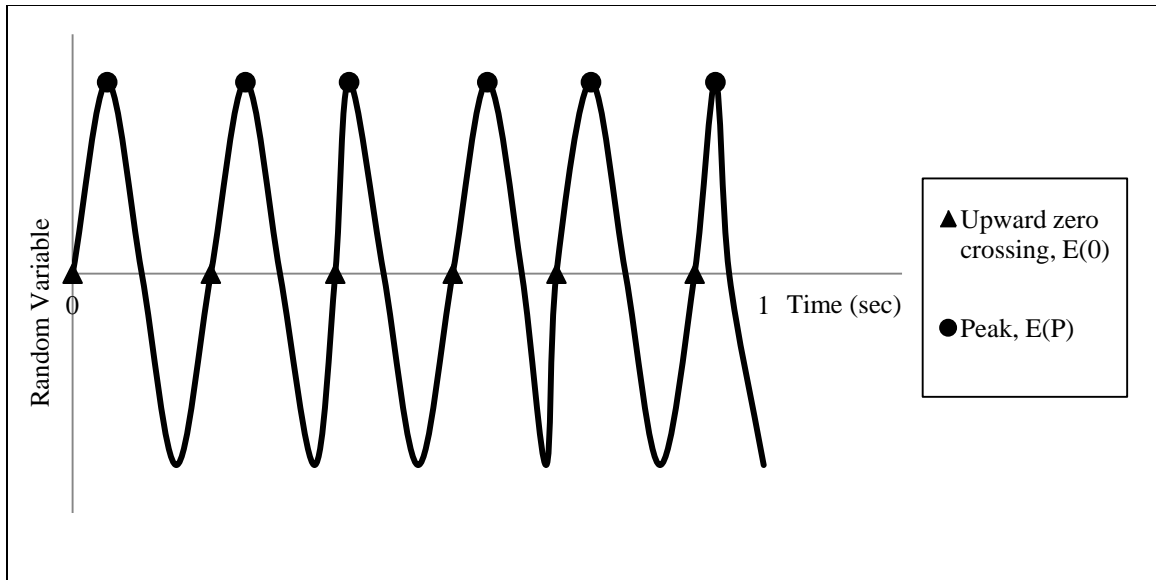


Figure 4-19. Upward Zero Crossings and Peaks in an Ideal Narrow Band Process

Table 4-2 shows the results of level crossings for test PRT-MM60-4.

Table 4-2. Level Crossings of Test PRT-MM60-4

Voltage	Mean Wind	Duration	Zero Level	Peaks	C_{if}
	Speed (m/s)	(sec)	Crossings, $E(0)$	$E(P)$	$(E0/EP)$
0.5	0.74	0-60	129	187	0.69
1.0	1.27	61-120	80	188	0.43
1.5	3.37	121-180	15	200	0.08
2.0	4.62	181-240	8	208	0.04
2.5	6.06	241-300	5	195	0.03
3.0	7.11	301-360	3	191	0.02
3.5	8.48	361-420	2	184	0.01
4.0	9.39	421-480	2	180	0.01
4.5	10.99	481-540	5	75	0.07

Table 4-2 shows that zero crossing counting, $E(0)$ from the power spectral density may not provide satisfactory results. Figure 4-20 shows three random time-histories with three different irregularity factors, C_{if} . The time-histories obtained in the wind tunnel are visibly more irregular than that shown below with the lowest irregularity factor. The very low values of irregularity factor, C_{if} , indicate that a narrow-band assumption *is not valid* for the wind tunnel field and peak counting from the moments of the power spectral density will not correlate well with number of cycles and therefore should not be used.

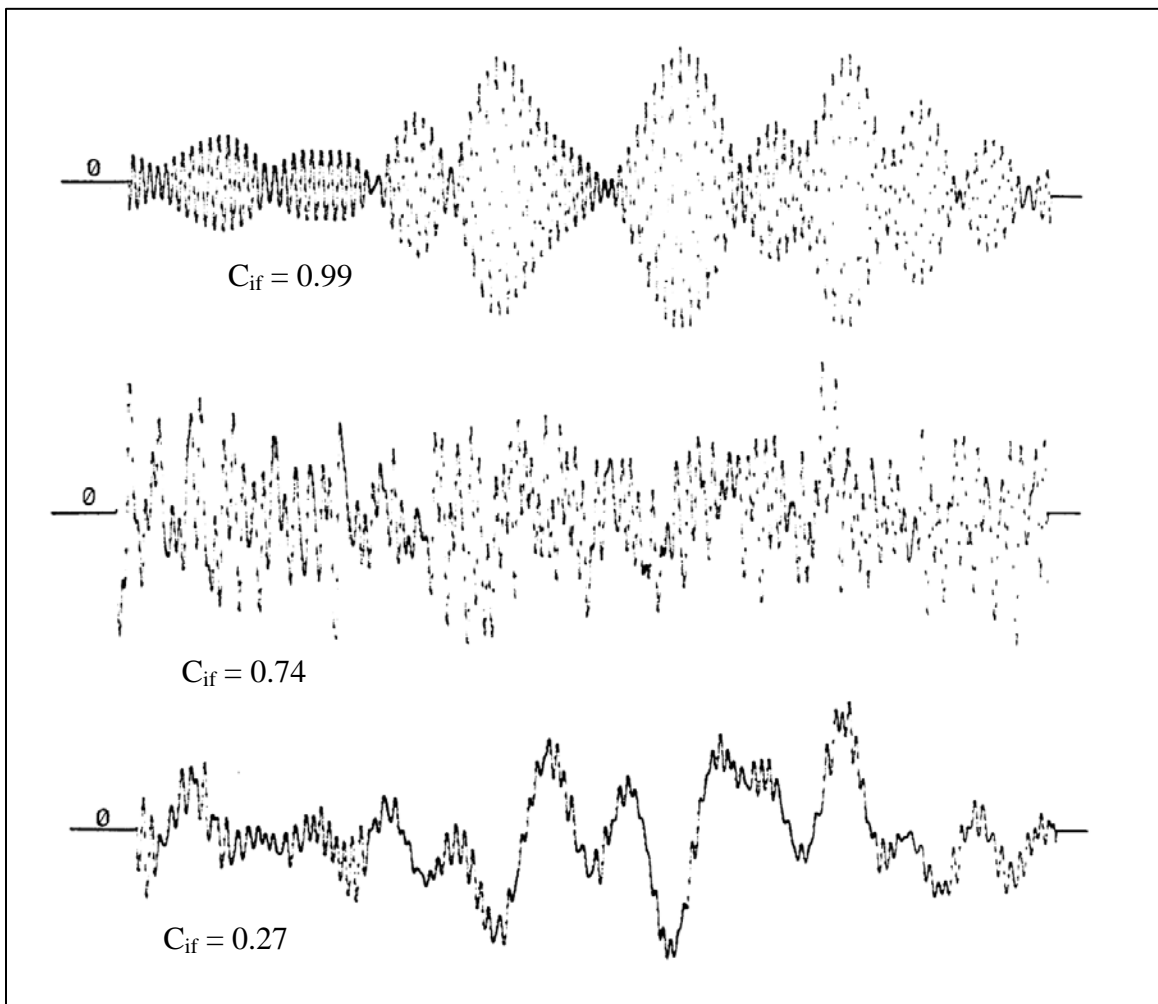


Figure 4-20. Time-Histories with Different Irregularity Factor (Dirlik, 1985)

4.2.6 Cycle Counting Method

ASTM E1049 provides a variety of methods for cycle counting. These methods are often used in fatigue analysis. Counting the number of load cycles in a random process can be performed with the rainflow cycle counting method in the time domain, which gives reliable results and has been used in other similar studies (Leblanc et al., 2010).

The rainflow method models the fluctuations in a random time-history as a flow of rain over the undulations of a pagoda style roof. In this method, rainflow initiates at the beginning of the time-history. The flow stops until one of the following conditions is met: flow comes opposite to a maximum more positive (or a minimum more negative) than the maximum (minimum) it started from, also when it meets the flow from above pagoda. Figure 4-21 demonstrates the rainflow method. The rain initiating at peak-1, (a minimum) falls on peak-2 and 4, and stops opposite peak-5, because peak-5 is more negative than peak-1. Hence, the range from peak-1 to peak-4 is extracted as a half-cycle. Similarly peak-2 stops opposite peak-4, which is more positive than peak-2. However, the rain starting at peak-3 stops at 2, where it meets rain from the roof above. It is noted that when a half-cycle is extracted by the second condition, there already exists a corresponding half-cycle of equal magnitude extracted by the first condition, and two together make one full cycle. In Figure 4-21, range 2-3 and range 3-2 make a full cycle (Dirlik, 1985).

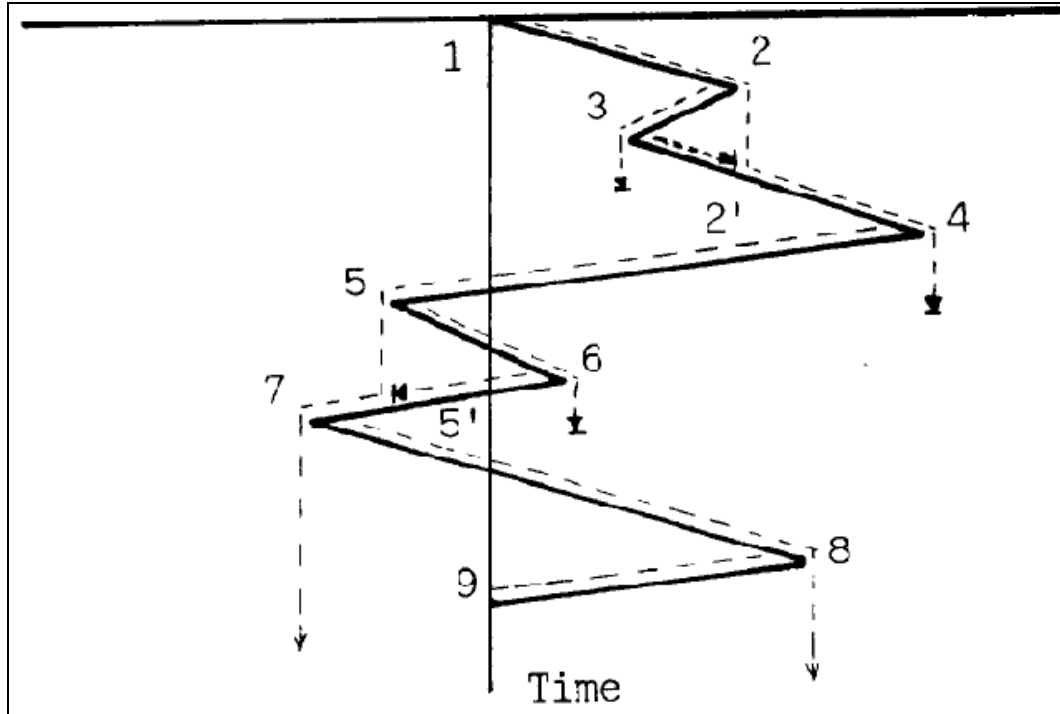


Figure 4-21. The Rainflow Method (Dirlik, 1985)

In this research, counting the number of cycles (fluctuations) in the wind speed time history is crucial. In Figure 4-22 a time-history of wind from the hotwire in test PRT-MM60-4 is given. The superimposed red line in the record represents the mean value of wind speed at any loading interval for the stepped increments. The rainflow counting method is used to break the irregular time-history of the wind speed recorded by the hotwire anemometer into numbers of cycles of different amplitudes, with their start times and duration.

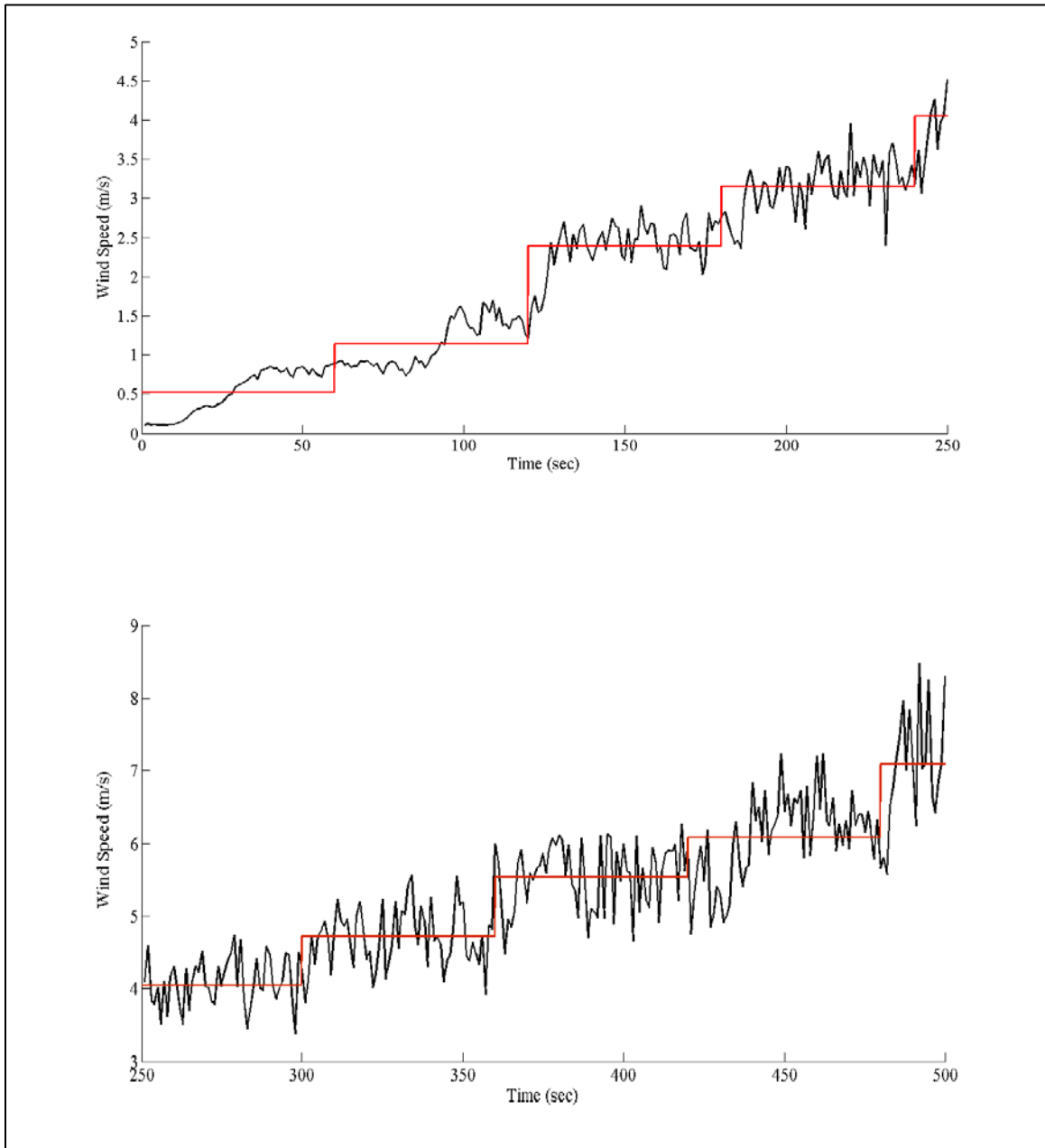


Figure 4-22. Time-History of Wind Speed Test PRT-MM60-4

The result of cycle counting in accordance with the rainflow method is given for test PRT-MM60-4 in Table 4-3. The results of other tests are presented in Appendix C.

In Table 4-3(a), cycle amplitude, cycle mean value, start time and duration of each cycle is presented. Total number of cycles is the summation of cycle number. The full results for test PRT-MM60-4 are presented in Table 4-3(b).

Table 4-3(a). Detail of Rainflow Counting for Mean Wind Speed 3.4 m/s in Test PRT-MM60-4

Cycle Amplitude	0.08	0.11	0.14	0.09	0.12	0.23	0.26	0.20	0.00	0.28	0.07
Cycle M.Value	1.67	1.64	2.29	2.45	2.46	2.43	2.45	2.42	2.47	2.47	2.61
Cycle Number	0.5	0.5	1	1	1	1	1	1	1	1	1
Start Time	121	122	127	134	143	137	131	150	153	146	157
Cycle Duration	2	2	2	2	2	6	4	2	2	12	2
Continued											
Cycle Amplitude	0.04	0.13	0.06	0.35	0.02	0.68	0.44	0.40	0.11	0.09	
Cycle M.Value	2.35	2.41	2.38	2.46	2.69	2.22	2.46	2.42	2.71	2.68	
Cycle Number	1	1	1	1	1	0.5	0.5	0.5	0.5	0.5	
Start Time	160	165	172	163	178	123	155	174	176	177	
Cycle Duration	2	4	2	12	2	64	38	4	2	6	

Table 4-3(b). Total Number of Rainflow Cycles in Test PRT-MM60-4

Voltage	Mean Wind Speed (m/s)	Duration (sec)	Total Number of cycles
0.5	0.7	0-60	9.5
1.0	1.3	61-120	18
1.5	3.4	121-180	17.5
2.0	4.6	181-240	18.5
2.5	6.1	241-300	16.5
3.0	7.1	301-360	18.5
3.5	8.5	361-420	20
4.0	9.4	421-480	21
4.5	10.99	481-540	16.5

Since the “quasi-static” approach is applicable, the drag force directly correlates with the wind speed and it will be acceptable to determine the cyclic loads from the rainflow method in our further discussions in Chapter 4 and for the accumulated rotation of the pile in Chapter 5. It should be noted that the same procedure was undertaken for data from the strain gauge; comparison with the total number of cycles from the hotwire and the strain gauge derived loads showed good agreement.

As shown in Table 4-3(a), any cycle (or group of cycles) obtained from the rainflow counting has its own amplitude and mean value. Since we are interested in the effects of cyclic loads, the amplitudes of the cycles along with their mean values will be investigated. The amplitude is defined as half of the distance between a peak and trough in a cycle; in the other words amplitude is equal to half of the cycle range.

Figures 4-23 to 4-25 show histograms of cycle amplitudes for three wind speed intervals for test PRT-MM60-4. Rayleigh probability distributions have been fitted, with the aid of the distribution fitting toolbox in MATLAB, to the histograms obtained from the rainflow method to give an insight into the range of cycle amplitudes in the random wind flow. The bins are defined in accordance with Scott’s bin rule. A Rayleigh distribution was chosen due to simplicity and previous use in some research works studying fatigue analysis under random cyclic loads (Wirsching & Light, 1980 and Dirlik, 1985). As can be seen, the small amplitude cycles have significant weights in the density of the cycles obtained from the rainflow counting method from the wind tunnel flow.

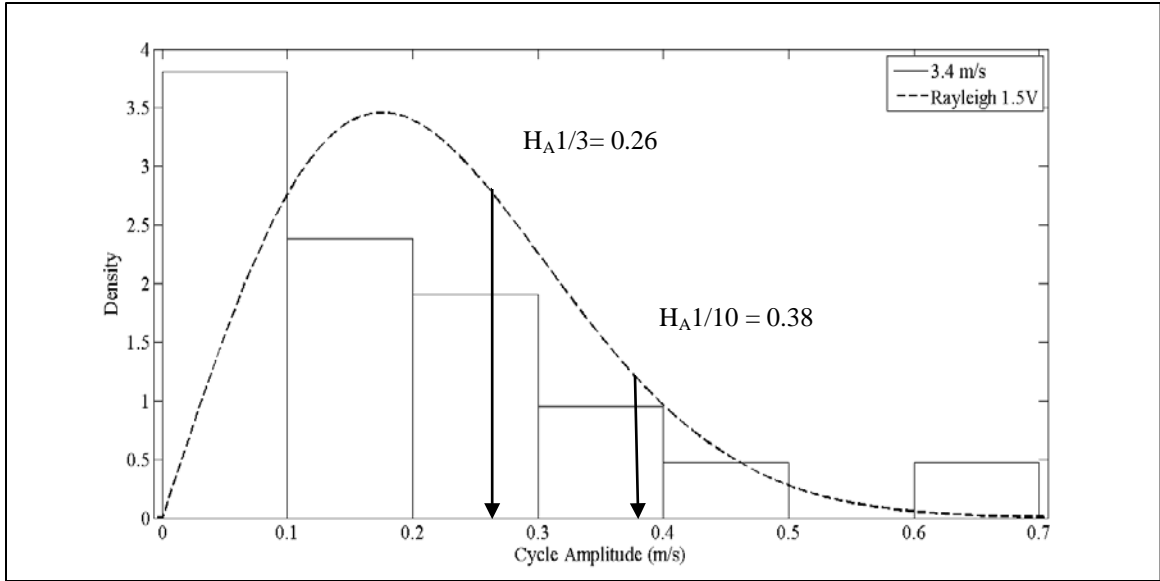


Figure 4-23. Probability Distribution of Cycle Amplitude for Mean Wind Speed of 3.4 m/s

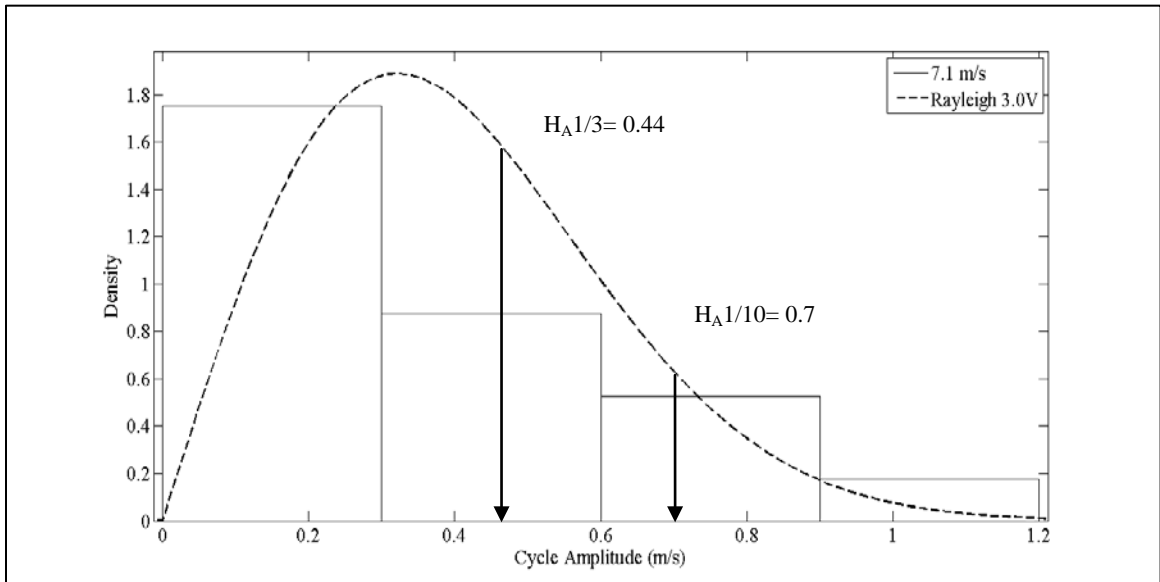


Figure 4-24. Probability Distribution of Cycle Amplitude for Mean Wind Speed of 7.11 m/s

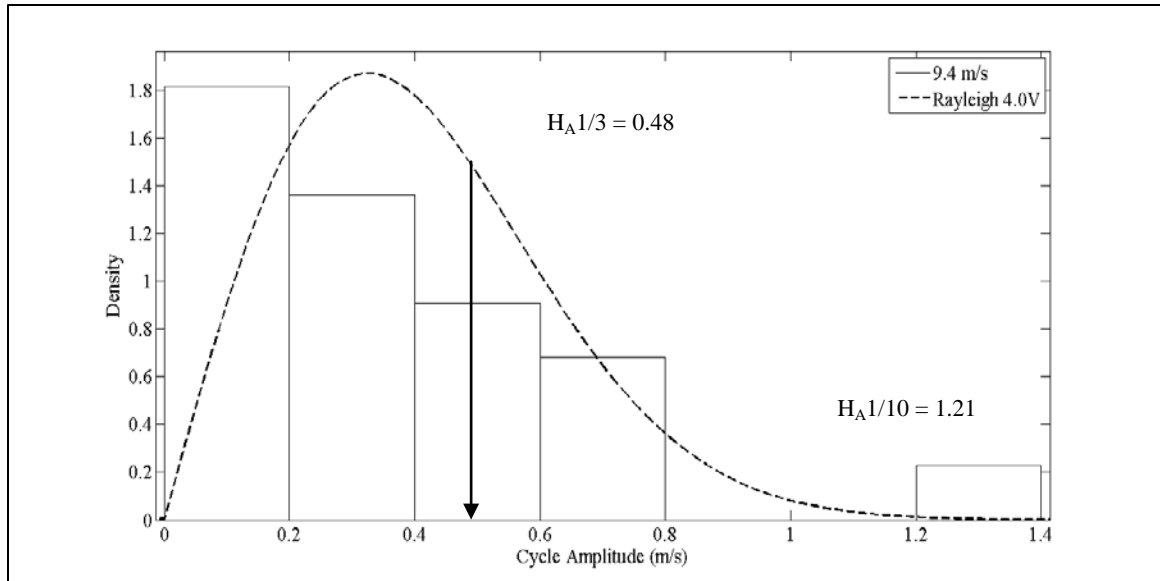


Figure 4-25. Probability Distribution of Cycle Amplitude for Wind Speed of 9.4 m/s

Since the relative proportions of the cycle (fluctuations) amplitudes in the wind and the associated loads are important, some measures of the differences between the different Rayleigh distributions of loading and response will be sought.

One approach will be to adopt a method that the offshore oil and gas industry uses for wave loading of platforms to characterize the Rayleigh distributions and provide loading information for the plate tests. The mean, largest 1/3 of the cycles ($H_A1/3$), and largest 1/10 of the cycles ($H_A1/10$) of the wind speed fluctuations (cycles) for each wind speed are tabulated in Table 4-4. Two statistical parameters: skewness, β_s , and kurtosis, β_k , can also be used to characterize the Rayleigh distributions of the cycle amplitudes. The values of kurtosis and skewness shown in Table 4-4 are approximately within the range that Goda (2010) suggested for ocean waves ($3 < \beta_k < 9$ and $0 < \beta_s < 2$).

Table 4-4. Statistical Parameters for Cycle Amplitudes in Test PRT-MM60-4

Voltage	Mean Wind Speed	Mean value of Rayleigh Distribution	Variance of the Rayleigh Distribution	Kurtosis β_k	Skewness β_s	$H_A1/3$	$H_A1/10$
0.5	0.7	0.11	0.003	8.41	2.65	0.128	0.186
1	1.3	0.12	0.004	9.02	2.49	0.142	0.205
1.5	3.4	0.22	0.013	4.69	1.43	0.259	0.379
2	4.6	0.30	0.02	4.08	1.42	0.355	0.517
2.5	6.1	0.36	0.035	2.88	0.74	0.422	0.625
3	7.1	0.40	0.044	2.90	0.86	0.438	0.691
3.5	8.5	0.39	0.042	1.93	0.28	0.464	1.178
4	9.4	0.40	0.045	5.04	1.45	0.479	1.214
4.5	10.99	0.77	0.164	2.22	0	0.911	1.333

The skewness is a measure of the asymmetry of the probability distribution of a random variable. A positive skewness indicates that the tail on the right side is longer than the tail on the left side, and the bulk of the values lie to the left of the mean. In a similar way, kurtosis is a descriptor of the shape of the probability distribution of a random variable, and measures the “peakedness” of the distribution. In the other words, a high kurtosis distribution has a sharper peak, and longer, fatter tails, while a low kurtosis distribution has a more rounded peak, and shorter, thinner tails. The variations of the skewness and kurtosis with mean wind speed are plotted in Figure 4-26. It can be seen that both skewness and kurtosis decrease with increasing wind speed, which indicates that cycle amplitudes with the values closer to the mean value occur more often, the proportion of smaller cycles reduces and the length of the tail reduces (hence the number and magnitude of extreme values reduce).

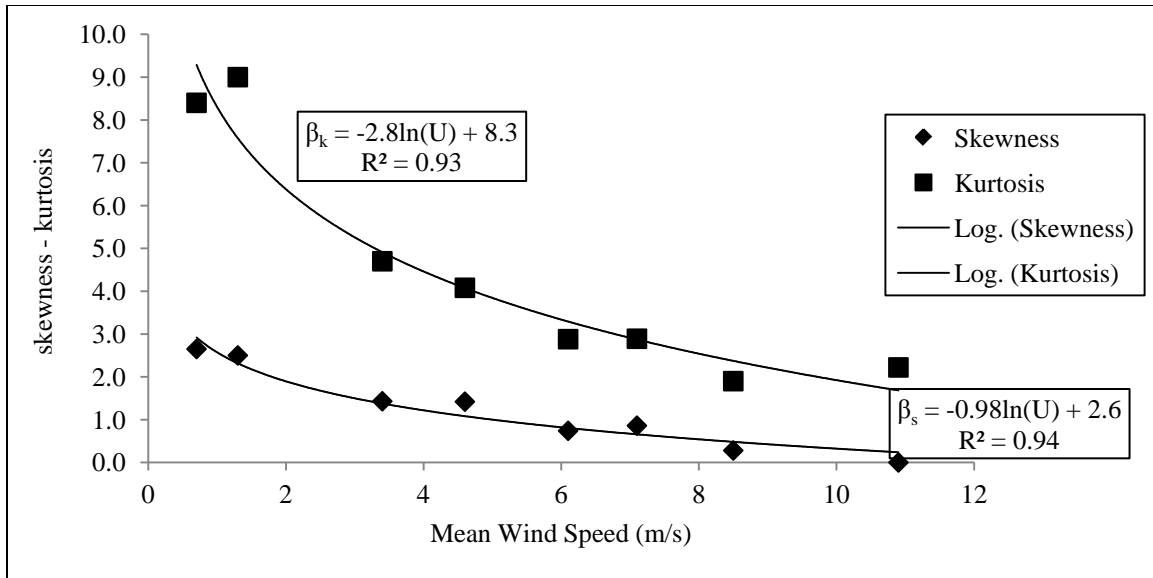


Figure 4-26. Skewness and Kurtosis of Cycle Amplitudes for Test PRT-MM60-4

In the offshore literature, the term “significant wave height” ($H_A/3$) is used as a means to introduce a well-defined and standardized statistic to denote the characteristic height of the random waves in a sea state. It is defined in such a way that it corresponds to what an observer will see when estimating visually the average wave height. This has been found to be a very useful design aid for offshore engineering. The significant wave height is found to be a function of the zeroth moment (M_0) of the Rayleigh distribution. This concept may also be useful to see the variations of the characteristic cycle amplitudes of the wind field with mean wind speed.

Figure 4-27 shows the variations of the characteristic cycle amplitudes with mean wind speed and it can be seen that higher characteristic cycle amplitudes occur for increasing mean wind speeds. The ratio of $H_A/3$ and $H_A/10$ is seen to increase for greater wind speeds, which agrees with the observations of the skewness decreasing with wind speed;

hence there is a link between these different parameters characterizing the Rayleigh distribution.

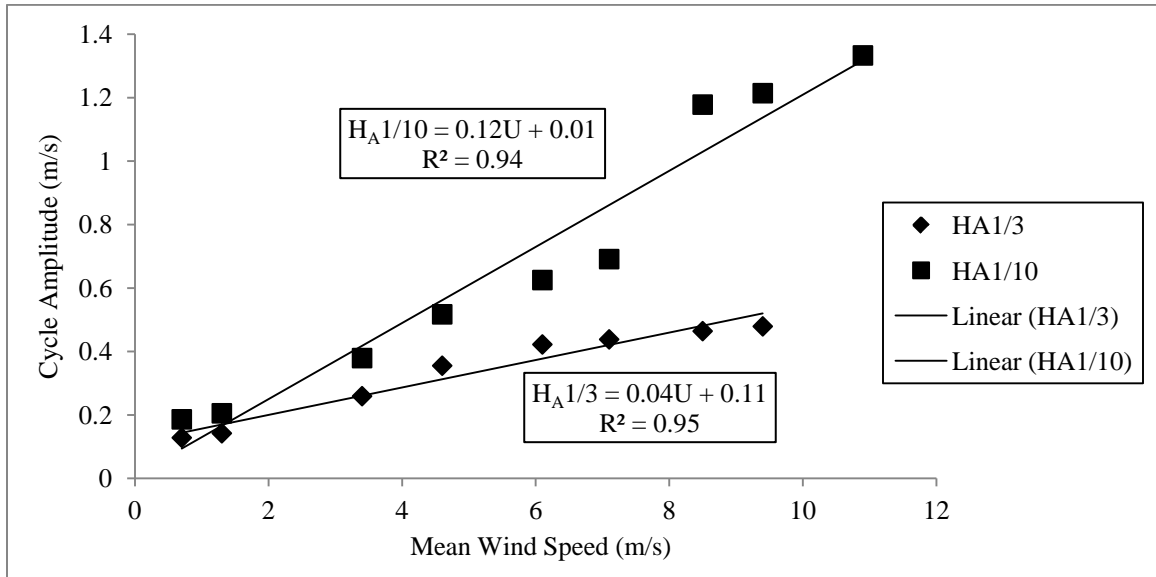


Figure 4-27. Cycle Amplitude Variations with Mean Wind Speed for Test PRT-MM60-4

4.3 Summary

The focus of this chapter was providing information on the characteristics of the random loads from the wind field.

Drag coefficient, turbulence intensity, gust factor and peak factor were calculated for the wind tunnel tests. It was observed that drag coefficient is almost insensitive to wind speed and high variations are probable around the mean value. Turbulence intensity was also insensitive to mean wind speed, and experimental values for gust and peak factors show good agreement with other studies.

The probability of resonance was estimated and it was found to be low; hence the quasi-static portion of the response was dominant. The probability density of the wind was also

estimated and the Gaussian distribution showed a good fit of the histograms of wind speed for different wind speed intervals.

The total number of cycles in the wind record was obtained from the rainflow counting method. The amplitude of cycles was also investigated and it was shown that the skewness and kurtosis of the cycle amplitudes decrease with higher mean wind speeds. It was understood that a narrow-band assumption for the wind history may not lead to proper estimation of the number of cycles.

RESPONSE OF PILES TO LATERAL LOADS

5.1 Overview

This chapter focuses on the lateral behavior of piles in response to static and random variable amplitude cyclic loads. The lateral behavior of piles is affected by a number of parameters, such as, initial soil condition, groundwater level, geometry and flexural rigidity of the pile, and the characteristics and eccentricity of the lateral load. Different concepts and methods for analysis of the laterally loaded pile have been previously explained in Chapter 2.

Two well-known general solutions for laterally loaded piles are: subgrade reaction modulus (commonly known as the p-y method) and the elastic continuum approach. These two methods were initially developed for flexible piles, rather than rigid ones. Leblanc et al. (2010) hinted that the majority of monopiles serving as foundations for wind turbines are well within the range of rigid pile behavior. Thus it appears that the p-y method may be extensively used for analysis of laterally loaded piles, without considering their flexural rigidity (Leblanc et al., 2010). This has been suggested as one important disadvantage for the current design methodology of laterally loaded piles.

In some portions of the literature, terms such as, shaft or pier have been used to emphasize the rigidity of the pile. Poulos & Hull (1989) suggested equation 5.1 for evaluating the transition limits from rigid to flexible behavior for laterally loaded piles. In

the current research, small scale piles were used with Λ equal to 2, 24, and 389 for short, medium and long pile, respectively (see equation 5.1). In geotechnical engineering, a shallow foundation is defined to have depth over diameter ratio (D/B) less than 2.5, a caisson foundation has $2.5 < D/B < 5$, and a deep foundation (pile) has a D/B over 5; this classification suggests that our models lies in a range of caisson foundations, although Agaiby et al. (1992) consider short rigid piles to have D/B in the range of 2.6 to 9.

$$\text{(Rigid)} \quad 4.8 \leq \Lambda = \frac{E_s D^4}{E_p I_m} \leq 388.6 \text{ (Flexible)} \quad (5.1)$$

Where, E_s is soil Young's modulus, E_p is pile Young's modulus, I_m is moment of inertia of the pile cross section, and D is pile length.

In this research, the main focus has been on the effects of the characteristics of random variable amplitude cyclic lateral loads on the behavior of rigid piles. Moreover, the effects of the pile geometry and load-eccentricity have been investigated through a series of static tests. The problem of the accumulated ground-line displacement/rotation under random variable amplitude cyclic loads is also discussed in this chapter, along with the "ratcheting" behavior of the piles.

5.2 Static Response of Piles to Lateral Loads

A series of ground-line and moment static tests were performed to characterize the response of model piles to static loads. These tests were also used as a basis for better understanding of the random variable amplitude cyclic tests. The effects of load-eccentricity and geometry of the piles are addressed in this section.

5.2.1 Hyperbolic Representation of Load-Displacement

Semi-empirical hyperbolic representation of the load - displacement curve has been used for this study for the interpretation of pile responses to lateral loads (e.g. Manoliu et al., 1985; Agaiby et al., 1992; Achmus et al., 2009). Classic solutions for laterally loaded piles, such as, Brinch Hansen (1961), Broms (1964), Reese et al. (1974) and Meyerhof & Ranjan (1972) are also compared with this approach. In this work, the capacity will be obtained from fitting a hyperbola to the load - displacement curve. Hyperbolic capacity is obtained from an upper-bound solution for laterally loaded piles. In other words, hyperbolic capacity will not be reached in practice and it only comes into play at excessive displacements. The load-displacement relation can be characterized with equation 5.2 to obtain the hyperbolic capacity, H_h and initial stiffness, K_i .

$$y_s/H = a + by_s \quad (5.2)$$

Where, $1/a$ is equal to initial stiffness, K_i , y_s is ground-line displacement, H is horizontal force, and $1/b$ is equal to hyperbolic capacity, H_h (the limit of equation 5.3). By rearranging equation 5.2 the load -displacement relation can be shown in a different form (equation 5.3):

$$H = y_s / (1/K_i + y_s/H_h) \quad (5.3)$$

In this method, K_i shapes the initial pseudo-linear portion of the load-displacement curve and H_h controls the final projection of the curve. Agaiby et al. (1992) commented on the hyperbolic representation of a load-displacement relation as an objective tool, which is compatible with the assumptions made when calculating the ultimate capacity using the

simple two-dimensional models reviewed in Chapter 2 (e.g. Hansen, 1961; Broms, 1964). It should be noted that the hyperbolic capacity is a projected load that is never achieved, much like the stress conditions assumed around a shaft when calculating the ultimate capacity.

5.2.2 Location of the Zero Rotation Point

Before proceeding to the load - displacement characteristics, the zero-rotation depth, (Z_r), should be obtained to calculate the ultimate capacity of the laterally loaded pile. The zero rotation point is the ground depth where the rigid pile rotates. The depth of zero rotation point, Z_r , affects the ultimate capacity of pile obtained from any classic solution (e.g. Broms, 1964). Z_r can be precisely determined by placing stress cells within the soil body along the entire length of a flexible pile. By interpolation between stress cell measurements, Z_r is the depth that zero change in stress is observed. Theoretically, by considering the force and moment equilibrium on the pile and using postulated on-pile force profiles, Z_r , can be estimated (Guo, 2008). The on-pile force profile differs from one approach to another (e.g. Brinch Hansen, 1961; Broms, 1964; Reese et al., 1971).

Z_r was obtained from the pile equilibrium of forces and moments and found to be between 7 and 8 cm for the moment and ground-line tests on the medium size pile. Z_r/D can also be estimated to be approximately 0.8 by trial & error using the procedure presented in Chapter 3 for the wind tunnel tests. It should be mentioned that Z_r/D is higher for the ground-line tests. Agaiby et al. (1992) studied the impact of e/D on Z_r . By increase the eccentricity of load, Z_r will move to shallower depths. As shown in Chapter 2, Z_r/D varies from 0.79 for a ground-line test to 0.70 for a test with eccentricity of 20.

Changes in the location of the Z_r can be correlated with reduction in pile lateral capacity while the eccentricity of load increases.

Broms (1964) replaced the passive stresses below the Z_r , with a concentrated load at the pile tip as shown in Figure 5-1. It was assumed that the passive soil pressure in front of the pile acts over the entire depth and he suggested equation 5.4 for the ultimate capacity of a laterally loaded pile, H_u .

$$H_u = 0.5 \gamma B D^3 K_p / (e + D) \quad (5.4)$$

Where, K_p = Rankine maximum passive coefficient, e is the load eccentricity, γ is soil unit weight, D is the pile length, B is the pile diameter, and H is the horizontal force. Equation 5.4 shows the relationship between the load eccentricity and the ultimate capacity.

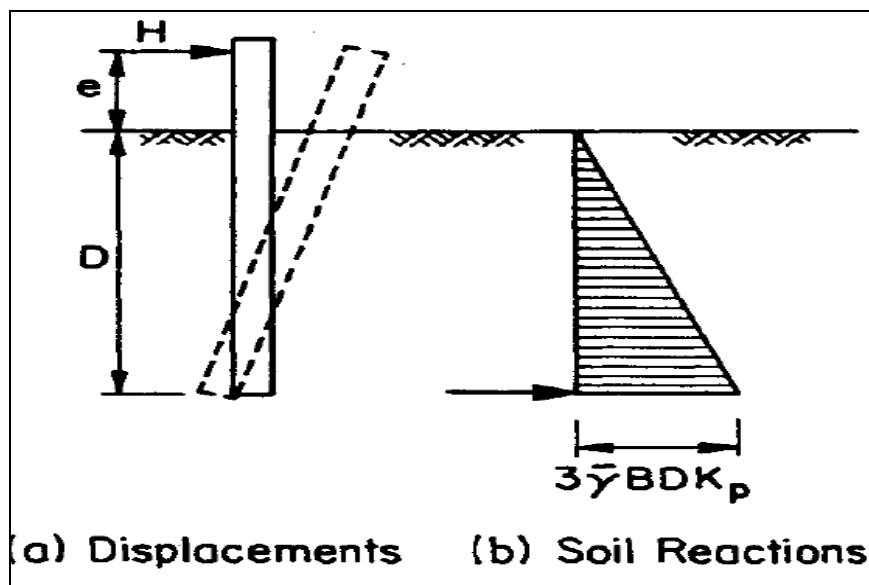
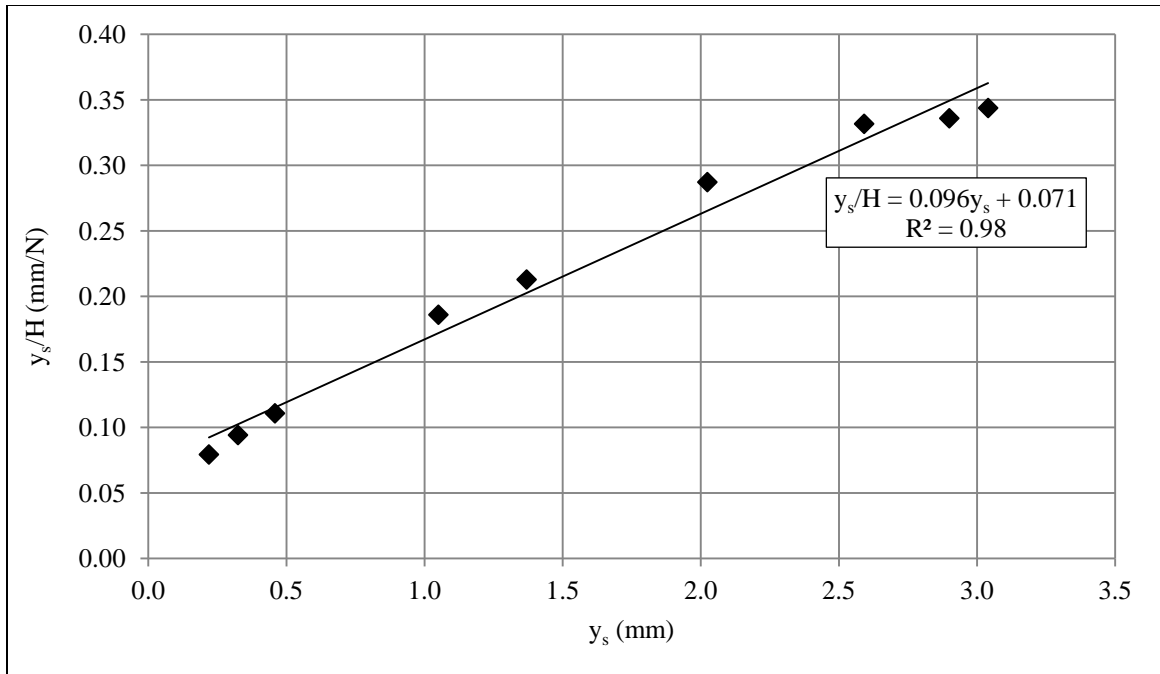


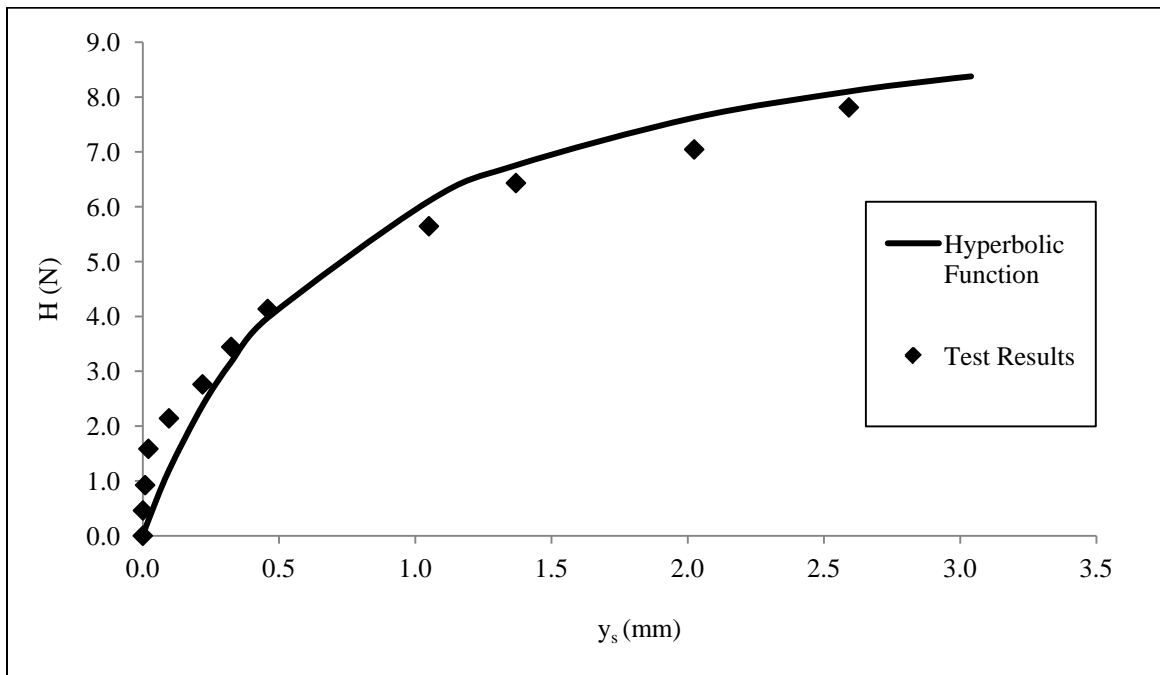
Figure 5-1. Simplified Broms Yield Stress Distribution (Agaiby et al., 1992)

5.2.3 Static Ground-line Tests

Figures 5-2 through 5-4 depict the evaluation of parameters a and b and the fitted curves for the static ground-line tests. Results of the ground-line tests are given for the three sizes of pile. Generally, there is a close agreement between the response obtained from the experiments and the fitted hyperbolas. The slope of the fitted line in the transformed plot, gives the hyperbolic capacity and the intercept of the fitted line is equal to the value of the initial stiffness.

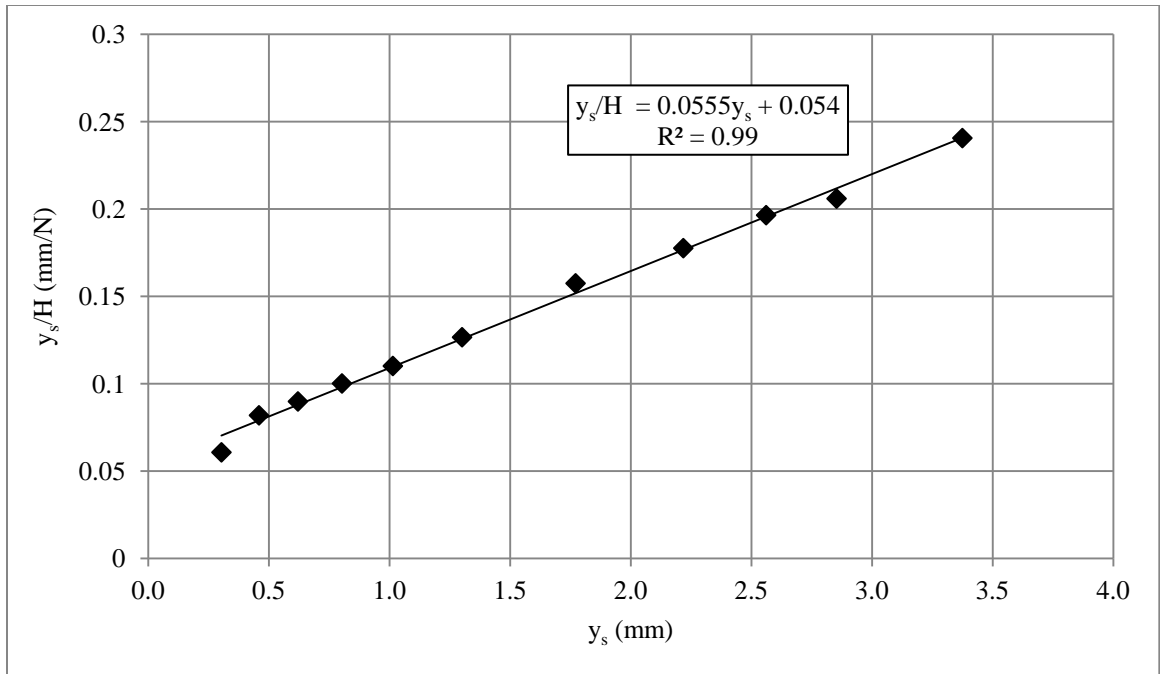


(a) Transformed Plot of Experimental Data

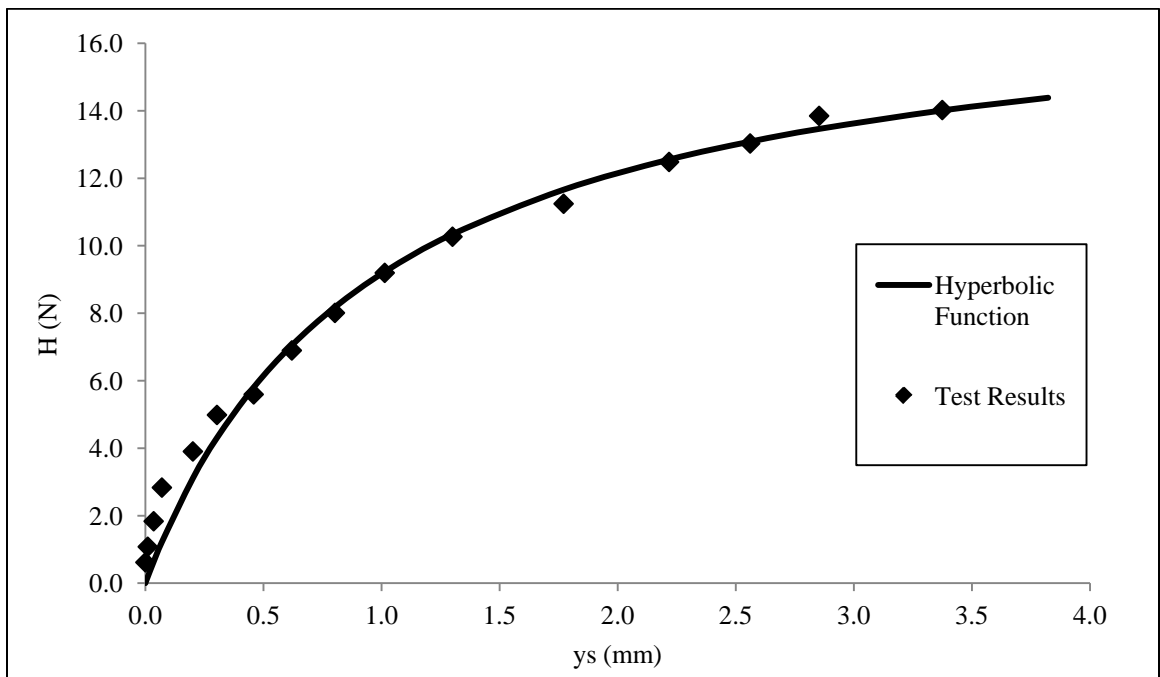


(b) Comparison of Hyperbolic Curve and Test Results

Figure 5-2. Hyperbolic Evaluation of Short Pile in Ground-line Testing

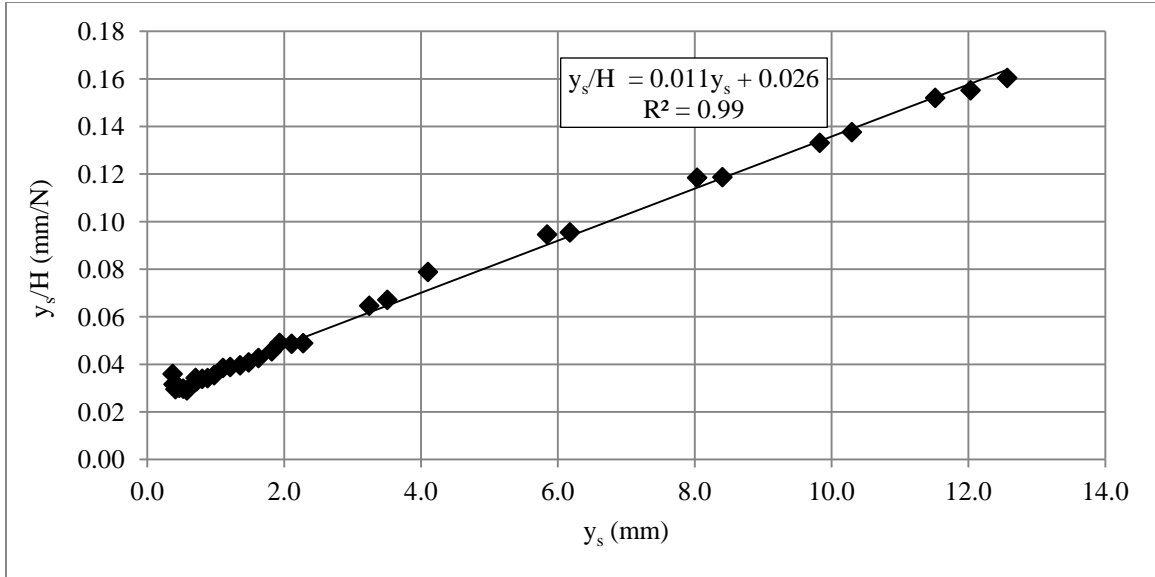


(a) Transformed Plot of Experimental Data

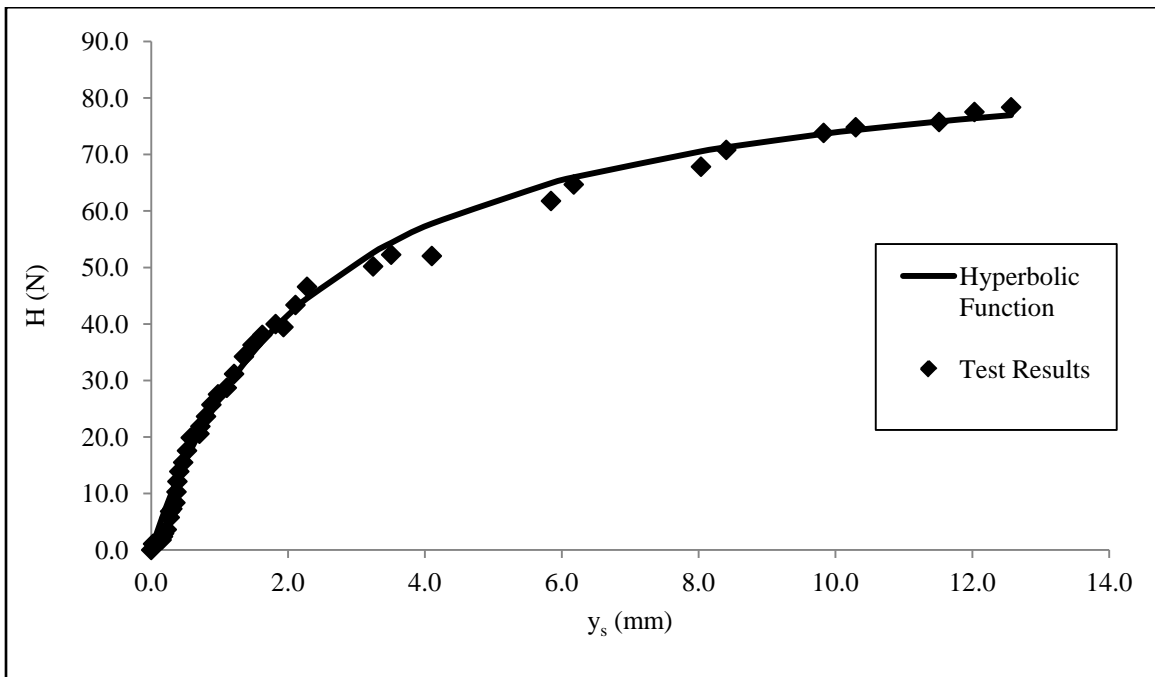


(b) Comparison of Hyperbolic Curve and Test Results

Figure 5-3. Hyperbolic Evaluation of Medium Pile in Ground-line Testing



(a) Transformed Plot of Experimental Data



(b) Comparison of Hyperbolic Curve and Test Results

Figure 5-4. Hyperbolic Evaluation of Long Pile in Ground-line Testing

Values of the hyperbolic capacity and initial stiffness for the static ground-line tests are shown in Table 5-1:

Table 5-1. Hyperbolic Parameters of Static Tests

Ground-Line Tests					
Short Pile		Medium Pile		Long Pile	
K_i (N/mm)	H_h (N)	K_i (N/mm)	H_h (N)	K_i (N/mm)	H_h (N)
14.0	10.4	18.7	18.0	37.2	91.0

Values obtained for the hyperbolic capacity of piles can be compared with values obtained from classic solutions, i.e. Hansen (1961) or Broms (1964). Figure 5-5 presents the ratio of the 4 ultimate capacity solutions, (H_u), over the hyperbolic capacity, H_h , with D/B ratio.

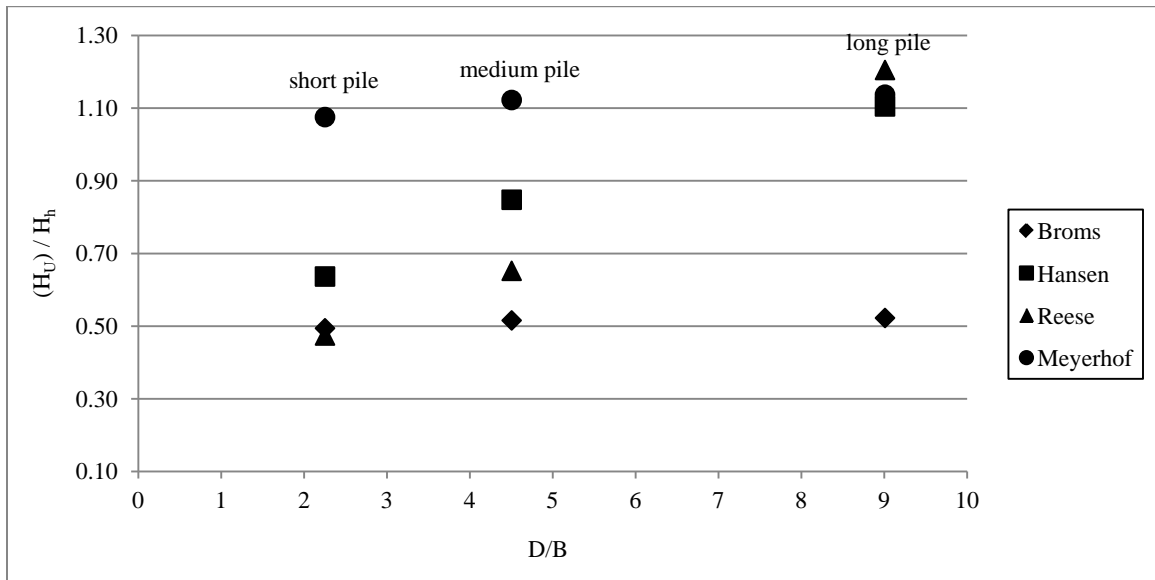


Figure 5-5. Comparison of Hyperbolic Capacity with Other Solutions for Laterally Loaded Piles

As can be seen in Figure 5-5, the hyperbolic capacity obtained from the hyperbolic interpretation of the load - displacement curve for the short pile is higher than the values

calculated from the classic solutions, except for the ultimate capacity from the Meyerhof & Ranjan (1972) method (equation 2.23). Most of the classic solutions consider no lateral pressure at the ground-line, so low values for short model pile were expected. Also, these solutions are using simplifying assumptions, such as, neglecting the shear stresses along the side of the pile and two-dimensional consideration of a three-dimensional problem. It can be seen that the Meyerhof & Ranjan (1972) interpretation is in closer agreement with the hyperbolic capacities, while the Hansen (1961) and Reese et al. (1974) have the same ratio for the large pile, this is not the case for two other piles (equations 2.21, 2.24 and 2.25). As can be observed in Figure 5-6, Reese et al. (1974) and Hansen (1962) do not follow a linear trend with depth and show close agreement at deeper depths. On the other hand, Meyerhof & Ranjan (1972) method and Broms (1964) method (equation 2.22) follow a linear trend with depth and their ratios over the hyperbolic capacity remain almost constant. The reason the Meyerhof & Ranjan (1972) approach gives higher values compared to the other solutions may arise from neglecting the active Coulomb force in the solution. Broms (1964) is the most conservative solution and predicts half of the hyperbolic capacity for all of the model piles. Agaiby et al. (1992) suggested the Hansen (1961) solution be used for estimation of pile lateral capacity.

Agaiby et al. (1992) showed that classic solutions give closer values to the hyperbolic capacity in dense sands compared to loose sands. All of these solutions are based on yield stress mobilization along the length of the pile at the soil-pile interface. The variation of yield stress in Ottawa sand ($D_r = 34\%$) with depth is shown in Figure 5-6 based on the above classic solutions. Figure 5-6 also confirms good agreement between Reese et al.

(1974) and Hansen (1962). Hansen (1962) is preferred over the Reese et al. (1974) solution due to the simplicity of the equation and the low number of input parameters.

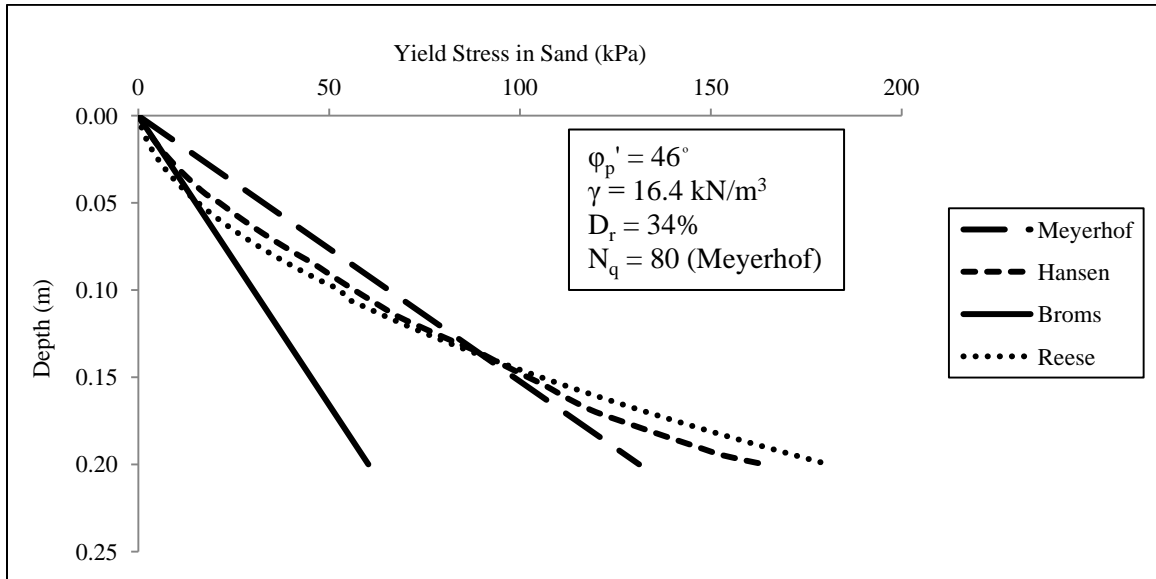


Figure 5-6. Yield Stress in Sand vs. Depth from Classic Solutions

The initial stiffness parameter, K_i , helps define the initial part of the load-displacement response. Equation 5.5 (Agaiby et al., 1992) provides a solution for estimating K_i based on the eccentricity of load, e , geometry of the pile, D/B , and soil modulus at the pile tip, E_s . The sand modulus measured with the oedometer test was found to be equal to $E_s = 1111.1\sigma_v^{0.1923}$ and details of the test were given in Chapter 3.

$$K_i = \frac{E_s D}{\left[I_1 + \left(\frac{e}{D} \right) I_2 \right]} \quad (5.5)$$

Where, I_1 and I_2 are two influence factors given by equations 5.6 and 5.7 as below:

$$I_1 = 3.181 + 9.701 \log \left(\frac{D}{B} \right) \quad (5.6)$$

$$I_2 = 2.409 + 12.71 \log \left(\frac{D}{B} \right) \quad (5.7)$$

Where, B = Pile diameter, D = Pile length and e = load eccentricity. Values of K_i obtained from equation 5.5 are given in Table 5-2.

Table 5-2. Theoretical Initial Stiffness for Model Piles in Ground-line Tests

Ground-line		
Short Pile	Medium Pile	Long Pile
K_i (N/mm)	K_i (N/mm)	K_i (N/mm)
13.9	19.2	29.7

The results presented in Table 5-2 are in general agreement with the experiment results previously presented in Table 5-1, except for the long pile, which has a higher initial stiffness when obtained from the experimental tests.

The effect of the pile length, D , can also be investigated by considering values of H_h obtained for the ground-line static tests. Instead of pile length, D , usually its ratio over the diameter of the pile, B , is considered for the investigation of the effects of the pile geometry on its ultimate capacity. In Figure 5-7, the hyperbolic capacity obtained from the ground-line static tests has been plotted with D/B ratio. This plot shows the increase in the capacity of the pile under lateral loading with the increase in pile length for the ground-line static tests. The same trend is also expected for the moment tests, although because of sizing limitations the long pile was not tested.

In Figure 5-7, a second order polynomial is fitted to the plot of the hyperbolic capacity variations with ratio of the pile length over its diameter, D/B . Although a number of functions can be fitted as effectively through 3 points, a polynomial trend is consistent with the simplified Broms (1964) solution as in equation 5.4. It is noted that some other

studies fitted a linear function (Agaiby et al., 1992). Note that this trend is not necessarily representative of flexible piles.

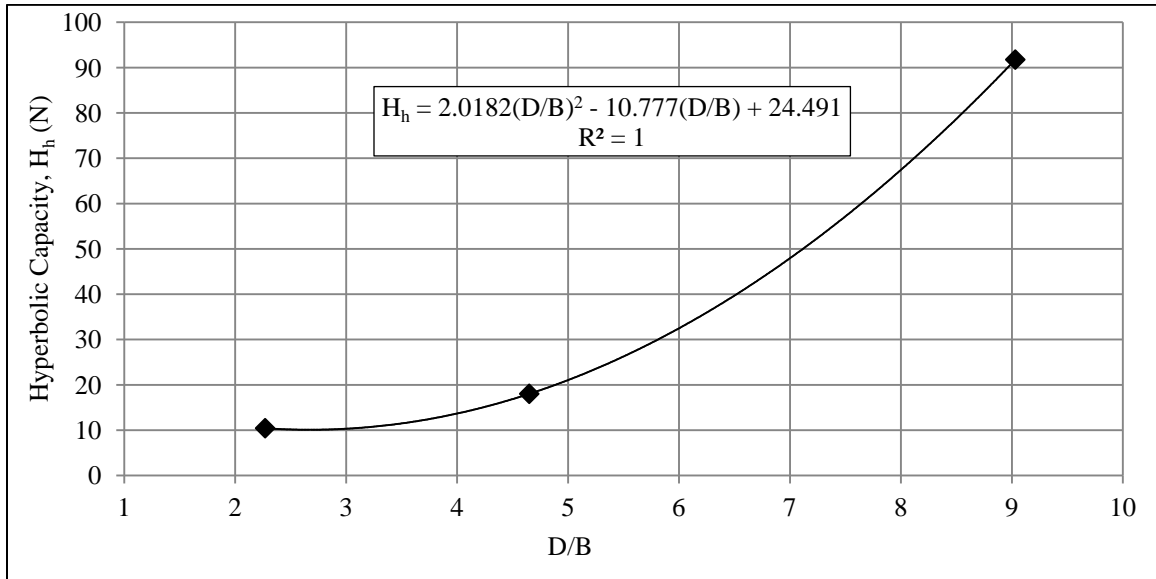


Figure 5-7. Effect of Pile Geometry on Hyperbolic Capacity of Piles in Ground-line Tests

Figure 5-8 illustrates the variations of K_i with D/B in the static ground-line tests.

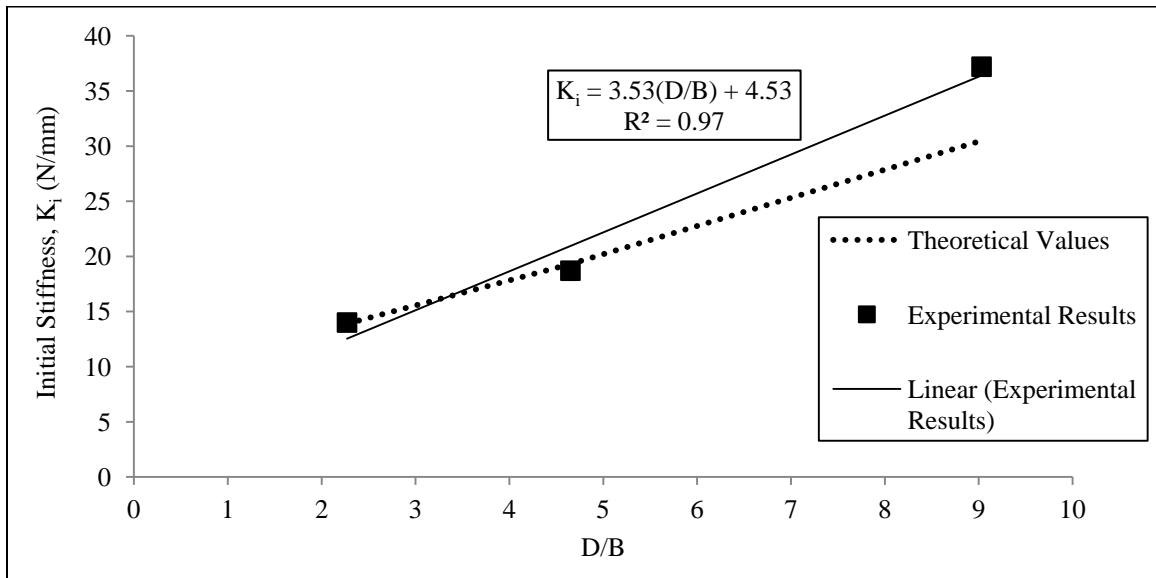
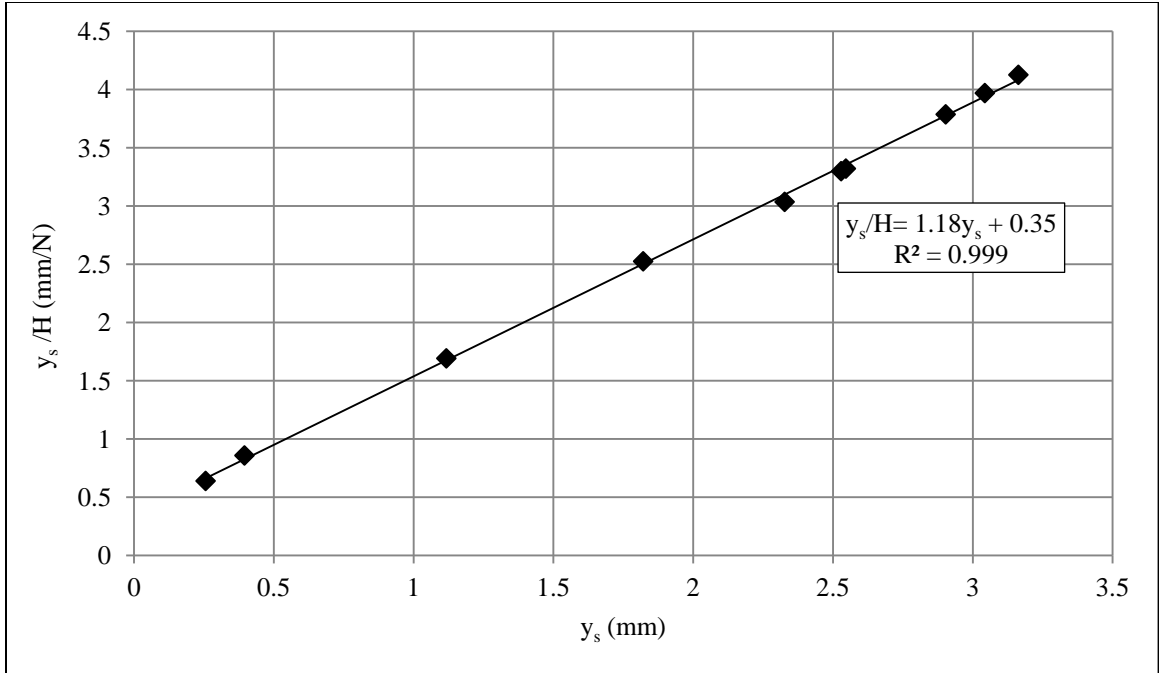


Figure 5-8. Effect of Pile Geometry on Initial Stiffness of Piles in Ground-line Tests

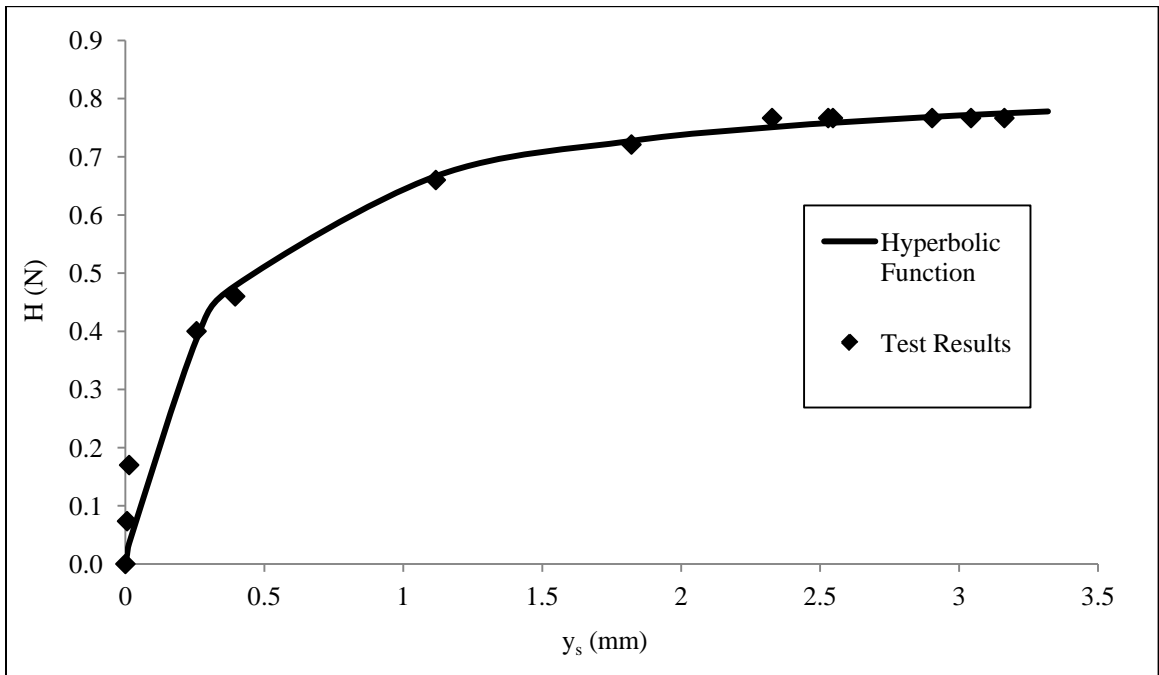
A linear function is fitted to three points in Figure 5-8, which shows the effect of D/B ratio on initial stiffness of the piles. The theoretical line is plotted using equation 5.5 which gives the initial stiffness of the pile under lateral loading. It can be seen that the long pile shows higher initial stiffness in the experiment. There is reasonable correlation between the experimental and theoretical results.

5.2.4 Static Moment Tests

In Figure 5-9 and 5-10, hyperbolic representation of the moment test results is given for the short and medium piles. For these two tests, the theoretical values are also compared with the experimental results. Unfortunately, the geometry of the static test box did not accommodate the large pile for the moment tests. The variations of the hyperbolic capacity and initial stiffness are plotted on the same graph with their theoretical values.

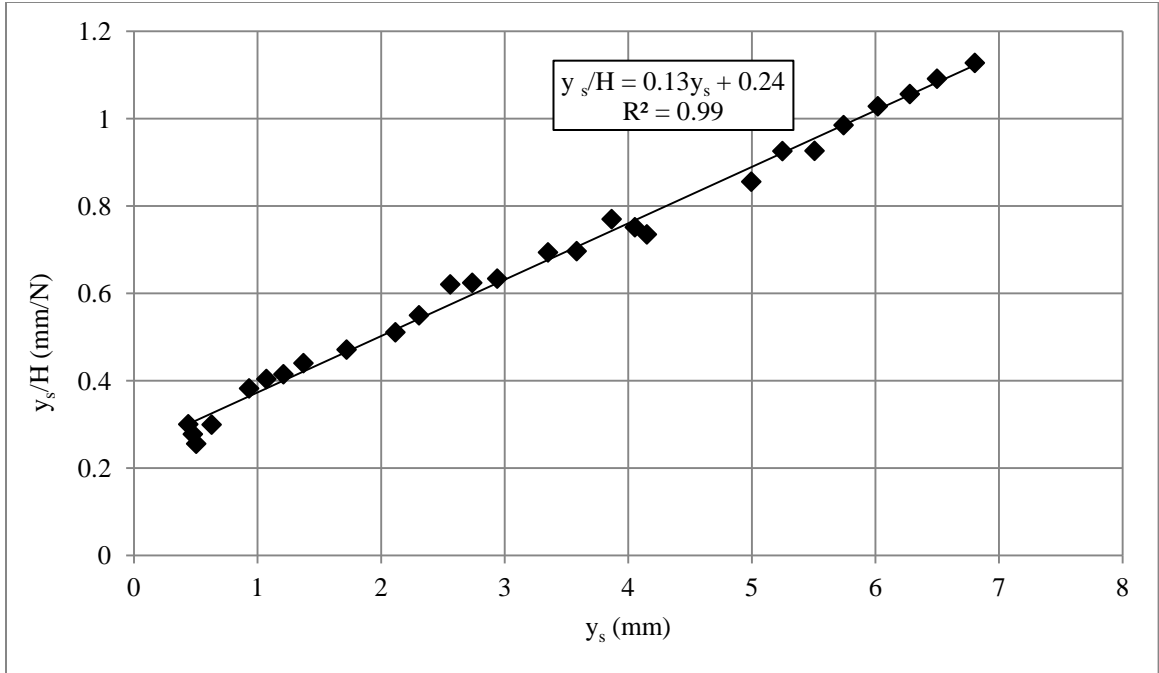


(a) Transformed Plot of Experimental Data

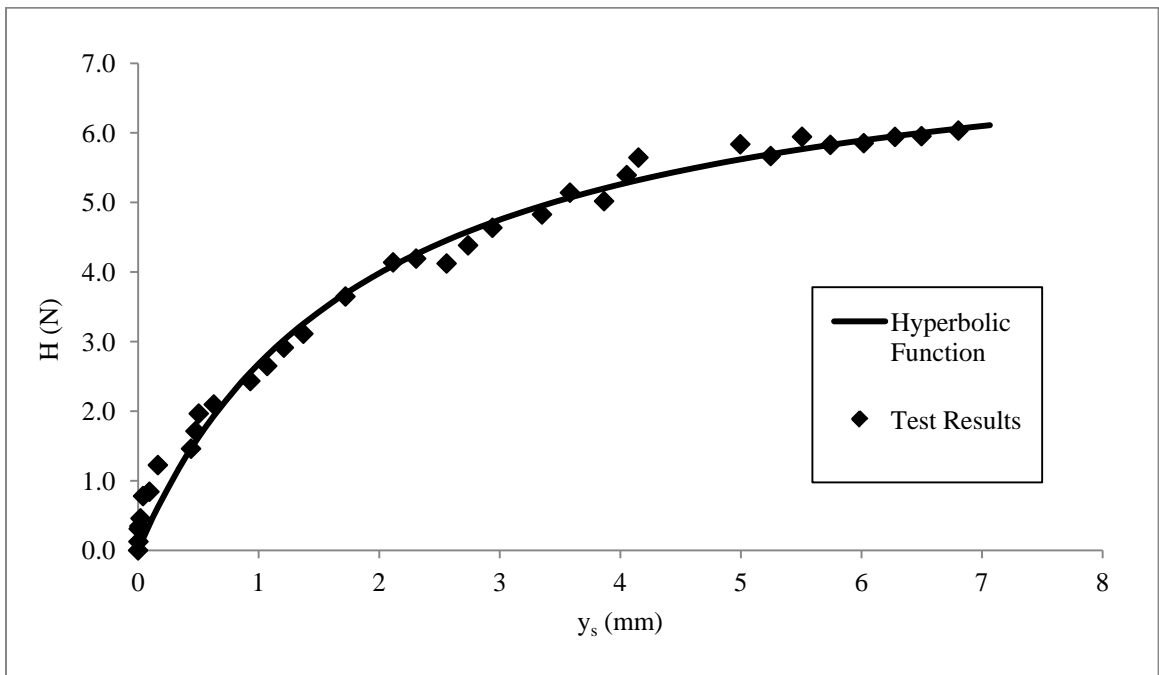


(b) Comparison of Hyperbolic Curve and Test Results

Figure 5-9. Hyperbolic Evaluation of Short Pile in Moment Testing



(a) Transformed Plot of Experimental Data



(b) Comparison of Hyperbolic curve and Test Results

Figure 5-10. Hyperbolic Evaluation of Medium Pile in Moment Testing

Table 5-3 summarizes the hyperbolic parameters for the static moment tests.

Table 5-3. Hyperbolic Parameters for Static Moment Tests

Short Pile		Medium Pile	
K_i (N/mm)	H_h (N)	K_i (N/mm)	H_h (N)
2.8	0.85	4.1	7.7

Reductions in the ultimate capacity of a pile with increase in the load-eccentricity were expected, as discussed earlier in this chapter. This reduction is mainly due to change in the Z_r location. Broms (1964) simplified solution is used in Figure 5-11 to compare theoretical values of the ultimate capacity with the hyperbolic capacity obtained in the moment tests.

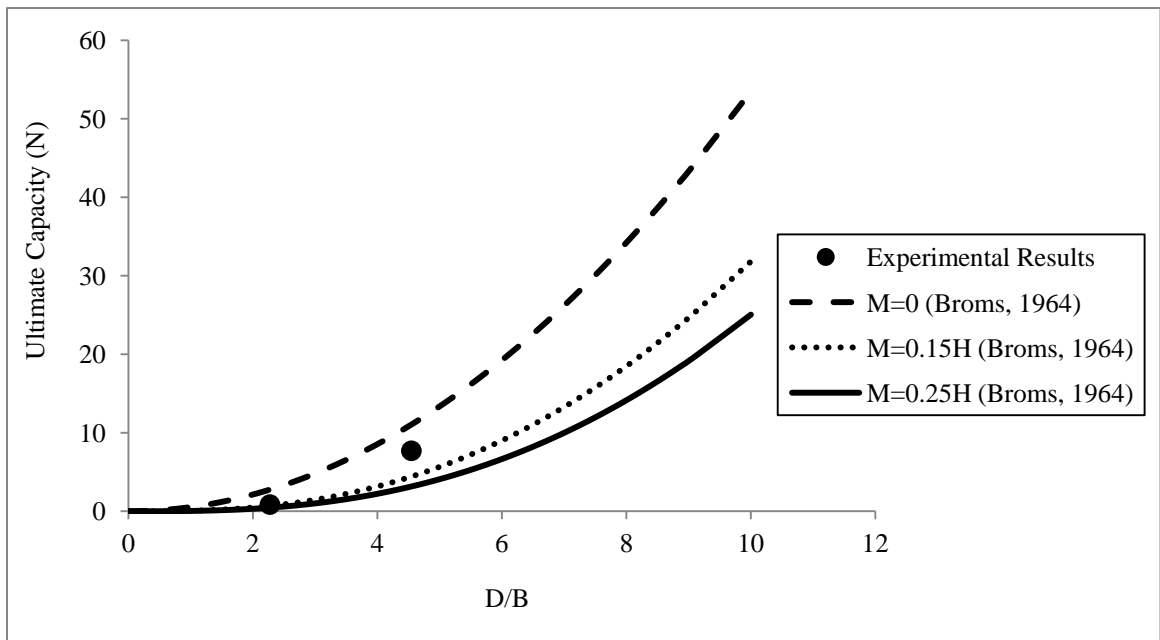


Figure 5-11. Comparison of Hyperbolic Capacity with Broms Simplified Solution (1964) for the Moment Tests

It can be seen that Broms simplified solution as presented in equation 5.4, underestimates the ultimate capacity. The underestimation of the hyperbolic capacity by Broms (1964) is also noticed in the ground-line static tests. The underestimation might be linked to the empirical multiplier in Broms solution (equation 2.22). Kishida & Nakai (1977) suggested that the multiplier was obtained empirically and it can take as high as 8.7 for friction angle of 45° . Moreover, the sizing effects were ignored in this study and it might have certain effects on the results.

The initial stiffness decreases with increase in the load eccentricity. Figure 5-12 illustrates the reduction of initial stiffness, K_i , with eccentricity ratio over the pile length, (e/D). Theoretical values have been calculated from equation 5.5.

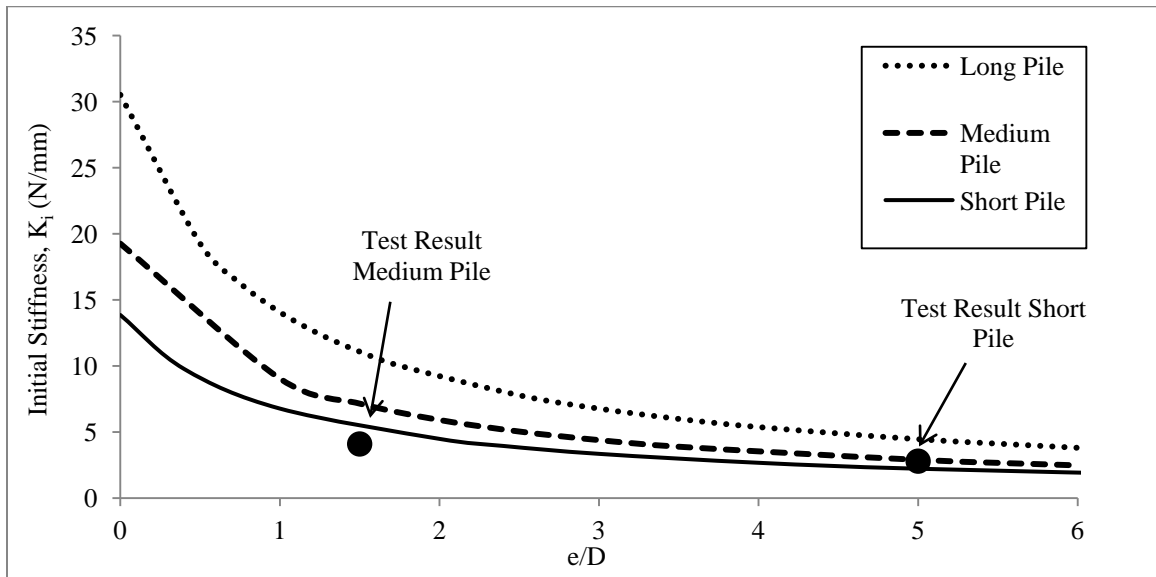


Figure 5-12. Variation of Initial Stiffness with e/D

5.3 Random Variable Amplitude Cyclic Loading

The main goal of this research is to study the lateral behavior of piles under random variable amplitude cyclic lateral loads. The boundary layer wind tunnel laboratory at Western University was used to generate wind as a source of random variable amplitude cyclic load on the small scale models as described earlier in Chapter 3. Wind can be a significant source of environmental load on infrastructure. For some infrastructure, such as wind turbines (either offshore or onshore), wind pressure is the dominant load to be dealt with in the design, since significant wind loads are applied to the structure for almost the entire service life.

Stationary load processes with random variable amplitudes are usually idealized as cyclic loads. This is the common practice in structural engineering due to benefits of simplifying the dynamic analysis. Counting the number of loading cycles in the random time-history was explained in Chapter 2 and 4. Cuellar et al. (2009) used the term “lateral cyclic quasi-static load” for investigation of the wind effects on offshore wind turbines. Even with the quasi-static assumption, the effect of the number of loading cycles is an important issue to be investigated. In some research, the cyclic load has been imposed by centrifugal methods or via a loading actuator, thus, the cyclic loads tend to have constant amplitude and counting loading cycles is trivial.

In this research, the number of “random” variable amplitude loading cycles is obtained by using the rainflow cycle counting methods as explained in Chapter 4 and various approaches have been taken to characterize the nature of the cycles. In geotechnical engineering, the p-y method is the common approach for analysis of laterally loaded

piles. For the case of cyclic loads, the p-y method does not take into the account the direct effects of the number of loading cycles.

5.3.1 Hyperbolic Interpretation of the Cyclic Results

Tests were performed in the BLWTL at Western University for the short and medium model piles. The long pile did not reach “visual” failure as explained in Chapter 3. Tests were performed in 30-second, 60-second, and 90-second loading intervals for the medium pile and 30-second and 60-second loading intervals for the short pile. Figure 5-13 shows the incremental wind speed increases for tests on the medium pile. Similar wind speed increases were executed for the short pile up to “failure”.

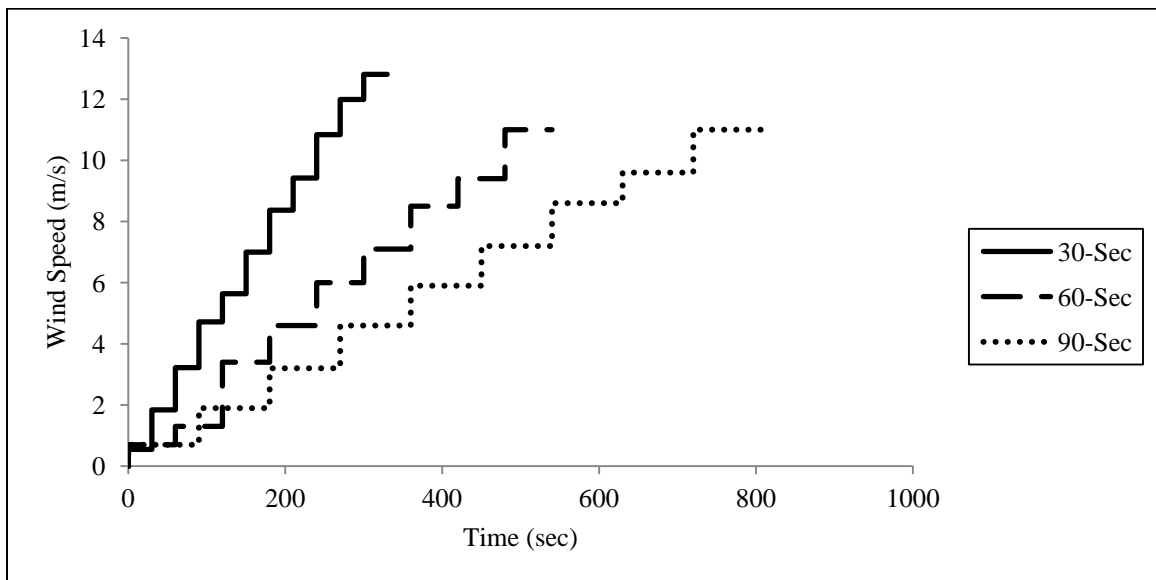


Figure 5-13. Wind Speed Increments for Tests on Medium Pile

The data acquisition system of the wind tunnel records data at high frequency. For most of the tests, the frequency of data recording, F_s , was chosen to be 300 Hz. These data points have been treated in accordance with procedure described earlier in Chapter 3 to give traceable data points (average values per wind speed increment).

Summarized information from the wind tunnel testing is presented in tables, such as Table 5-4, which presents results obtained from test PRT-MM60-4. The results of all other tests are presented in Appendix C. The first column of Table 5-4 represents the mean wind speed at each increment (step) and is used here as a reference wind speed. This table also gives the mean values of the laser displacement transducers, pitots, hotwire anemometer, accelerometer and strain gauge. These values will be used to calculate the drag forces, rotation, and displacement of the model pile according to the procedures explained in Chapter 3.

Table 5-4. Results of Wind Tunnel Test PRT-MM60-4

Mean Wind Speed (m/s)	Laser 22cm (cm)	Laser 31cm (cm)	Laser 26cm (cm)	Pitot 33cm (m/s)	Pitot 25cm (m/s)	Hotwire (m/s)	Accelerometer (% of g)	Strain Gauge (%)
0.7	2.55	2.57	2.57	1.24	0.74	0.52	0.0%	0.00E+00
1.3	2.55	2.57	2.57	1.99	1.27	1.14	2.9%	6.37E-04
3.4	2.53	2.54	2.54	3.82	3.37	2.39	10.3%	3.00E-03
4.6	2.48	2.48	2.48	5.16	4.62	3.15	14.8%	5.36E-03
6.1	2.39	2.36	2.37	6.61	6.06	4.05	17.1%	9.09E-03
7.1	2.26	2.19	2.22	7.79	7.11	4.72	18.7%	1.38E-02
8.5	2.09	1.95	2.01	9.20	8.48	5.54	18.5%	1.96E-02
9.4	1.78	1.55	1.64	10.14	9.39	6.08	18.2%	2.41E-02
10.9	1.26	0.83	1.01	11.88	10.87	6.94	16.9%	3.33E-02
11.1	0.69	0.28	0.33	12.08	11.10	7.10	15.8%	3.54E-02

In practice, many building codes are based on a “quasi-static” assumption for calculation of the forces from the wind pressure exerted on structures. The background portion of the response is “quasi-static”, while the resonant portion is related to the dynamic characteristics of the structure. For structures with a natural frequency high enough to

avoid resonance the quasi-static portion of the response is the most important and dominant part. Using the quasi-static assumption, the force acting on any structure can be calculated from the drag equation 5.8 (ibid equation 2.6):

$$F_D = 0.5 \rho_a C_D A_F U^2(t) \quad (5.8)$$

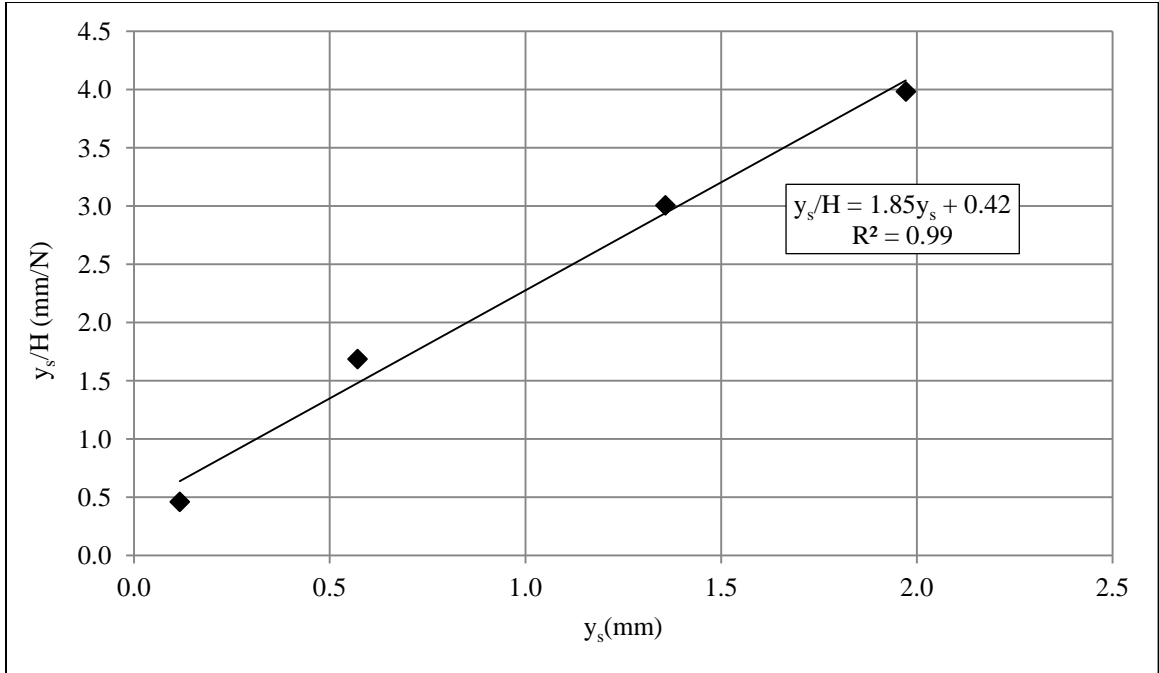
Where, $U(t)$ is the instantaneous wind speed, which can be broken into two components. Since acquiring instantaneous wind speed is cumbersome and not practical, the drag force is calculated separately for the mean wind speed and fluctuating part. Drag force, F_D , based on mean wind speed for a constant wind speed period is used throughout this thesis. Values of wind speed were obtained from the pitot that was level with the centroid of the plate (Pitot 25cm in Table 5-4). The horizontal load, H , applied to the pile is assumed to be equal to the drag force, F_D . The moment on the pile can be obtained by considering the centroid of the plate as the resultant point of action of the horizontal force. Table 5-5 presents horizontal load, H , applied bending moment, M , rotation angle of the pile, θ and ground-line displacement, y_s for each reference wind speed in the wind tunnel test PRT-MM60-4.

Table 5-5. Horizontal Force and Applied Bending Moment in Test PRT-MM60-4

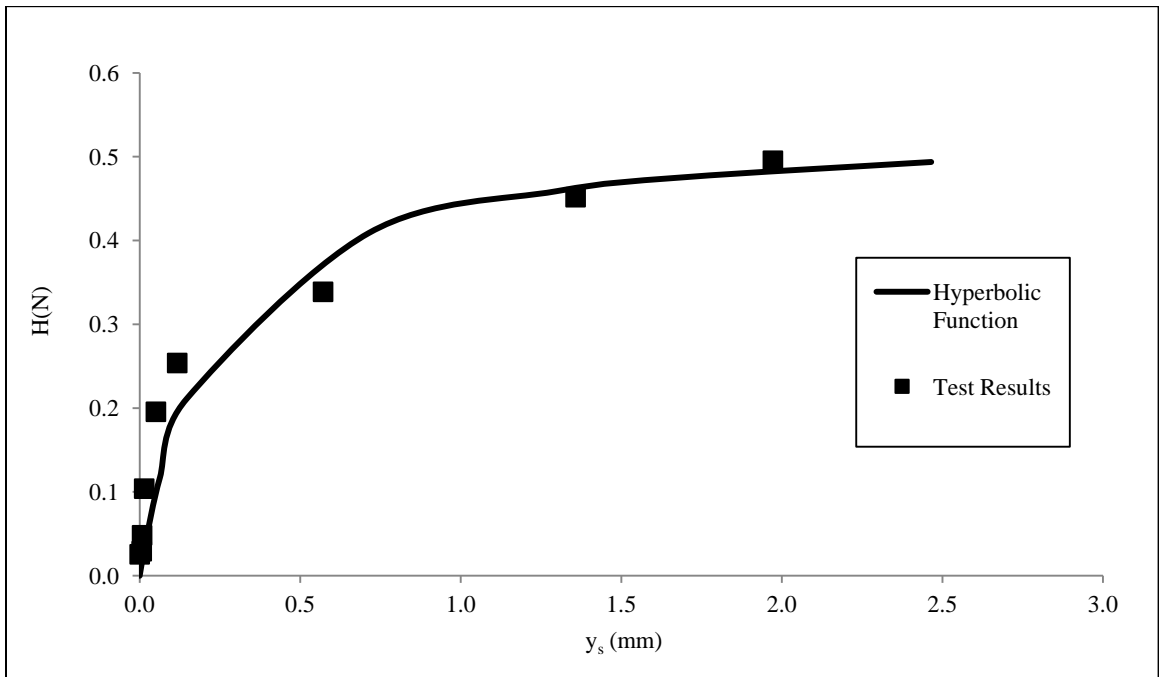
Voltage (V)	Wind Speed (m/s)	Applied Moment (N.m)	Horizontal Force (N)	θ (Degree)	y_s (mm)
0.5	0.74	0.00	0.01	0.00	0.00
1	1.27	0.02	0.03	0.00	0.00
1.5	3.37	0.05	0.23	0.02	0.03
2	4.62	0.11	0.43	0.09	0.13
2.5	6.06	0.16	0.75	0.23	0.32
3	7.11	0.24	1.03	0.44	0.61
3.5	8.48	0.33	1.46	0.74	1.03
4	9.39	0.43	1.79	1.29	1.80
4.5	10.9	0.6	2.40	2.27	3.18
4.5	11.10	0.63	2.50	3.40	4.76

Again, the results of all other tests are also presented in Appendix C.

Figure 5-14 and 5-15 depict hyperbolic representations of the short pile tests with 30-second and 60-second loading intervals. The results of the wind tunnel tests on the short pile are also compared with static test results.

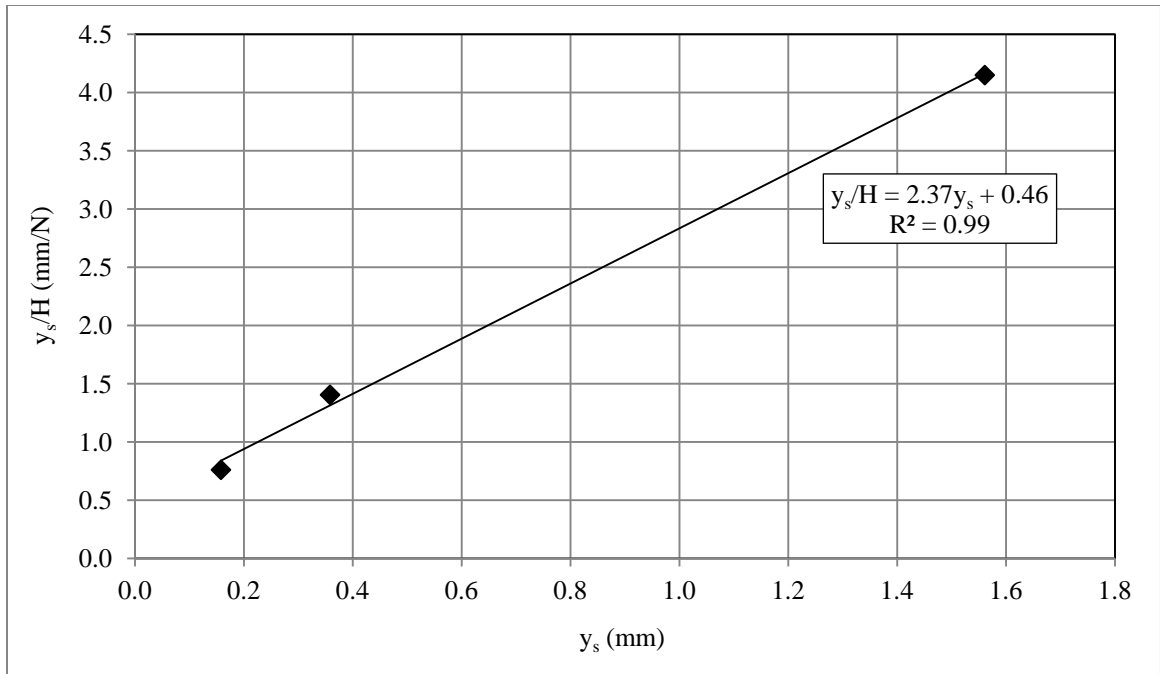


(a) Transformed Plot of Experimental Data

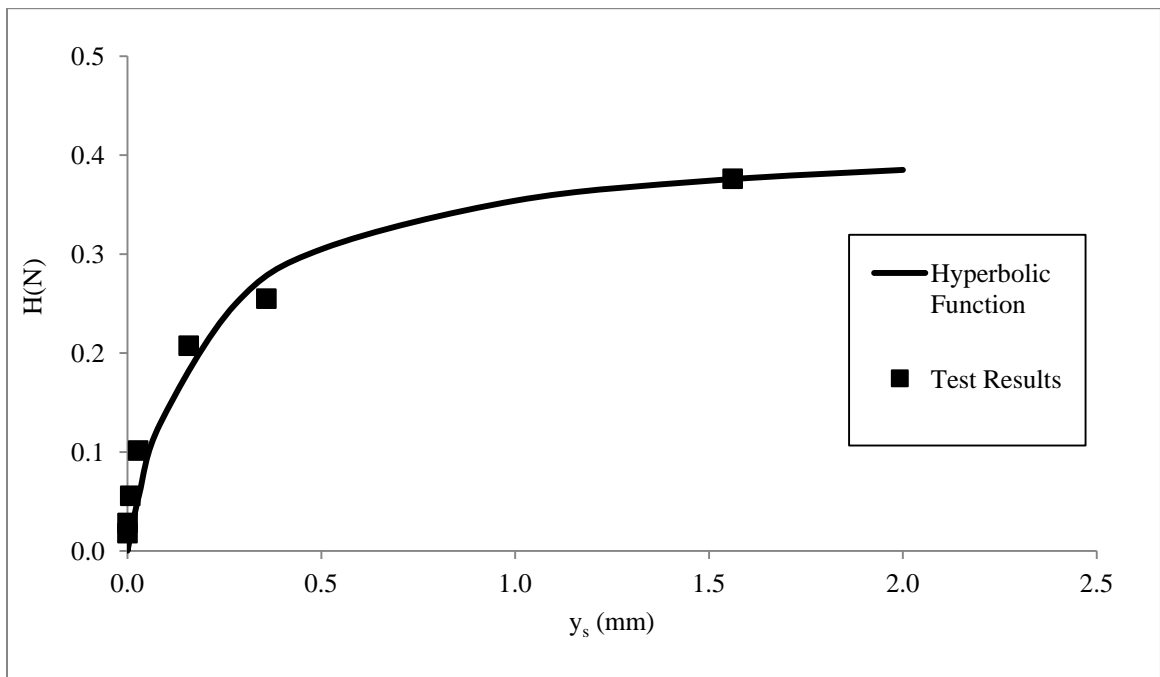


(b) Hyperbolic Curve and Test Results

Figure 5-14. Hyperbolic Evaluation of Wind Tunnel test PRT-SM30-1



(a) Transformed Plot of Experimental Data



(b) Hyperbolic Curve and Test Results

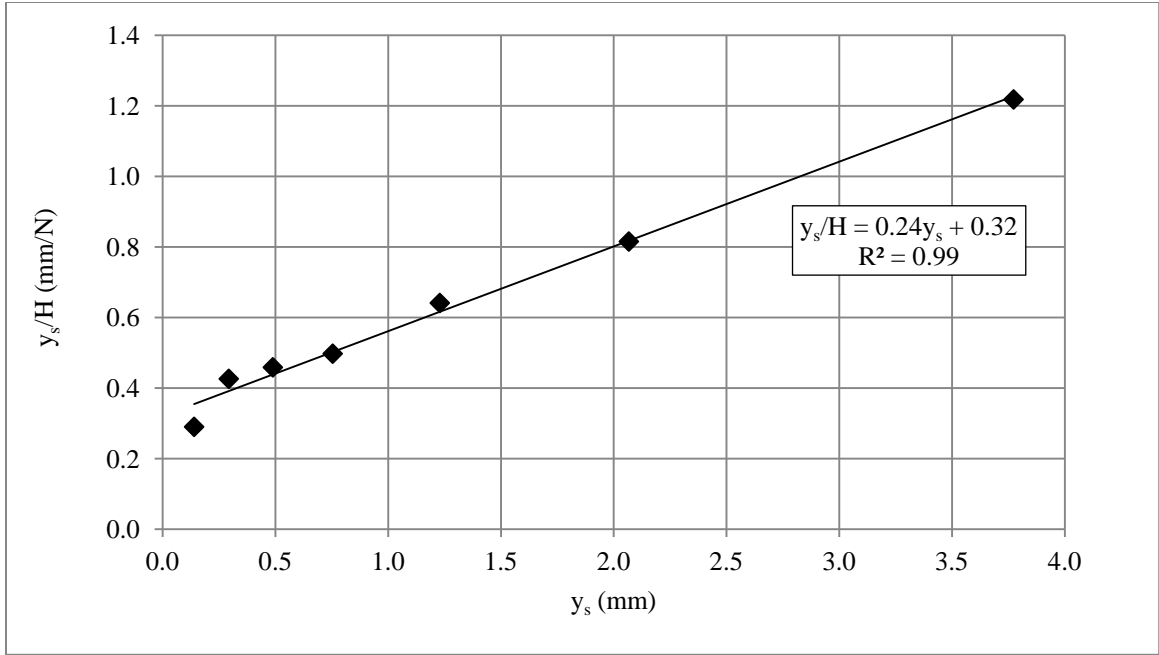
Figure 5-15. Hyperbolic Evaluation of Wind Tunnel Test PRT-SM60-1

Table 5-6 summarizes the hyperbolic parameters obtained from the tests on the short pile in the wind tunnel, as well as the static tests for comparison. Table 5-6 shows that initial stiffness, K_i , decreases for the short pile for the wind load tests, compared to the value from the static test. Also this reduction continues to occur for increasing total numbers of load cycles. Moreover, with an increase in the total number of load cycles and the range of loading cycles (determined from rainflow counting), the hyperbolic capacity of the short pile, H_h , also decreases. Table 5-6 also tabulates the ratio of initial stiffness obtained in the wind tunnel, K_{iw} , to the static initial stiffness K_{is} , and the ratio of hyperbolic capacity in the wind tunnel, H_{hw} , to the static hyperbolic capacity, H_{hs} .

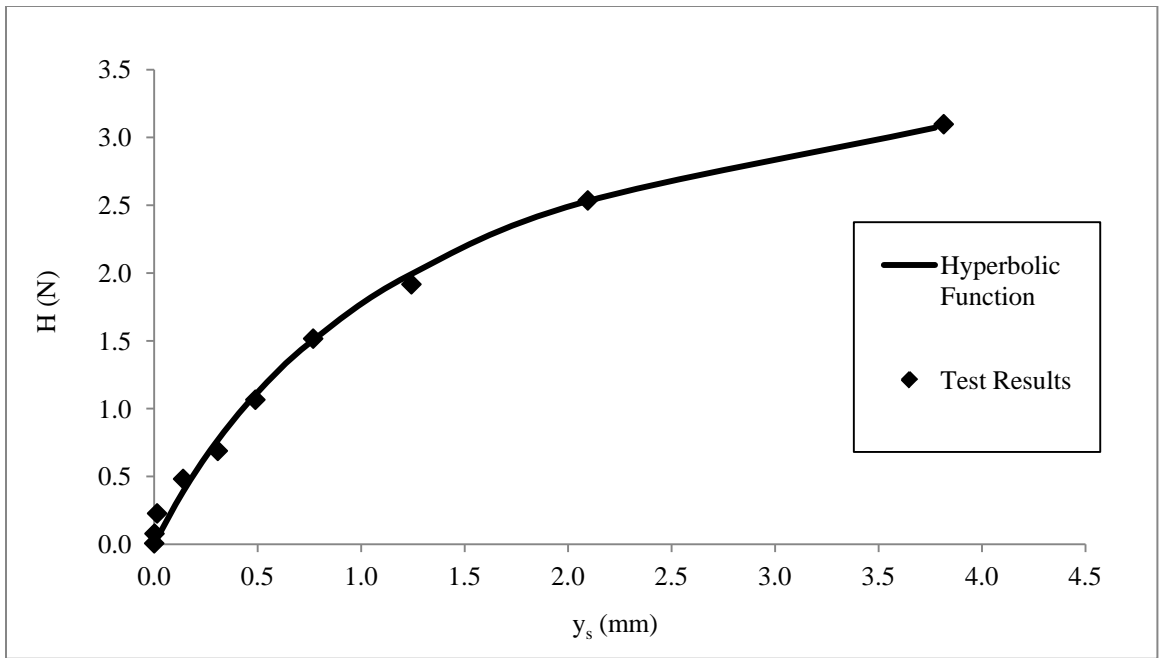
Table 5-6. Summary of Wind Tunnel Test on Short Piles and Comparison with Static Tests

Test	Total Number of Cycles (N_{Total})	H_h (N)	K_i (N/mm)	K_{iw} / K_{is}	H_{hw}/H_{hs}
Static	-	0.85	2.85	-	-
PRT-SM30-1	30	0.54	2.37	0.83	0.6
PRT-SM60-1	51	0.42	2.19	0.77	0.5

Figures 5-16 to 5-18 present the results of the wind tunnel tests on the medium pile.

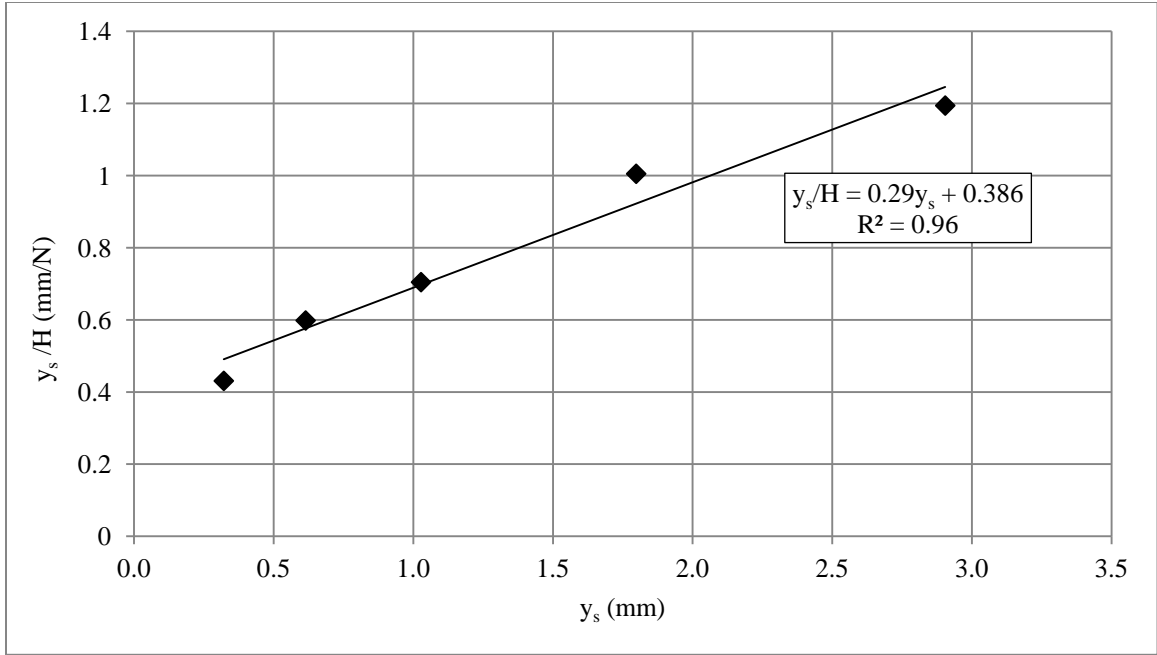


(a) Transformed Plot of Experimental Data

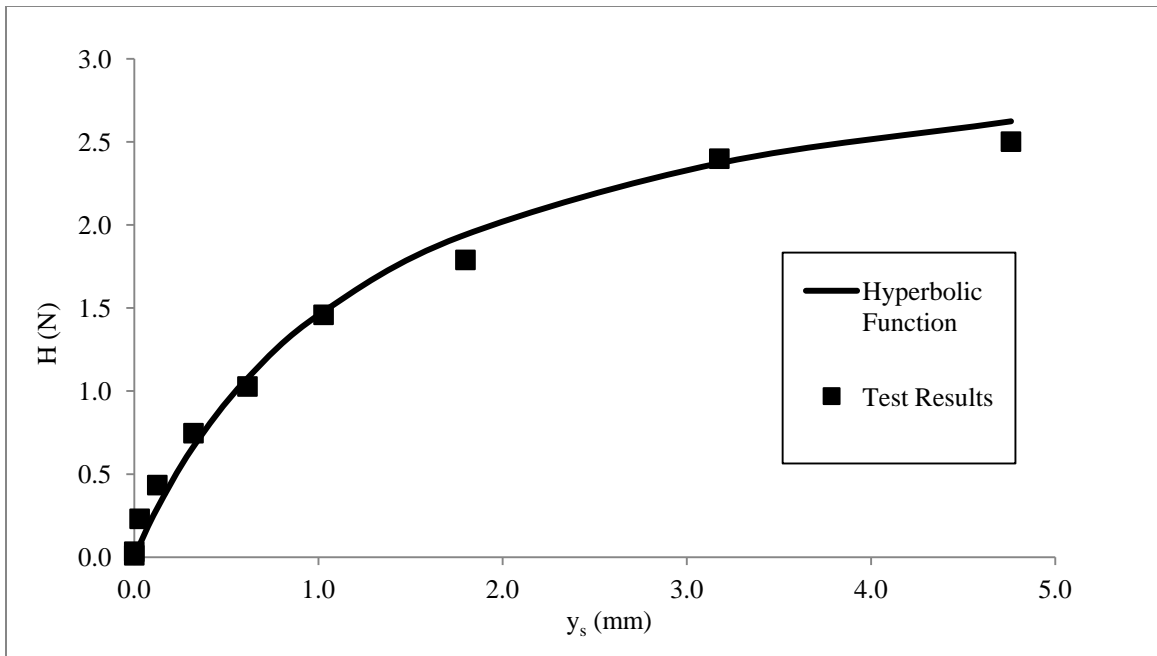


(b) Hyperbolic Curve and Test Results

Figure 5-16. Hyperbolic Evaluation of Wind Tunnel Test PRT-MM30-2

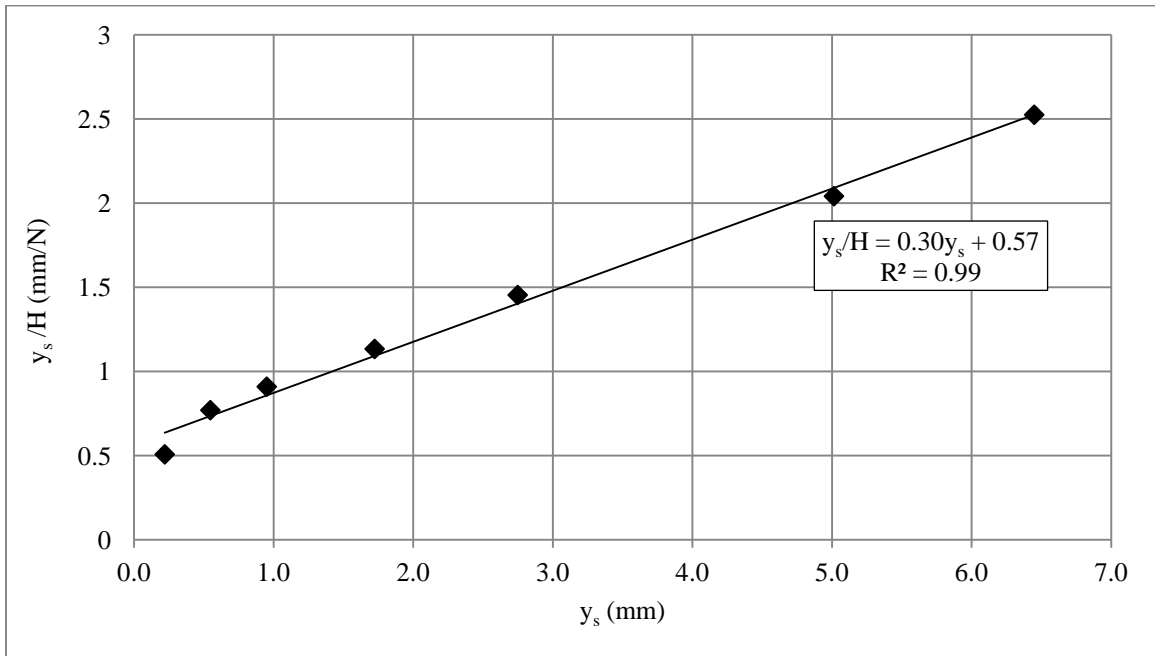


(a) Transformed Plot of Experimental Results

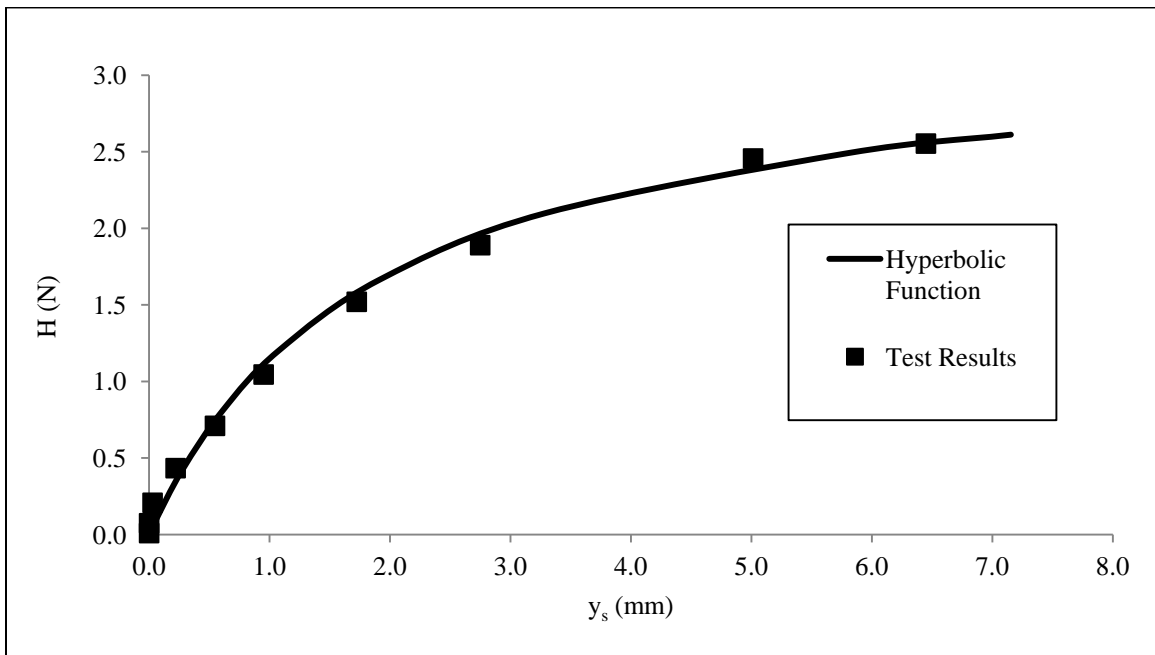


(b) Hyperbolic Curve and Test Results

Figure 5-17. Hyperbolic Evaluation of Wind Tunnel Test PRT-MM60-4



(a) Transformed Plot of Experimental Results



(b) Hyperbolic Curve and Test Results

Figure 5-18. Hyperbolic Evaluation of Wind Tunnel Test PRT-MM90-1

Again the hyperbolic capacity, H_h and the initial stiffness, K_i can be obtained from Figures 5-16 through 5-18. Table 5-7 gives the summary of the hyperbolic parameters for the tests on the medium pile. The static test result is also presented and can be used to estimate the reductions in the hyperbolic parameters.

Table 5-7. Comparison of Initial Stiffness and Hyperbolic Capacity in Wind Tunnel Testing on Medium Pile

Test	Total Number of Cycles (N_{Total})	K_i (N/mm)	H_h (N)	K_{iw} / K_{is}	H_{hw} / H_{hs}
static	-	4.1	7.7	-	-
PRT-MM30-2	91	3.06	4.18	0.75	0.55
PRT-MM60-4	156	2.59	3.42	0.61	0.44
PRT-MM90-1	261	1.76	3.30	0.43	0.43

As shown in Table 5-7, with increasing total numbers of loading cycles, H_h decreases. The initial stiffness also decreases.

The reduction in the hyperbolic capacity is observed in tests on the medium pile, in a similar fashion for the short pile and the rate of decrease in the hyperbolic capacity with greater total number of loading cycles is fairly consistent. On the other hand, the initial stiffness, K_i , does not follow the same trend observed for the short pile and reduces slightly in the tests on the medium pile.

By assigning the static test a nominal single cycle of load, the variation of K_i and H_h can be plotted for the short pile. Figures 5-19 and 5-20 tabulate variations of K_i and H_h , respectively.

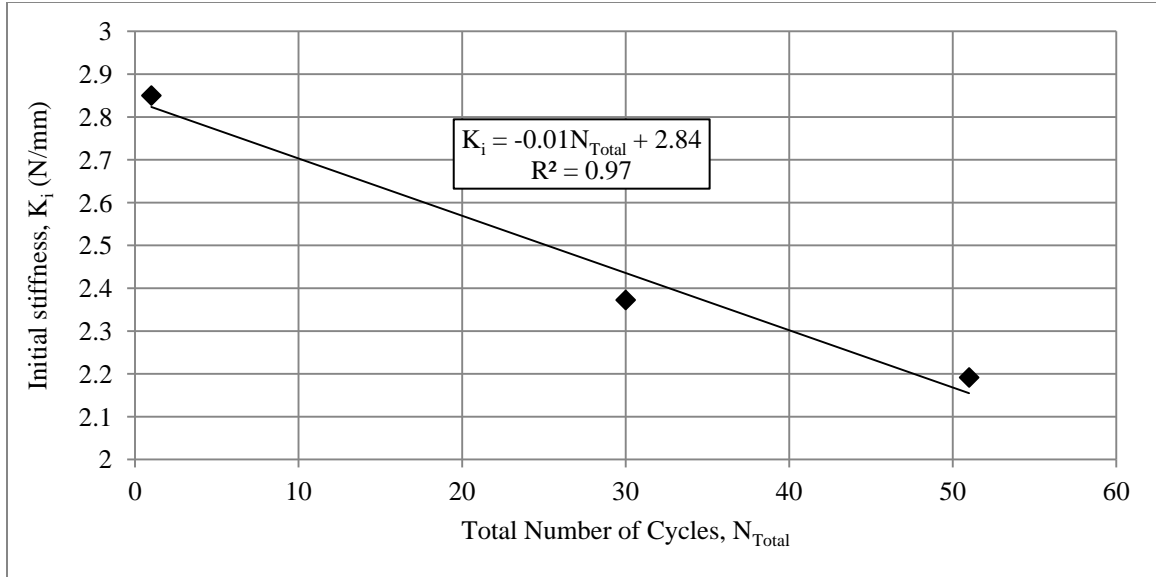


Figure 5-19. Variation of Initial Stiffness with Total Number of load Cycles for the Short Pile

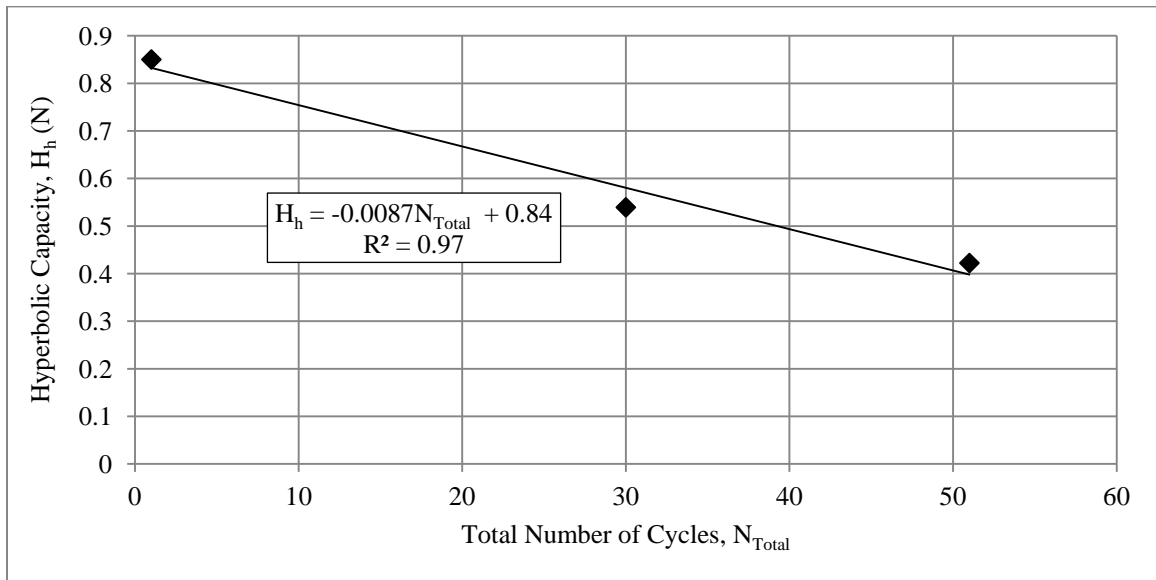


Figure 5-20. Variation of Hyperbolic Capacity with Total Number of Load Cycles for the Short Pile

Figure 5-21 and 5-22 shows the variation in K_i and H_h with the total number of loading cycles for the medium pile, respectively.

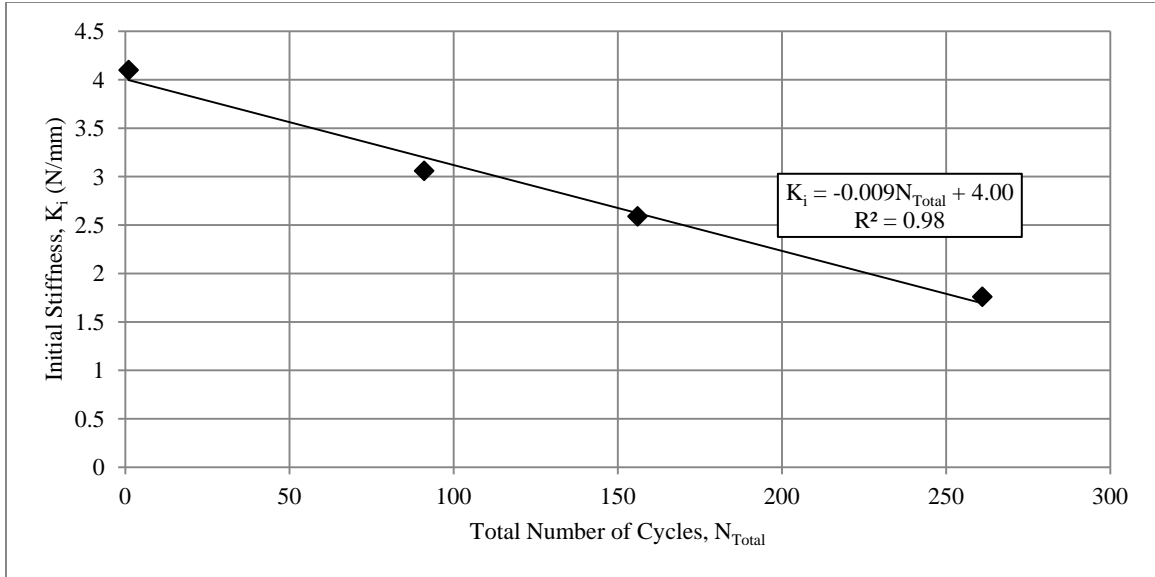


Figure 5-21. Variation of Initial Stiffness with Total Number of Load Cycles for Medium Pile

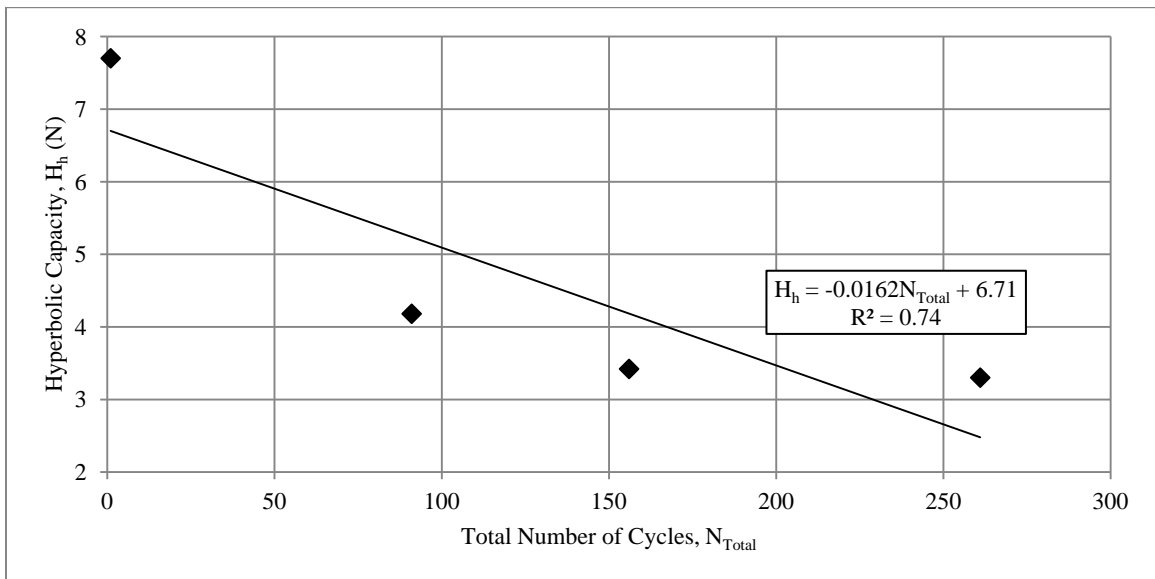


Figure 5-22. Variation of Hyperbolic Capacity with Total Number of Load Cycles for Medium Pile

It should be noted that the suggested trend in Figures 5-19 to 5-22 is relatively crude, since N_{Total} includes a number of variable amplitude cycles with different mean loads, so

there is a loss of information in the rainflow counting process and the results should be treated with some caution.

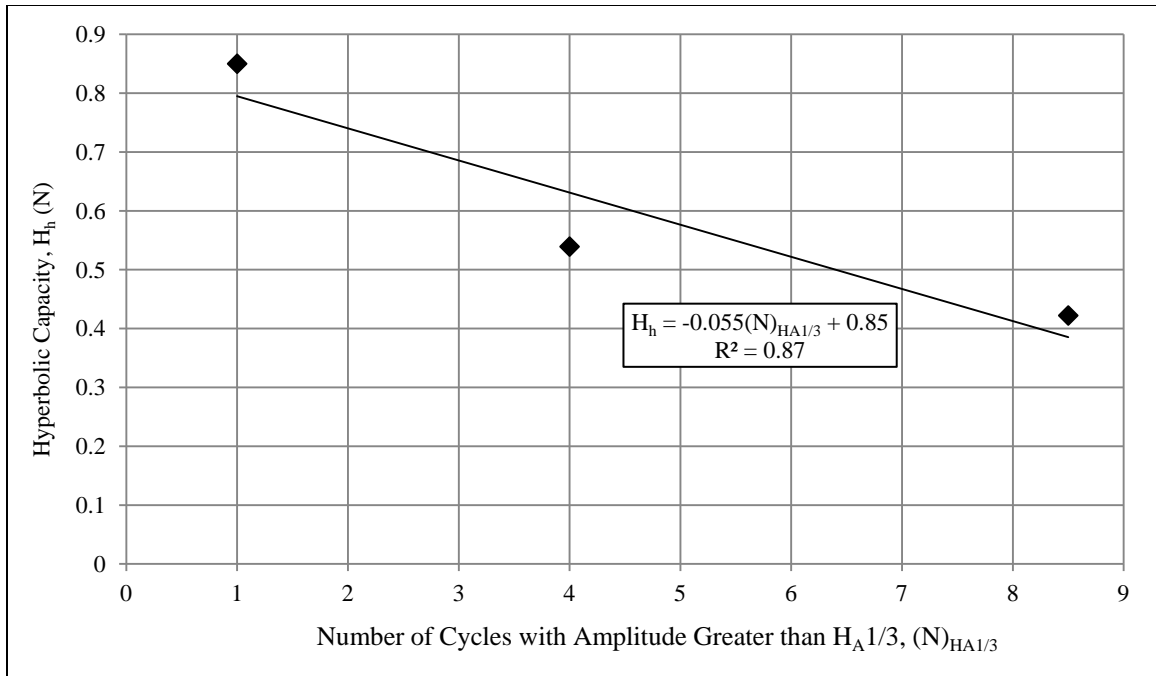
The largest 1/3 of the cycles ($H_A1/3$), and largest 1/10 of the cycles ($H_A1/10$), were introduced in Chapter 4. It is of interest to consider the effects of the largest of the rainflow counting (RFC) number of cycles with greater amplitudes than $H_A1/3$ and $H_A1/10$ on the hyperbolic capacity. Table 5-8 shows the number of RFC cycles with greater amplitudes than $H_A1/3$ and $H_A1/10$, for all wind tunnel tests.

Table 5-8. Number of Cycles with Amplitude Greater than $H_A1/3$ & $H_A1/10$

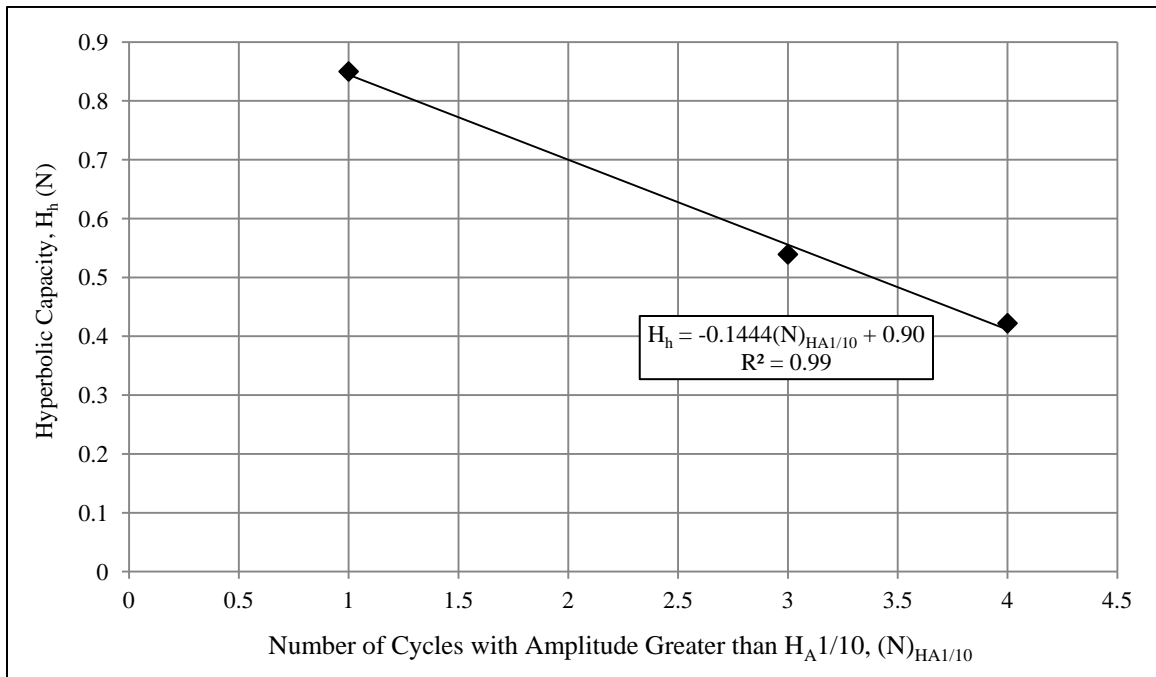
Test	$(N)_{H_A1/3}$	$(N)_{H_A1/10}$
PRT-SM30-1	4	3
PRT-SM60-1	9	4
PRT-MM30-2	22	8.5
PRT-MM60-4	41	10
PRT-MM90-1	57	24

Figure 5-23(a) & (b) shows the variations of hyperbolic capacity for short piles with respect to $(N)_{H_A1/3}$ and $(N)_{H_A1/10}$, respectively. Comparing Figure 5-20 with Figure 5-23 (a) and (b) it can be concluded that $(N)_{H_A1/10}$ gives better fit quality.

Similar consideration for the medium pile was given using the parameter to improve the fitting quality. Since, the S-N curve relation is not available for laterally loaded piles under different mean load values, we can consider different interpretations. Figure 5-24 (a) and (b) shows the variations of hyperbolic capacity for the medium pile with respect to $(N)_{H_A1/3}$ and $(N)_{H_A1/10}$.

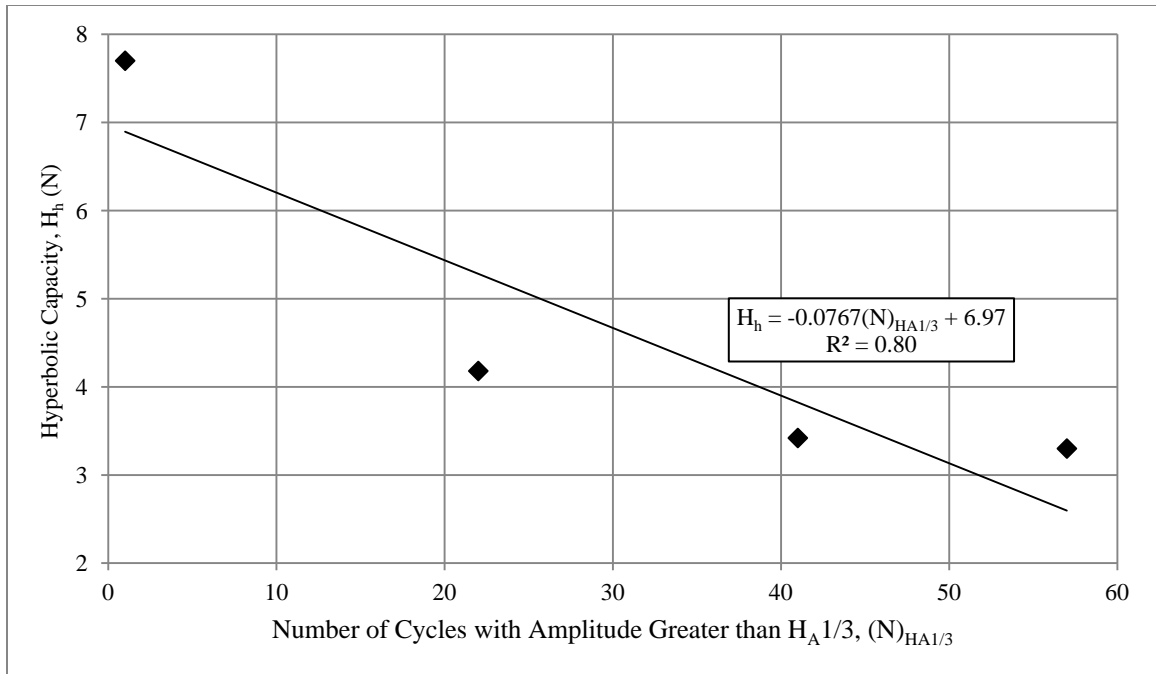


(a) Variations of Hyperbolic capacity vs. $(N)_{H_A 1/3}$ for Short Pile

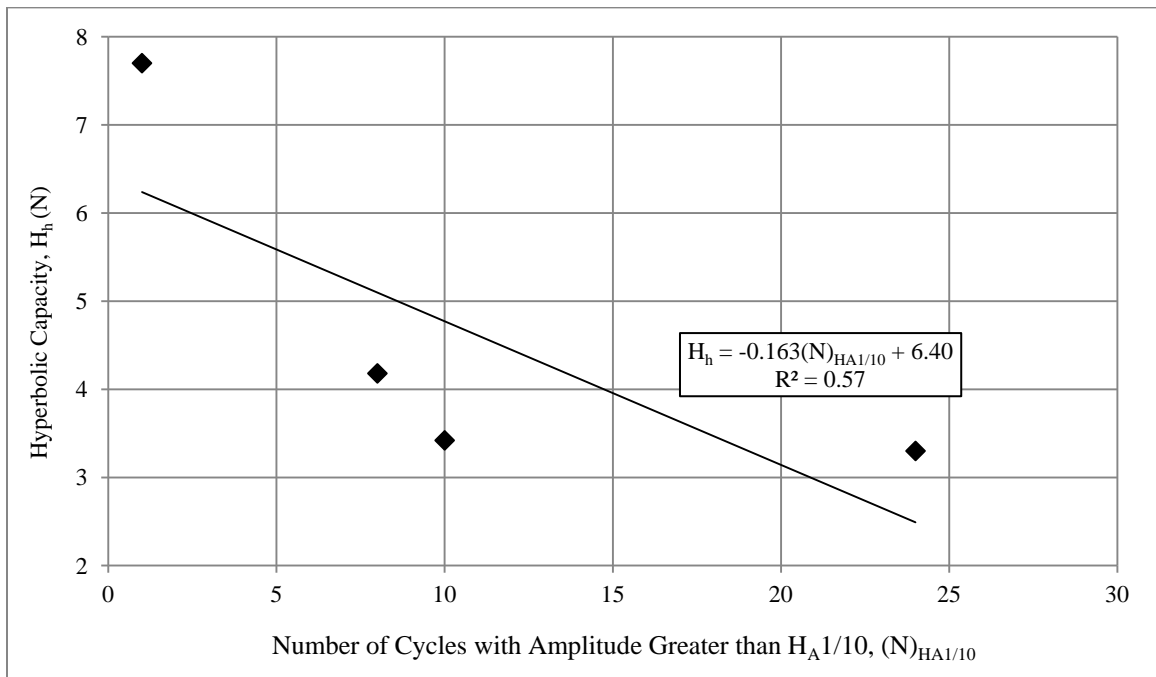


(b) Variations of Hyperbolic capacity vs. $(N)_{H_A 1/10}$ for Short Pile

Figure 5-23. Variations of Hyperbolic Capacity with Respect to Different Interpretation for Number of Cycles



(a) Variations of Hyperbolic Capacity vs. $(N)_{HA1/3}$ for Medium Pile



(b) Variations of Hyperbolic Capacity vs. $(N)_{HA1/10}$ for Medium Pile

Figure 5-24. Variations of Hyperbolic Capacity with Respect to Different Interpretation for Number of Cycles

The hyperbolic capacity obtained for both sizes of pile in the wind tunnel tests have also been normalized as can be seen in Figure 5-25, using a load factor, L_f in equation 5.9.

$$L_f = \frac{e/D}{\gamma D^3} \quad (5.9)$$

Where, D is pile diameter, e is load eccentricity and γ is soil unit weight.

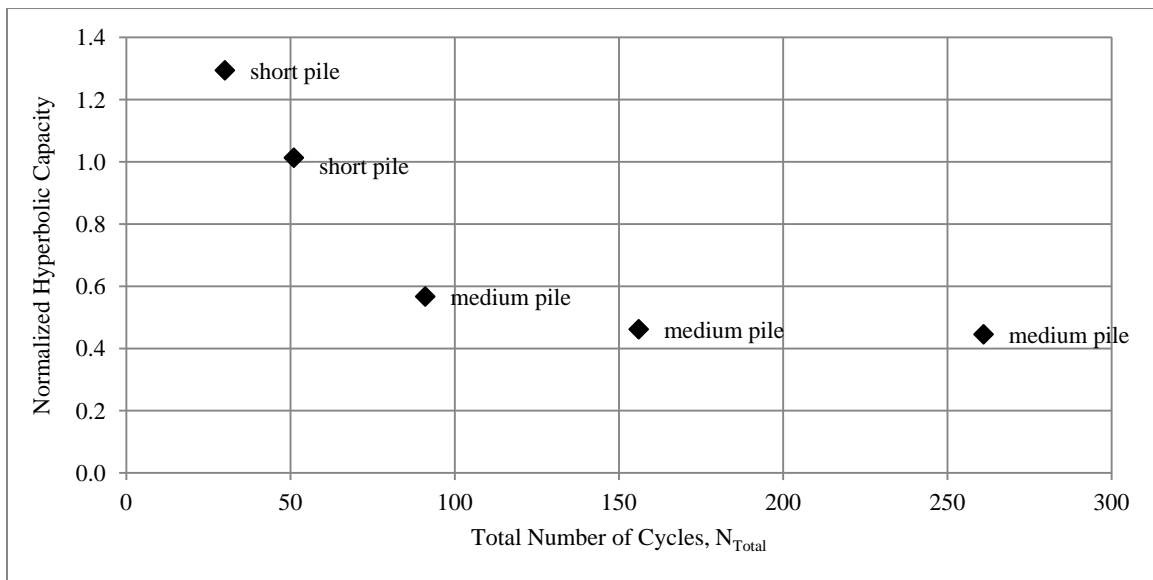


Figure 5-25. Normalized Hyperbolic Capacity for Wind Tunnel Tests

The trends in Tables 5-6 and 5-7 are in general agreement with previous studies that consider lower ultimate capacity and greater displacement under the effects of cyclic loading (e.g. Little & Briaud, 1988; Long & Vanneste, 1994). Note that these projects were essentially performed under constant amplitude cyclic loads due to scarcity of a database on tests under variable amplitude cyclic loads. It can be seen that variable amplitude cycles also significantly reduce the capacity and stiffness.

Agaiby et al. (1992) commented on the rate of displacement accumulation as a function of maximum load level and cyclic load ratio. They suggested that for equal load ratios

(H_{cyc}/H_{max}), the displacement accumulation rate is relatively insensitive to the cyclic load level (i.e. amplitude of cyclic load). However, the displacement accumulation increases linearly with an increase of the cyclic load ratio. Moreover, Agaiby et al. (1992) suggested that metastable behavior occurs if the displacement exceeds the displacement correspondent to 70 % of hyperbolic capacity, H_h .

It should be noted that variations of the initial stiffness or hyperbolic capacity of these piles have not been formulated in a conventional analysis method such as the p-y method. General recommendation for the case of cyclic load is a 10 % reduction for the soil resistance (DNV, 2007). The current tests indicate about 50 % reductions in stiffness and strength of the pile-soil system and variations with total number of cycles from the rainflow method, although it should be noted that the wind tunnel tests were taken to complete failure and thus the effects of geometric changes (increasing rotation) are included. As was discussed earlier, there was no attempt to address scaling issues and size effects were also not taken into account in this study.

It is worth mentioning that some other studies have observed the densification of loose sands under the effects of cyclic load. For instance, Cuellar et al. (2009) studied the behavior of piles at small-scale and defined two distinct phases as explained in Chapter 2. They believe that densification or rearrangement occurs as a function of soil relative density and causes the subsidence of sand around the pile. This “densification” was not the main subject of this study, although some observations during the testing program suggested soil subsidence does occur around the pile vicinity.

An additional, constant wind speed test was performed in the wind tunnel as shown in Figure 5-26. The test includes eight loading intervals at a mean wind speed of 4.5 m/s. The loading intervals were separated from each other with non-loading relaxation intervals of approximately 30 seconds long. Figure 5-26 presents time-history of ground-line displacement and horizontal force during the test (note that this did not reach failure). It can be seen that 48% of final ground-displacement occurred during the first loading interval, and this suggests that the first cyclic loading interval stiffens the lateral behavior of piles (Agaiby et al, 1992).

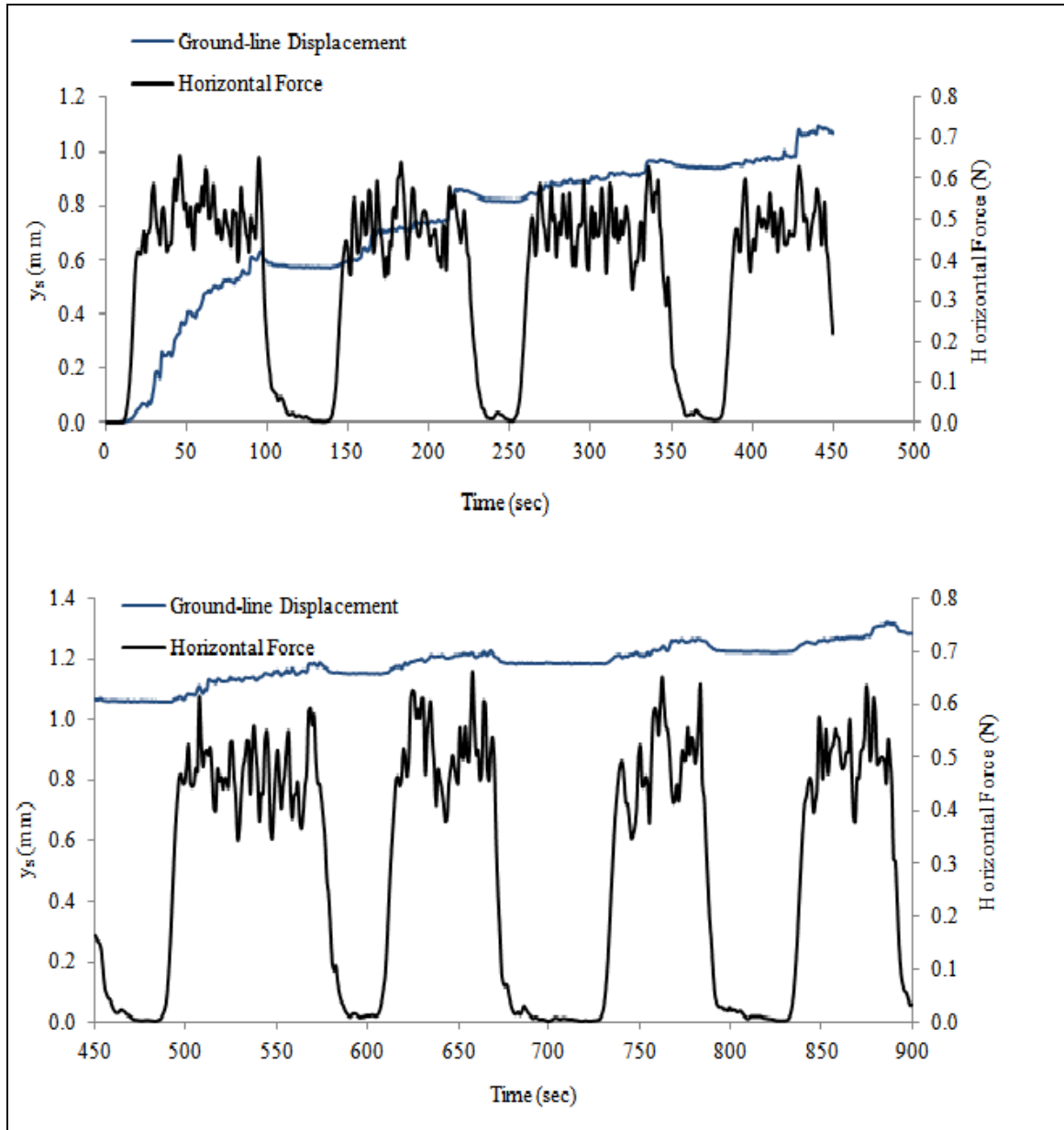


Figure 5-26. Constant Wind Speed Test Result

5.3.2 Accumulated Displacement

The lateral behavior of piles under random cyclic wind load has been studied from the point of view of capacity in the previous section. As is suggested in Chapter 2 for pile foundations, often the more stringent limit state is serviceability. Serviceability can be satisfied by limiting either the rotation or the ground-line displacement. There are

numerous recommendations that define ultimate capacity as some magnitude of displacement or rotation. The p-y method and elastic continuum approach are favored design and analysis approaches, because they incorporate displacement parameters for calculating the pile ultimate lateral capacity. However, neither of them can fully incorporate the role of cyclic loads in the reduction of the capacity or the increase in the ground-line displacement. For the case of cyclic loading, accumulated rotation/displacement is an important point of interest for many studies, including this research. It has been explained previously that displacement of a laterally loaded pile is a function of pile geometry, load eccentricity and initial soil condition. Moreover, in the case of random variable amplitude cyclic loading, special attention should be given to the characteristics of the load itself. One of the disadvantages of current design methodology is that the displacement obtained is independent of the number of loading cycles, which is a basic characteristic of the lateral load. The problem of accumulated displacement/rotation is complex and there is no globally accepted method available. The accumulated displacement and rotation is therefore studied here for the model piles under random variable amplitude cyclic wind load, to give general understanding and observations to be used in further works.

Some researchers suggest a degradation parameter, t , to be implemented in various solutions to take into account the effects of cyclic load (e.g. Little & Briaud, 1988; Lin & Liao, 1999; Long & Vanneste, 1994). In this research, the accumulation of the ground-line displacement is studied with considering load intervals and measuring the accumulation of the ground-line displacement in that load interval with respect to total number of cycles from rainflow method.

In Figure 5-27 the load-displacement curves for static, 30-second load interval (PRT-MM30-2), 60-second load interval (PRT-MM60-4), and 90-second load interval (PRT-MM90-1) on the medium pile have been plotted for comparison. The Figure shows how the medium pile behaves under random wind loads. Essentially, by increasing the duration of load application, the total number of loading cycles is increased. It is expected that lower displacements/rotation will occur under static test conditions. It can be concluded in general terms that the greater the number of total loading cycles, the greater the displacement/rotation.

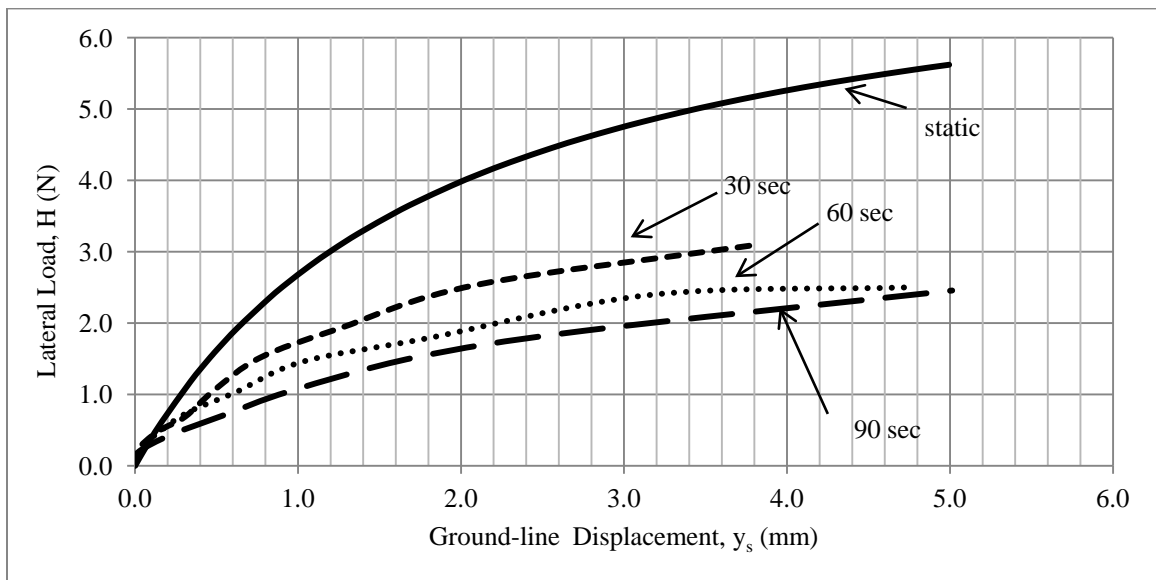


Figure 5-27. Load-Displacement Curve for Medium Pile in Sand

Figure 5-28 shows the load-displacement curves for static, 30-second load interval (PRT-SM30-1) and 60-second load interval (PRT-SM60-1) tests have been plotted for comparison for the short piles. The same trend is observed for the short pile tests that occurred for the medium piles.

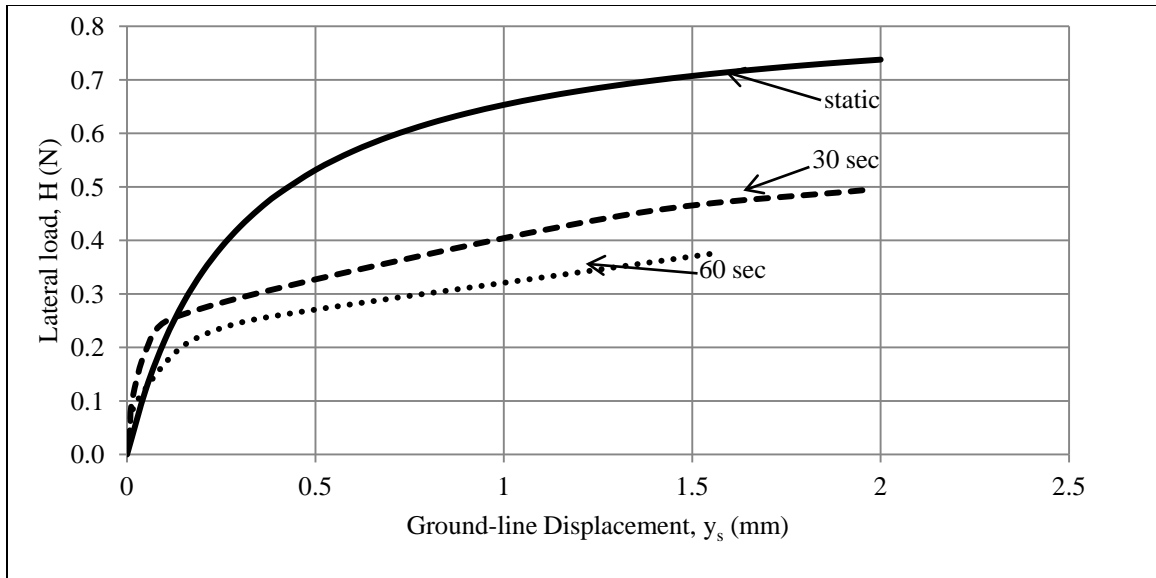


Figure 5-28. Load-Displacement Curve for Short Pile in Sand

In both Figures 5-27 and 5-28 the rate of displacement accumulation decreases, Agaiby et al. (1992) suggests that this might indicate stabilization is occurring. The stabilization (i.e. stiffer behavior) was also observed in the non-failure constant wind speed test as in Figure 5-26.

As a first attempt, a degradation parameter will be obtained for accumulation of ground-line displacement with respect to total number of cycles. Equation 5.10 is proposed for the accumulation of ground-line displacement in cyclic tests.

$$(y_s)_N - (y_s)_1 = tN \quad (5.10)$$

Where, N is number of cycles and t is a degradation factor.

Figure 5-29 to 5-31 show the degradation parameter in the different load intervals for tests PRT-MM30-2, PRT-MM60-4 and PRT-MM90-1, respectively. It is worth mentioning that these degradation parameters are obtained from ground-line displacement, and for a general case they might be obtained at different depths from

results of the reported full scale pile tests. This is very important particularly for the p-y method that gives the deflection, y , at any depth along the pile.

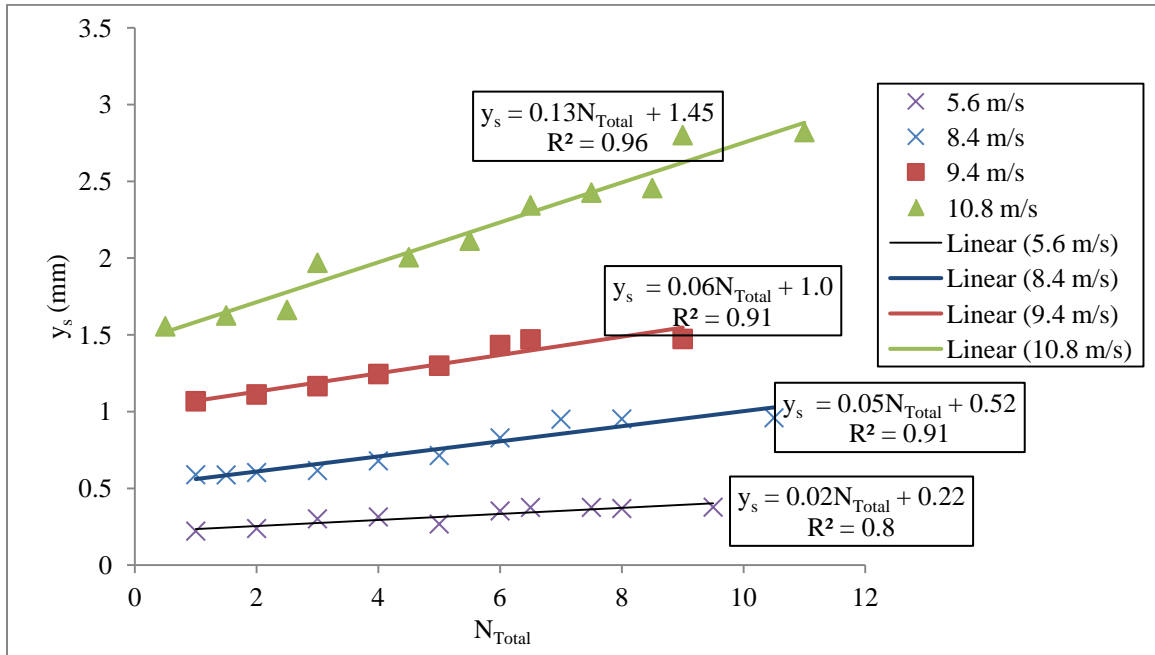


Figure 5-29. Degradation Parameter for Test PRT-MM30-2

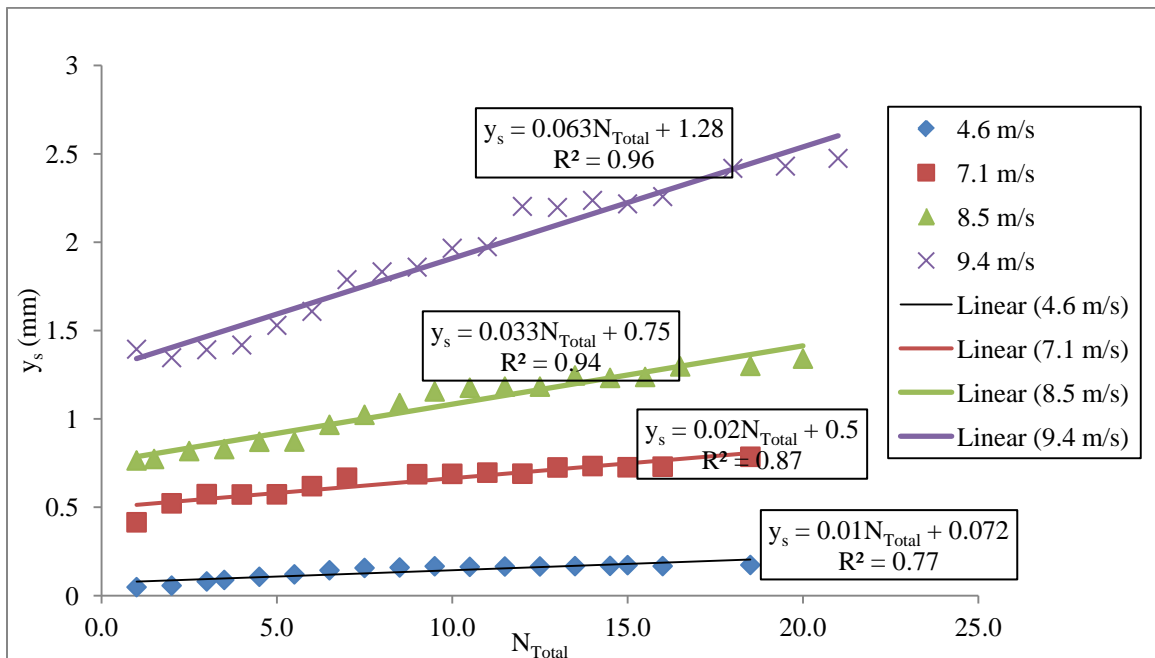


Figure 5-30. Degradation Parameter for Test PRT-MM60-4

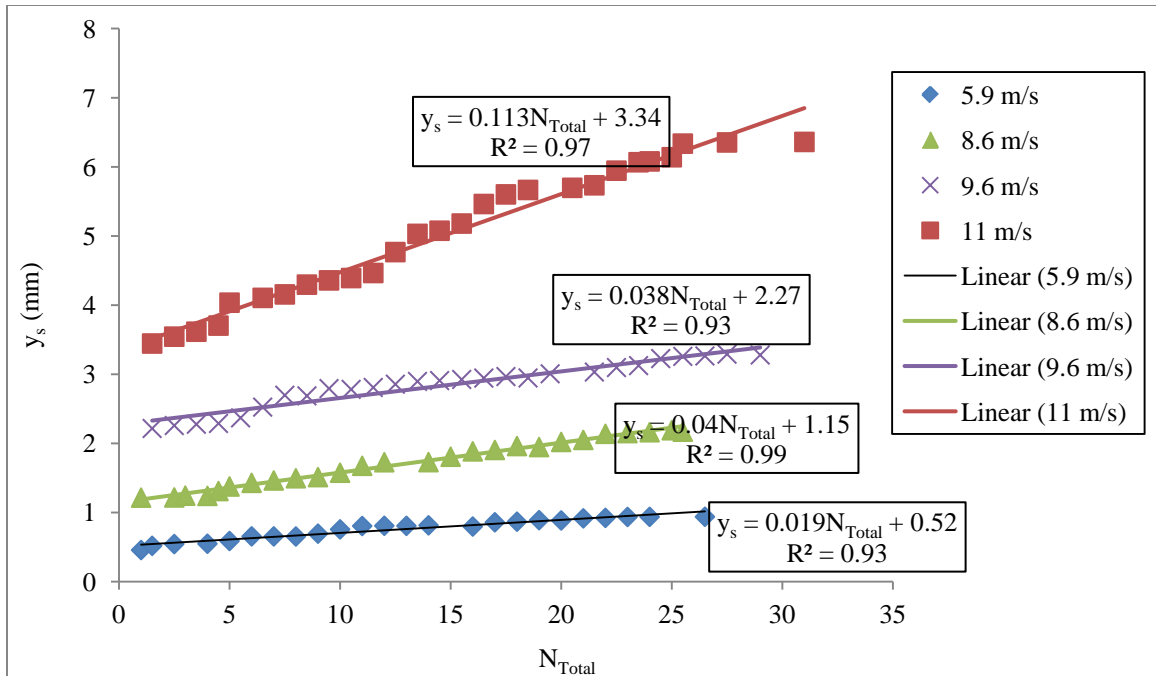


Figure 5-31. Degradation Parameter for Test PRT-MM90-1

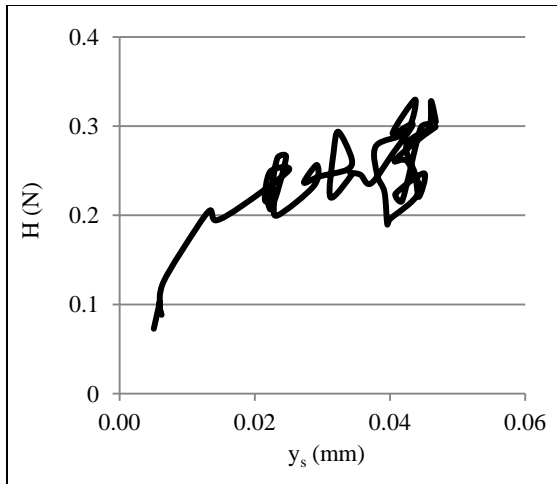
As can be seen from above plots, t varies between 0.01 and 0.13. The degradation parameter, t , increases with higher mean wind speed (load level). Agaiby et al. (1992) obtained values between 0.012 and 0.105 for constant amplitude tests in loose sand. It can be concluded that for higher wind speeds, the degradation parameter may be higher than the one obtained for constant amplitude tests.

5.4 Alternative Approaches for Assessing Random Cycle Effects

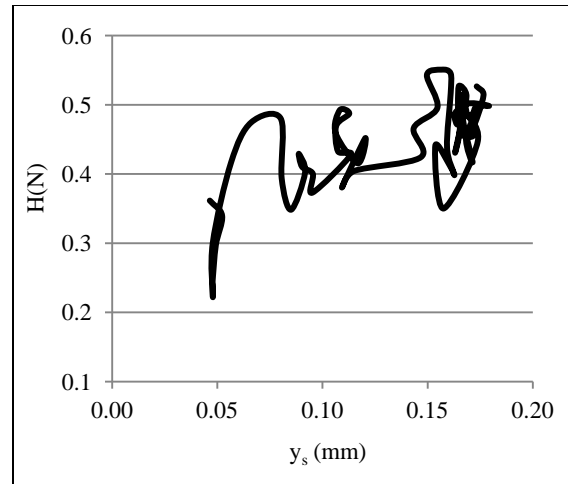
In this section, the effects of various parameters, such as, mean load level, cyclic load amplitude and its distribution will be considered to assess the accumulation of the ground-line displacement. Since, ratcheting behavior was observed in our testing program, it is also of interest to measure the impacts of high amplitude cycles on the ratcheting behavior of the piles; this may enable us to investigate whether the largest

displacements occur with general cycle accumulation or coincide with larger amplitude cycles in the wind load records.

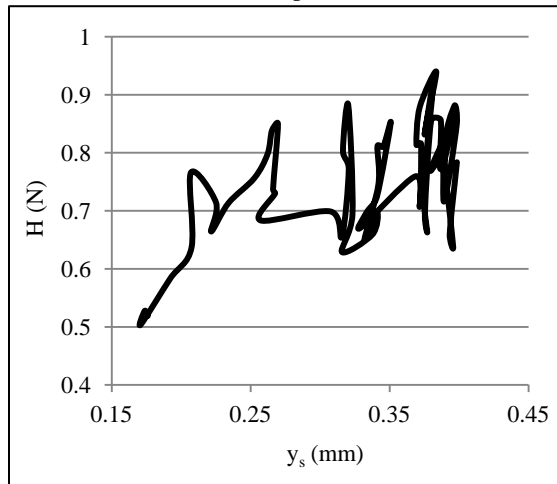
Figures 5-32 shows the plots of horizontal force vs. ground-line displacement for different mean wind speeds in test PRT-MM60-4. Figure 5-32 shows a general increase in ground-line displacement, y_s , with time at each wind speed and increasing rates with greater mean wind speed. Moreover, some load and unload cycles are evident in each time period for a single mean wind speed. Some of these have a typical elastic unload gradients with reducing y_s , whilst others show increasing displacement during unloading.



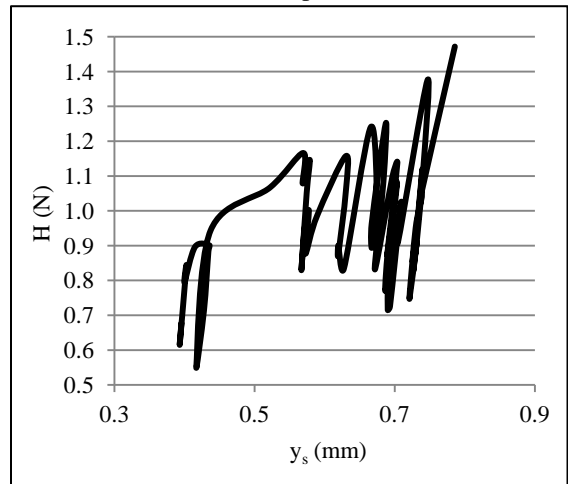
(a) Mean Wind Speed of 3.4 m/s



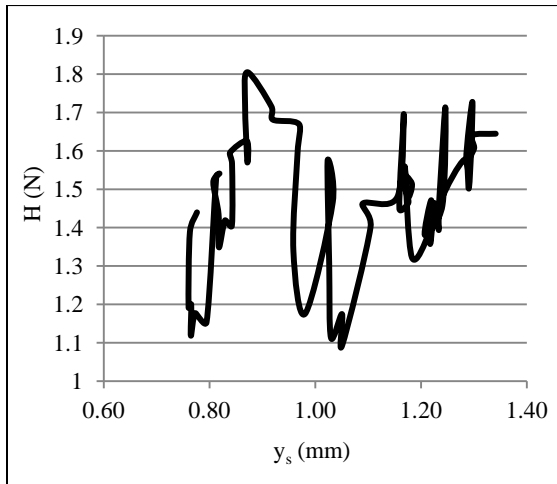
(b) Mean Wind Speed of 4.6 m/s



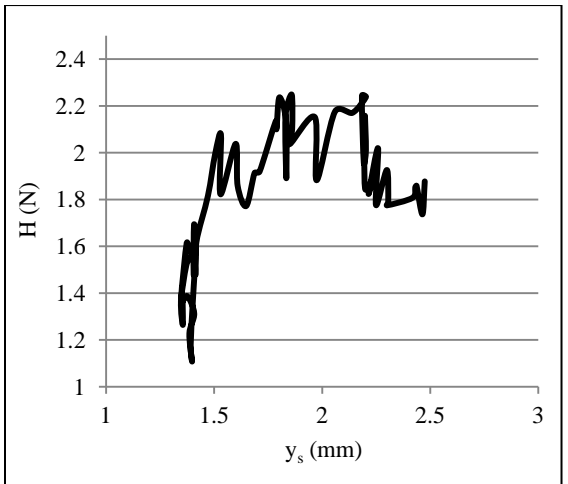
(c) Mean Wind Speed of 6.1 m/s



(d) Mean Wind Speed of 7.1 m/s



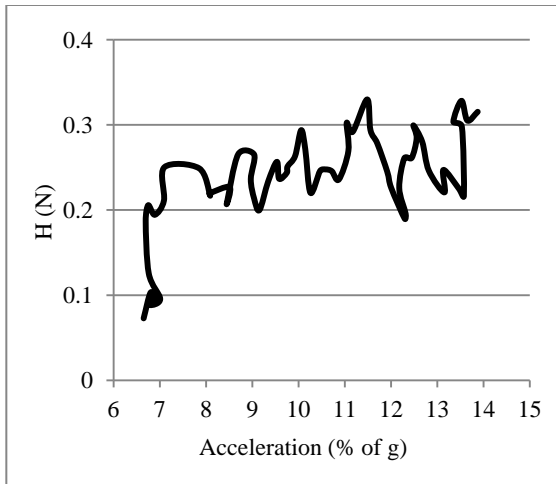
(e) Mean Wind Speed of 8.5 m/s



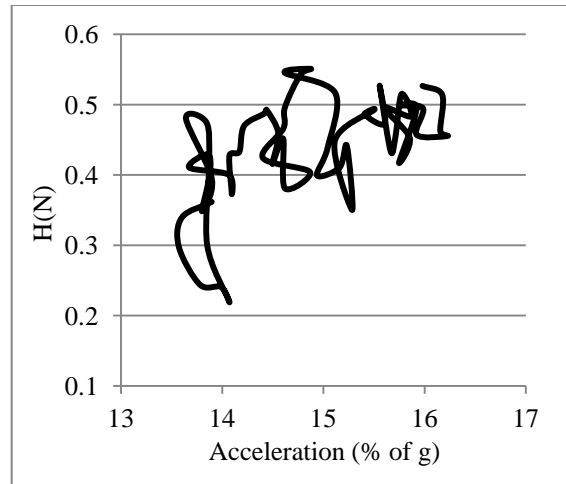
(f) Mean Wind Speed of 9.4 m/s

Figure 5-32. Load – Ground-line Displacement Curves for Test PRT-MM60-4

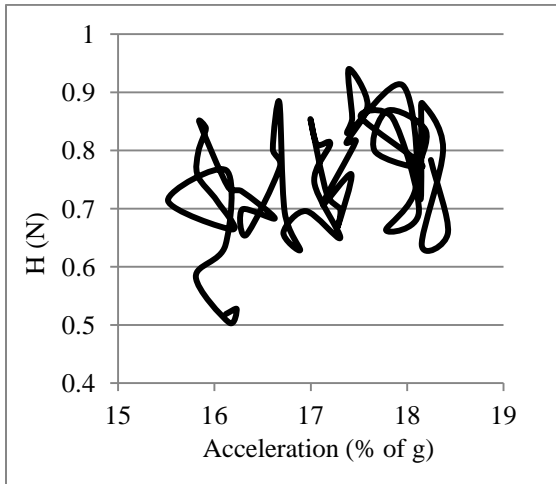
Figure 5-33 shows the plots of horizontal force vs. acceleration for different mean wind speed in test PRT-MM60-4. It can be seen that at earlier mean wind speed general increase occurs in acceleration with load cycles. At higher mean wind speed, general acceleration variations occur around a mean value, with no significant accumulation being observed. Moreover, accelerations are higher with greater average wind speeds, but values are relatively static for last three wind speeds. These observations suggest that soil stiffness is relatively even on either side of the pile later in the tests.



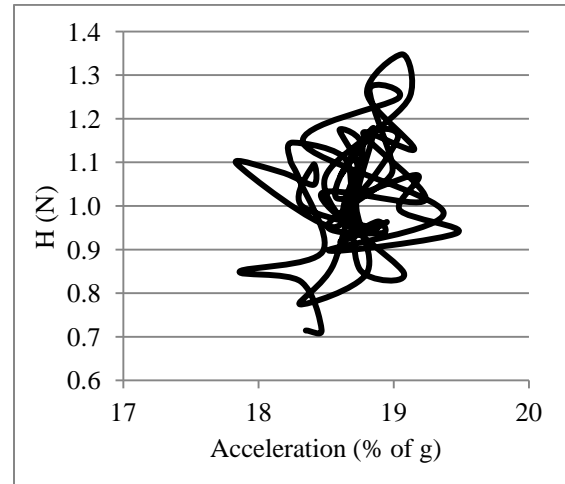
(a) Mean Wind Speed of 3.4 m/s



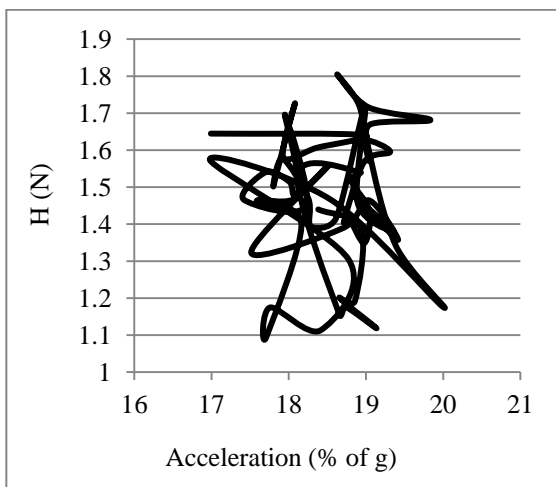
(b) Mean Wind Speed of 4.6 m/s



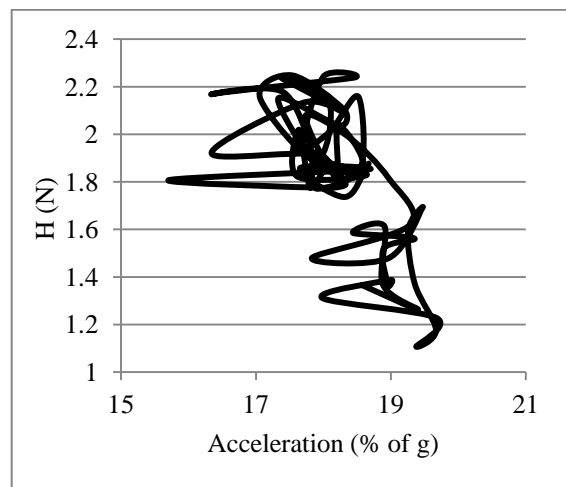
(c) Mean Wind Speed of 6.1 m/s



(d) Mean Wind Speed of 7.1 m/s



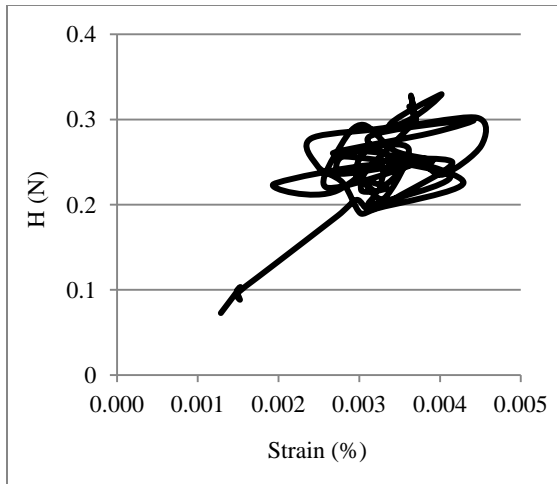
(e) Mean Wind Speed of 8.5 m/s



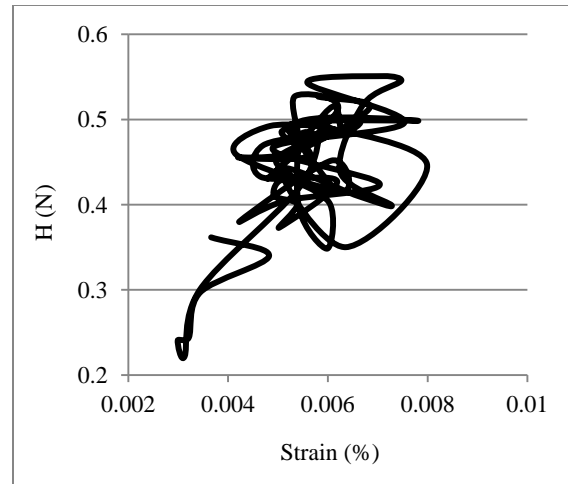
(f) Mean Wind Speed of 9.4 m/s

Figure 5-33. Load – Acceleration Curves for Test PRT-MM60-4

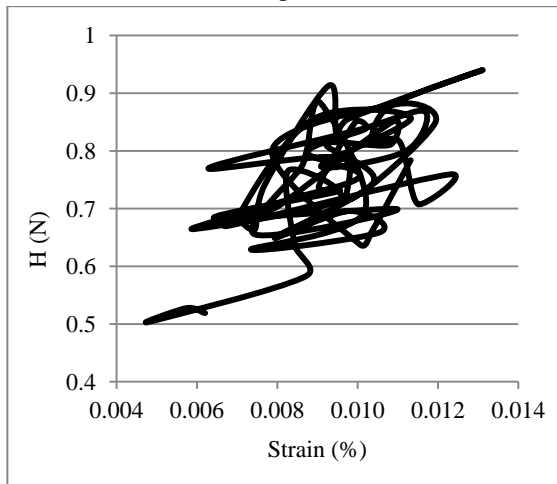
Figure 5-34 shows the plots of horizontal force vs. strain (of the base of the pole) for different mean wind speeds in test PRT-MM60-4. Again, general increase in strains with increasing average wind speeds is observed. For the first few mean wind speeds, initial increases in strain occur and then this settles down to variations around the mean value. For later mean wind speeds, the data just shows variations around the mean; however, the highest mean wind speed shows more accumulation and suggests possible breakdown of the soil structure.



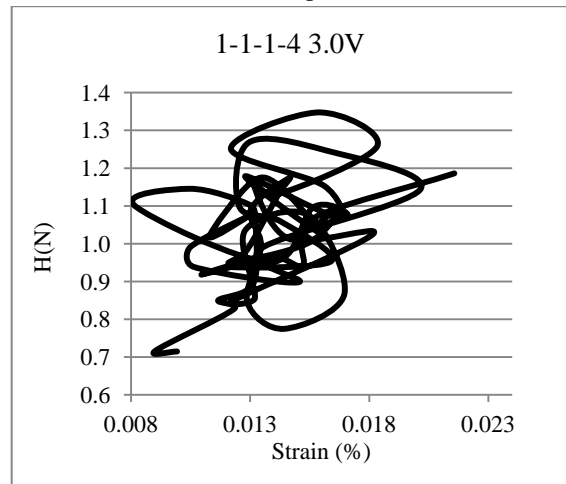
a) Mean Wind Speed of 3.4 m/s



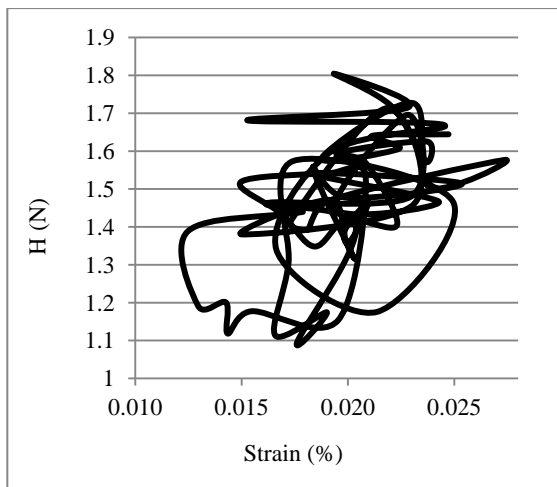
(b) Mean Wind Speed of 4.6 m/s



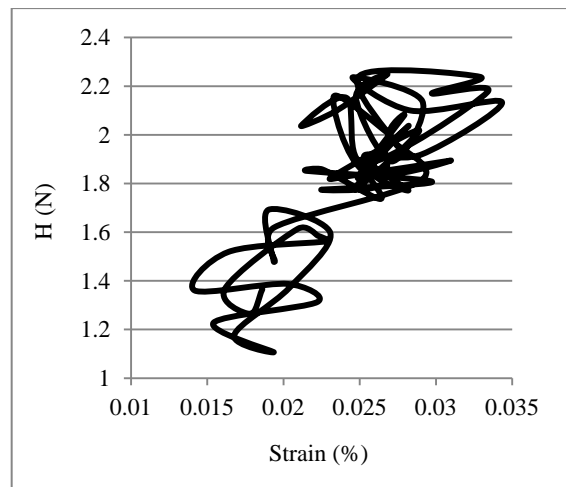
(c) Mean Wind Speed of 6.1 m/s



(d) Mean Wind Speed of 7.1 m/s



(e) Mean Wind Speed of 8.5 m/s



(f) Mean Wind Speed of 9.4 m/s

Figure 5-34. Load – Strain Curves for Test PRT-MM60-4

We can investigate the accumulation of ground-line displacement from fitting Rayleigh functions to the histograms of ground-line displacement fluctuations. The variations of the skewness and kurtosis of the wind speed fluctuations (cycle amplitudes) were studied with increasing mean wind speed in Chapter 4. The range of kurtosis was between 9 and 2 and the range of skewness was between 2.65 and zero. Figure 5-35 shows that the skewness and kurtosis of ground-line displacement fluctuations remain almost unchanged and they do not follow the same trend that was previously observed for amplitude of cycles in the wind speed time-history. Hence, the distribution of ground-line displacement fluctuations is almost insensitive to mean wind speed value.

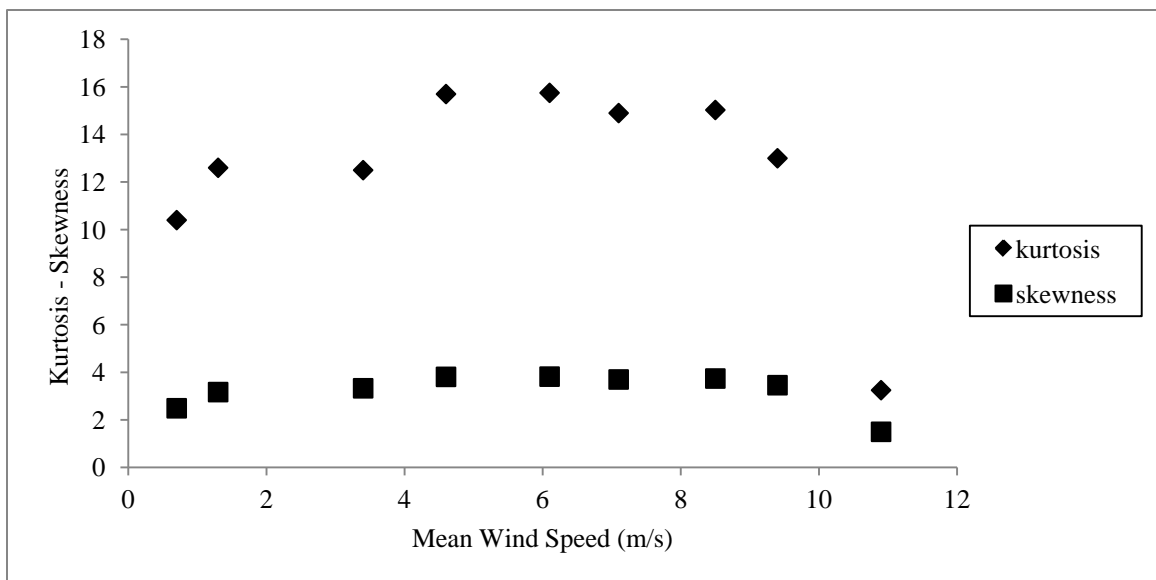


Figure 5-35. Skewness and Kurtosis of Ground-line Displacement Fluctuations for Test PRT-MM60-4

Similarly, it is of interest to study the variations of $H_A1/3$ and $H_A1/10$ for ground-line displacement fluctuations with mean wind speed.

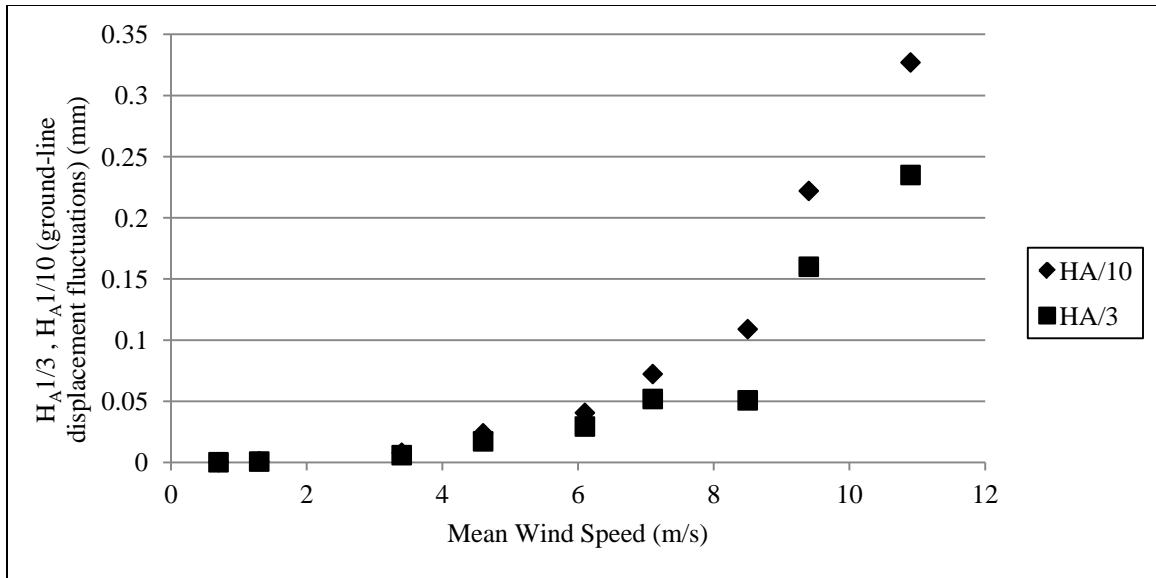


Figure 5-36. Variations of $H_A1/3$ & $H_A1/10$ for Ground-line Displacement Fluctuations in Test PRT-MM60-4

Figure 5-36 shows the non-linear increasing fluctuations in the largest 10% and 33% of the ground-line displacements with increasing mean wind speed. Figure 5-37 shows the variations of the $H_A1/10$ of ground-line displacement fluctuations $(H_A1/10)_{gl}$ vs. the cycle amplitudes $(H_A1/10)_{wc}$, indicating relatively uniform increases of the highest 10% of displacement cycles, compared to wind cycles. A similar trend was observed for $H_A1/3$.

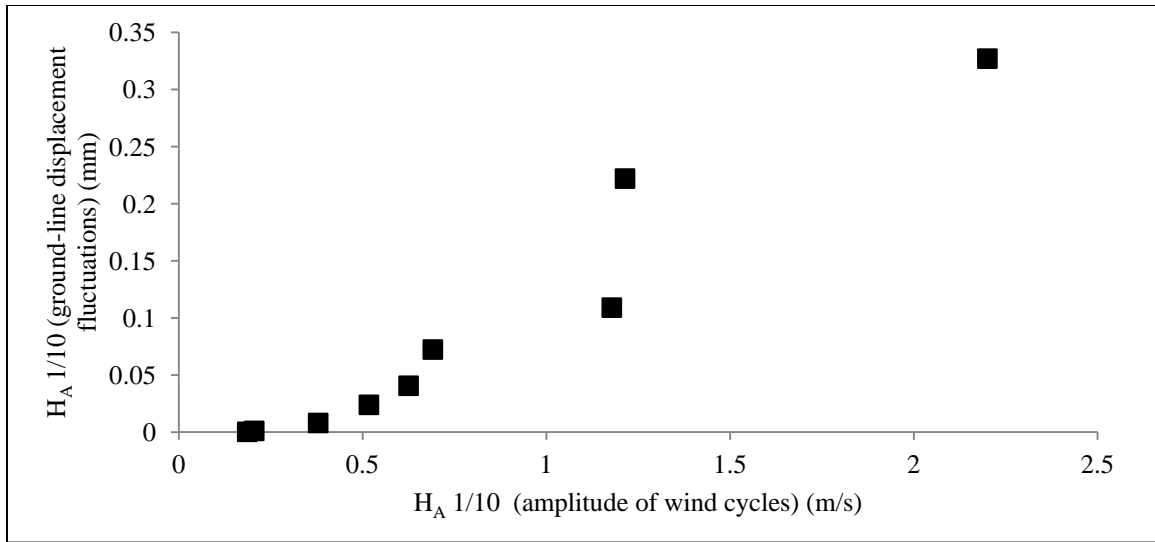


Figure 5-37. Variations of $H_A 1/10$ of Ground-line Displacement Fluctuations with Cycle Amplitudes in Test PRT-MM60-4

Observations from Figure 5-36 and 5-37 suggest that greater fluctuation of the ground-line displacement occurs with higher cycle amplitudes. The significance of load mean value can be understood by considering the ground-displacement as an “incremental damage” at each load interval. Table 5-9 shows the incremental damage at each load interval for test PRT-MM60-4.

Table 5-9. Damage Accumulation for Test PRT-MM60-4

Voltage	T (sec)	Mean Wind Speed (m/s)	Mean Lateral Force, H (N)	$(y_s)_0$	$(y_s)_{accum.}$	Incremental Damage, $D_{increment.}$
0.5	60	0.74	0.011	0	0	0%
1	60	1.27	0.033	0	0.01	0%
1.5	60	3.37	0.231	0.01	0.04	1%
2	60	4.62	0.434	0.05	0.12	2%
2.5	60	6.06	0.746	0.174	0.223	5%
3	60	7.11	1.027	0.395	0.39	8%
3.5	60	8.48	1.459	0.776	0.56	11%
4	60	9.39	1.789	1.35	1.12	23%
4.5	60	11.0	2.45	2.46	2.42	50%

Figure 5-38 shows the incremental damage with respect to mean load level.

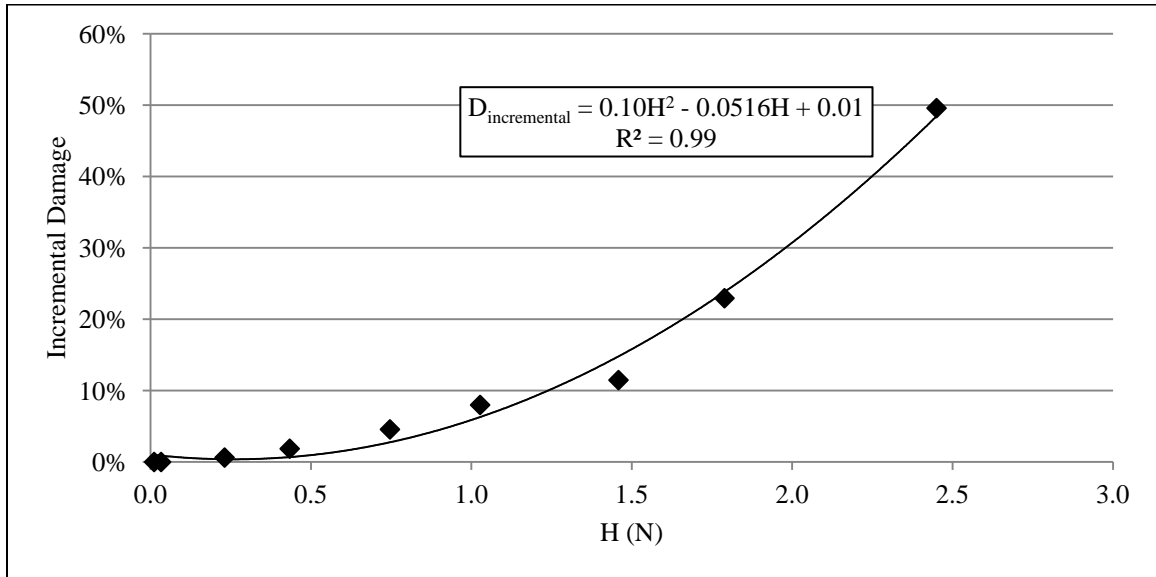


Figure 5-38. Accumulation of Damage with Mean Load Level

Figures 5-39 to 5-41 show the fluctuations of ground-line displacement in the last three loading intervals for test PRT-MM60-4. It can be seen that jumps in the ground-line displacements are associated with high amplitude fluctuations in the wind speed. The correlation between wind speed fluctuations and ground-line displacement is low, but the ground-line displacement shows a good correlation with total number of cycles from the rainflow method.

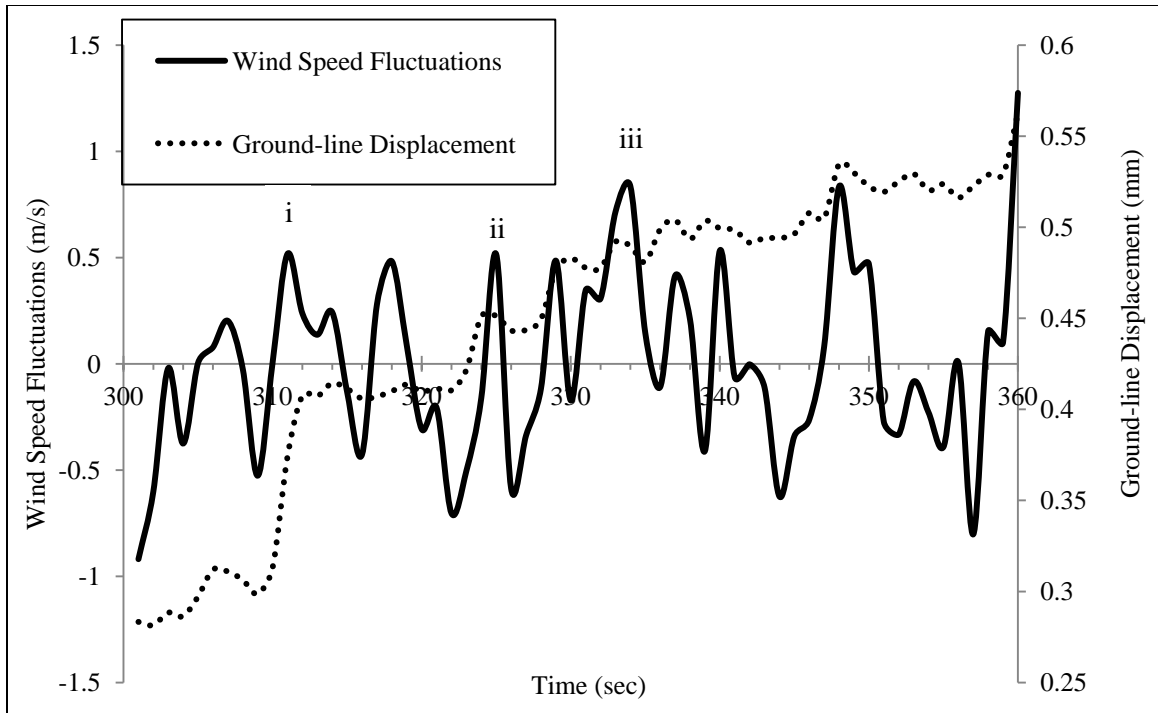


Figure 5-39. Ground-line Displacement and Wind Speed Fluctuations for Mean Wind Speed of 7.1 m/s for test PRT-MM60-4

At 310 seconds, a sudden increase in ground-line displacement (point i) coincides with a high amplitude cycle. In this load interval, the correlation coefficient between wind speed fluctuations and accumulation of ground-line displacement is 0.3, which is relatively low. Further smaller jumps in displacement coincide with points ii and iii (at 323 and 333 seconds).

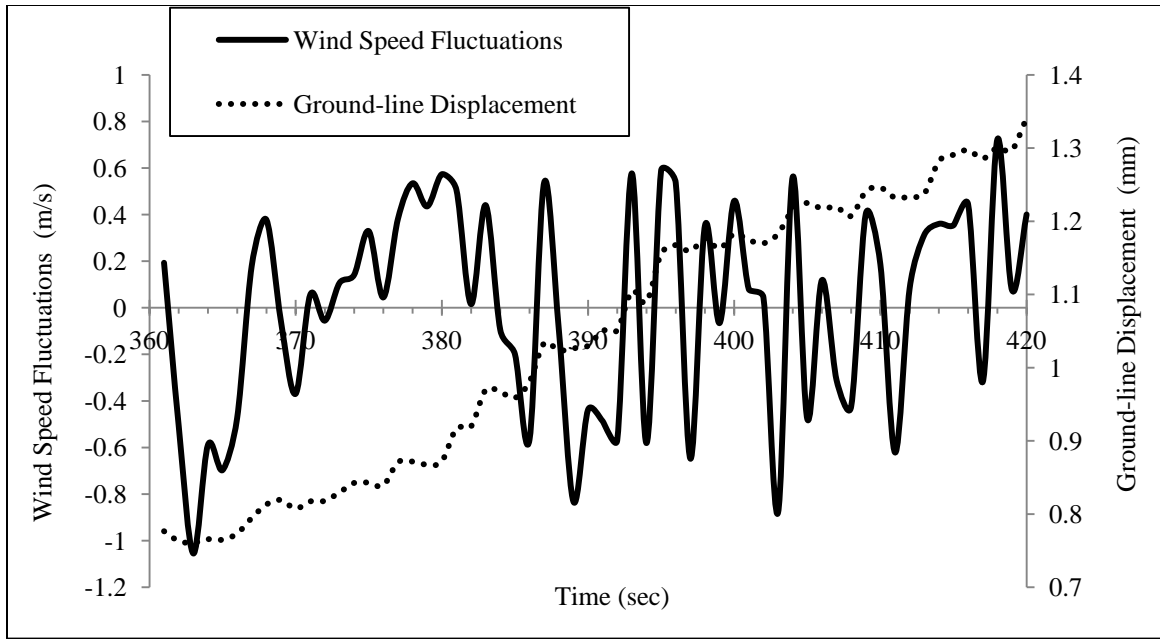


Figure 5-40. Ground-line Displacement and Wind Speed Fluctuations for Mean Wind Speed of 8.5 m/s for test PRT-MM60-4

However, the data in Figure 5-40 shows very little correlation between displacement and peak wind loads, with a general accumulation occurring with time.

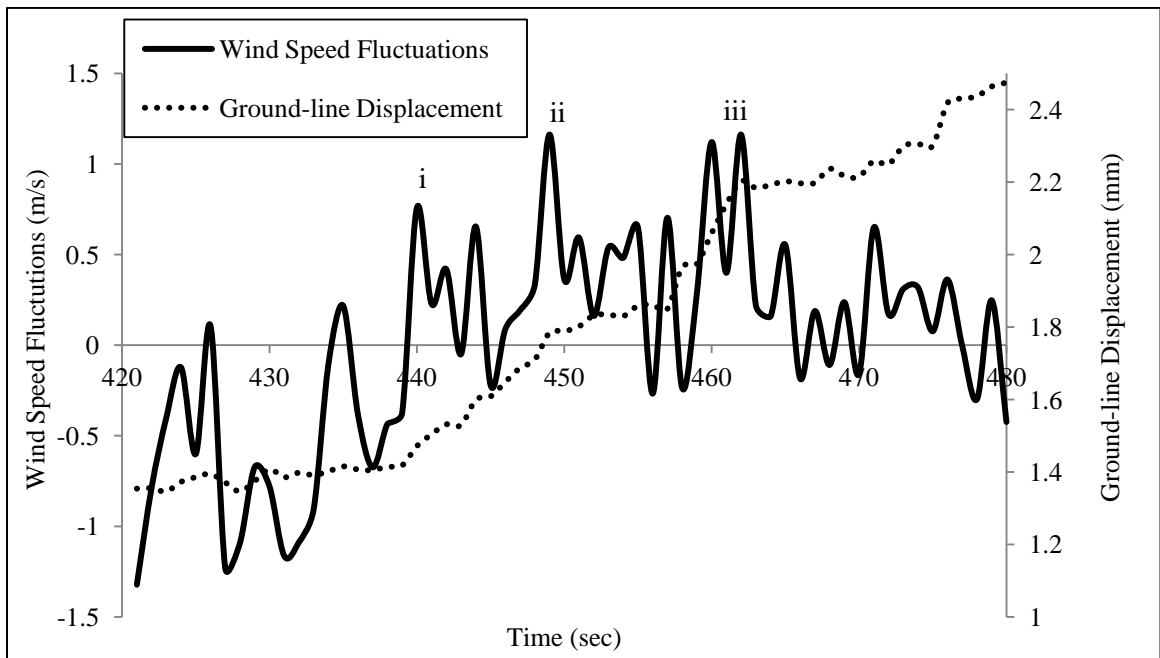


Figure 5-41. Ground-line Displacement and Wind Speed Fluctuations for Mean Wind Speed of 9.4 m/s for test PRT-MM60-4

Similar trends to Figure 5-39 can be seen in Figure 5-41, although it can be seen that some high amplitude cycles do not cause a sudden increase. Correlations between wind speed fluctuations and ground-line displacement are equal to 0.5 in this time interval. It should be noted that, in all three loading intervals, the correlation coefficient is above 0.9 between total number of cycles and ground-line displacement. However, observations made during testing suggest that ratcheting does occur.

A flow around soil mechanism for pipeline uplift in very loose sands has been proposed by Deljoui (2012). This mechanism is depicted in Figure 5-42 and shows a mechanism similar to the Randolph & Houlsby mechanism (1984) for soft clay, but displaying more asymmetry.

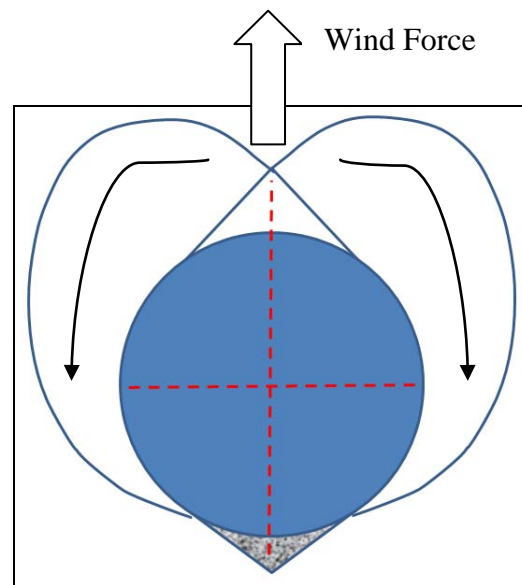


Figure 5-42. Pipeline Uplift Mechanism (Deljoui, 2012)

Force-displacement curves for pipeline uplift following peak loads show considerable fluctuations, which have been attributed to formation and shedding of a series of shear

bands ahead of the pipeline as mechanisms become successively less kinematically optimal (Randolph & Houlsby, 1984). Hence, although there is a weak correlation between peak loads and displacements, this may be more to do with the soil deformation mechanism evolution.

5.5 Summary

The behavior of laterally cyclically loaded piles has been studied in this chapter. Different factors, such as, the geometry of the pile, load eccentricity and the characteristics of the lateral loads were addressed through a series of static and random variable amplitude cyclic tests.

The wind tunnel was used in this research to create stationary, variable amplitude cyclic loads. Variations of the initial stiffness and hyperbolic capacity with the total number of loading cycles were investigated and reductions were observed to occur with greater number of cycles.

It was found that load-eccentricity will reduce initial stiffness and hyperbolic capacity of laterally loaded piles, moreover the pile length will improve the behavior of piles under lateral loads.

Some of the findings are qualitative and can be used as verification of other studies. Although current studies give valuable information especially for understanding the behavior of piles under wind random loads, this needs further validation at larger scale. The observations suggest that the fluctuations in the ground-line displacement (ratcheting) is more prone to occur in higher amplitude cycles. Moreover, the higher amplitude cycles occur in higher mean wind speed.

The test results confirm that increasing number of loading cycles leads to an increase in the ground-line displacements of a pile. The effects of random variable amplitude loads were found to be significant on initial stiffness and hyperbolic capacity of model piles. Also, the accumulation of ground-line displacement shows good relation with mean load value.

CONCLUSIONS

6.1 Summary of Research

Piles are frequently used as a foundation for numerous offshore and onshore infrastructures, which are subjected to significant lateral random variable amplitude cyclic loads from natural sources. Current design approaches do not take into account some important aspects of the problem, such as, the nature of the cyclic loads and the accumulation of ground-line displacement with cycling.

In this research, a novel wind tunnel testing program was designed to partially address the shortcomings of current design methodology of piles under random variable amplitude cyclic lateral loads. Small scale models were tested in the wind tunnel, which is a robust tool for generating random variable amplitude scaled boundary layer wind fields. It should be noted that the results from this study should be used with some caution since the material behavior only reflects loose sand conditions and the scaling effects are currently undetermined.

A semi-empirical hyperbolic representation was used to describe the load-displacement relations of the model piles. The model was tested under static and cyclic load conditions with different eccentricities. The effects of random variable amplitude cyclic loads on the initial stiffness and hyperbolic capacity were investigated. In addition, the accumulation of ground-line displacements was studied, and a degradation parameter was

obtained to address the accumulation of ground-line displacements with numbers of cycles obtained from the Rainflow counting method. Using the results obtained from the static tests, the effects of load-eccentricity and pile geometry on the hyperbolic parameters were also studied. Finally, comparison was made between the experimental results and theoretical interpretations for ultimate capacity and initial stiffness. This chapter provides the main conclusions from the research project and some suggestions for future research work.

6.2 Key Study Findings

- The drag coefficient varied for the plate from 0.96 to 1.17 for different mean wind speeds.
- The plate drag coefficient was relatively insensitive to the wind speed, although variations of up to 40% of the mean value were observed in the stochastic time-histories.
- The variation of the peak factor with wind speed was negligible and the value remained almost constant at around 3.5.
- The value for gust factor was obtained for different wind speed; the gust factor was found to be 1.5 and almost independent of mean wind speed.
- The turbulence intensity remained almost constant for different wind speed at around 0.15.
- Good agreement was observed between wind speed histograms and the Gaussian probability distribution.

- Counting zero crossings and peaks was found to be less suitable for cycle counting in the wind speed time-history due to a very low coefficient of irregularity (i.e. it is a wide band phenomenon).
- In general, the semi-empirical hyperbolic representation of the load-displacement curve demonstrated good agreement with the experimental results.
- The hyperbolic capacities were higher than the ultimate capacity obtained from the Broms (1964) solution; the Meyerhof & Ranjan (1974) method gave closer agreements with the hyperbolic capacity in the ground-line tests.
- Good agreement was found between the experimental values of initial stiffness and the values obtained from the theory of Agaiby et al. (1992) for small and medium piles in the ground-line tests.
- Hyperbolic capacity and initial stiffness were found to increase with larger pile lengths.
- Load eccentricity causes a reduction in both initial stiffness and hyperbolic capacity.
- Reductions in both initial stiffness and hyperbolic capacity occurred under random variable amplitude cyclic loads when compared to the static test results.
- The initial stiffness and hyperbolic capacity reduce with greater total numbers of cycles obtained from Rainflow counting.
- Comparison of the load-displacement curves in static and random variable amplitude cyclic tests show that ground-line displacements are greater for random variable amplitude cyclic tests.

- The degradation parameter, which accounts for the accumulation of the ground-line displacement, varied between 0.01 and 0.13.
- The above degradation parameters are higher than the predictions of Agaiby et al. (1992), based on constant amplitude cyclic loads.
- Based on observations from the test results, the ratcheting behavior often occurs with the high amplitude cycles in the wind speed time-history.

6.3 Future Works

The problem of random variable amplitude cyclic loads seems to be very crucial in the design of infrastructures working under the effects of loads from environmental sources, such as, wind or sea waves. It is believed that more research works is needed to study several aspects of random variable amplitude cyclic loads.

For further work, different scales need to be investigated, and more attempts are needed to reconcile wind and soil scales for further tests.

Although it might be of interest to test under longer loading intervals, this will lead to study the behavior of piles under more number of cycles, and capture the probable stabilization in the pile behavior.

In this research, Rayleigh distribution was used for studying cycle amplitudes, it might be of interest to consider other distributions, such as, Weibull or Dirlik in further studies.

Leblanc et al. (2010) suggest that Miner's law might be used for estimation of the degradation of soil under effects of random variable amplitude cyclic loads. Application of damage accumulation law needs the degradation parameter for soils to be obtained. It

is suggested to place stress cells within the soil body to better understand the stress variations in the soil medium to estimate degradation of the soil.

REFERENCES

- Achmus, M., Kuo, Y., & Abdel-Rahman, K. (2009).** Behavior of Monopile Foundations under Cyclic Lateral Load. *Computer and Geotechnics*, Vol. 36: 725-735. doi: 10.1016/j.compgeo.2008.12.003.
- Agaiby, S. W., Kulhawy, F.H., & Trautman, C. H. (1992).** Experimental Study of Drained Lateral and Moment Behavior of Drilled Shafts during Static and Cyclic Loading. Research Project 1493-4, Cornell University: Geotechnical Engineering Group.
- Allotey, N. K. (2006).** Nonlinear Soil-Structure Interaction in Performance-based Design. Ph.D. thesis, University of Western Ontario, London, Ont.
- Allotey, N. & El Naggar, M.H. (2008).** A Consistent Soil Fatigue Framework Based on the Number of Equivalent Cycles. *Geotech. Geol Eng*, Vol. 26: 65-77. DOI 10.1007/s10706-007-9147-2.
- Allotey, N. & El Naggar, M. H. (2008).** A Numerical Study into Lateral Cyclic Nonlinear Soil-Pile Response. *Canadian Geotechnical Journal*, Vol. 45: 1268-1281.
- API (2003).** *Recommended Practice for Planning, designing, and constructing fixed offshore platforms: Working Stress Design*. RP2A-WSD.
- ASCE 7-05, (2006).** *Minimum Design Loads for Buildings and Other Structures*, American Society of Civil Engineers, Reston, Virginia.
- ASTM International (2006).** *Standard test Methods for Minimum Index Density and Unit Weight of Soils Calculation of Relative Density*. D4254.
- ASTM International (2009).** *Standard Test Methods for Particle-Size Distribution of Soils Using Sieve Analysis*. D6913.
- ASTM International (2005).** *Standard Practices for Cycle Counting in Fatigue Analysis*. E1049.
- Bailey, A., & Vincent, N.D.G. (1939).** Wind Pressure Experiments of the Seven Bridge. *J. Instn. Civ. Engrs*, Vol. 11: 363-380.
- Baker, B. (1884).** The Forth Bridge. *Engineering*, Vol. 38: 213-215.
- Basu, D., Salgado, R., & Prezzi, M. (2009).** A Continuum Based Model for Analysis of Laterally Loaded Piles in Layered Soils. *Geotechnique*, 59(2): 127-140.

- Bearman, P. W. (1971).** An investigation of the Forces on Flat Plates Normal to a Turbulent Flow. *Journal of Fluid Mechanics*, 46(1): 177-198.
- Benasciutti, D., & Tovo, R. (2005).** Comparison of Spectral Methods for Fatigue Analysis of Broad-band Gaussian Random Processes. *Probabilistic Engineering Mechanics*, 21: 287-299. doi: 10.1016/j.probengmech.2005.10.003
- Bishop N.W.M. (1999).** Vibration Fatigue Analysis in the Finite Element Environment. XVI Encuentro Del Grupo Espanol de Fractura Conference.
- Bolton, M. D. (1986).** The strength and Dilatancy of Sand. *Geotechnique*, 36(1): 65-78.
- Borden, R. H., & Gabr, M. A. (1987).** LTBASE: Lateral Pier Analysis Including Base and Slope Effect. Research Report FHWA/NC/86-001, North Carolina State University, Raleigh.
- Broms, B. B. (1964).** Lateral Resistance of Piles in Cohesionless Soils. *Journal of The Soil Mechanics and Foundation Division, ASCE*, 90(SM3): 123-156.
- Brown, D. A., Morrison, C., & Reese, L. C. (1988).** Lateral Load Behavior of Pile Group in Sand. *Journal of Geotechnical Engineering, ASCE*, 14(11): 1261-1276.
- Budhu, M., & Davies, T. G. (1987).** Nonlinear Analysis of Laterally Loaded Piles in Cohesionless Soils. *Canadian Geotechnical Journal*, Vol. 24: 289-296.
- Byrne, B. W., & Hously, G. T. (2003).** Foundation for Offshore Wind Turbines. Phil. Trans. Royal Society, 360: 2909-2930. 10.1098/rsta.2003.1286
- Christensen, N. H. (1961).** Model Tests with Transversally Loaded Rigid Piles in Sand. Report 12, Danish Geotechnical Institute: 10-16.
- Cuellar, P., Baebler, M., & Rucker, W. (2009).** Ratcheting Convective Cells of Sand Grains around Offshore Piles. *Springer, Granular Matter*, 11(6): 379-390.
- Davenport, A. G. (1995).** How Can We Simplify and Generalize Wind Loads. *Journal of Wind Engineering and Industrial Aerodynamics*, 54/55: 657-669.
- Davenport, A. G. (1961).** The Application of Statistical Concepts to the Wind Loading of Structures. *ICE Proceedings*, 19(4): 449-471.
- Davies, T. G. & Budhu, M. (1987).** Non-Linear Analysis of Laterally Loaded Piles in Heavily Overconsolidated Clays. *Geotechnique*, 36(4): 527-538.
- Deacon, E. L. (1955).** Gust Variation with Height up to 150 Meters. *Quarterly Journal of the Royal Meteorological Society*, Vol. 81: 562-573.
- Det Norske Veritas (DNV, 2007).** *Design of Offshore Wind Turbine Structures*.

- Deljoui, P. (2012).** Upheaval Buckling of Offshore Pipelines in Homogeneous and Layered Soils. Department of Civil & Environmental Engineering, University of Western Ontario, London, Ontario, Canada.
- Dirlik, T. (1985).** Application of Computers in Fatigue Analysis. Department of Engineering, University of Warwick.
- Duncan, M. J., Evans Jr. L. T., & Ooi P. S K. (1994).** Lateral Load Analysis of Single Piles and Drilled Shafts. *Journal of Geotechnical Engineering*, ASCE, 120(5): 1018-1033.
- Durst, C. S. (1960).** Wind Speeds over Short Periods of Time. *Meteorological Magazine*, Vol. 89: 181-186.
- Engineering Sciences Data Unit (ESDU, 1970).** Fluid Forces and Moments on Flat Plates, *Engineering Sciences Data Unit*, Item 70015.
- Goda, Y. (2010).** Random Seas and Design of Maritime Structures, 3rd edition. Advanced Series on Ocean Engineering, 33(xxiv), World Scientific, Hackensack, NJ, Singapore.
- Green, R. A., & Terri, G. A. (2005).** Number of Equivalent Cycles Concept for Liquefaction Evaluations – Revisited. *Journal of Geotechnical and Geoenvironmental Engineering*, ASCE 131(4): 477-488.
- Guo, W. D. (2008).** Laterally Loaded Rigid Piles in Cohesionless Soil. *Canadian Geotechnical Journal*, Vol. 45: 676-697.
- Hansen, J. B. (1961).** The Ultimate Resistance of Rigid Piles against Transversal Forces. *Danish Geotechnical Institute*, Report 12: 5-9.
- Hancock, J. & Bommer, J. J. (2005)** The Effective Number of Cycles of Earthquake Ground Motion. *Earthquake engrg Struct. Dyn.* Vol. 34: 637-664.
- Hetenyi, M. (1946).** Beams on Elastic Foundation. University of Michigan Press, Ann Arbor.
- Holmes, J. D. (2001).** Wind Loading of Structures. Spon Press.
- Kagawa, T. & Kraft, L. M. (1980).** Lateral Load-Deflection Relationships of Piles Subjected to Dynamic Loadings. Soils and Foundations, *Japanese Society of Soil Mechanics and Foundation Engineering*, 20(4): 19-36.
- Kareem, A. (1980).** Dynamic Effects of Wind on Offshore Structures. 12th Offshore Technology Conference: 235-246.
- Kishida, H. & Nakai, S. (1977).** Large Deflection of a Single Pile under Horizontal Load. *Proceedings of 9th International Conference on Soil Mechanics and Foundation Engineering*, Specialty Session 10, Tokyo: 87-92.

- Leblanc, C., Byrne, B. W., & Houlsby, G. T. (2010).** Response of Stiff Piles to Random Two-way Lateral Loading. *Geotechnique*, 60(9): 715-721.
- Leblanc, C., Houlsby, G. T., & Byrne, B. W. (2010).** Response of Stiff Piles in Sand to Long-Term Cyclic Lateral Loading. *Geotechnique*, 60(2): 79-90.
- Letchford, C. W., (2001).** Wind Loads on Rectangular Signboards and Hoardings. *Journal of Wind Engineering and Industrial Aerodynamics*, Vol. 89: 135-151.
- Lin, S., & Liao, J. (1999).** Permanent Strains of Piles in Sand due to Cyclic Lateral Loads. *Journal of Geotechnical and Geoenvironmental Engineering, ASCE*, 125(9): 798-802.
- Little, R. L., & Briaud, J. L. (1988).** Cyclic Horizontal Load Tests on Six Piles in Sands at Houston Ship Channel. Research Report 5640 to USAE Waterways Experiment Station, Civil Engineering, Texas A&M University.
- Long, J. H., & Vanneste G. (1994).** Effects of Cyclic Lateral Loads on Piles in Sand. *Journal of Geotechnical Engineering, ASCE*, 120(1): 225-244.
- Manoliu, I., Dimitriu, D.V., & Radulescu, N. (1985).** Load-Deformation Characteristics of Drilled Piers. *Proceedings of 11th International Conference on Soil Mechanics and Foundation Engineering*, Vol. 3: 1553-1558.
- Matlock, H., & Reese, L. C. (1962).** Generalized Solutions for Laterally Loaded Piles. *Transactions, ASCE* 127: 1220:1248.
- Matsuishi, M. & Endo, T. (1968).** Fatigue of Metals Subjected to Varying Stress. Presented at Japanese Society of Mechanical Engineers, Fukuoka, Japan.
- McClelland, B., & Focht, J. (1958).** Soil Modulus for Laterally Loaded Piles. *Trans. ASCE*, 123: 1049-1086.
- Meyer, B. J. (1979).** Analysis of Single Piles Under Lateral Loading. Thesis, University of Texas, Austin.
- Meyerhof, G. G. & Ranjan, G. (1972).** The Bearing Capacity of Rigid Piles under Inclined Loads in Sand. I: Vertical Piles. *Canadian Geotechnical Journal*, Vol. 9: 430-446.
- Naeim, F. (2001).** The Seismic Design Handbook. 2nd Edition, Kluwer Academic Publishers.
- Poulos, H. G. (1971).** Behavior of Laterally Loaded Piles – Single Piles. *Journal of the Soil Mechanics, ASCE*, 97(SM5): 711-732.
- Poulos, H. G. (1973).** Load-Deflection Prediction for Laterally Loaded Piles. *Australian Geomechanics Journal*, G3 (1): 1-8.

- Poulos, H., & Hull, T. (1989).** The Role of Analytical Geomechanics in Foundation Engineering. In *Foundation Engineering: Current Principles and Practices*, Vol. 2: 1578-1606.
- Prakash, S. (1962).** Behavior of Pile Groups Subjected to Lateral Loads. Thesis, University of Illinois, Urbana.
- Quinn, A. D., Baker, C. J., & Wright, N. G. (2001).** Wind and Vehicle Induced Forces on Flat Plates- Part 1: Wind Induced Force. *Journal of Wind Engineering and Industrial Aerodynamics*, Vol. 89: 817-829.
- Randolph, M. F. (1981).** The Response of Flexible Piles to Lateral Loading. *Geotechnique*, 31(2): 247-259.
- Randolph, M. F., & Houlsby, G. T. (1984).** The limiting Pressure on a Circular Pile Loaded Laterally in Cohesive Soil. *Geotechnique*, 34(4): 613-623.
- Reese, L. C., & Matlock, H. (1956).** Nondimensional Solutions for Laterally Loaded Piles with Soil Modulus Assumed Proportional to Depth. *Proceedings of the VIII Texas Conference on Soil Mechanics and Foundation Engineering*, 41 pp. University of Texas, Austin.
- Reese, L. C., & Wang, S. T. (2001).** Design of Foundations for a Wind Turbine Employing Modern Principles. Conference: *From Research to Practice in Geotechnical Engineering*: 351-365.
- Reese, L. C., & Van Impe, W. F. (2010).** Single Piles and Pile Groups under Lateral Loading, 2nd Edition, CRC Press.
- Reese, L.C., Cox, W. R., & Coop, F. D. (1974).** Analysis of Laterally Loaded Piles in Sand. *Proceedings, 6th Offshore Technology Conference*, Vol. 2: 473-483.
- REN21. (2011).** *Renewables 2011 Global Status Report*.
- Rice, S. O. (1954).** Mathematical Analysis of Random Noise, Random Papers on Noise and Stochastic Processes, Dover, New York, 1954.
- Rowe, P. W. (1962).** The stress-Dilatancy Relation for Static Equilibrium of an Assembly of Particles in Contact. *Proc. Roy. Soc. London A269*: 500-527.
- Rychlik, I. (1987).** A new Definition of the Rainflow Cycle Counting Method. *International Journal of Fatigue*, 9(2): 119-121.
- Sa'adon, N. M., Pender, M. J., Orense, R. P., & Abdul Karim A. R. (2009).** A Macro-Element for Pile Head Response to Cyclic Lateral Loading. *NZSEE Conference*, Paper Number 47.
- Sherlock, R. H. (1947).** Gust Factors for the Design of Buildings. *International Association for Bridge and Structural Engineering*, Vol. 8: 204-236.

- Solari, G. (1993).** Gust Buffeting. I: Peak Wind Velocity and Equivalent Pressure. *Journal of Structural Engineering*, 119(2): 365-382.
- Standards Australia (1989).** Minimum Design Loads on Structures. Part 2: Wind Loads. *Standards Australia*, North Sydney, Australian Standard AS1170.2.
- Stanton, T.E. (1925).** Report on Measurement of the Pressure of the Wind on Structures. *Proc. Instn Civ. Eng*, Vol. 219: 125-158.
- Terzaghi, K. (1955).** Evaluation of Coefficients of Subgrade Reaction. *Geotechnique*, 4(4): 297-326.
- Vickery, B. J. (1965).** On the Flow behind a Coarse Grid and its Use as a Model of Atmospheric Turbulence in Studies related to Wind Loads on Buildings. National Physical Laboratory (U.K.) Aero Report 1143.
- Wirsching, P. H., & Light, M. C. (1980).** Fatigue under Wide Band Random Stresses. *Journal of the Structural Division, ASCE*, 106(ST7): 1593-1606.

INSTRUMENT CALIBRATION AND PROPERTY TESTS

Table A-1. List of Calibration Coefficients for Different Instruments

Ch. Number	Ch. Name	Recorded Parameter	Calibration Coefficient	Unit
1	Reference Pitot 1	wind speed	29.917√	ft/sec
2	Reference Pitot 2	wind speed	29.917√	ft/sec
3	Reference Pitot 3	wind speed	29.917√	ft/sec
4	Thermometer	Temperature	NA	NA
5	LT 1	distance	1	cm
6	LT 2	distance	1	cm
7	LT 3	distance	1	cm
8	Pitot 1	wind speed	29.917√	ft/sec
9	Pitot 2	wind speed	29.917√	ft/sec
10	Hotwire Anemometer	wind speed	10	ft/sec
11	Accelerometer	acceleration	9.81	m/sec ²
12	Strain gauge bridge	strain	0.00012	mm/mm

Strain Gauge Bridge Calibration

Strain gauge bridge was calibrated by considering the pole as a cantilever beam; applying static weights and record the readings. The strain value obtained from theory of a cantilever beam under moment loads plotted vs. readings from strain gauge in Figure A-2. As can be seen slope of the line is 0.00012; which is the calibration factor used in this research.

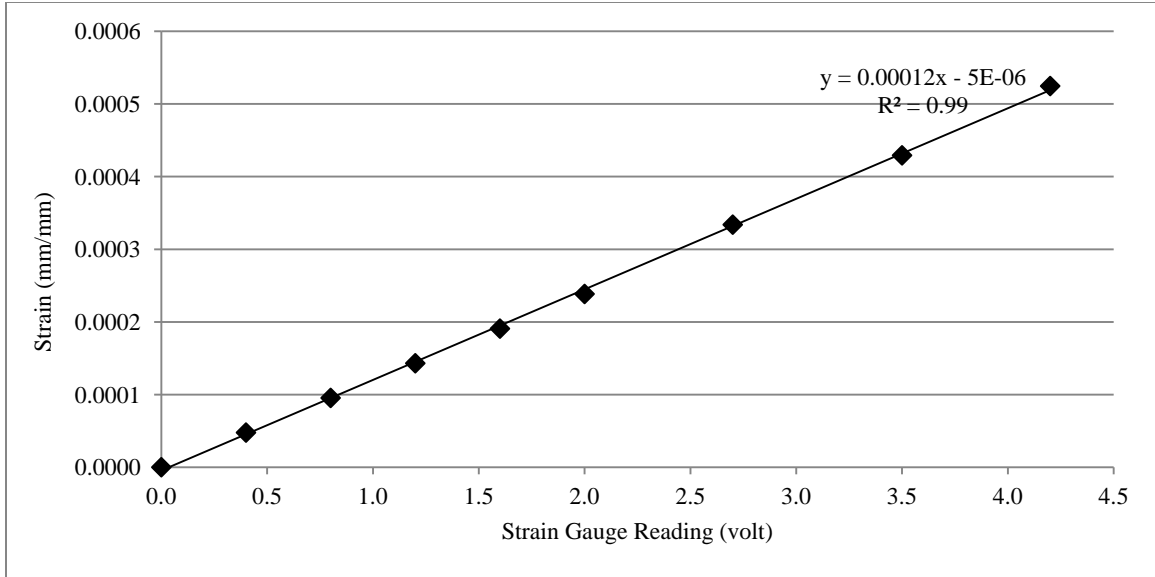


Figure A-1. Strain Gauge Bridge Calibration

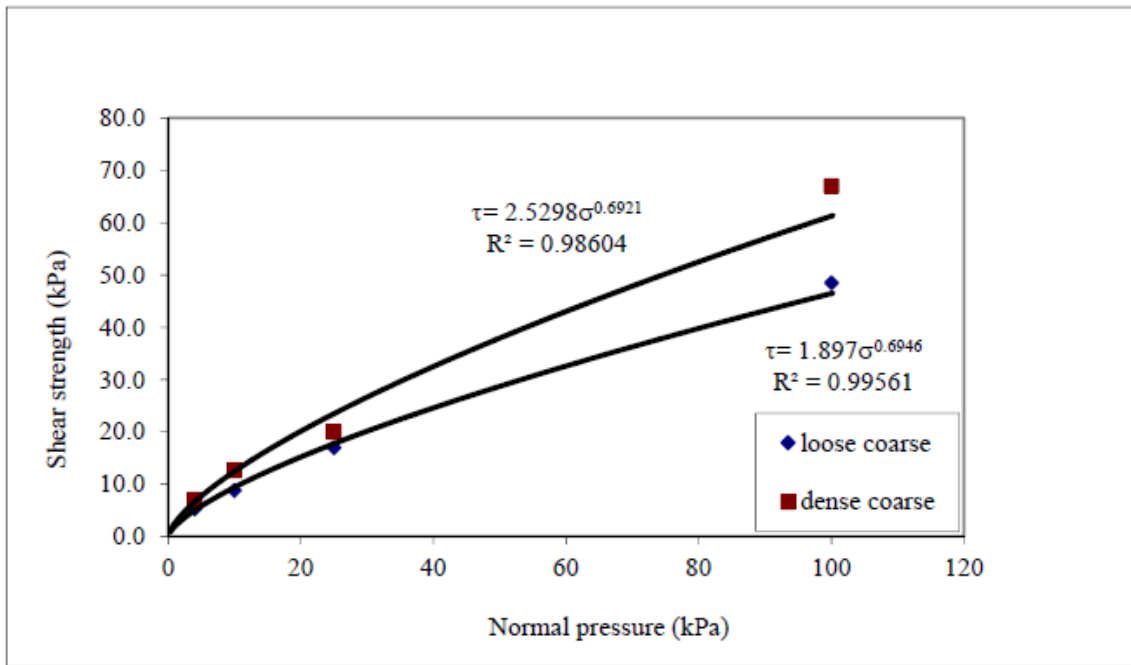


Figure A-2. Direct Shear Test Results on Ottawa Sand with Peak Nonlinear Failure Envelope

PICTURES

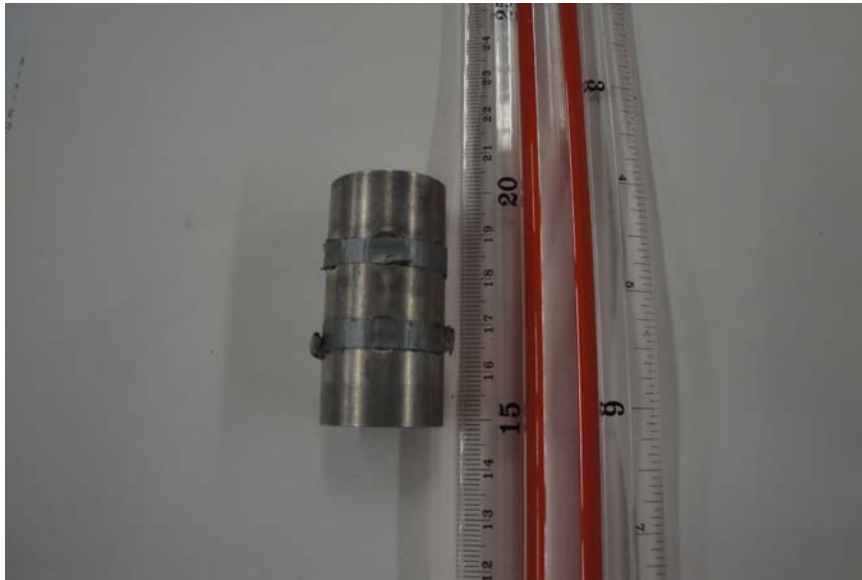


Figure B-1. Short Model Pile



Figure B-2. Long Model Pile



Figure B-3. Pile, Pole, Plate Model

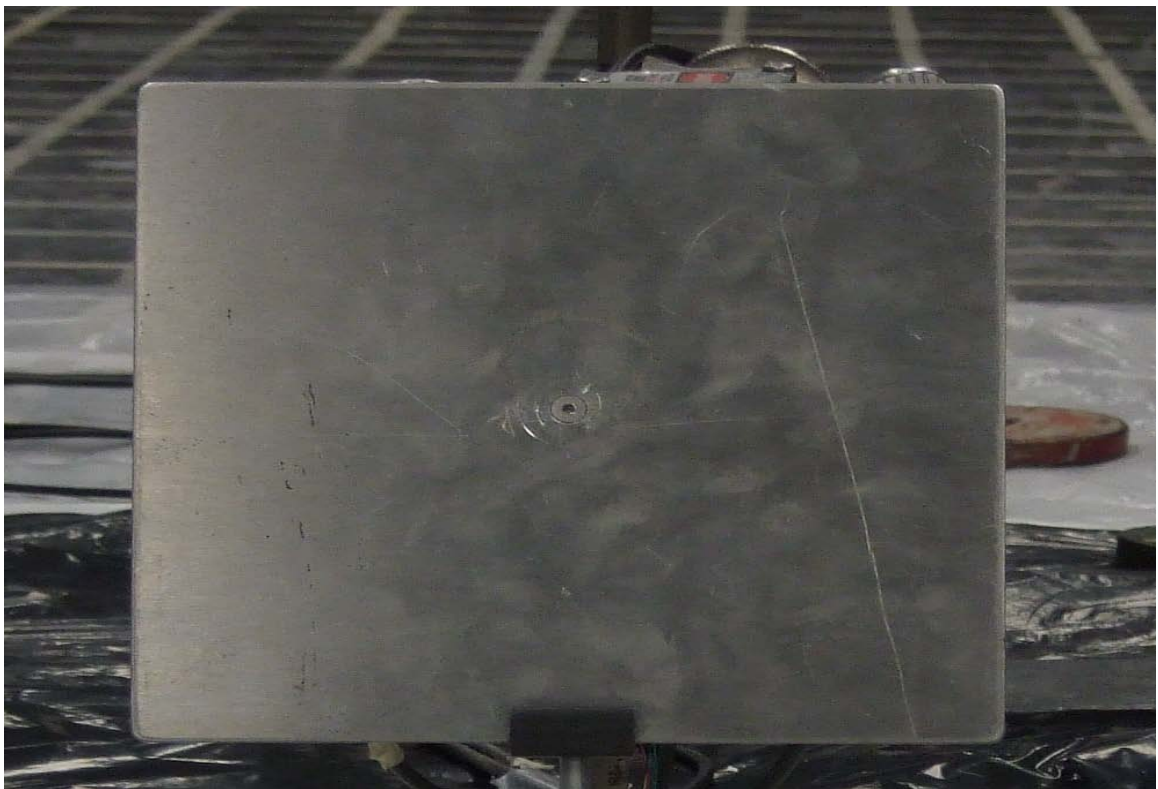


Figure B-4. Model Plate

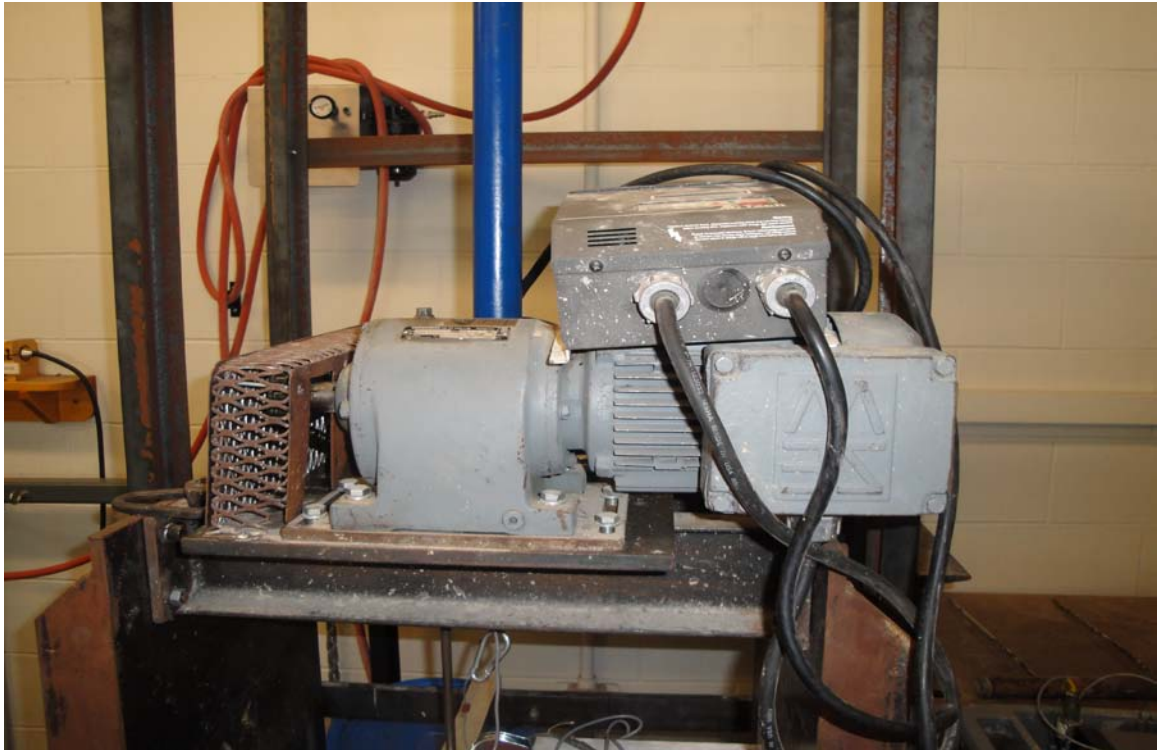


Figure B-5. Gearbox System and Moving Rod of Static Test Setup

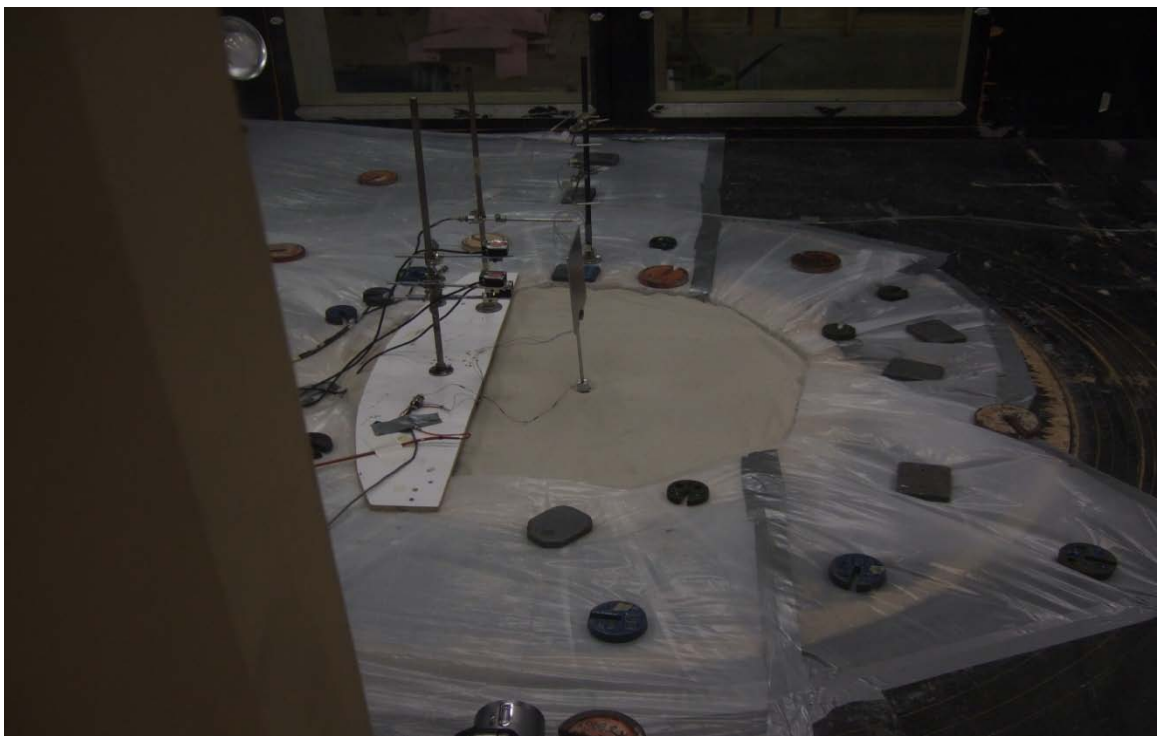


Figure B-6. Wind Tunnel Testing

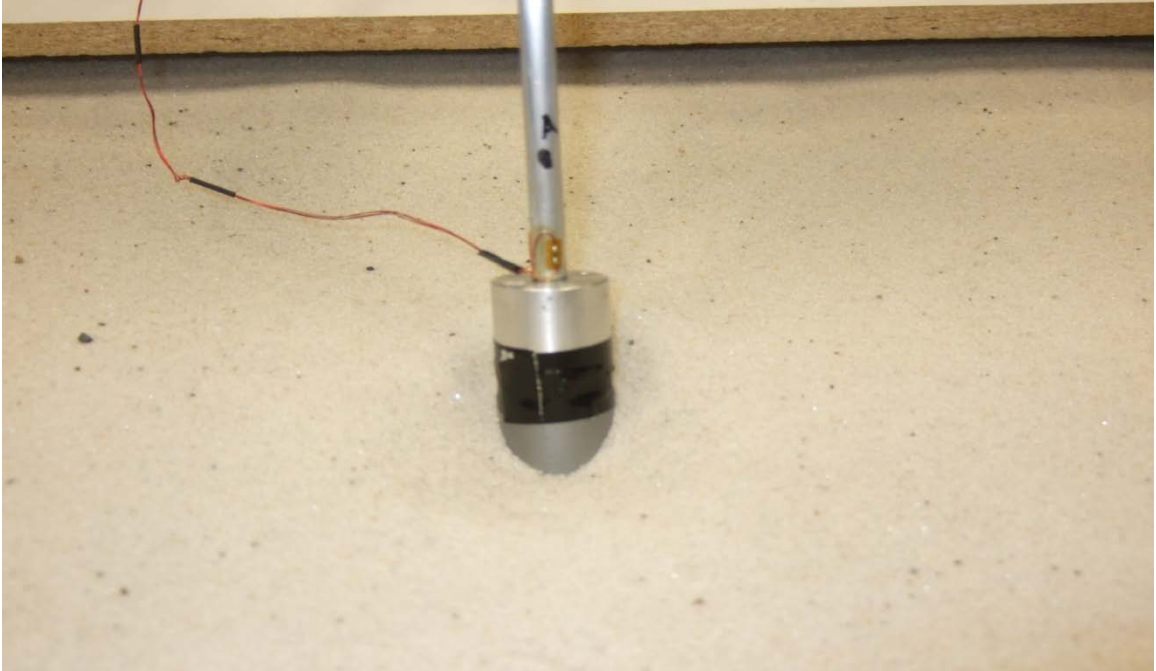


Figure B-7. Strain Gauge Bridge

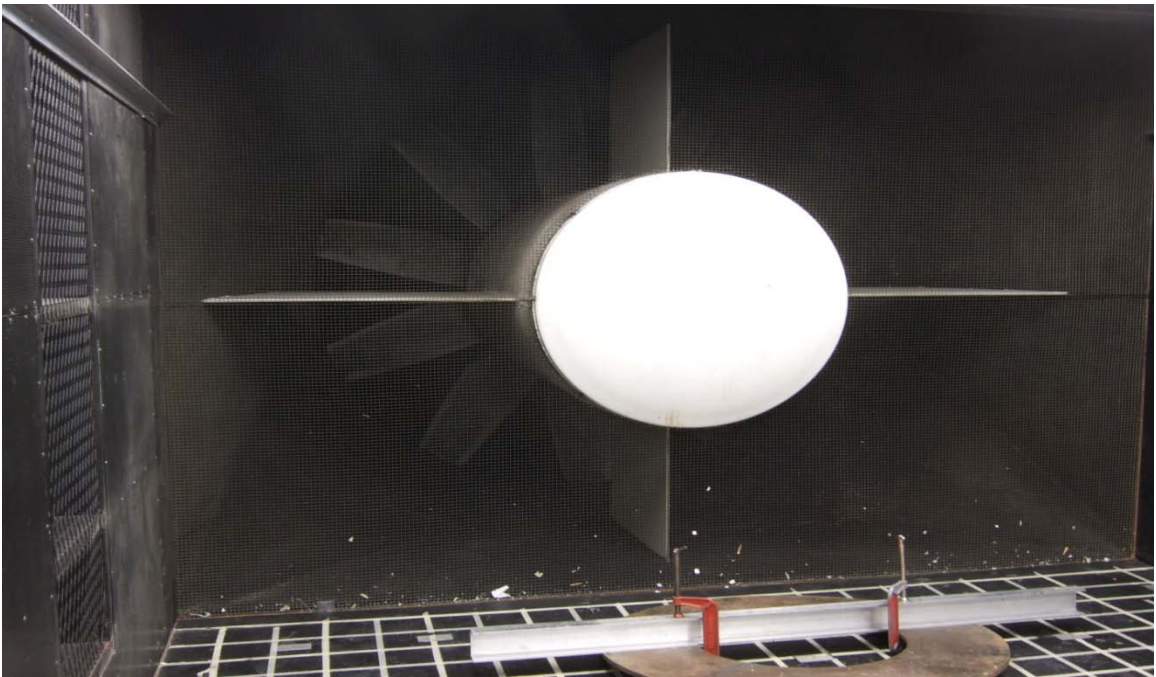


Figure B-8. Wind Tunnel Fan

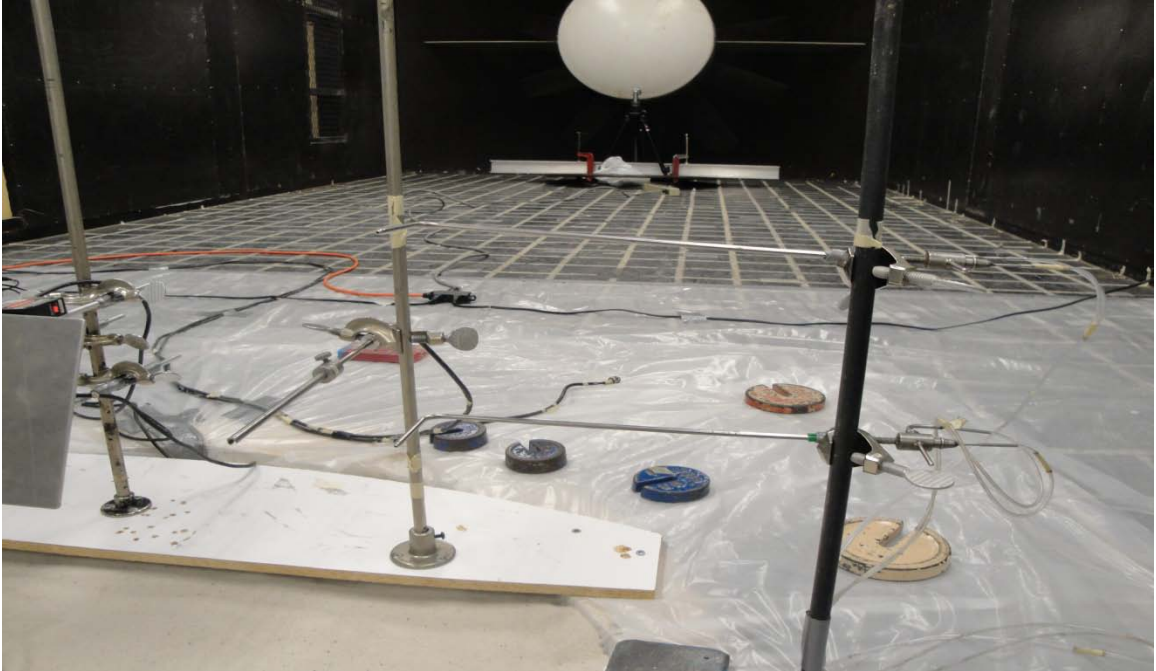


Figure B-9. Pitots and Hotwire Anemometer in Wind Tunnel Testing



Figure B-10. Reference Pitots in Wind Tunnel Testing

WIND TUNNEL RESULTS

Table C-1. List of Wind Tunnel Tests with their File Names

Number	TEST NUMBER	PILE	POLE	Fs
PRT-MM60-1	SIGN0111snE99R053P002a	Medium	Medium	300
PRT-MM60-2	SIGN0111snE99R054P001a	Medium	Medium	300
PRT-MM60-3	SIGN0111snE99R054P002a	Medium	Medium	300
PRT-MM60-4	SIGN0111snE99R001P003a	Medium	Medium	500
PRT-MM90-1	SIGN0111snE99R002P001a	Medium	Medium	300
PRT-MM30-1	SIGN0111snE99R001P001a	Medium	Medium	200
PRT-MM30-2	SIGN0111snE99R001P002a	Medium	Medium	500
PRT-MM30-3	SIGN1snE99R001P004	Medium	Medium	200
PRT-MM30-4	SIGN1snE99R001P005	Medium	Medium	200
PRT-MM30-5	SIGN1snE99R001P006	Medium	Medium	200
PRT-SM60-1	SIGN0111snE99R047P001a	Short	Medium	300
PRT-SM60-2	SIGN0111snE99R048P001a	Short	Medium	300
PRT-SM60-3	SIGN0111snE99R049P001a	Short	Medium	300
PRT-SM30-1	SIGN1snE99R001P001	Short	Medium	200
PRT-SM30-2	SIGN1snE99R001P002	Short	Medium	200
PRT-SM30-3	SIGN1snE99R001P003	Short	Medium	200
PRT-LL30-1	SIGN1snE99R007P001	Long	Long	200
PRT-LL30-2	SIGN1snE99R007P002	Long	Long	200

Test PRT-MM30-2:

Voltage	Laser	Laser	Laser	Pitot	Pitot	Hotwire (m/s)	Acceleromete r (m/s ²)	Strain Gauge (Volt)
	22cm (cm)	31cm (cm)	26cm (cm)	33cm (m/s)	25cm (m/s)			
0.5	3.6796	3.4757	3.6010	0.9543	0.5456	0.4144	0.1204	0.0166
1	3.6759	3.4702	3.5946	2.1947	1.8427	1.3668	0.2323	0.0854
1.5	3.6579	3.4665	3.5702	3.6325	3.2155	2.3290	0.8004	0.2553
2	3.6013	3.3733	3.5018	5.1438	4.7202	3.2849	1.3657	0.5155
2.5	3.5371	3.2764	3.4229	6.2498	5.6373	3.9059	1.7983	0.7521
3	3.4550	3.1578	3.3231	7.7209	7.0260	4.7661	2.0576	1.1197
3.5	3.3360	2.9940	3.1816	9.1409	8.3688	5.5811	2.2207	1.5430
4	3.1398	2.7278	2.9466	10.2632	9.4162	6.2028	2.3147	2.0100
4.5	2.7922	2.2601	2.5234	11.8183	10.8421	7.1277	2.2828	2.7001
5	2.1389	1.3670	1.7147	13.1716	11.9869	7.7519	2.1297	3.4672
5.5	1.2172	0.4650	0.5744	13.8915	12.8056	8.3916	1.8943	4.1946

Voltage	Mean Wind			
	Speed (m/s)	H (N)	θ (angle)	y_s (mm)
0.5	0.55	0.01	0.00	0.00
1.0	1.84	0.08	0.00	0.00
1.5	3.22	0.23	0.01	0.01
2.0	4.72	0.48	0.10	0.14
2.5	5.64	0.69	0.21	0.29
3.0	7.03	1.07	0.35	0.49
3.5	8.37	1.52	0.54	0.75
4.0	9.42	1.92	0.88	1.23
4.5	10.84	2.54	1.48	2.07
5.0	11.99	3.10	2.70	3.77
5.5	12.81	3.534	3.93	5.50

Voltage	Mean Wind Speed (m/s)	Duration (sec)	Total Number of Cycles
0.5	0.55	30	4.5
1	1.84	30	6
1.5	3.22	30	8.5
2	4.72	30	8.5
2.5	5.64	30	9.5
3	7.03	30	11.5
3.5	8.37	30	10.5
4	9.42	30	9
4.5	10.84	30	11
5	11.99	30	11.5

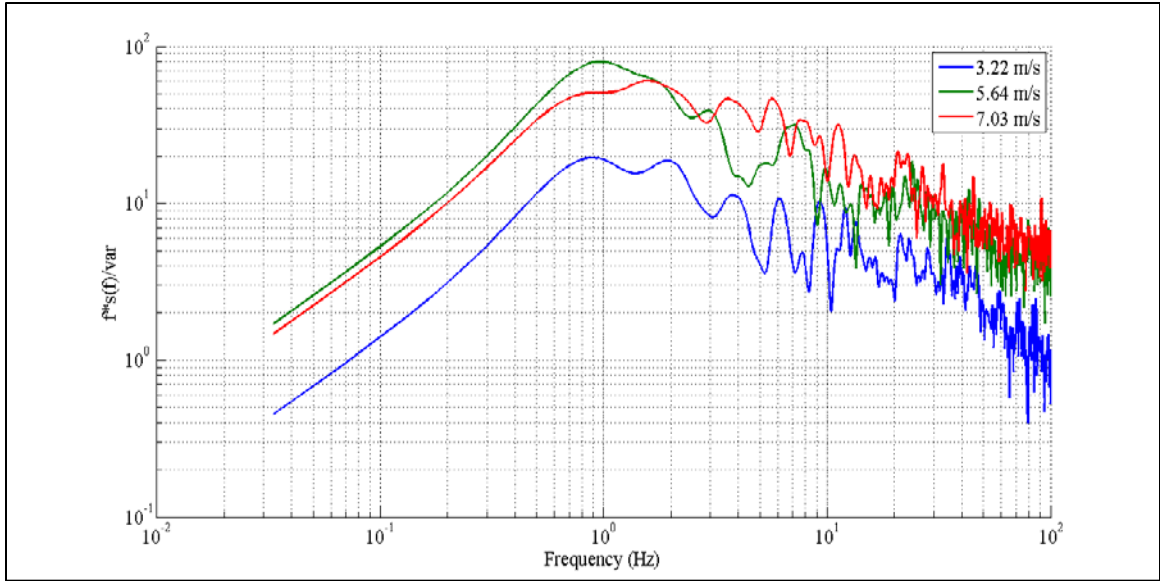


Figure C-1. PSD of Wind Speed Fluctuations

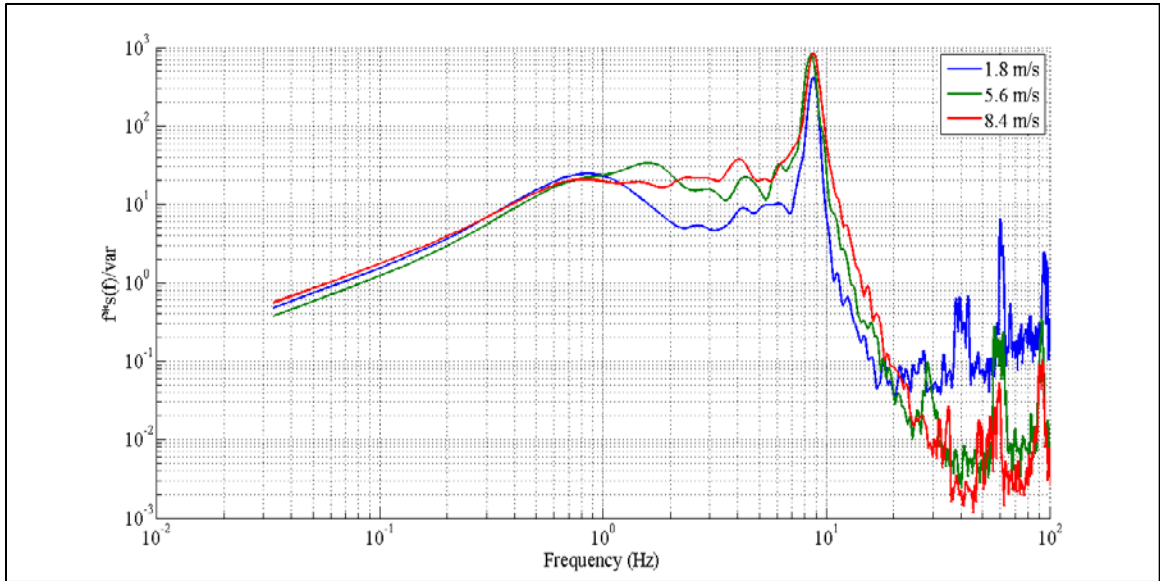


Figure C-2. PSD of Response

Test PRT-MM90-1:

Voltage	Laser 22cm (cm)	Laser 31cm (cm)	Laser 26cm (cm)	Pitot 33cm (m/s)	Pitot 25cm (m/s)	Hotwire (m/s)	Accelerometer (m/s ²)	Strain Gauge (Volt)
0.5	3.1072	3.1871	3.4154	1.3224	0.6997	22.5780	0.3720	0.0280
1	3.1005	3.1780	3.4065	2.5174	1.9130	16.9241	1.0324	0.1180
1.5	3.0772	3.1451	3.3751	3.7158	3.1998	13.5030	1.6926	0.2565
2	2.9859	3.0211	3.2586	5.1557	4.6242	14.3900	2.0295	0.5183
2.5	2.8402	2.8412	3.0899	6.5409	5.9159	15.1887	2.1998	0.8282
3	2.6609	2.6020	2.8642	7.8321	7.1774	15.9810	2.2646	1.2010
3.5	2.3316	2.1786	2.4627	9.4149	8.6550	16.8598	2.2477	1.7282
4	1.9088	1.5576	1.8305	10.5580	9.6505	17.5037	2.1397	2.2448
4.5	1.0091	1.2228	0.6980	11.9811	11.001	18.2925	1.8547	2.9157
5	0.4353	NA	0.0769	12.0891	11.217	18.4853	1.7022	3.3952

Voltage	Mean Wind Speed (m/s)	H (N)	θ (angle)	y_s (mm)
0.5	0.700	0.010	0.00	0.00
1	1.913	0.074	0.00	0.00
1.5	3.200	0.208	0.02	0.03
2	4.624	0.434	0.16	0.22
2.5	5.916	0.710	0.39	0.54
3	7.177	1.046	0.67	0.94
3.5	8.655	1.520	1.21	1.70
4	9.650	1.890	1.94	2.70
4.5	11.001	2.456	3.53	4.93
5	11.217	2.554	4.53	6.34

Voltage	Mean Wind Speed (m/s)	Duration (sec)	Total Number of Cycles
0.5	0.7	90	17
1	1.9	90	22
1.5	3.2	90	21.5
2	4.6	90	29
2.5	5.9	90	26.5
3	7.2	90	26.5
3.5	8.7	90	28
4	9.7	90	29
4.5	11.0	90	31
5	11.2	90	30

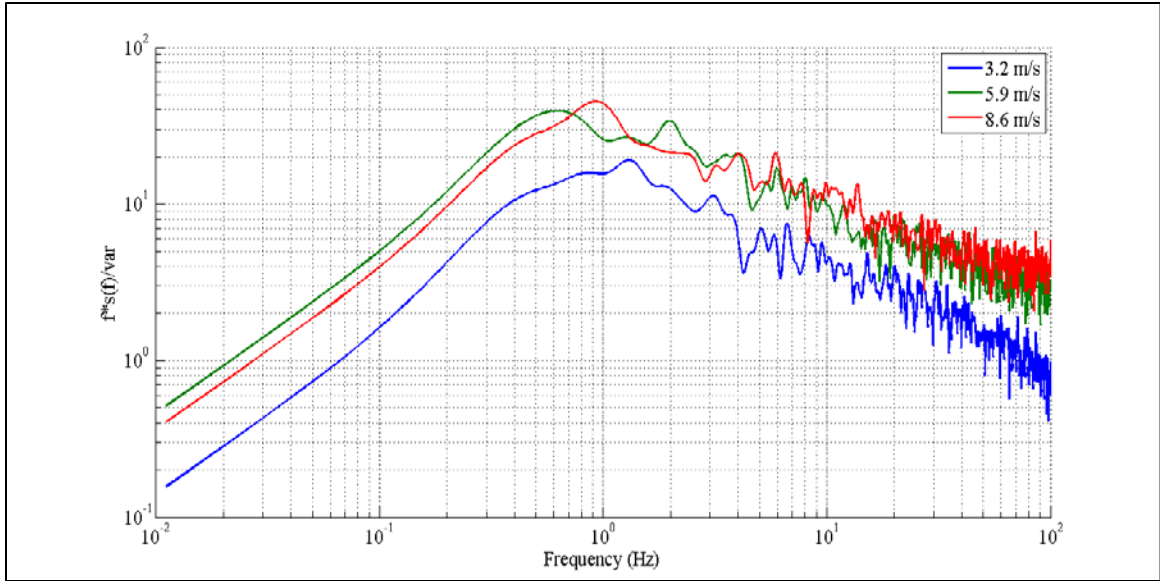


Figure C-3. PSD of Wind Speed Fluctuations

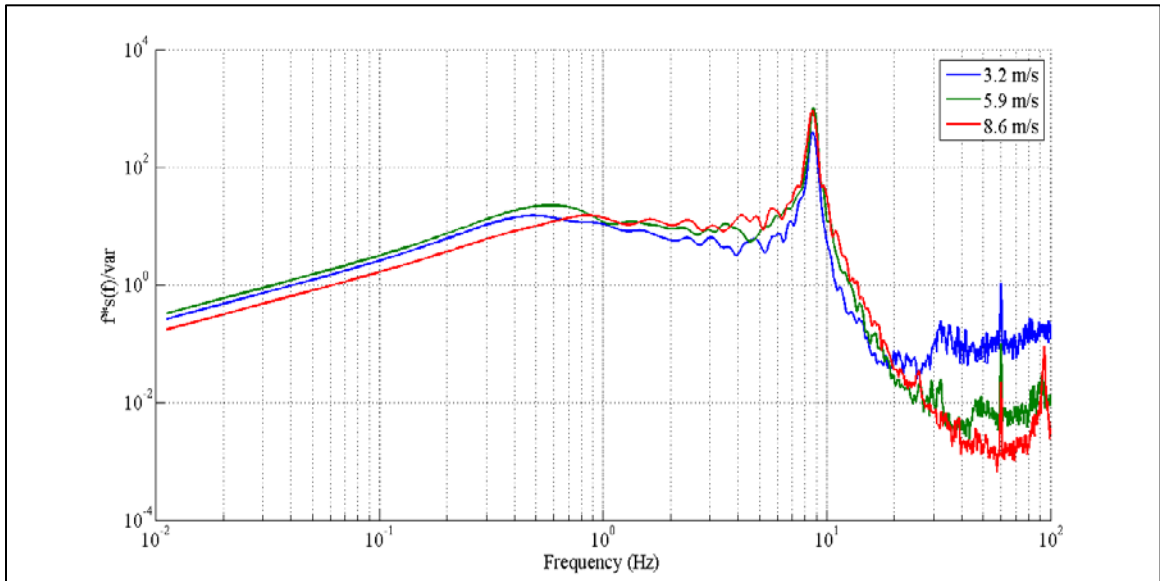


Figure C-4. PSD of Response

Test PRT-SM30-1:

Voltage	Laser	Laser	Laser	Pitot	Pitot	Hotwire	Accelerometer	Strain
	22cm (cm)	31cm (cm)	26cm (cm)	33cm (m/s)	25cm (m/s)	(m/s)	(m/s ²)	Gauge (Volt)
0.5	NA	4.4166	4.7851	1.1633	1.159	0.0686	0.0000	0.0517
1	NA	4.4142	4.7815	0.9309	1.901	0.8989	0.0513	0.1332
1.5	NA	4.3914	4.7513	2.0245	3.320	1.8207	0.3514	0.3798
2	NA	4.0881	4.3536	3.0017	4.401	2.5812	1.1437	0.6027
2.5	NA	3.6427	3.7648	3.4184	4.939	3.1095	1.8379	0.7022

Voltage	Mean Wind	H (N)	θ (angle)	y_s (mm)
	Speed (m/s)			
0.5	1.16	0.026	0.0045	0.0039
1	1.95	0.076	0.0154	0.0135
1.5	3.32	0.225	0.1199	0.1046
2	4.40	0.395	1.3809	1.2054
2.5	4.94	0.495	2.8223	2.4649

Voltage	Mean Wind Speed (m/s)	Duration (sec)	Num cycles
0.5	1.16	30	5
1	1.9	30	5
1.5	3.3	30	8.5
2	4.4	30	8.5
2.5	4.9	10	2.5

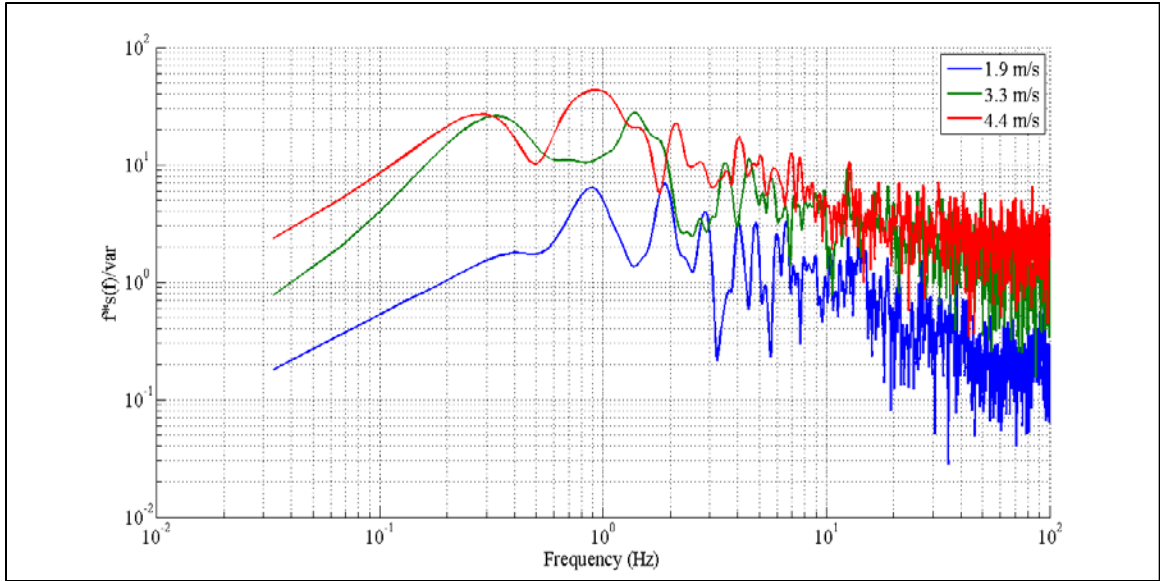


Figure C-5. PSD of Wind Speed Fluctuations

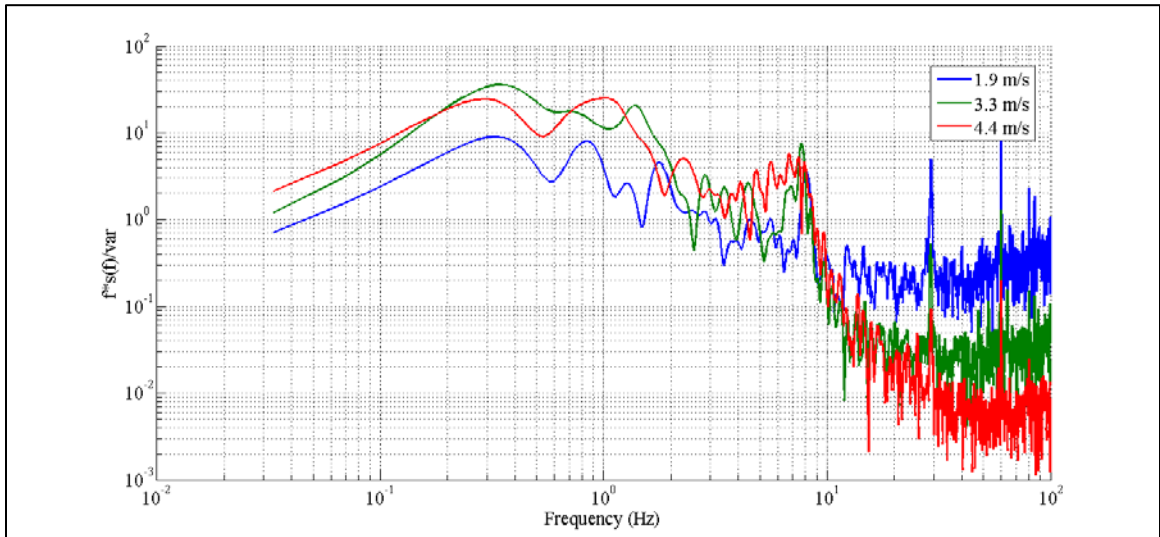


Figure C-6. PSD of Response

Test PRT-SM60-1:

Voltage	Laser 22cm (cm)	Laser 31cm (cm)	Laser 26cm (cm)	Pitot 33cm (m/s)	Pitot 25cm (m/s)	Hotwire (m/s)	Accelerometer (m/s ²)	Strain Gauge (Volt)
0.5	6.3416	7.1090	6.5121	1.5103	1.0363	0.5698	0.4465	0.0300
1	6.3170	7.0667	6.7845	2.5314	1.9469	0.9785	0.6432	0.1087
1.5	6.1776	6.8671	6.6652	3.8834	3.3705	1.5382	1.1705	0.2926
2	5.4409	5.8382	5.8003	4.7260	4.3048	1.9016	1.2118	0.5593

Voltage	Mean Wind Speed (m/s)	H (N)	θ (angle)	y_s (mm)
0.5	1.06	0.023	0.0001	0.0001
1	1.94	0.079	0.0653	0.0570
1.5	3.37	0.231	0.4488	0.3916
2	4.30	0.376	2.3073	2.0146

Voltage	Mean Wind Speed (m/s)	Duration (sec)	Total Number of Cycles
0.5	1.06	60	13.5
1	1.9	60	12.5
1.5	3.4	60	17.5
2	4.3	20	7

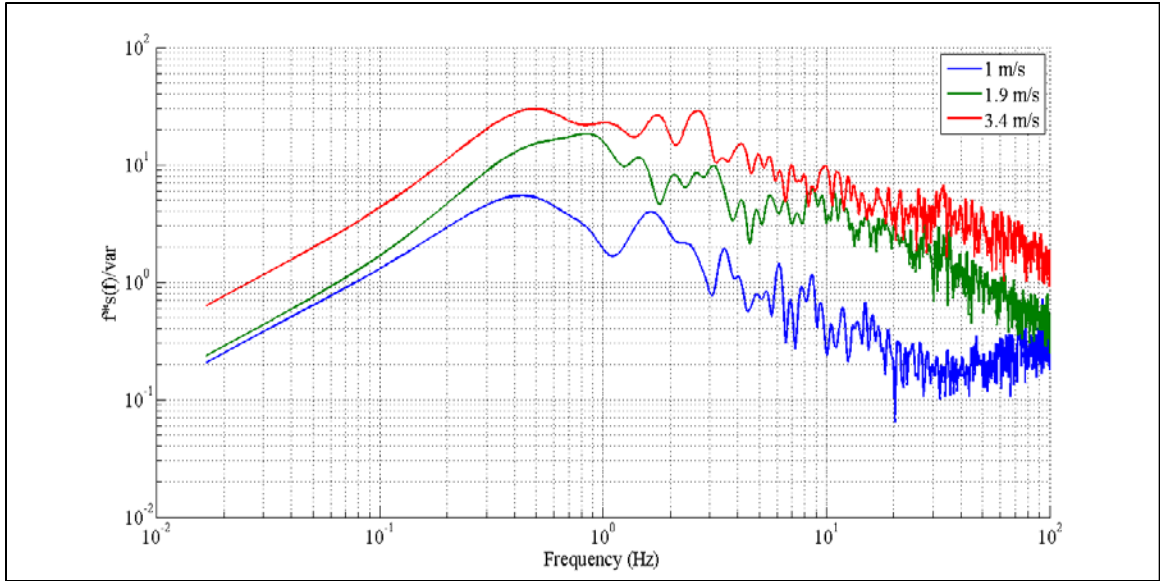


Figure C-7. PSD of Wind Speed Fluctuations

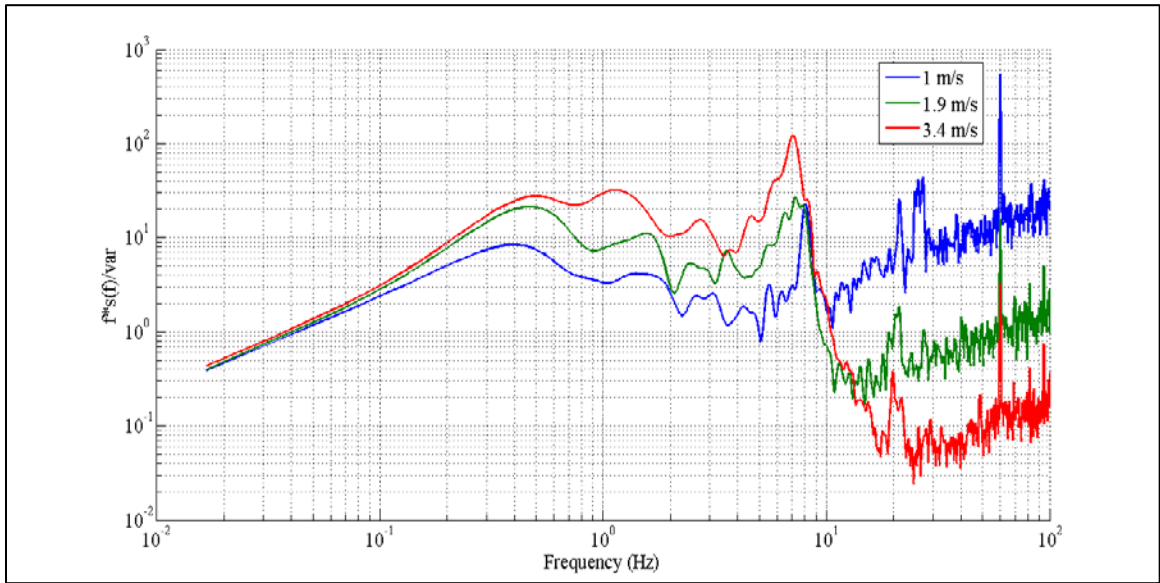


Figure C-8. PSD of Response

CURRICULUM VITAE

Name:	Alireza Varshoi	
Post Secondary Education and Degrees:	M.E.Sc., Geotechnical Engineering Western University London, Ontario, Canada	2010-2012
	B.E.Sc., Civil Engineering K. N. Toosi University of Technology Tehran, Tehran, Iran	2004-2008
Honours and Awards:	Western Graduate Research Scholar	2010-2012
Related Work Experience:	Teaching Assistant Western University	2010-2012
Publications:	Varshoi, A. , and Newson, T. (2012) Response of Pile Foundations to Random Cyclic Loads. Geo-Manitoba Conference. (Abstract Accepted)	